Dynamique et instabilités de combustion des flammes swirlées

Paul Palies

École Centrale Paris

THÈSE

presentée par

Paul Palies

pour l'obtention du

GRADE de DOCTEUR

Formation doctorale : **Energétique**

Laboratoire d'accueil : **Laboratoire d'Energétique Moléculaire et Macroscopique, Combustion (EM2C) du CNRS et de l'ECP**

Dynamique et instabilités de combustion des flammes swirlées

Soutenue le Lundi 11 Octobre 2010

Composition du jury :

MM.	Baillot	F.	Rapporteur
	Nicoud	F.	Rapporteur
	Bailly	C.	Président
	Gondret	P.	Membre
	Larroya-Huguet	J.C.	Membre
	Durox	D.	Directeur
	Schuller	T.	Encadrant
	Candel	S.	Directeur

Ecole Centrale des Arts et Manufactures
Grand Etablissement sous tutelle
du Ministère de l'Education Nationale
Grande Voie des Vignes
92295 CHATENAY MALABRY Cedex
Tél. : 33 (1) 41 13 10 00 (standard)
Télex : 634 991 F EC PARIS

Laboratoire d'Énergétique Moléculaire et Macroscopique, Combustion (E.M2.C.)
UPR 288, CNRS et École Centrale Paris
Tel. : 33 (1) 41 13 10 31
Telecopie : 33 (1) 47 02 80 35

2010 - 2010ECAP0029

À mon père.

Chercher ne signifie rien en peinture.
Ce qui compte, c'est trouver.

Pablo Picasso.

The Arts (1923).

Remerciements

La présente thèse est un travail de trois années mené au laboratoire EM2C qui dépend de l'Ecole Centrale Paris et du Centre National de la Recherche Scientifique. Bien qu'il n'y ait qu'un nom, le mien, en page de garde, il s'agit d'un travail d'équipe au sein d'un laboratoire où travaillent de nombreuses personnes que je me dois de remercier.

Ainsi, mes remerciements s'adressent en premier lieu à Nasser Darabiha puis à Estelle Iacona, pour leur accueil au laboratoire.

Je tiens à vivement remercier mes trois encadrants, Sébastien Candel, Daniel Durox et Thierry Schuller qui m'ont offert la possibilité de travailler sur un sujet passionnant pendant ces trois années. Sébastien a toujours été disponible pour discuter des avancées dans mes travaux tout en me communiquant une grande motivation. Daniel m'a suivi quotidiennement pendant ces trois années en me formant notamment aux sciences expérimentales. Enfin, Thierry a aussi contribué significativement à l'avancée de ma thèse. Au-delà des compétences techniques et des connaissances scientifiques riches, denses et rigoureuses que Sébastien, Daniel et Thierry ont su me transmettre, je retiens aussi de ce travail des valeurs importantes telles que l'engagement, le travail, la solidarité et l'humilité. Je n'oublierai pas tous les conseils qu'ils m'ont donné et toutes les méthodes de travail qu'ils m'ont transmises.

Je souhaite par ailleurs remercier Laurent Gicquel, Pascal Morenton et Geoff Searby pour leur aide et leurs conseils sur certains points dans mon travail de thèse.

Je souhaite remercier tous les membres du jury de ma soutenance de thèse. Christophe Bailly pour avoir présidé ce jury, Françoise Baillot et Franck Nicoud pour avoir été rapporteur de celle-ci, et finalement Philippe Gondret et Juan-Carlos Larroya-Huguet pour leur présence.

Je voudrais remercier aussi les chercheurs et enseignants-chercheurs du laboratoire qui participent à faire de ce laboratoire un lieu intellectuellement stimulant : Anne Bourdon, Sébastien Ducruix, Benoit Fiorina, Olivier Gicquel, Christophe Laux, Marc Massot, Franck Richecoeur, Philippe Rivière, Denis Veynante et Laurent Zimmer.

Mes remerciements s'adressent aussi aux ingénieurs d'étude et de recherche, Jérôme Beaunier, Matthieu Boileau et Deanna Lacoste, aux techniciens Erika Jean-Bart, Samira El-Ghazi, Yannick Le Teno, Jordan Marescaux et aux agents administratifs du laboratoire EM2C, Anne-Cécile Aiach, Stéphanie Joseph et Virginie Martinez.

Je remercie les docteurs récemment diplômés pour les moments chaleureux et amicaux passés au laboratoire : Patrick Duchaine, Yoann Mery, Nicolas Tran, Ronan Vicquelin. Ces remerciements vont aussi aux post-doctorants : Hector Gomart, Thomas Schmitt et Gaofeng Wang. Et j'adresse mes encouragements aux futurs docteurs : Tapish Agarwal, Pierre Auzillon, Frédéric Boudy, Jean-François Bourgouin, Miloud Chahlafi, Alexis Cuquel, Sébastien Depraz, François Doisneau, Max Duarte, Farrah Kaddouri, Layal Hakim, Damien Kah, Ammar Lamraoui, Jingxuan Li, Théodore Providakis, Sorour Refahi, Diane Rusterholtz, Alessandro Scarpato, Diana Tudorache et Simon Vassant.

Je remercie enfin le noyau dur de ma famille, ma courageuse mère Marie-Christine, Christian, ma petite soeur Valentine, Julien et Léna pour leur soutien depuis toujours. Je pense aussi à mes adorables grands-parents Michel et Colette. Je pense aussi à mes oncles, tantes, cousins et cousines Mai et Palies qui font que cette famille est très soudée et que c'est toujours un grand bonheur de se retrouver.

Abstract

This work is concerned with the dynamics of premixed confined turbulent swirling flames submitted to acoustic velocity disturbances. The general objective is to gain an understanding of the mechanisms governing the response of these flames and to derive predictive methods for combustion instabilities. Swirling flows are first reviewed in terms of swirl numbers and novel expressions for them are given. Perturbed form of the swirl number are suggested taking into account acoustic disturbances in the flow. The experimental system comprises an upstream manifold, an injector equipped with a swirler and a transparent flame tube allowing direct visualization of the flame motion. Two operating points are investigated corresponding to different bulk velocities. The upstream manifold and the flame tube of the burner can be easily change to test several configurations. The burner acoustic is also analyzed in term of coupled cavities approach to determined the resonant frequencies of the system in non reactive cases. Experiments are carried out to measure the system eigen frequencies and the estimate damping coefficient of the various burners arrangements. A criterion for decoupling acoustic mode is suggested. The flow dynamics is examined in terms of mode conversion occurring at the swirler or downstream an airfoil cascade. This part of the work, carried out with numerical simulations, shows that when submitted to an acoustic wave, a swirler gives rise to an azimuthal convective wave in addition to the transmitted acoustic wave. Both axial and radial swirlers are prone to this mechanism as confirmed by experiments. It is found that this mode conversion process has a strong impact on the flame dynamics in swirling flames combustors. Combustion dynamics is then analyzed by measuring the flame describing function (FDF) of this burner. This FDF is used to determine the response of the flame to acoustic velocity disturbances propagating on the upstream flow. It is shown that the Strouhal number is a suitable dimensionless group to characterize the swirling flame response. The flame dynamics is also analyzed with an ensemble of diagnostics including pressure probes, photomultipliers and laser Doppler velocimeter (LDV). A model for the linear swirling flame transfer function is derived theoretically. The physical mechanisms driving the response of the flame are identified : vortex rollup and swirl number fluctuations. The vortex rollup is associated to the acoustic wave transmitted downstream of the swirler and entering in the combustor while the swirl number fluctuations are directly linked to the mode

conversion mechanisms downstream the swirler which induced different axial and azimuthal speeds upstream the flame. The rollup phenomena acts at the extremity of the flame while swirl number fluctuations act on the flame angle. These competiting mechanisms act constructively or destructively leading to low or high gains in the flame response depending on the frequency. These mechanisms are retrieved by large eddy simulations of the flame dynamics. Finally, an instability analysis is carried out by combining the experimental flame describing function (FDF) and an acoustic model of the combustor to determine the frequency and the amplitude of the velocity disturbances at the limit cycle. A good agreement between predictions and experiments is obtained in most cases indicating that the method is suitable subject to further developments.

Résumé

Ce travail traite de la dynamique des flammes turbulentes prémélangées confinées et swirlées soumises à des perturbations de vitesses acoustiques. L'objectif général est d'acquérir une compréhension des mécanismes régissant la réponse de ces flammes et d'en tirer des méthodes de prévision des instabilités de combustion. Les écoulements swirlés sont d'abord examinés en termes de nombre de swirl et de nouvelles expressions sont données pour cette quantité. On traite notamment des effets de perturbations de vitesse et une expression est proposée qui tient compte des fluctuations de vitesses dans l'écoulement. Le système utilisé pour l'étude expérimentale comprend une cavité amont, un injecteur équipé d'un swirler et un tube à flamme transparent permettant la visualisation directe du mouvement de la flamme. Deux points de fonctionnement sont étudiés correspondant à des vitesses débitantes différentes. La cavité amont et le tube à flamme du brûleur peuvent être facilement changés pour étudier plusieurs configurations différentes. L'acoustique du brûleur est également analysée au moyen d'une approche de cavités couplées pour déterminer les fréquences de résonance du système en configuration non-réactive. Des expériences sont menées pour mesurer les fréquences propres du système et l'estimation du coefficient d'amortissement est réalisée à partir de la réponse du système à une modulation externe. Un critère de découplage des mode acoustiques est proposé. La dynamique de l'écoulement est examinée en termes de conversion de modes au niveau de la vrille (swirler) ou dans une grille d'aubes. Cette partie du travail, effectuée au moyen de simulations numériques montre que lorsqu'une grille ou une vrille sont soumis à une onde acoustique, le swirler donne naissance à une onde azimutale convective en plus de l'onde acoustique axiale transmise. Les deux types de swirlers, axial et radial, donnent lieu à ce mécanisme, un fait confirmé par des expériences. Il est montré que ce processus de conversion de mode a un impact important sur la dynamique de la flamme swirlée. La dynamique de la combustion est ensuite analysée en mesurant la fonction de transfert généralisée ainsi que les distributions de taux de dégagement de chaleur au cours du cycle d'oscillation. La fonction de transfert est utilisée pour déterminer la réponse de la flamme à des perturbations acoustiques se propageant dans l'écoulement en amont de la flamme. Il est aussi montré que le nombre de Strouhal est un groupe sans dimensions qui permet de caractériser la réponse de la flamme. La dynamique est également analysée au moyen d'un

ensemble de diagnostics comprenant des sondes de pression, un photomultiplicateur et un vélocimètre laser Doppler. Un modèle pour la fonction de transfert linéaire de la flamme est dérivé théoriquement à partir d'une description de la flamme au moyen de l'équation pour une variable de champ G. Les mécanismes physiques de la réponse de la flamme sont identifiés : enroulement tourbillonnaire et fluctuations du nombre de swirl. L'enroulement tourbillonnaire est associé à l'onde acoustique transmise en aval du swirler et qui pénètre dans la chambre de combustion. Tandis que les fluctuations du nombre de swirl sont directement liées aux mécanismes de conversion de mode au swirler qui induit différentes vitesses pour les perturbations axiales et azimutales. L'enroulement tourbillonnaire enroule l'extrémité de la flamme tandis que les fluctuations du nombre de swirl agissent sur l'angle de la flamme. Ces deux mécanismes en compétition se combinent de manière constructive ou destructive conduisant à des gains faibles ou élevés dans la réponse de la flamme en fonction de la fréquence. Ces mécanismes sont retrouvés par simulation aux grandes échelles (LES). Enfin, une analyse d'instabilité est réalisée en combinant la fonction de transfert généralisée expérimentale et un modèle acoustique du brûleur afin de déterminer la fréquence et l'amplitude des perturbations de vitesse au cycle limite. Un bon accord entre les prévisions et les résultats d'expériences est obtenu dans la plupart des cas, ce qui indique que la méthode est appropriée pour de futurs développements.

Introduction

Partie I : Flammes swirlées, configuration expérimentale et acoustique du système

Chapitre 1 : Ecoulements et flammes swirlées

Les écoulements swirlés sont couramment rencontrées en mécanique des fluides, en combustion et dans de nombreuses applications industrielles comme les turbines à gaz ou les turboréacteurs. Ces écoulements en rotation sont généralement caractérisés par le nombre de swirl, un groupement sans dimensions dont la définition est d'abord donnée. On déduit de cette expression une forme perturbée de ce nombre qui fait intervenir la différence entre les fluctuations relatives de vitesse azimutale et axiale. On considère dans un deuxième temps l'effet de l'évolution de l'angle des pales pour un swirler axial. Comme l'angle des pales change avec le rayon, le nombre de swirl peut être estimé au moyen d'une intégration numérique. Une expression est donc déduite en tenant en compte de l'angle au bord de fuite des pales de la vrille. La dernière partie du chapitre traite des effets instationnaires sur le nombre de swirl. On montre dans ce chapitre qu'il est possible de prendre en compte les termes d'accumulation de moment angulaire azimutal et de quantité de mouvement axiale. Une synthèse rassemble finalement les expressions obtenues pour le nombre de swirl.

Chapitre 2 : Description de l'expérience et diagnostics

L'expérience de laboratoire et les diagnostics utilisés dans ce document sont décrits dans ce chapitre. La description porte sur les différents éléments de l'installation et traite notamment des swirlers. Les diagnostics de mesures associées à la vélocimétrie laser (LDV), au photomultiplicateur et aux microphones sont ensuite exposés. On décrit la transformée d'Abel qui est utilisée dans ce manuscrit pour déduire la structure de flamme des images d'émission et analyser la dynamique de la flamme swirlées au cours d'un cycle d'oscillation. Deux méthodes de détermination du taux de dégagement de chaleur d'une flamme sont ensuite comparées. La première utilise un photomultiplicateur qui capte toute la lumière rayonnée par la flamme. La seconde est basée sur la somme de l'intensité lumineuse reçue par les pixels d'une caméra ICCD sans filtre. Il est démontré que les signaux déduits de ces deux types de capteurs sont en bon accord.

Chapitre 3 : Acoustique des systèmes de combustion : données expérimentales et analyse théorique

La réponse acoustique du système de cavités couplées est examinée dans ce chapitre. Cette réponse est d'abord étudiée expérimentalement pour chaque système afin de déterminer les fréquences de résonance. Le taux d'amortissement est également obtenu pour les diverses configurations. On traite ensuite des conditions pour lesquelles les modes acoustiques d'une chambre remplie de produits de combustion chauds peuvent être considérées comme découplés de l'acoustique de la partie amont de la chambre de combustion fournissant les réactifs frais. On introduit à cet effet un paramètre de couplage est $\Xi = (c_b\rho_b)/(\rho_u c_u)S_2/S_3 \simeq (T_u/T_b)^{(1/2)}(S_2/S_3)$ où T_u et T_b sont respectivement les températures des gaz frais et des gaz brûlés, S_3/S_2 est le rapport des sections entre cavité aval et dispositif d'injection. Il est démontré que l'acoustique du système peut être analysé en découplant les signatures acoustiques de la partie aval de la partie amont pour des petites valeurs du paramètre Ξ. Cette séparation est possible pour les petites valeurs de l'impédance de sortie de la chambre, lorsque la sortie de la chambre est ouverte correspondant aux conditions atmosphériques ou pour des fortes valeurs de l'impédance de sortie, lorsque par exemple la chambre est équipée d'une tuyère sonique. Le cas d'une cavité amont caractérisée par une résonance de type Helmholtz est étudié en détail lorsque l'impédance de sortie est modifiée. Il est démontré que les instabilités de combustion auto-entretenues se développent de préférence autour du mode résonant de la cavité amont. Les relations exactes dans lesquelles les modes de la cavité amont et de la cavité aval sont découplés sont obtenues.

Partie II : Dynamique de l'écoulement et de la combustion

Chapitre 4 : Processus de conversion de mode dans une grille d'aubes et dans un swirler

Quand une onde acoustique interagit avec une grille d'aubes, un mode tourbillonnaire est généré et il en résulte des perturbations de vitesses transversales. Ce processus de conversion de mode est étudié pour expliquer la dynamique des écoulements observés lorsque des vrilles (swirlers) sont soumises à des perturbations acoustiques incidentes. Le phénomène est d'abord etudié dans le cas d'une grille dans une configuration bidimensionnelle au moyen d'une analyse théorique fondée sur le modèle du disque actuateur. Ce modèle est simplifié pour tenir compte du faible nombre de Mach de l'écoulement. Le champ de vitesse en aval de la grille possède deux composantes, une perturbation axiale associée à l'onde acoustique transmise et une perturbation transversale correspondant à l'onde tourbillonnaire générée aux bords de fuite de la grille. Le modèle fournit l'amplitude des deux composantes et définit leur déphasage. Des simulations numériques sont réalisées dans une deuxième étape pour valider ce modèle dans le cas d'un faible nombre de Reynolds : Re = 2 700 basé sur la longueur de corde des aubes. Des diagrammes spatio-temporels des perturbations de vitesses déduits de ces simulations sont utilisés pour mettre en évidence les deux types de modes. Les expériences sont ensuite effectuées dans le cas d'une vrille (swirler) axiale placée dans une conduite cylindrique et soumise à des ondes acoustiques planes émises en amont. Les amplitudes et phases des deux composantes de vitesse mesurée dans les directions axiale et azimutale sont en bon accord avec les estimations théoriques et avec les calculs numériques.

Chapitre 5 : Dynamique combinée d'un swirler et d'une flamme swirlée turbulente

La dynamique de flammes prémélangées swirlées est étudiée en analysant leur réponse aux perturbations de vitesses incidentes. Une fonction de transfert généralisée est déterminée en balayant une gamme de fréquences allant de 0 à 400 Hz et en changeant la fluctuation de vitesse entre 0 et 72 % de la vitesse débitante. Le taux de dégagement de chaleur instationnaire est déduit de l'intensité d' émissions du radical OH^*. Cette information globale est complétée par des transformées d'Abel d'images formées par moyenne synchronisée par la phase. On obtient ainsi la distribution d'émission lumineuse. En supposant que l'intensité lumineuse est proportionnelle au taux de dégagement de chaleur, il est possible de déduire la distribution des taux de dégagement de chaleur instationnaires en W m^{-3} et observer l'évolution de la distribution spatiale de cette quantité au cours du cycle de modulation et pour différentes fréquences de forçage. Ces données peuvent être utiles pour la détermination des régimes d'instabilité mais aussi donnent des indications sur les mécanismes qui contrôlent la dynamique des flammes swirlées. Il est montré expérimentalement et analytiquement que le swirler soumis à des ondes acoustiques provenant de l'amont génère une onde

tourbillonnaire en aval. La flamme est donc soumise à une perturbation acoustique axiale transmise au travers de la vrille qui se propage à la vitesse du son et à une perturbation de vitesse azimutale qui est convectée par l'écoulement. Il en résulte que la réponse de la flamme est déterminée par les effets combinés de ces perturbations de vitesse axiale et azimutale. Les perturbations axiales provoquent l'enroulement d'un tourbillon à l'extrémité de flamme tandis que les perturbations de vitesses azimutales génèrent une oscillation angulaire de la base de la flamme. La phase entre les perturbations incidentes est contrôlée par le délai de convection des perturbations entre la sortie du swirler et la base de la flamme. L'interférence constructive ou destructive entre les différentes perturbations provoque respectivement des forts ou faibles gains dans la réponse de la flamme. On peut ainsi expliquer les caractéristiques principales de la fonction de transfert des flammes swirlées.

Chapitre 6 : Effet de la géométrie du swirler et du nombre de swirl sur la fonction de transfert généralisée

Ce chapitre traite de la réponse des flammes swirlées soumises à des perturbations de vitesses acoustiques lorsque la rotation de l'écoulement est produite par un swirler axial ou radial. L'objectif est de comparer les réponses obtenues dans ces deux cas. La réponse est caractérisée en terme de fonction de transfert généralisée, qui élargit la fonction de transfert de flamme en considérant non seulement la fréquence mais aussi l'amplitude des perturbations de vitesses. Cet outil a montré sa pertinence dans l'étude des instabilités de combustion couplées par l'acoustique. Les résultats indiquent que pour les deux types de swirlers, la dynamique est essentiellement similaire pour les gains et les phases de la réponse. Il est également constaté que la valeur du nombre de swirl influence fortement la réponse en terme de gain. La forme caractéristique de la fonction de transfert généralisée, avec un minimum et un maximum local, se retrouve pour les deux cas de swirlers. Cette réponse caractéristique correspond à des mécanismes décrits précédemment (fluctuations du nombre de swirl et enroulement d'un tourbillon à l'extrémité de la flamme). Les fluctuations du nombre de swirl sont induites par l'interaction des perturbations acoustiques incidentes avec le swirler. Cela génère dans les deux cas (axial et radial) une onde transmise acoustique et une onde tourbillonnaire convectée. Cette dernière est caractérisée par des perturbations de vitesses azimutales. Le processus de conversion de mode à l'origine de ce dernier type de perturbation a déjà été démontré dans le cas d'une vrille axiale. Il est ici étudié dans la géométrie radiale. Il est montré que le processus de conversion de mode pour les deux géométries est très similaire et qu'il produit des effets identiques sur la dynamique de flamme et donc sur la réponse.

Chapitre 7 : Simulations aux grandes échelles de flammes swirlées perturbées

La dynamique d'une flamme swirlée prémélangée turbulente est étudiée au moyen de la simulation numérique aux grandes échelles. La réponse de la flamme est déterminée en introduisant un forçage acoustique externe à deux fréquences de modulation correspondant à des valeurs caractéristiques de la fonction de transfert de flamme obtenues expérimentalement. Ces valeurs caractéristiques de la réponse diffèrent en terme de gain. Les mécanismes physiques sous-jacents identifiés expérimentalement sont étudiés numériquement. Les simulations confirment que les fluctuations du nombre de swirl et que le vortex rollup régissent la réponse de la flamme. Il est également confirmé que le premier mécanisme est associé à un processus de conversion de mode qui a lieu lorsque les ondes acoustiques impactent le swirler. La perturbation de vitesse axiale acoustique sur le côté en amont du swirler génère une onde acoustique axiale et une perturbation convective azimutale en aval de celui-ci. Ces mécanismes sont restitués par les simulations numériques. Les calculs indiquent également que les tourbillons responsables du rollup sont synchronisés par le forçage acoustique à la sortie des lèvres de l'injecteur. Ces tourbillons sont ensuite convectés dans la couche de cisaillement du jet et interagissent sur la flamme en provoquant le roll-up de l'extrémité de la flamme. Ce processus interfère avec les oscillations de l'angle de la flamme induite par les fluctuations du nombre de swirl. La phase entre l'angle de la flamme et la formation des tourbillons au bord de l'injecteur détermine la durée de vie du tourbillon avant son interaction avec la flamme et contrôle l'intensité de cette interaction. Lorsque cette durée de vie est réduite, le tourbillon ne peut pas se développer pleinement et la réponse de la flamme reste faible. Pour les plus longues durées de vie, le tourbillon peut se développer pleinement et produire de plus grandes perturbations du taux de dégagement de chaleur. Ce processus dépend de la fréquence qui détermine la phase entre les fluctuations du nombre de swirl et la génération des tourbillons.

Chapitre 8 : Modélisation de la fonction de transfert de flammes swirlées

Un modèle analytique est établi pour la réponse linéaire de flammes swirlées soumises à des perturbations de vitesses. La dynamique de la flamme est représentée par une version linéarisée de l'équation pour une variable de champ G. Les fluctuations turbulentes sont d'abord moyennées pour obtenir une équation cinématique pour le champ moyen. Une moyenne de phase est ensuite appliquée aux perturbations acoustiques pour obtenir une équation pour le champ G perturbée. Il est d'abord conclu que le mouvement de flamme est dû aux effets combinés des perturbations de vitesses axiales et azimutales. Les fluctuations du nombre de swirl sont modélisées en supposant que la vitesse de combustion turbulente est modulée par ces perturbations de vitesses. Il est ensuite montré que la réponse

des flammes swirlées peut être déduite de la fonction de transfert des flammes en "V" soumises à des perturbations de vitesses axiales. Il est toutefois important de tenir compte de la différence de phase résultant de la propagation des perturbations axiales et azimutales. Cette différence de phase, résultant de la différence des vitesses de propagation des perturbations acoustiques et convectives, est déterminée expérimentalement. Les fonctions de transfert théoriques sont comparées aux mesures pour deux vitesses débitantes différentes et pour un nombre de swirl fixé $S = 0.55$. Un bon accord est obtenu. On montre en particulier que le gain minimal obtenu pour un nombre de Strouhal de 0.5 est bien reproduit par le modèle théorique.

Partie III : Instabilités de combustion des flammes swirlées

Chapitre 9 : Instabilités de combustion

Les instabilités thermo-acoustiques sont analysées au moyen d'une représentation non-linéaire de la dynamique de la flamme basée sur la fonction de transfert généralisée ("Flame Describing Function" ou FDF). Dans ce cadre, la réponse de la flamme est déterminée en fonction de la fréquence et de l'amplitude des perturbations qui interagissent avec la flamme. Cette fonction de transfert généralisée, déterminée expérimentalement, est combinée avec une représentation matricielle de l'acoustique du système et permet un calcul des taux de croissance et des fréquences d'oscillation en fonction de l'amplitude des perturbations. Ces données peuvent être utilisées pour déterminer les régimes d'instabilité, les changements de fréquence et les niveaux d'amplitude au cycle limite. L'oscillation au cycle limite est obtenue lorsque le taux de croissance dépendant de l'amplitude est égal au taux d'amortissement dans le système. Il faut pour cela déterminer la valeur du taux d'amortissement qui est ici déduit de mesures de la courbe de résonance du brûleur. Les résultats obtenus sont comparés à des données d'expériences systématiques effectuées en faisant varier la géométrie du brûleur. Un bon accord est obtenu entre les prévisions et les observations.

Conclusion et perspectives

Contents

Nomenclature

Latin Characters :

c_p	Specific heat [J kg^{-1} K^{-1}]
d	Injector or swirler diameter [m]
f	Frequency [Hz]
k	Wavenumber [m^{-1}]
l	Element size [m]
$\dot{m}_f$	Fuel mass flow rate [kg s^{-1}]
p	Pressure [Pa]
$\dot{q}$	Local heat release rate [W m^{-3}]
r	Radial coordinate [m]
s	Entropy [J kg^{-1} K^{-1}]
t	Time [s]
u	Axial velocity [m s^{-1}]
v	Azimuthal or transverse velocity [m s^{-1}]
x	Axial coordinate [m]
A	Amplitude of the incident acoustic wave [Pa]
A_f	Flame surface [m^2]
B	Amplitude of the velocity component associated to the vorticity wave [m s^{-1}]
D	Flame tube diameter [m]
E	Total energy
$\mathcal{F}$	Flame describing function
G	Gain of the flame transfer function
G_θ, J_θ	Angular momentum flux
G_z, J_z	Axial momentum flux
I	Light intensity
L	Flame tube length or swirler axial size [m]
Q	Quality factor
$\dot{Q}$	Global heat release rate [W]
R	Reflection coefficient or radius
S	Section area [m^2]
S_T	Turbulent burning velocity [m s^{-1}]
T	Transmission coefficient or temperature
U_b	Injector bulk velocity [m s^{-1}]
Y_{FO}	Fuel mass fraction

Non-dimensional numbers :

He	Helmholtz number
Re	Reynolds number
Ro	Rossby number
St	Strouhal number
S	Swirl number

Greek Characters :

α	Flame angle or damping coefficient	φ	Phase difference between azimuthal and axial velocity component
β	Scaling factor [W m^{-3}]	ζ	Axial sensitivity factor
χ	Azimuthal sensitivity factor	ζ_3	Specific impedance at the system outlet
δ	Trailing edge blade angle	Δh	Heat released by conversion of a unit mass of fuel [J kg^{-1}]
η	Heat release ratio $\overline{\dot{Q}_{lw}}/\overline{\dot{Q}}$	Γ	Circulation
γ	Specific heat ratio	Ω	Rotation rate [s^{-1}]
λ	Laser wavelength [nm]	Φ	Phase of the flame transfer function
ω	Angular frequency [s^{-1}]	Ξ	Coupling parameter
ϕ	Equivalence ratio		
ψ	Phase of images		
ρ	Fluid density [kg m^{-3}]		
τ	Convective time delay [s]		
θ	Swirl exit flow angle		

Subscripts :

lw	Lower window	1	Cascade upstream section
uw	Upper window	2	Cascade downstream section
r	Radial direction		
θ	Azimuthal direction	a	acoustic
x, z	Axial direction	v	vorticity
u	Unburnt gases		
b	Burnt gases		

Abbreviations :

FDF	Flame Describing Function	ORZ	Outer Recirculation Zone
FTF	Flame Transfer Function	PLIF	Planar Laser Induced Fluorescence
HW	Hotwire	PM	Photomultiplier
ICCD	Intensified Charge-Coupled Device	PVC	Precessing Vortex Core
IRZ	Inner Recirculation Zone	RANS	Reynolds Average Navier-Stokes
LDV	Laser Doppler Velocimetry	RMS	Root mean square [m s^{-1}]
LES	Large Eddy Simulation		
LPM	Lean Premixed Mode		

Introduction

Combustion is a multidisciplinary field involving a combination of fluid mechanics, thermodynamics, chemical kinetics and transport phenomena. It has a broad range of applications including energy conversion, industrial processes, aeronautical and space propulsion (see Figure 1 for an illustration). In many applications and in particular in the high performance systems used in propulsion or energy conversion, combustion can couple with the acoustics of the system and lead to various types of instabilities. This phenomenon brings together the complexities of combustion and those related to acoustics and unsteady fluid motions giving rise to a wide range of challenging issues. Some of these problems are the subject of the present investigation and will be described in detail later on. At this point, it is worth gathering some additional background on combustion to show

Figure 1: Aerospace propulsion applications of combustion. (a) : Airbus A380 equipped with four jet engines. (b) : Spacecraft launcher Ariane 5. (c) : CFM 56-7 engine (Snecma and GE). (d) : Air to air missile from MBDA.

its importance.

It is first interesting to note that 98% of the energy used in transportation is issued from oil and transformed into mechanical energy through combustion (Institut Français du Pétrole, `www.ifp.fr`). It is also worth remembering that on a worldwide basis 85% of the primary energy is delivered by combustion systems, see Iacona *et al.* (2009). In France combustion is less used because most of the French electrical energy has a nuclear origin with a percentage of 80% while it is around 20% from combustion. To fix the ideas a few energy conversion systems based on combustion are shown in Fig. 2.

In this general context, it is important to improve combustion technologies by enhancing systems efficiency and reducing the environmental impact in terms of emissions. It is known that conversion of hydrocarbon fuels into burnt products generates green house gases like CO_2 and pollutants like unburnt hydrocarbons HC, nitric oxides NO_x and carbon monoxide CO. Amongst other harmful consequences, nitric oxides NO_x and unburnt hydrocarbons are major contributors to the formation of smog and production of near ground level ozone. Carbon dioxyde, which is the leading greenhouse gas, can only be reduced by higher efficiency thermodynamic cycles and associated systems. With regard to emissions, it is difficult to simultaneously reduce the levels of NO_x and CO but it is possible to use closed loop control to adjust operating point to minimize these emissions. Low operating costs require high efficiency devices. As an example, the fuel efficiency per passenger-km of today's subsonic aircraft has been increased by about 70 % compared to a reference value some 40 years ago (Penner *et al.* (1999)).

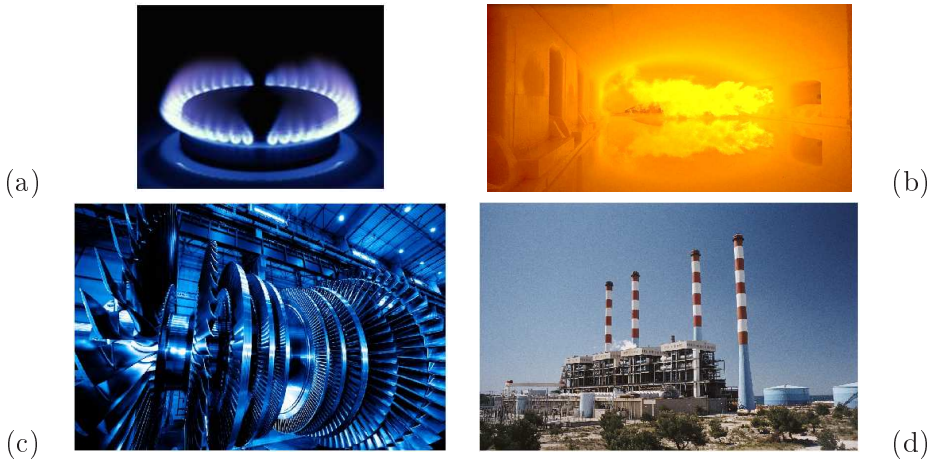

Figure 2: Energy conversion systems based on combustion. (a) : Domestic boiler. (b) : Industrial glass furnace. (c) : Gas turbine from Alstom. (d) : Fossil fuel powerplant from EDF in France.

This has been achieved directly through combined scientific progress, technological advances and clever engineering.

One method for nitric oxides NO_x emissions reduction consists in burning in a lean premixed mode where fuel and air are premixed before they reach the combustion region. It is known however that this combustion mode is more susceptible to dynamical phenomena like blow-off and flashback as reviewed for example by Plee and Mellor (1978) and to instabilities as explained for example by Culick (2001); Candel (2002) and in the collective book edited by Lieuwen and Yang (2005). Combustion instabilities have been investigated for a long time but still raises many fundamental and more practical challenges. The basic issues are to develop an understanding of the flame dynamics and associated unsteady heat release processes, derive predictive methods for combustion instabilities and imagine advanced methods for reduction and control of dynamical phenomena.

Combustion dynamics problems are reviewed in many articles (see for example Candel (2002)) and in a collective book edited by Lieuwen and Yang (2005). The case of swirling flames which is the subject of the present work is specifically considered in a recent article by Huang and Yang (2009). Acoustically coupled combustion instabilities are considered in a wide range of publications many of which are cited in these reviews. The physical mechanisms responsible for the coupling between acoustics and combustion are now well documented. The unsteady heat release rate stands out as the driving source of the process. This is generally delayed with respect to incident perturbations and may trigger an unstable acoustic-flame coupling as explained in the early literature by Crocco (1968), Putnam (1971) or in a more recent monograph from Culick (2001). Different paths can produce these delayed perturbations in heat release rate, but in most cases they are associated with convection of flow perturbations, see for example Candel (2002), or fluctuations of the mixture composition, see for example Lieuwen and Zinn (1998). Much of the recent understanding has come from some fundamental experiments under well controlled conditions (see for example Ducruix *et al.* (2003)). Extension to turbulent flames and specifically to turbulent swirling flames is more difficult but a considerable effort has been devoted to the analysis of the combustion dynamics of these systems (see for example Külsheimer and Büchner (2002); Weigand *et al.* (2006); Bellows *et al.* (2007); Kim *et al.* (2010); Palies *et al.* (2010)).

Much effort has been expanded to solve instability problems in propulsion systems like liquid rocket engines (see for example a classical report on the subject assembled by Harrje and Reardon (1972)), or solid rocket motors (see for example by De Luca *et al.* (1992)). Industrial applications have also been considered and this topic is covered in a monograph due to Putnam (1971). Most of the current research is concerned with instabilities of swirling flames in relation with problems encountered in gas turbines involving longitudinal acoustic modes or

azimuthal disturbances, see for example Fritsche *et al.* (2007) and Meier *et al.* (2007) and references included in the review by Huang and Yang (2009).

While considerable progress has been accomplished we show in this document that much remains to be done to develop predictive tools for combustion instabilities and devise solutions for reduction and suppression of oscillations. There is also a need for well controlled experiments enabling a detailed investigation of swirling flame dynamics. This study will be carried out in what follows by making use of a novel burner, equipped with a swirling injector. The general design follows that adopted in the previous flame dynamics studies carried out in our laboratory by Ducruix *et al.* (2000); Durox *et al.* (2005); Birbaud *et al.* (2006). We also follow the same logic as that adopted by Schuller *et al.* (2003a); Noiray *et al.* (2006) to examine self-sustained oscillations .

This document is focused on a few central aspects of the problem and uses a combination of experiments, numerical simulations and analysis to deal with the following issues :

- Swirling flame dynamics : the objective is to characterize the flame response in terms of a describing function. This generalized function corresponds to a family of transfer functions which also depend on the input level. The flame dynamics is also analyzed to identify processes which determine the flame response.

- Mode conversion processes at swirler : it is deduced from experiments that the swirler acts as a mode converter and generates a vorticity wave when it is submitted to an acoustic disturbance. The vorticity wave is manifested as azimuthal velocity perturbations convected by the flow and propagating on the downstream side of the swirler. A set of studies is developed to analyze this process and deduce its consequences for the flame response.

- Combustion instabilities of swirling flames : the goal is to predict the frequencies and amplitudes at the limit cycle and compare predictions with experiments. The method is based on the Flame Describing Function (FDF) framework.

At this point it is worth reviewing the relevant literature. This is done below where we successively consider the three points.

The swirling flame dynamics is considered in a large number of articles and it is difficult to write a short review. This aspect will be covered in more detail in the following chapters. It is concluded that some of the key mechanisms driving

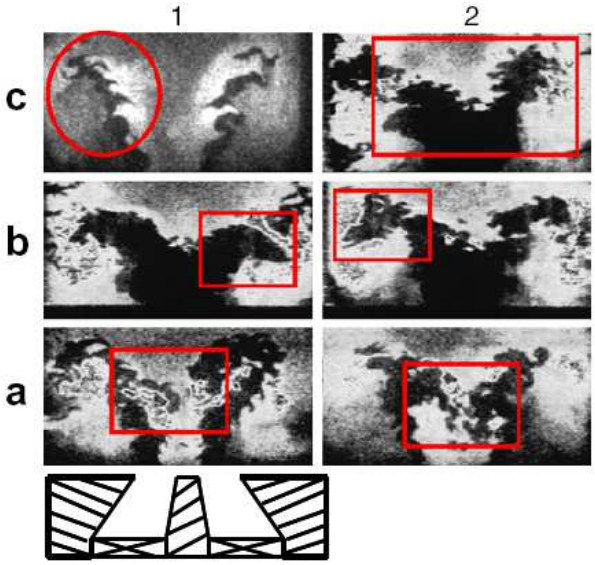

Figure 3: Flame dynamics from Thumuluru *et al.* (2009).

the response of swirling flames need to be identified. In general, nonlinear processes which appear under self-sustained oscillations need to be documented in a systematic fashion. Mechanisms like vortex rollup have been studied previously for example by Bellows *et al.* (2007) but only for a reduced set of frequencies and over a limited range. It is also important to remember that perturbations of various types need to be considered. One class is formed by velocity fluctuations which accompany pressure oscillations, see Poinsot *et al.* (1987); Yu *et al.* (1991); Paschereit *et al.* (2000). Another type of perturbation consists in equivalence ratio disturbances, which can be created by the differential response of fuel and air injectors to pressure waves generated by unstable combustion, see Keller (1995); Lieuwen and Zinn (1998); Sengissen *et al.* (2007). In the case of swirling flames, flame transfer functions are often defined in a limited range of frequencies and only correspond to linear perturbations (see for example Borghesi *et al.* (2009)). Some articles consider the dynamics of swirling flames experimentally as Külsheimer and Büchner (2002); Weigand *et al.* (2006); Bellows *et al.* (2007); Kim *et al.* (2010) but the understanding of the driving sources are not fully documented. Only a few investigations (Armitage *et al.* (2006); Thumuluru *et al.* (2007); Bellows *et al.* (2007)) are dealing with nonlinear effects of flow modulations on the dynamics of confined turbulent swirling flames. An accurate study of the swirling flame dynamics and on the nonlinear response is needed to explain some phenomena observed and for the prediction of limit cycles in self-sustained combustion oscillations regimes.

A second aspect which needs to be examined in more detail concerns the mode

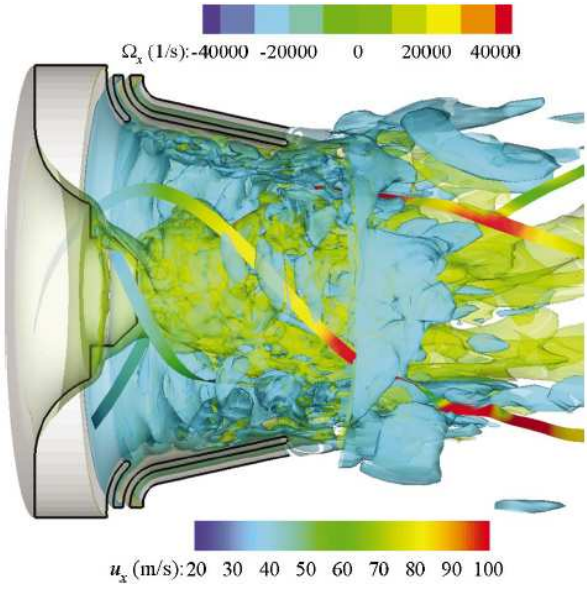

Figure 4: Flow dynamics in swirl injector from Wang *et al.* (2007).

conversion taking place at a swirler submitted to incident acoustic waves. This has already been studied but the origin and the influence on the flame is not examined in Wang and Yang (2005). The mechanism of swirl number fluctuations induced by this conversion process has been inferred but not fully identified and its impact on the flame response is only briefly considered by Komarek and Polifke (2010). The work of Hirsch *et al.* (2005) has theoretically shown that swirl strength fluctuations was present in the flow downstream the swirler. The behavior of turbulent premixed swirling flames submitted to acoustic disturbances needs to be revisited by taking this mechanism also into account. Because the mode conversion process is so important it is worth reviewing similar conversion mechanisms described in the technical literature. This can then be analyzed in the case of a two dimensional airfoil cascade. When an acoustic wave impinges on such a system a convective vorticity mode is generated giving rise to transverse velocity perturbations. This problem covered in the classical textbooks of Horlock (1978) and Greitzer *et al.* (2004) has been extensively investigated in the domain of turbomachinery for example by Kaji and Okazaki (1970), Koch (1971) and Morfey (1973b) in early works and more recently by Peake and Kerschen (1997) and Glegg (1999). It is important because such interactions induce fluctuating forces on the blades generating noise. Conversion of entropy fluctuations by a cascade has been worked out analytically by Cumpsty and Marble (1977b) and was pursued by Cumpsty (1979). It is shown that the interaction gives rise to acoustic pressure waves. These studies are used as starting points of the model developed in the present document. Most of the previous studies consider high Mach number flows found in axial compressors or turbines, the case of low Mach

flows is less well documented and the present developments try to fill this need.

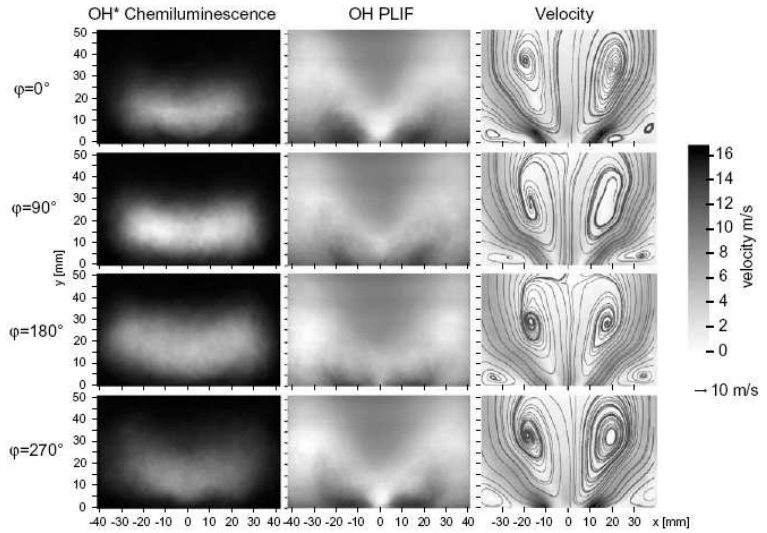

Figure 5: Self-sustained instability by Stöhr *et al.* (2009). The cycle of oscillation is characterized by OH* emissions images (left column), laser induced fluorescence of OH (central column) and velocity and streamline distribution (right column).

Another important challenge is that of the prediction of combustion instabilities in swirling flame combustor taking into account the nonlinear flame response. Previous investigations indicate that it is possible to find the linear stability map of various types of burners but this is restricted to small perturbations and cannot account for the limit cycle oscillations observed in practice. It is well known that nonlinear mechanisms dominate the dynamics of real systems. These nonlinearities determine the limit cycle amplitudes, triggering of instabilities (the mechanism by which an unstable oscillation appears when the system experiences a finite amplitude perturbation), mode switching (the change in frequency observed during operation of practical devices) and hysteresis, see Wicker and Yang (1996); Dowling (1997); Dowling (1999); Lieuwen and Neumeier (2002a); Stöhr *et al.* (2009). It has been shown recently that these combustion dynamics nonlinearities could be represented with a unified framework developed by Noiray *et al.* (2008) in which the flame transfer function (FTF) is replaced by a flame describing function concept (FDF) which depends on the amplitude of perturbations impinging on the flame. A frequency domain stability analysis then yields growth rates and frequencies which depend on amplitude. Application of the FDF to the analysis of the stability of an unconfined by Noiray *et al.* (2008) or confined by Candel *et al.* (2009) multipoint injection laminar burner indicates that it is possible to predict with reasonable accuracy many of the phenomena listed previously. The present study follows these lines to determine frequencies and amplitudes at the limit cycle of a self-sustained instability.

Thesis objectives and contents

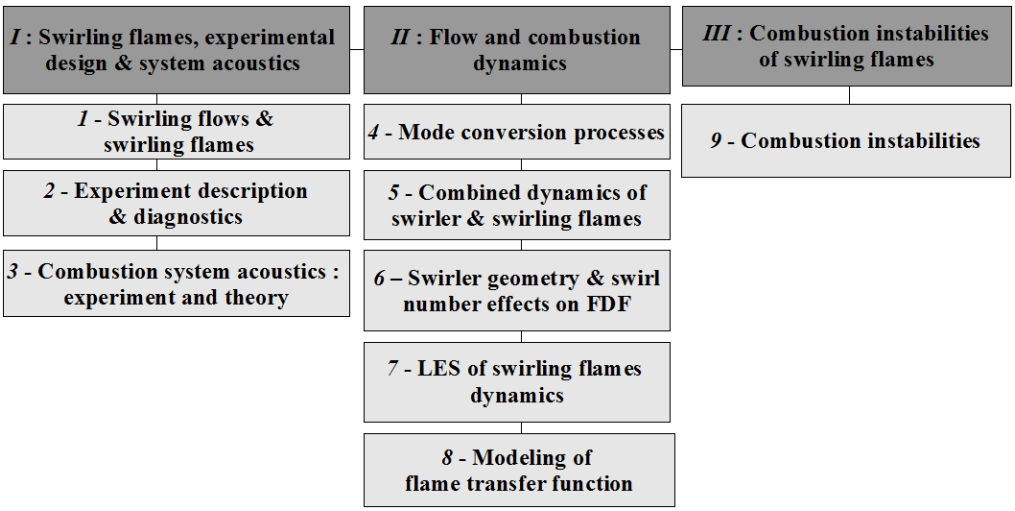

Figure 6: Block-diagram of the thesis manuscript.

The present research focuses on premixed turbulent swirling flames dynamics. This work comprises three main parts as shown in the block-diagram of Fig. 6 :

- Swirling flames, experimental design and system acoustics
- Flow and combustion dynamics
- Combustion instabilities of swirling flames

The block-diagram in Fig. 6 gives the global organization while a more visual presentation can be found in Fig. 7. The content of the nine chapters composing this document are successively considered in what follows.

Part I

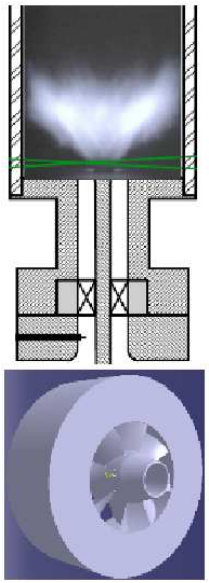

Swirling flames, experimental design and system acoustics

1 - Swirling flows & swirling flames
2 - Experiment description and diagnostics
3 - Combustion system acoustics : experiment and theory

Part II

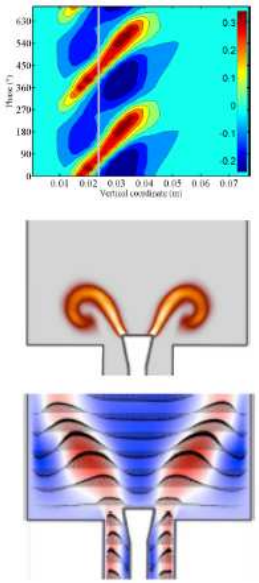

Flow and combustion dynamics

4 - Mode conversion processes
5 - Combined dynamics of swirler and turbulent swirling flames
6 - Swirler geometry and swirl number effects on FDF
7 - LES of swirling flame dynamics
8 - Modeling of FTF

Part III

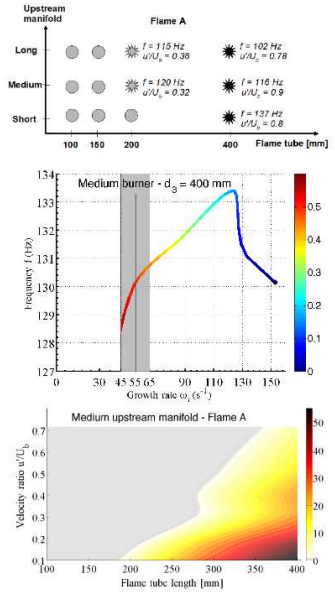

Combustion instabilities in swirling flames

9 - Combustion instabilities

Figure 7: Block-diagram of the thesis manuscript.

Part I : Swirling flames, experimental design and system acoustics

The first part of the manuscript includes background material on swirling flows. It introduces expressions used to evaluate the swirl number which is classically used to determine the rotation rate of the flow (**chapter 1**). The swirl number may be deduced from geometrical parameters like the vane angle. In the case of axial swirlers, the vane angle depends on the radius and the swirl number can be obtained by numerical integration. This extends known results like those contained in Gupta *et al.* (1984). The effect of perturbations on the swirl number is also discussed. It is shown that swirl number fluctuations can be calculated in terms of the incoming velocity disturbances. These results are used to design the experiment (**chapter 2**) and later on in the data interpretation. The swirling flame experiment is described in **chapter 2**. Instrumentation, diagnostics and data processing are presented in this chapter as well. A method is proposed to determine the heat release rate in the flame at various instants during a cycle of oscillation by processing phase average chemiluminescence images. **Chapter 3** deals with the acoustic response of generic combustion systems which include an upstream manifold, an injector and a flame tube. This response is investigated experimentally for a set of burners providing the eigenfrequencies. The damping rate is also determined for these configurations. A coupled cavity analysis is also used to predict resonant frequencies which are then compared with experimental data. This investigation is pursued with an analysis of conditions under which acoustic modes of a chamber filled with hot combustion products can be considered decoupled from the plenum acoustics supplying the fresh reactants through a injection manifold. The aim is to provide an index Ξ which can be used to see whether elements located on the upstream of the reaction region can be considered acoustically decoupled from downstream elements of the combustor.

Part II : Flow and combustion dynamics

This part is concerned with the dynamics of swirling flows and swirling flames. The analysis begins with an investigation of the mode conversion process taking place when acoustic waves impinge on a swirler (**chapter 4**). The phenomenon is first studied in the case of a two dimensional airfoil cascade using a model derived from an actuator disk theory. The model provides the amplitude of both axial and azimuthal velocity components and defines their phase shift. Numerical simulations and experiments are then carried out to confirm model predictions. The aerodynamics of the flow entering the combustor chamber is also examined and a comparison of mode conversion processes between axial and radial swirlers is carried out. The dynamics of swirling flames is considered in **chapter 5**. The study begins with experimental determinations of flame describing functions following the framework developed by Noiray *et al.* (2008). The dynamics of

two premixed confined swirling flames is studied by examining their response to incident velocity perturbations. A Strouhal number is used to characterize the response in an attempt to collapse transfer function data. The flame dynamics is then investigated with chemiluminescence images. It is shown that the flame is submitted to a transmitted axial acoustic perturbation which propagates at the speed of sound and to an azimuthal velocity perturbation which is convected at the flow velocity. It will be demonstrated that the net result is that the dynamical response and unsteady heat release rates are determined by the combined effects of these axial and induced azimuthal velocity perturbations. **Chapter 6** concerns the influence of the swirler geometry on the flame describing function. Two swirlers, axial and radial are investigated. The swirl number is also used as parameter to see impact on the flame response. **Chapter 7** is devoted to the understanding of mechanisms based on Large Eddy Simulations (LES) using the AVBP code (see Schönfeld and Rudgyard (1999); Staffelbach *et al.* (2009)). The dynamics of a turbulent premixed confined swirling flame is investigated using LES. The flame response is determined by introducing an external acoustic forcing at two modulation frequencies corresponding to characteristic values of the flame describing function obtained experimentally. Swirl number fluctuations and vortex roll-up are retrieved in the simulation and as their effect on the flame dynamics. Calculations also indicate that vortex shedding takes place at the injector lip outlet. Vortices originating from this region are convected by the flow, impinge on the flame and roll-up the flame tip. This process interferes with the flame motion induced by swirl number fluctuations to define the flame response in terms of heat release rate. **Chapter 8** reports a possible modeling of the linear flame transfer function. An analytical model is derived for the linear response of swirling flames submitted to acoustic velocity disturbances. Theoretical transfer functions of swirling flames are not so common and do not fully reproduce characteristic features of the flame response, see Huang and Yang (2005); Borghesi *et al.* (2009), except the study from Komarek and Polifke (2010). Many previous studies do not account for the presence of an azimuthal velocity disturbance convected by the flow in addition to the initial axial component propagating at the speed of sound. This feature which is reported in some recent investigations (Wang and Yang (2005); Komarek and Polifke (2010); Huang and Yang (2009)) is however not included in most of these studies with the exception of Komarek and Polifke (2010) which provides a phenomenological representation of the FTF. The flame dynamics is represented by a linearized version of the G-equation in the present analysis. It is first concluded that the flame motion results from the combined effects of axial and azimuthal velocity perturbations. The latter disturbances are generated at the swirler when this element is submitted to axial velocity fluctuations, they are convected by the flow and impinge on the flame. In this disturbance field the swirl number is perturbed and this is effectively modeled by assuming that the turbulent burning velocity is modulated by the axial and azimuthal velocity perturbations. Theoretical transfer functions ob-

tained are compared with measurements corresponding to two bulk velocities at a constant mean swirl number $S = 0.55$.

Part III : Combustion instabilities of swirling flames

Chapter 9 leads an instability analysis based on the FDF methodology. Thermo-acoustic instabilities are analyzed here by making use of a nonlinear representation of the flame dynamics based on the describing function. The flame describing function determined experimentally in the previous chapters is combined with an acoustic transfer matrix representation of the system to estimate growth rates and oscillation frequencies as a function of perturbation amplitude. This equilibrium is obtained when the amplitude dependent growth rate equals the damping rate in the system. This requires an independent determination of this last quantity which is here based on measurements of the resonance response curve. Results obtained are compared with observations from systematic experiments carried out by varying the test combustor geometry.

Part I

Swirling flames, experimental design and system acoustics

Chapter 1

Swirling flows and swirling flames

Abstract : *Swirling flows are commonly encountered in fluid mechanics and combustion research and in a variety of industrial applications like gas turbines or jet engines. The swirl number is the natural dimensionless group used to characterize swirling flows. The derivation of the swirl number is briefly reviewed. This is then used to derive a perturbed form of this number. We next consider the effect of the vane angle evolution and its influence on the swirl number of axial swirlers. As the vane angle changes with the radius, the swirl number can be estimated by numerical integration. An expression of the swirl number is derived which takes into account the swirler vane angle. The last part of this chapter is concerned with unsteady effects on the swirl number. This analysis takes into account the unsteady momentum terms in the axial and azimuthal momentum fluxes. Finally, a synthesis gathers swirl number expressions found in the present work and briefly reviewed those in the literature.*

Résumé : *Les écoulements swirlés sont couramment rencontrées en mécanique des fluides, en combustion et dans de nombreuses applications industrielles comme les turbines à gaz ou les turboréacteurs. Ces écoulements en rotation sont généralement caractérisés par le nombre de swirl, un groupement sans dimensions dont la définition est d'abord donnée. On déduit de cette expression une forme perturbée de ce nombre qui fait intervenir la différence entre les fluctuations relatives de vitesse azimutale et axiale. On considère dans un deuxième temps l'effet de l'évolution de l'angle des pales pour un swirler axial. Comme l'angle des pales change avec le rayon, le nombre de swirl peut être estimé au moyen d'une intégration numérique. Une expression est donc déduite en tenant en compte de l'angle au bord de fuite des pales de la vrille. La dernière partie du chapitre traite des effets instationnaires sur le nombre de swirl. On montre dans ce chapitre qu'il est possible de prendre en compte les termes d'accumulation de moment angulaire azimutal et de quantité de mouvement axiale. Une synthèse rassemble finalement les expressions obtenues pour le nombre de swirl.*

1.1 Physical mechanisms in swirling flows

Swirling flows are commonly found in industrial applications and give rise to many fundamental issues. Effects of swirl are exploited in many systems to stabilize flames and obtain a compact combustion region. Swirl is used to reduce the combustor size (see for example Galley (2006)). The flow dynamics in swirling flames is controlled by the level of swirl (the rate of rotation in the flow) which can be characterized by the swirl number. Changes in this number result in changes in the geometry of the flow as illustrated in Fig. 1.1.

It is specifically shown that when the swirl number is increased a reverse flow is generated inside the combustor. This yields an inner recirculation zone (IRZ) where burnt gases continuously ignite the fresh stream fed from the injector. The inner recirculation zone is associated with the vortex breakdown phenomenon which has been extensively investigated (see for example the review by Lucca-Negro and O'Doherty (2001)). This phenomenon appears for a critical swirl number when the axial pressure gradient is such that the flow has a stagnation point and as a consequence is reversed. There are three main vortex breakdown structures according to Sarkpaya (1971) respectively the double-helical mode, the axisymmetric mode and the helical mode. The first one is observed at low Reynolds number, the second also referred as bubble mode is characterized by a stagnation point on the flow axis followed by a recirculation zone. The last mode features a stagnation point on the flow axis where the center of the vortex

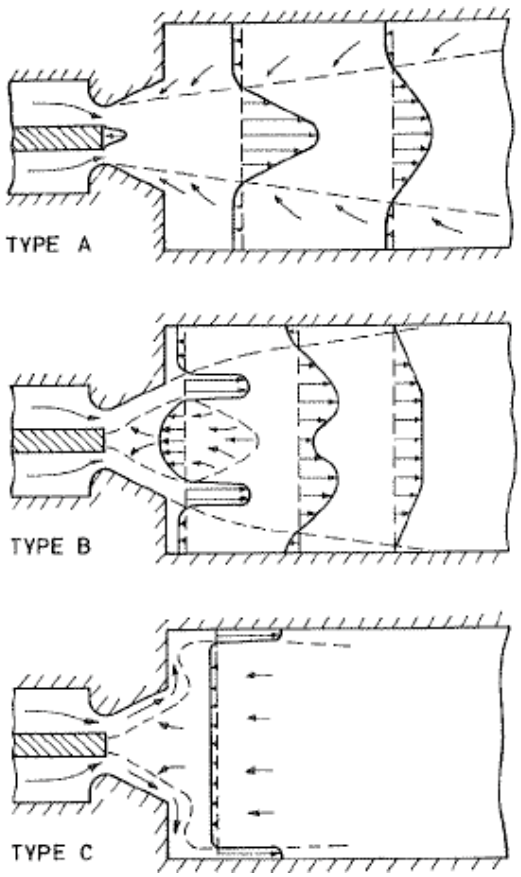

Figure 1.1: Flow patterns observed for swirling jets and flames issuing from divergent nozzles. The swirl number increases from type A to type C. Type A : with zero or low swirl number intensity, the annular air flow tends to separate from the nozzle surface near the nozzle throat. Flames produced with this type of flow have a fluctuating flame front positioned at a distance downstream from the burner exit. Type B : for an intermediate or high degree of swirl, the air flow is stably attached to the divergent nozzle walls and encloses a large torroidal vortex. A reverse flow zone is situated in the centers of the jet. This is typically the configuration used to stabilize swirling flames. Type C : this flow pattern represents the radial wall jet. Flames produced with this flow type are attached to the burner face and to the wall of the combustion chamber. Adapted from Beer and Chigier (1972).

executes a helical motion. This last mode is also designated as precessing vortex core (PVC) (see for example Syred and Beer (1972)).

One aspect of swirling flows concerns the occurrence of the precessing vortex core (PVC) which is one manifestation of vortex breakdown. This type has been reviewed by Syred (2006) for non reactive and reactive configurations. A typical swirl stabilized combustor presenting such PVC structure is shown in Fig. 1.2

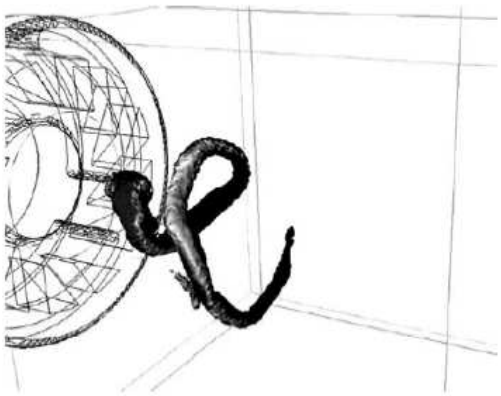

Figure 1.2: Isosurface of a low pressure level used to visualize an isothermal PVC formed at the exit of the swirl burner from Roux *et al.* (2005).

(borrowed from Roux *et al.* (2005)). One does not quite know if such PVC influence the structure and flame dynamics in reactive swirling flows. This issue can be investigated with numerical simulations as exemplified in Selle *et al.* (2004); Roux *et al.* (2005)

While much research has concerned stationary swirling flows and flames, the influence of unsteadiness is less well documented. It is specifically useful to explore the effect of incoming perturbations on the rate of rotation of the flow and examine the effect of such perturbations on the swirl number. One mechanism which will be examined in this document is shown in Fig. 1.3 in a block-diagram form showing the response of swirling flame as we investigated it in the present thesis. Acoustic waves impinging the swirler give rise to a transmitted axial acoustic

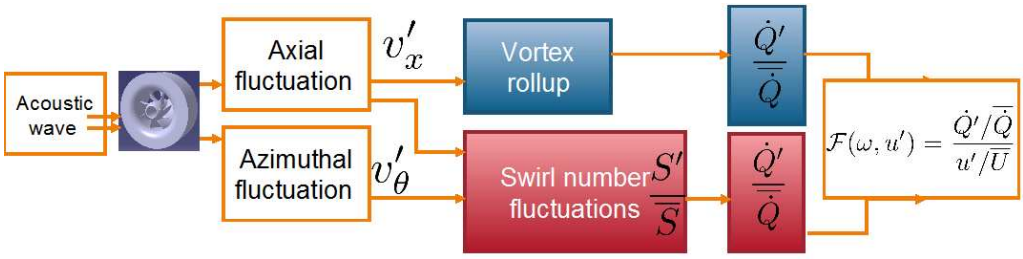

Figure 1.3: Block-diagram of the swirling flame dynamics. Mode conversion takes place at the swirler and induces swirl number fluctuations. An axial acoustic wave v'_x is transmitted while an azimuthal wave v'_θ is convected. Combination of both waves downstream the swirler generates swirl number fluctuations $S'/\overline{S}$ in the flow. The transmitted acoustic wave downstream the swirler gives rise to rollup at the flame tips. The interference of both swirl number fluctuations and rollup determine the level of the flame response. See Palies *et al.* (2010).

wave v'_x and to an azimuthal convective wave v'_θ which interfere downstream the swirler. As the swirl number depends upon both velocity signal v_x and v_θ, swirl number fluctuations $S'/\overline{S}$ occurs. That topic is investigated in the present manuscript. The axial acoustic wave induced a vortex rollup at the flame. The interference of both swirl number fluctuations and rollup determine the level of the flame response, see Palies *et al.* (2010) and chapter 6. Some indications on this mechanism are contained in Hirsch *et al.* (2005); Wang and Yang (2005); Komarek and Polifke (2010). Further information is provided in the present document (see chapters 5 and 7).

1.2 Theoretical derivation of swirl number

It is natural to introduce the swirl number and consider methods which can be used to estimate this quantity. The basic configuration of a confined swirling flow is displayed in Fig. 1.4.

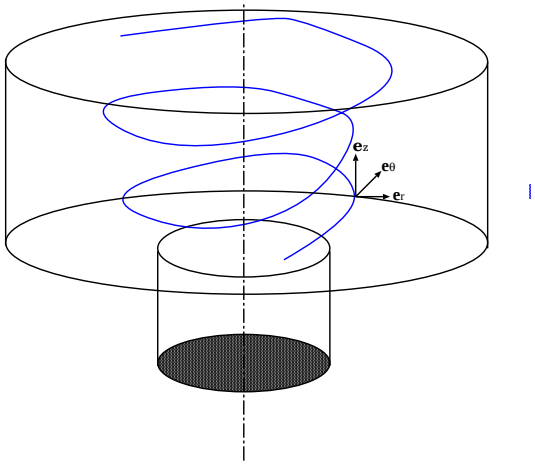

Figure 1.4: Swirling flow configuration. Cylindrical referential is shown.

As a starting point of the theoretical derivation (see Galley (2006)), it is convenient to use the mass and momentum equations written in cylindrical coordinates $(\mathbf{e}_r, \mathbf{e}_\theta, \mathbf{e}_z)$. The velocity of a fluid particle is defined as $\mathbf{v}(\mathbf{r}, t)$ and components of this vector are : v_r,v_θ and v_z.
It is convenient to introduce at this point the angular momentum flux G_θ :

$$G_\theta = \int_0^R \rho v_\theta v_z r^2 \, \mathrm{dr} \tag{1.1}$$

and the axial momentum flux G_z:

$$G_z = \int_0^R (\rho v_z^2 + p) r \, \mathrm{d}r \tag{1.2}$$

The swirl number is defined by taking the ratio of the angular momentum flux G_θ to the axial momentum flux G_z times the radius R :

$$S = \frac{G_\theta}{R\, G_z} = \frac{\int_0^R \rho v_\theta v_z r^2 \, \mathrm{d}r}{R \int_0^R (\rho v_z^2 + p) r \, \mathrm{d}r} \tag{1.3}$$

It is first interesting to show that under fairly general assumptions, G_θ and G_z do not depend on z so that the swirl number S defined by Eq. (1.37) is a conserved quantity. The derivation begins with the balance equations of fluid dynamics written in the absence of body forces.

The mass balance equation may be written in the form :

$$\frac{\partial \rho}{\partial t} + \frac{1}{r}\frac{\partial \rho r v_r}{\partial r} + \frac{1}{r}\frac{\partial \rho v_\theta}{\partial \theta} + \frac{\partial \rho v_z}{\partial z} = 0 \tag{1.4}$$

The radial momentum balance is :

$$\frac{\partial v_r}{\partial t} + \mathbf{v}\cdot\nabla v_r - \frac{v_\theta^2}{r} = -\frac{1}{\rho}\frac{\partial p}{\partial r} + \nu\left[\frac{\partial^2 v_r}{\partial z^2} + \frac{1}{r}\frac{\partial}{\partial r}\left(r\frac{\partial v_r}{\partial r}\right) + \frac{1}{r^2}\frac{\partial^2 v_r}{\partial \theta^2} - \frac{v_r}{r^2} - \frac{2}{r^2}\frac{\partial v_\theta}{\partial \theta}\right] \tag{1.5}$$

The azimuthal momentum balance may be cast in the form :

$$\frac{\partial v_\theta}{\partial t} + \mathbf{v}\cdot\nabla v_\theta + \frac{v_r\, v_\theta}{r} = -\frac{1}{\rho\, r}\frac{\partial p}{\partial \theta} + \nu\left[\frac{\partial^2 v_\theta}{\partial z^2} + \frac{1}{r}\frac{\partial}{\partial r}\left(r\frac{\partial v_\theta}{\partial r}\right) + \frac{1}{r^2}\frac{\partial^2 v_\theta}{\partial \theta^2} - \frac{v_\theta}{r^2} + \frac{2}{r^2}\frac{\partial v_\theta}{\partial \theta}\right] \tag{1.6}$$

The axial momentum balance is :

$$\frac{\partial v_z}{\partial t} + \mathbf{v}\cdot\nabla v_z = -\frac{1}{\rho}\frac{\partial p}{\partial z} + \nu\left[\frac{\partial^2 v_z}{\partial z^2} + \frac{1}{r}\frac{\partial}{\partial r}\left(r\frac{\partial v_z}{\partial r}\right) + \frac{1}{r^2}\frac{\partial^2 v_z}{\partial \theta^2}\right] \tag{1.7}$$

The following analysis relies on four additional assumptions : the flow is considered steady $\partial/\partial t \sim 0$, axisymmetric $\partial/\partial\theta \sim 0$ and viscous effects are assumed to be negligible compared to the inertial terms. The gravity term is generally negligible in the types of flows considered in this document.

With these hypothesis, the mass balance Eq. (1.4) becomes :

$$\frac{1}{r}\frac{\partial r v_r}{\partial r} + \frac{\partial v_z}{\partial z} = 0 \tag{1.8}$$

The radial momentum equation Eq. (1.5) yields :

$$v_r \frac{\partial v_r}{\partial r} + v_z \frac{\partial v_r}{\partial z} - \frac{v_\theta^2}{r} = -\frac{1}{\rho}\frac{\partial p}{\partial r} \tag{1.9}$$

The azimuthal momentum equation Eq. (1.6) gives :

$$v_r \frac{\partial v_\theta}{\partial r} + v_z \frac{\partial v_\theta}{\partial z} + \frac{v_r\, v_\theta}{r} = 0 \tag{1.10}$$

The axial momentum equation Eq. (1.7) becomes :

$$v_r \frac{\partial v_z}{\partial r} + v_z \frac{\partial v_z}{\partial z} = -\frac{1}{\rho}\frac{\partial p}{\partial z} \tag{1.11}$$

Furthermore, it is convenient to work with conservative forms of the balance equations. Only axial and azimuthal momentum equations are useful to analyze the swirl number definition.

The azimuthal momentum equation can be cast in conservative form as :

$$\frac{\partial \rho v_r v_\theta}{\partial r} + \frac{\partial \rho v_\theta v_z}{\partial z} + 2\rho \frac{v_\theta v_r}{r} \quad = \quad 0 \tag{1.12}$$

The conservative form of the axial momentum equation may be written as :

$$\frac{\partial \rho v_r v_z}{\partial r} + \frac{\partial \rho v_z^2}{\partial z} + \rho \frac{v_z v_r}{r} \quad = \quad -\frac{\partial p}{\partial z} \tag{1.13}$$

One may now integrate these last equations Eq. (1.12) and Eq. (1.13) over a constant section A of the flow field perpendicular to the z axis.

Azimuthal momentum equation : One may first multiply the azimuthal momentum equation Eq. (1.12) by r :

$$r\frac{\partial \rho v_r v_\theta}{\partial r} + r\frac{\partial \rho v_\theta v_z}{\partial z} + 2\rho v_\theta v_r = 0 \tag{1.14}$$

and integrate the azimuthal momentum equation over the section A :

$$\int_A \left[r\frac{\partial \rho v_r v_\theta}{\partial r} + r\frac{\partial \rho v_\theta v_z}{\partial z} + 2\rho v_\theta v_r \right] \mathrm{dS} = 0 \tag{1.15}$$

This yields :

$$\int_0^R \left[\int_0^{2\pi} r^2 \frac{\partial \rho v_r v_\theta}{\partial r} + r^2 \frac{\partial \rho v_\theta v_z}{\partial z} + 2r\rho v_\theta v_r \right] \mathrm{d}\theta \mathrm{dr} = 0 \tag{1.16}$$

As the system is axisymmetric, this leads to :

$$\int_0^R \left[r^2 \frac{\partial \rho v_r v_\theta}{\partial r} + r^2 \frac{\partial \rho v_\theta v_z}{\partial z} + 2 r \rho v_\theta v_r \right] \mathrm{dr} = 0 \tag{1.17}$$

The first and last terms in the bracket may be combined :

$$2 r \rho v_\theta v_r + r^2 \frac{\partial (\rho v_r v_\theta)}{\partial r} = \frac{\partial (r^2 \rho v_r v_\theta)}{\partial r} \tag{1.18}$$

One deduces the following expression for the azimuthal momentum balance :

$$\int_0^R \left[\frac{\partial (\rho r^2 v_r v_\theta)}{\partial r} + \frac{\partial (\rho r^2 v_\theta v_z)}{\partial z} \right] \mathrm{dr} = 0 \tag{1.19}$$

From this last equation, one finds that :

$$\frac{d}{dz} G_\theta = - \left[\rho v_r v_\theta r^2 \right]_0^R \tag{1.20}$$

For a flow in a cylindrical duct $v_r(R) = 0$ and Eq. (1.20) shows that the quantity G_θ is conserved along the z axis. It is important to note that when the section is not constant meaning that $R = R(z)$, the previous expression involves additional terms.

Axial momentum equation : The same process is applied to the axial momentum equation and yields :

$$\frac{d}{dz} \int_0^R (\rho v_z^2 + p) r \, \mathrm{dr} = - \left[r \rho v_r v_z \right]_0^R \tag{1.21}$$

from which one deduces that :

$$\frac{d}{dz} G_z = - \left[\rho v_r v_z r \right]_0^R \tag{1.22}$$

Since $v_r(R) = 0$ this indicates that the quantity G_z is conserved along the z axis.

Result : G_θ and G_z are respectively the azimuthal angular momentum flux and the axial momentum flux. These quantities will be conserved along the z axis when the right hand terms of Eq. (1.20) and Eq. (1.22) will be zero. This is achieved when the flow is confined with an axial swirler so that the radial velocities vanish at the boundaries $v_r(R) = v_r(0) = 0$. Hence, in a confined configuration with an axial or a radial swirler, the swirl number S is conserved

keeping in mind that turbulence effects and viscosity are neglected.

It is thus clear that the swirl number defined by :

$$S = \frac{G_\theta}{RG_z} = \frac{\int_0^R \rho v_\theta v_z r^2 \,\mathrm{d}r}{R\int_0^R (\rho v_z^2 + p) r \,\mathrm{d}r} \tag{1.23}$$

is independent of z.

1.3 Perturbative form of swirl number

It is possible to derive a linearized form of the swirl number S from equation Eq. (1.23) by considering a perturbed velocity field comprising axial and azimuthal velocity components :

$$\begin{aligned} v_z(r,z,t) &= \overline{v}_z(r) + v_z'(z,t) \\ v_\theta(r,z,t) &= \overline{v}_\theta(r) + v_\theta'(z,t) \end{aligned} \tag{1.24}$$

Neglecting the pressure term, only retaining first order terms in the flow perturbations and substituting Eq. (1.24) in Eq. (1.23) leads to the following expression of the linearized swirl number S :

$$S = \frac{\int_0^R \rho(\overline{v}_\theta \overline{v}_z + \overline{v}_\theta v_z' + \overline{v}_z v_\theta') r^2 \,\mathrm{d}r}{R\int_0^R (\rho \overline{v}_z^2 + 2\overline{v}_z v_z') r \,\mathrm{d}r} \tag{1.25}$$

After some simple manipulations, one obtains :

$$S = \frac{\int_0^R \rho \overline{v}_\theta \overline{v}_z r^2 \,\mathrm{d}r}{R\int_0^R \rho \overline{v}_z^2 r \,\mathrm{d}r} \left[\frac{1 + \frac{v_z'}{\overline{v}_z} + \frac{v_\theta'}{\overline{v}_\theta}}{1 + \frac{2v_z'}{\overline{v}_z}} \right] \tag{1.26}$$

where the mean swirl number $\overline{S}$ is defined by :

$$\overline{S} = \frac{\int_0^R \rho \overline{v}_\theta \overline{v}_z r^2 \,\mathrm{d}r}{R\int_0^R \rho \overline{v}_z^2 r \,\mathrm{d}r} \tag{1.27}$$

The linearized expression of the swirl number S may then be written as :

$$S = \overline{S}\left[1 + \frac{v_\theta'}{\overline{v}_\theta} - \frac{v_z'}{\overline{v}_z}\right] \tag{1.28}$$

One finds that the relative fluctuation in swirl number $S'/\overline{S}$ can be expressed in terms of the relative fluctuations in azimuthal and axial velocity components :

$$\frac{S'}{\overline{S}} = \frac{v_\theta'}{\overline{v}_\theta} - \frac{v_z'}{\overline{v}_z} \tag{1.29}$$

1.4 Effect of twisted vanes on swirl number

In many situations of practical interest, the flow is set in rotation with axial swirlers equipped with straight or twisted vanes. The analysis of the first type of swirler is carried out for example by Gupta *et al.* (1984). It is worth examining the latter case which is less well documented.

The vane angle effect on the steady swirl number is then investigated starting with the following expression :

$$S = \frac{\int_{r_1}^{r_2} \rho v_\theta v_z r^2 \, \mathrm{d}r}{r_2 \int_{r_1}^{r_2} (\rho v_z^2 + p) r \, \mathrm{d}r} \tag{1.30}$$

One can assume that the axial velocity v_z is constant over the radius r and that the density of the fluid is also constant. Neglecting the pressure term p one obtains (Ivanic *et al.* (2003)) :

$$S = \frac{2}{r_2(r_2^2 - r_1^2)} \int_{r_1}^{r_2} \frac{v_\theta(r)}{v_z} r^2 \, \mathrm{d}r \tag{1.31}$$

The ratio $v_\theta(r)/v_z$ can be directly linked to the angle $\delta(r)$ of the flow at the trailing edge of the vane of the swirler by $\tan\delta(r) = v_\theta(r)/v_z$.

This leads to the following expression :

$$S = \frac{2}{r_2(r_2^2 - r_1^2)} \int_{r_1}^{r_2} \tan\delta(r) r^2 \, \mathrm{d}r \tag{1.32}$$

This novel expression reflects the effect of the dependency of the swirl number on the angle of the trailing edge of the vane.

Aerodynamics modeling : There are three generic model flows which can be used to describe the flow generated by a swirler : (a) Solid body rotation, (b) Free vortex (c) A combination of solid body and free vortex flows. In practice, this defines the dependance of the azimuthal velocity component with respect the radius r.

The solid body rotation gives rise to the expression of $v_\theta^s(r)$, where Ω is the rotation rate of the flow :

$$v_\theta^s = \Omega r \tag{1.33}$$

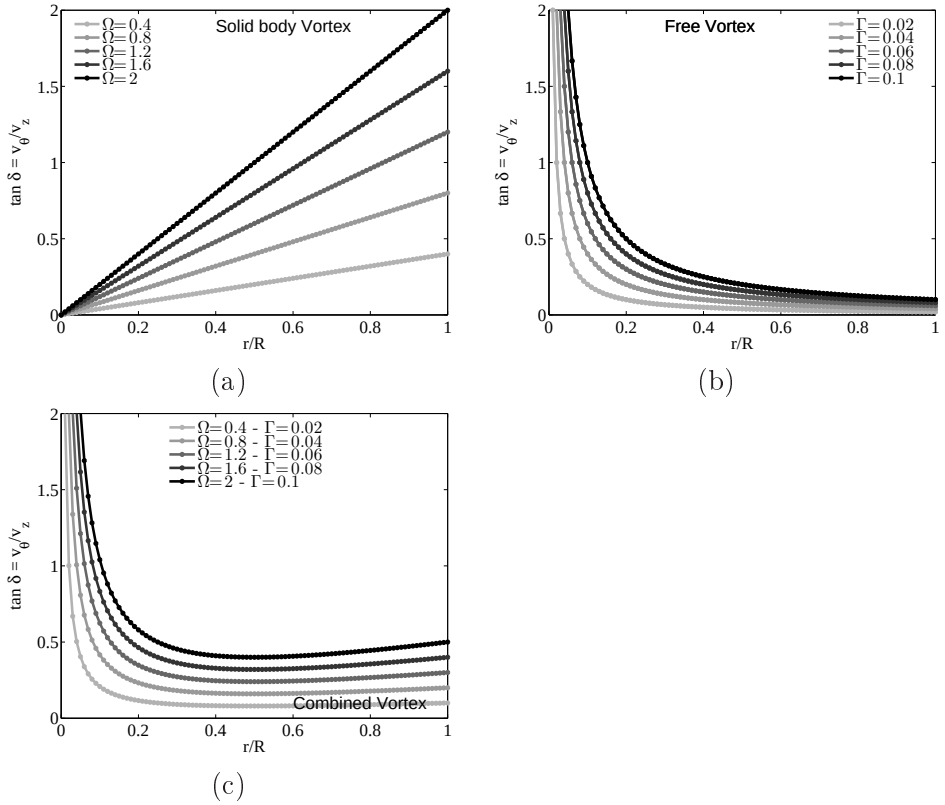

Figure 1.5: Radial distributions of velocity for three types of flows generated by a swirler. (a) : Solid body Vortex. (b) : Free Vortex. (c) : Combined Vortex.

The free vortex defines an expression of $v_\theta^f(r)$ where Γ is the circulation of the flow such that :

$$v_\theta^f = \frac{\Gamma}{r} \tag{1.34}$$

The combined solid body rotation and free vortex corresponds to $v_\theta^c(r)$:

$$v_\theta^c = \Omega r + \frac{\Gamma}{r} \tag{1.35}$$

It is possible to plot the radial distributions corresponding to the previous types of flows in terms of the ratio : $\tan\delta = v_\theta(r)/v_z$. Results are plotted in Figs. 1.5(a), (b) and (c).

It is easy to deduce the influence of the velocity distributions on the steady swirl number (see Fig. 1.6). This analysis is useful if the velocity distribution of a configuration is known and can be identified to one of the three generic flows considered previously.

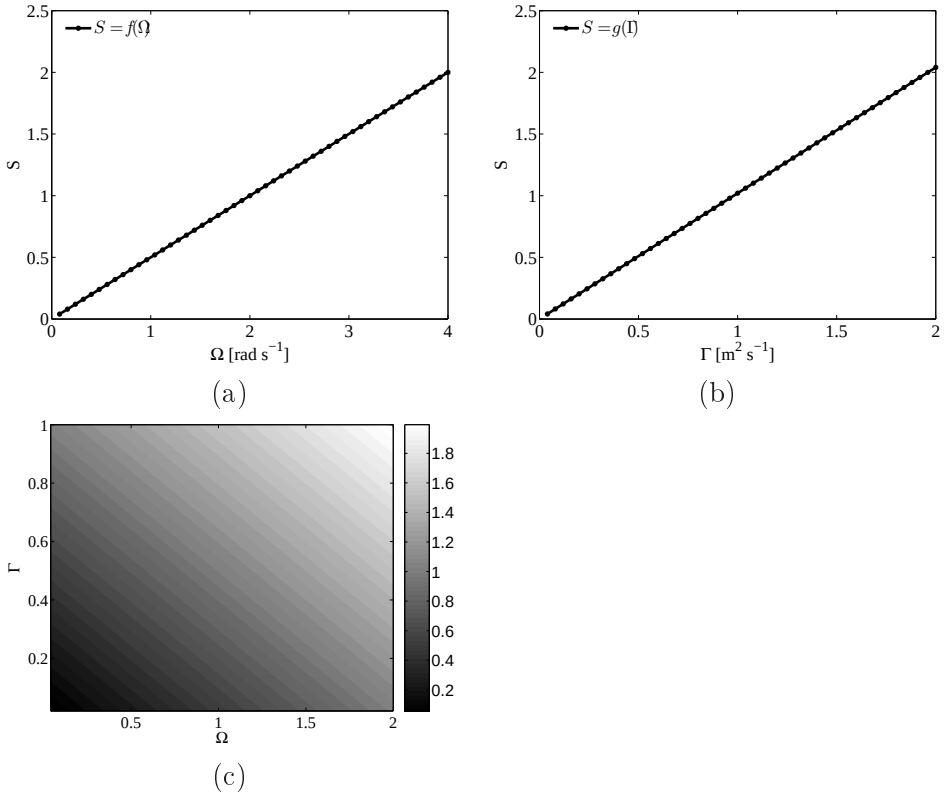

Figure 1.6: (a) : Swirl number S as a function of the rotation rate Ω. (b) : Swirl number S as a function of the circulation Γ. (c) : Swirl number S as a function of Ω and Γ.

Angle modeling : When the velocity distribution is not known, it is possible to determine the level of swirl by specifying the angle distribution of the swirler vanes. This is used in the swirler design process. The swirl number S defined by Eq. (1.32) can be numerically determined for a given $\delta(r)$ distribution. The following choice is made for this distribution :

$$\delta(r) = \delta_1 \left[1 + \alpha \left(\frac{r - r_1}{r_2 - r_1} \right)^m \right] \tag{1.36}$$

where α and m are coefficients and δ_1 is the vane angle at the trailing edge at $r = r_1$. Substituting this expression in Eq. (1.32), one obtains results plotted in Fig. 1.7. The white squares curve correspond to straight vanes expressions (Gupta *et al.* (1984)) in which $\delta(r)$ is a constant. The two others curves correspond to a preset value of the swirl number S and provide the angles δ_1 and δ_2 which need to be specified to reach this number. These curves have been obtained by using $\alpha = 1$ and $m = 1$. For example to obtain a swirl number of 0.6, it is necessary to have $\delta_1 = 23.5°$ and $\delta_2 = 47.5°$.

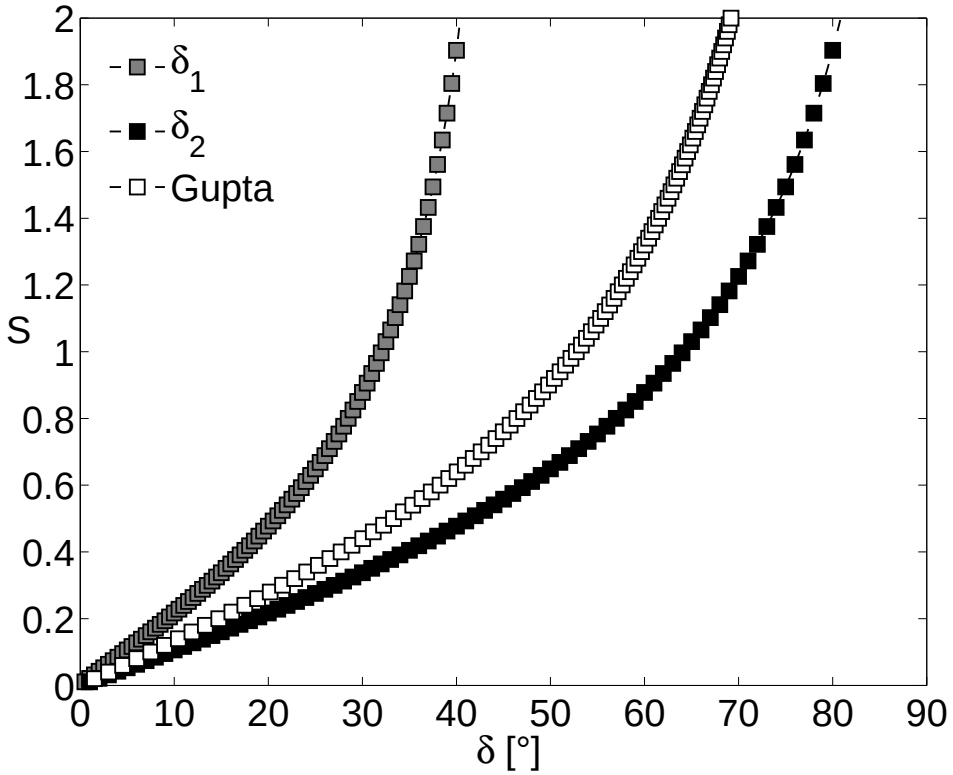

Figure 1.7: Swirl number S obtained with Eq. (1.32) taking into account the radius dependency of the axial swirler as a function of the angle of vane δ. Data obtained theoretically are compared with expressions based on straight vanes assumptions.

1.5 Theoretical derivation of unsteady swirl number

We have previously analyzed the fluctuations in swirl number induced by perturbations in the velocity components. However, this analysis was based on a steady flow expression of the swirl number. In the unsteady flow case, one wonders if this is still appropriate or if one should include unsteady angular momentum and momentum flux terms in the swirl number. This is investigated in what follows. This analysis is only meant to explore a possible modification of the definition of the swirl number which might be more adequate than the steady state expression.

We introduce a new definition of the swirl number :

$$S(t) = \frac{J_\theta}{R\,J_z} = \frac{1}{R}\frac{\int_z \int_0^R \frac{\partial \rho v_\theta}{\partial t} r^2 \,\mathrm{dr}\,\mathrm{dz} + \int_0^R \rho v_\theta v_z r^2 \,\mathrm{dr}}{\int_z \int_0^R \frac{\partial \rho v_z}{\partial t} r \,\mathrm{dr}\,\mathrm{dz} + \int_0^R (\rho v_z^2 + p) r \,\mathrm{dr}} \tag{1.37}$$

where :

$$J_\theta = \int_z \int_0^R \frac{\partial}{\partial t}(\rho v_\theta r^2)\,\mathrm{d}r\,\mathrm{d}z + G_\theta \tag{1.38}$$

and

$$J_z = \int_z \int_0^R \frac{\partial}{\partial t}(\rho v_z r)\,\mathrm{d}r\,\mathrm{d}z + G_z \tag{1.39}$$

These two quantities J_θ and J_z take into account unsteady accumulations terms. It is shown in what follows that both J_θ and J_z do not depend on z so that this unsteady swirl number is again constant in the flow but can vary with time.

The starting point is still the mass and momentum balance equations with unsteady terms.

The mass balance equation is :

$$\frac{1}{r}\frac{\partial r v_r}{\partial r} + \frac{\partial v_z}{\partial z} = 0 \tag{1.40}$$

Keeping the unsteady term, the radial momentum balance may be written as :

$$\frac{\partial v_r}{\partial t} + v_r\frac{\partial v_r}{\partial r} + v_z\frac{\partial v_r}{\partial z} - \frac{v_\theta^2}{r} = -\frac{1}{\rho}\frac{\partial p}{\partial r} \tag{1.41}$$

The azimuthal momentum equation takes the form :

$$\frac{\partial v_\theta}{\partial t} + v_r\frac{\partial v_\theta}{\partial r} + v_z\frac{\partial v_\theta}{\partial z} + \frac{v_r\, v_\theta}{r} = 0 \tag{1.42}$$

and the axial momentum balance may be written as :

$$\frac{\partial v_z}{\partial t} + v_r\frac{\partial v_z}{\partial r} + v_z\frac{\partial v_z}{\partial z} = -\frac{1}{\rho}\frac{\partial p}{\partial z} \tag{1.43}$$

The gravity term g is neglected in the last expression. It is convenient to work with conservative form of equations and one only needs axial and azimuthal momentum equations to obtain a working expression for the swirl number.

For the azimuthal momentum equation, one has:

$$\frac{\partial \rho v_\theta}{\partial t} + \frac{\partial \rho v_r v_\theta}{\partial r} + \frac{\partial \rho v_\theta v_z}{\partial z} + 2\rho\frac{v_\theta v_r}{r} = 0 \tag{1.44}$$

which can be also written under the form :

$$r\frac{\partial \rho v_\theta}{\partial t} + r\frac{\partial \rho v_r v_\theta}{\partial r} + r\frac{\partial \rho v_\theta v_z}{\partial z} + 2\rho v_\theta v_r = 0 \tag{1.45}$$

This equation can be integrated over a constant section of the flow field perpendicular to the z axis :

$$\int_0^R r^2 \frac{\partial}{\partial t}(\rho v_\theta)\mathrm{dr} + \int_0^R \frac{\partial}{\partial r}(\rho r^2 v_r v_\theta)\mathrm{dr} + \int_0^R r^2 \frac{\partial}{\partial z}(\rho v_\theta v_z)\mathrm{dr} = 0 \tag{1.46}$$

Then :

$$\int_0^R r^2 \frac{\partial}{\partial t}(\rho v_\theta)\mathrm{dr} + \int_0^R r^2 \frac{\partial}{\partial z}(\rho v_\theta v_z)\mathrm{dr} = -\Big[\rho r^2 v_r v_\theta\Big]_0^R \tag{1.47}$$

Substituting in this last equation the expression of G_θ, one obtains :

$$\int_0^R r^2 \frac{\partial}{\partial t}(\rho v_\theta)\mathrm{dr} + \frac{\mathrm{d}}{\mathrm{d}z} G_\theta = -\Big[\rho r^2 v_r v_\theta\Big]_0^R \tag{1.48}$$

And finally :

$$\frac{\mathrm{d}}{\mathrm{d}z}\left[\int_z \int_0^R r^2 \frac{\partial}{\partial t}(\rho v_\theta)\mathrm{drdz} + G_\theta\right] = -\Big[\rho r^2 v_r v_\theta\Big]_0^R \tag{1.49}$$

The axial momentum equation is :

$$\frac{\partial \rho v_z}{\partial t} + \frac{\partial \rho v_r v_z}{\partial r} + \frac{\partial \rho v_z^2}{\partial z} + \rho \frac{v_z v_r}{r} = -\frac{\partial p}{\partial z} \tag{1.50}$$

This equation can also be integrated over a constant section of the flow field perpendicular to the z axis.

Azimutal momentum equation : For the azimutal momentum equation and following the previous derivation resulting in Eq. (1.49), one obtains :

$$\frac{d}{dz} J_\theta = \frac{\mathrm{d}}{\mathrm{dz}}\left[\int_z \int_z r^2 \frac{\partial}{\partial t}\rho v_\theta \,\mathrm{drdz} + G_\theta\right] = -\Big[\rho v_r v_\theta r^2\Big]_0^R \tag{1.51}$$

Since $v_r(R) = 0$, one finds that :

$$\frac{d}{dz} J_\theta = 0 \tag{1.52}$$

Axial momentum equation : For the axial momentum equation and following the same derivation procedure, one has :

$$\frac{d}{dz} J_z = \frac{\mathrm{d}}{\mathrm{dz}}\left[\int_z \int_z r \frac{\partial}{\partial t}\rho v_z \,\mathrm{drdz} + G_z\right] = -\Big[\rho v_r v_z r\Big]_0^R \tag{1.53}$$

Since, $v_r(R) = 0$, one obtains :

$$\frac{d}{dz} J_z = 0 \tag{1.54}$$

Result : The previous derivation indicates that :

$$J_\theta = G_\theta + \int_z \int_0^R \frac{\partial}{\partial t} \rho v_\theta r^2 \, \mathrm{dr} \, \mathrm{dz} \tag{1.55}$$

and

$$J_z = G_z + \int_z \int_0^R \frac{\partial}{\partial t} \rho v_z r \, \mathrm{dr} \, \mathrm{dz} \tag{1.56}$$

are constant with respect to z.

Both axial and azimuthal unsteady terms appear in equations Eq. (1.55) and Eq. (1.56). The unsteady swirl number $S(t)$ can then be defined by :

$$S(t) = \frac{J_\theta}{RJ_z} = \frac{1}{R} \frac{\int_z \int_0^R \frac{\partial \rho v_\theta}{\partial t} r^2 \, \mathrm{dr} \, \mathrm{dz} + \int_0^R \rho v_\theta v_z r^2 \, \mathrm{dr}}{\int_z \int_0^R \frac{\partial \rho v_z}{\partial t} r \, \mathrm{dr} \, \mathrm{dz} + \int_0^R (\rho v_z^2 + p) r \, \mathrm{dr}} \tag{1.57}$$

This unsteady swirl number $S(t)$ is also constant in the flow.

1.6 Perturbative form of unsteady swirl number

To explore the previous formulation, it is convenient to derive a linearized version of Eq. (1.57). This is achieved in what follows. One considers that perturbed velocity field is given by :

$$\begin{aligned} v_z(r,z,t) &= \overline{v}_z(r) + v'_z(z,t) \\ v_\theta(r,z,t) &= \overline{v}_\theta(r) + v'_\theta(z,t) \end{aligned} \tag{1.58}$$

Substituting this velocity field in equation Eq. (1.57), integrating the expression over the distance L corresponding to the swirler axial size and only retaining first order terms one obtains :

$$S(t) = \frac{\int_0^R \rho(\overline{v}_\theta \overline{v}_z + \overline{v}_\theta v'_z + v'_\theta \overline{v}_z - i\omega v'_\theta L) r^2 \, \mathrm{dr}}{R \int_0^R \rho(\overline{v}_z^2 + 2\overline{v}_z v'_z - i\omega v'_z L) r \, \mathrm{dr}} \tag{1.59}$$

After some manipulations, one finds that :

$$S(t) = \frac{\int_0^R \rho \overline{v}_\theta \overline{v}_z r^2 \, \mathrm{dr}}{R \int_0^R \rho \overline{v}_z^2 r \, \mathrm{dr}} \left[\frac{1 + \frac{v'_\theta}{\overline{v}_\theta} + \frac{v'_z}{\overline{v}_z} - \frac{i\omega L}{\overline{v}_z} v'_\theta \overline{v}_\theta}{1 + \frac{2v'_z}{\overline{v}_z} - \frac{i\omega L}{\overline{v}_z} \frac{v'_z}{\overline{v}_z}} \right] \tag{1.60}$$

One finally obtains the following expression for the linearized unsteady swirl number :

$$S(t) = \overline{S}(t) \left[1 + \frac{v'_\theta}{\overline{v}_\theta} - \frac{v'_z}{\overline{v}_z} - i \frac{\omega L}{\overline{v}_z} \left(\frac{v'_\theta}{\overline{v}_\theta} - \frac{v'_z}{\overline{v}_z} \right) \right] \tag{1.61}$$

Swirl number S	$\frac{\int_0^R \rho v_\theta v_z r^2 \,\mathrm{dr}}{R\int_0^R (\rho v_z^2+p) r \,\mathrm{dr}}$
Linearized form S	$\overline{S}\left[1+\frac{v'_\theta}{\overline{v}_\theta}-\frac{v'_z}{\overline{v}_z}\right]$
Fluctuation $S'/\overline{S}$	$\frac{v'_\theta}{\overline{v}_\theta}-\frac{v'_z}{\overline{v}_z}$
Unsteady swirl number $S(t)$	$\frac{1}{R}\frac{\int_z\int_0^R \frac{\partial \rho v_\theta}{\partial t} r^2 \,\mathrm{dr}\,\mathrm{dz}+\int_0^R \rho v_\theta v_z r^2 \,\mathrm{dr}}{\int_z\int_0^R \frac{\partial \rho v_z}{\partial t} r \,\mathrm{dr}\,\mathrm{dz}+\int_0^R (\rho v_z^2+p) r \,\mathrm{dr}}$
Linearized form $S(t)$	$\overline{S}(t)\left[1+\frac{v'_\theta}{\overline{v}_\theta}-\frac{v'_z}{\overline{v}_z}-i\frac{\omega L}{\overline{v}_z}\left(\frac{v'_\theta}{\overline{v}_\theta}-\frac{v'_z}{\overline{v}_z}\right)\right]$
Fluctuation $S'(t)/\overline{S}(t)$	$\left[\frac{v'_\theta}{\overline{v}_\theta}-\frac{v'_z}{\overline{v}_z}\right]\left[1-i\frac{\omega L}{\overline{v}_z}\right]$

Table 1.1: Theoretical work of the present study on swirl numbers.

The relative fluctuation of the linearized unsteady swirl number is such that :

$$\frac{S'(t)}{\overline{S}(t)}=\left[\frac{v'_\theta}{\overline{v}_\theta}-\frac{v'_z}{\overline{v}_z}\right]\left[1-i\frac{\omega L}{\overline{v}_z}\right] \tag{1.62}$$

1.7 Synthesis

A synthesis of swirl numbers derived in the previous sections is given in Table. 1.1.

It is also interesting to summarize the various swirl number relations found in the literature. These numbers are gathered in Table. 1.2. The classical swirl number expression Eq. (1.23) includes a pressure term which is often difficult to estimate but is generally small compared to the momentum flux term. The pressure term is sometimes replaced by a term $1/2v_\theta^2$ (see for example Ribeiro and Whitelaw (1980)) or it is simply removed as in Ivanic *et al.* (2003) which is reasonable for low velocity configurations. For turbulent incompressible flows, expressions have been derived by Chigier and Chervinsky (1967); Mattingly and Oates (1986) which include turbulent fluctuations but the Reynolds stress term $\overline{v'_\theta v'_z}$ is difficult to obtain experimentally. Many simplifications are available in the literature as in Gupta *et al.* (1984) where the swirl number is given as a function of the trailing edge angle of the swirler vanes. This correlation can be

improved by taking into account the vane angle profile as shown in a previous section. In analytical studies of vortex breakdown, another definition has been proposed with a velocity distribution taken at the origin z_0 (see Billant *et al.* (1998)). Finally, it is also possible to define the swirl number as the inverse of the Rossby number (Liang and Maxworthy (2005)). An overview of these expressions are gathered in Table. 1.2.

Classical swirl number	$S = \frac{\int_{r_1}^{r_2} \rho v_\theta v_z r^2 \,\mathrm{d}r}{r_2 \int_{r_1}^{r_2} (\rho v_z^2 + p) r \,\mathrm{d}r}$
Ribeiro and Whitelaw (1980)	$S = \frac{\int_0^{\infty} \rho v_\theta v_z r^2 \,\mathrm{d}r}{r_2 \int_0^{\infty} \rho (v_z^2 - \frac{1}{2} v_\theta^2) r \,\mathrm{d}r}$
Ivanic *et al.* (2003)	$S = \frac{\int_{r_1}^{r_2} \rho v_\theta v_z r^2 \,\mathrm{d}r}{r_2 \int_{r_1}^{r_2} \rho v_z^2 r \,\mathrm{d}r}$
Mattingly and Oates (1986)	$S = \frac{\int_{r_1}^{r_2} \rho (\overline{v}_\theta \overline{v}_z + \overline{v'_\theta v'_z}) r^2 \,\mathrm{d}r}{r_2 \int_{r_1}^{r_2} (\rho \overline{v}_z^2 + \rho \overline{v'^2_z} + (p - p_\infty)) r \,\mathrm{d}r}$
Chigier and Chervinsky (1967)	$S = \frac{\int_{r_1}^{r_2} \rho (\overline{v}_\theta \overline{v}_z + \overline{v'_\theta v'_z}) r^2 \,\mathrm{d}r}{r_2 \int_{r_1}^{r_2} \rho (\overline{v}_z^2 - \frac{1}{2}\overline{v}_\theta^2 + \overline{v'^2_z} - \frac{1}{2}(\overline{v'^2_\theta} + \overline{v'^2_r})) r \,\mathrm{d}r}$
Gupta *et al.* (1984)	$S = \frac{2}{3} \frac{1 - (r_2/r_1)^3}{1 - (r_2/r_1)^2} \times \tan\delta$
Palies (2010)	$S = \frac{2}{r_2 (r_2^2 - r_1^2)} \times \int_{r_1}^{r_2} \tan\delta(r) r^2 \,\mathrm{d}r$
Billant *et al.* (1998)	$S = \frac{2 v_\theta (r_2/2, z_0)}{v_z (0, z_0)}$
Liang and Maxworthy (2005)	$S = \frac{r_2 \Omega}{v_z}$

Table 1.2: Synthesis on swirl numbers.

Chapter 2

Experimental setup and diagnostics

Abstract : *The laboratory-scale experiment and diagnostics used in this thesis are now described. The focus is on the different parts of the setup and specifically on the swirler devices. Diagnostics associated to LDV and heat release rate measurements are then detailed. The Abel transform method is presented and will be used in this manuscript to analyze swirling flame dynamics. Two methods are described which can be used to determine the heat release rate. The first uses a photomultiplier which captures the whole light radiated by the flame. The second is based on the sum of the pixel light intensity received by an ICCD camera without any filter. It is shown that a good agreement between both techniques is obtained indicating that the light emission recorded by the ICCD camera mainly originates from free radicals in the flame.*

Résumé : *L'expérience de laboratoire et les diagnostics utilisés dans ce document sont décrits dans ce chapitre. La description porte sur les différents éléments de l'installation et traite notamment des swirlers. Les diagnostics de mesures associées à la vélocimétrie laser (LDV), au photomultiplicateur et aux microphones sont ensuite exposés. On décrit la transformée d'Abel qui est utilisée dans ce manuscrit pour déduire la structure de flamme des images d'émission et analyser la dynamique de la flamme swirlées au cours d'un cycle d'oscillation. Deux méthodes de détermination du taux de dégagement de chaleur d'une flamme sont ensuite comparées. La première utilise un photomultiplicateur qui capte toute la lumière rayonnée par la flamme. La seconde est basée sur la somme de l'intensité lumineuse reçue par les pixels d'une caméra ICCD sans filtre. Il est démontré que les signaux déduits de ces deux types de capteurs sont en bon accord.*

2.1 Introduction

This chapter introduces the main elements of the experiment. The setup is described in section 2.2. The axial and radial swirlers design is discussed in section 2.3. And section 2.4 is a review of diagnostics with special attention to the laser Doppler velocimeter and to the Abel transform procedure. That last section also presents a novel method to determine the heat release rate of a flame based on the postprocessing of chemiluminescence images.

2.2 Laboratory-scale experiment

The burner sketched in Fig. 2.1 comprises a standard body including a driver unit, a settling chamber, a contraction ended by a constant diameter duct where a swirler is installed, a horizontal end piece and a cylindrical flame tube. An air/methane premixed flow is delivered from the premixing unit through two diametrally opposed apertures at the base of the burner. The flow then crosses a grid and a honeycomb in order to break the largest turbulent scales. The gas then traverses a convergent unit to decrease the boundary layer thickness, reduce the level of turbulence and generate a flat velocity profile at the swirler input. The rotation of the flow is generated by an axial swirler equipped with vanes arranged periodically around a central rod ($d = 6$ mm in diameter). This central rod is terminated with a small cone (10 mm in diameter at its base) which is used to stabilize the flame in the swirling flow and to minimize flashback. The outer diameter of the injection tube is $d = 22$ mm. The tube confining the flame is made of quartz allowing optical visualization of the flame and transmitting

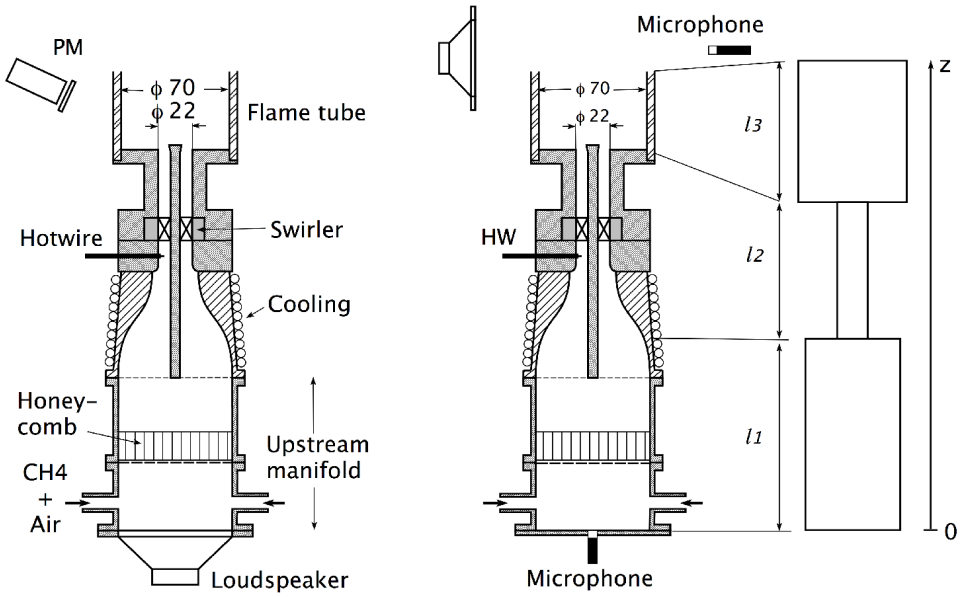

Figure 2.1: (a) : Experimental configuration used to measure flame describing functions. (b) : Without the loudspeaker, this setup is also used to obtain frequencies and amplitude of velocity disturbances u'/U_b under self-sustained limit cycle operation. (c) : Idealized representation of the burner geometry. Three lengths of the upstream manifold l_1 can be used together with three different length of the flame tube l_3.

its radiation in the near ultraviolet. Its diameter is 70 mm and the length l_3 can take different values : 100 mm, 150 mm, 200 mm and 400 mm respectively. There are also three lengths l_1 available for the upstream manifold : short (96 mm), medium (160 mm) and long (224 mm). The upstream manifold diameter is 65 mm. The length of the convergent unit is 60 mm. Combination of these elements yields twelve geometrical configurations.

The equivalence ratio is set equal to $\phi = 0.7$ in all experiments except with the radial swirler at $S = 0.65$ where the equivalence ratio is 0.63. A premix unit is used to mix methane and air far upstream mass flow controllers. Two operating conditions A and B were investigated corresponding respectively to two bulk flow velocities $U_b = 2.67$ m s^{-1} and 4.13 m s^{-1}, determined in the injector tube downstream of the swirler. The corresponding Reynolds numbers are respectively Re = 3 900 and Re = 6 000.

Air is provided by the laboratory filtered network and the generating pressure is 6 bars. The G20 methane is stored on site. Flow rate control during experiments is performed by means of mass flowcontrollers : maximum flow rates of

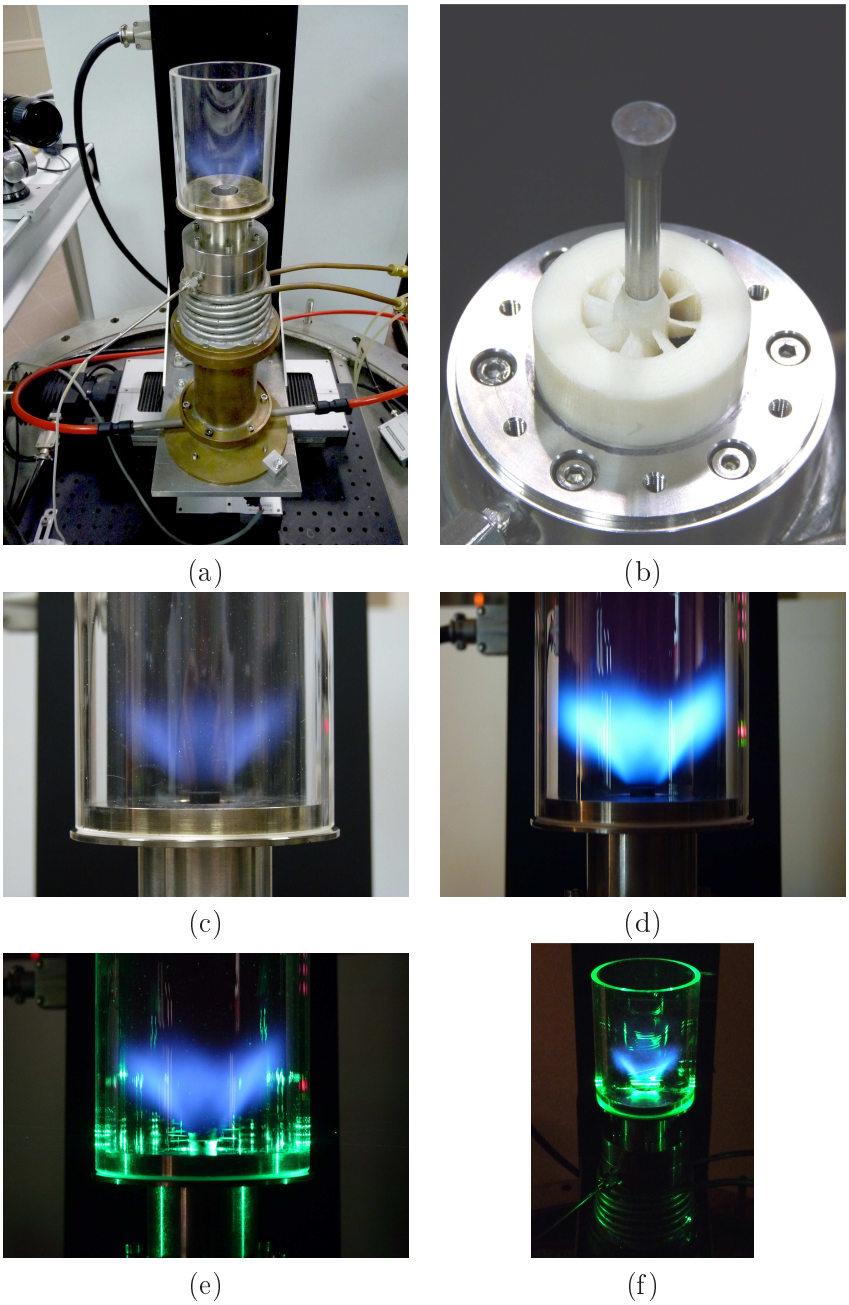

Figure 2.2: Photos from the experiment. (a) : global view of the setup. (b) : close-up view of the swirler and the rod. (c) : view of the flame inside the quartz tube. (d) : saturated image of the flame. (e) & (f) : flame and laser operating.

4.2 l s^{-1} for the air stream and of 0.6 l s^{-1} for the methane stream. Recorded data are processed with Labview and Matlab. Loudspeakers are also used in the experiments presented hereby, either to determine the burner acoustics by

exciting the eigenmodes of the system or to modulate the upstream flow velocity. Characteristics of the different tools are gathered in Table 2.1.

In Fig. 2.2, we show photographs of the experiments. (a) : global view of the setup with the burner consisting in three parts : the flame tube, the injector and the upstream manifold. The cooling tubes are also visible. (b) : close-up view of the swirler and the rod. (c) : view of the flame inside the quartz tube. (d) : saturated image of the flame. (e) & (f) : flame and laser under operation.

Table 2.1: Materials and diagnostic tools characteristics.

Equipment	Manufacturer	Reference
Flow-controller (Air)	Bronkhorst	F202AC-FAC55V, 5 Nm^3h^{-1} with C_3H_8
Flow-controller (CH_4)	Bronkhorst	F201AC-FAC33V, 50 $Nl\,min^{-1}$ with N_2
Microphone (5Hz-20kHz, 50mV/Pa)	Brüel & Kjaer	4189
Microphone preamplifier	Brüel & Kjaer	2669
Microphone amplifier	Brüel & Kjaer	Nexus Conditioning Amplifier
Hot wire probe	Dantec Dynamics	55P16
Power supply	Dantec Dynamics	Mini CTA 54T30
Photomultiplier	Electron Tubes Limited	91295B
Current to voltage convertor	Electron Tubes Limited	Transimpedance Amplifier A1
Loudspeaker	Focal	4K211
Sinusoidal wave generator	Hameg	HM8040
Loudspeaker amplifier	Europsonic	PA-9402

2.3 Swirlers

The swirler location is shown in Fig. 2.3. Three swirler geometries have been designed in this thesis : one axial and two radials which differs by their swirl numbers. The main part of the work presented in the manuscript concerns the axial swirler. This swirler is sketched in Fig. 2.4 while one of the radial swirler is sketched in Fig 2.5. Both geometries are widely encountered in industrial applications likes gas turbines or jet engines and in research studies. The geometry of the swirlers was optimized to obtain a predetermined value of the swirl number corresponding to a flow featuring a well established inner recirculation zone. Another objective was to reduce the perturbation level produced downstream of the swirler due to the presence of the blades. This was obtained by using NACA 8411 airfoils to design the blades. The result of the design process is a swirler comprising vanes periodically spaced. The swirler was manufactured by fast prototyping of plastic material, see Palies *et al.* (2009). The surface quality is moderately smooth but sufficient for the present purpose. In this study, the swirl number is determined experimentally by integrating the profiles of mean axial and azimuthal velocities measured at the injector outlet.

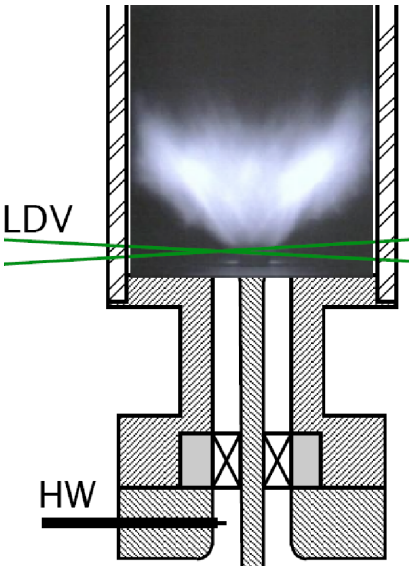

Figure 2.3: Close-up view of the upper part of the burner.

Axial swirler : The axial swirler is made of eight vanes periodically spaced by 45°. The vanes are twisted, so that the angle at the trailing edge evolves linearly from 30° at the hub to a value of 58° at the vane tip. Twisting is employed to impose the same rotation to the flow streamlines along the vane. In the absence of twist there would be regions near the vane tip in which the flow might not be deflected enough. The evolution angle at the trailing edge as a function of the radius is given by :

$$\delta(r) = \delta_1 \left[1 + \alpha \left(\frac{r - r_1}{r_2 - r_1} \right)^m \right] \tag{2.1}$$

where $\alpha = 1$ and m=1 are the coefficients of the profile and $\delta_1 = 30°$ is the vane angle at the trailing edge at $r = r_1$.

Radial swirler : The radial swirlers are made of eighteen vanes periodically spaced by 20°. Vanes are made of NACA 8411 airfoils profiles. Two parameters characterized the radial geometry : the thickness of the circular inlet section of the swirler and the trailing edge angle of the vanes. The trailing edge angle is equal to 58° for the first one and 72° for the second one. The thickness of the circular inlet section is 6 mm for the first swirler and 4 mm for the second one. They provide two distincts swirl numbers respectively $S = 0.55$ and $S = 0.65$.

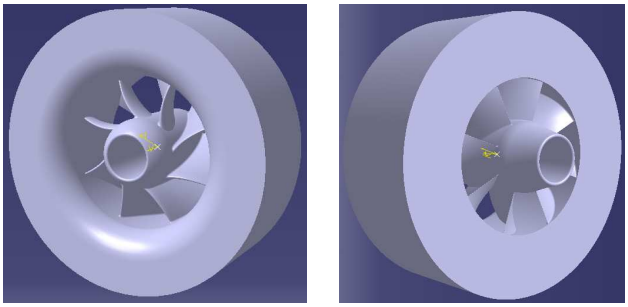

(a) (b)

Figure 2.4: Axial swirler geometry. (a) : upstream side. (b) : downstream side.

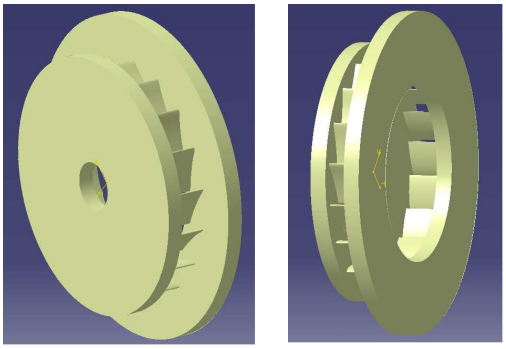

(a) (b)

Figure 2.5: Radial swirler geometry with thickness $h = 4$ mm. (a) : upstream side. (b) : downstream side.

2.4 Diagnostics

LDV : Velocity profiles were obtained by laser Doppler velocimetry (LDV), under automated displacement control and data acquisition. Light delivered by the green line of a 5W Argon-ion Laser ($\lambda = 514.5$ nm) is scattered by the seeded particles and collected by a filtered photomultiplier. Velocity is deduced from the Doppler bursts by a frequency counter. In all experiments, the reference oscillating velocity is measured at $z = 2.9$ mm above the edge of the nozzle. Micronic oil droplets are generated by a perfume atomizer, see Durox *et al.* (1999). The mean droplet diameter is 2.5 μm and the droplet size dispersion is small (80% of the size distribution is under 5 μm). The seeding rate, set at about 25 000 validated data samples per second (over 70% validation) assures well resolved measurements in a wide range of frequencies between 10 and 400 Hz (Durox *et al.* (2004)). These data rate and validation percentage can be achieved by a mode of the frequency counter allowing multiple counts per particle, with Bragg frequency shift of 0.1 MHz. When the frequency counter mode is switched to deliver one count per particle, the data rate drops to about 5 000 samples per second and the validation percentage becomes 60%. This ensures that there is typically only one particle at a time in the probe volume.

Mean velocity profiles measured by LDV at the outlet of the injector for the three geometries are now investigated. The swirl number calculation is done according to the following formulae from Gupta *et al.* (1984) and realized on the right side of the velocity profiles :

$$S = \frac{\int_0^R \rho\, u\, v\, 2\,\pi\, r^2\, dr}{R \int_0^R \rho\, u^2\, 2\,\pi\, r\, dr} \tag{2.2}$$

where ρ is the fluid density, u and v respectively the axial and azimuthal velocity components, r the radius and R the characteristic outer radius.

The comparison is first achieved between the axial and the radial swirlers and results of measurements are sketched in Fig. 2.6. The calculated swirl numbers are close to $S = 0.55$ for both swirlers. For the axial swirler, Fig. 2.6 (a), it is observed that velocity profiles are not perfectly symmetric and this effect is due to the wakes of the vanes behind the swirler. The maximum of axial velocity is close to 4.1 m s^{-1} while the maximum of azimuthal velocity is near 2.4 m s^{-1}. For the radial swirler, Fig. 2.6 (b), we also distinguished little differences in the symmetry of the profiles. In this case, the maximum axial velocity is close to 3.8 m s^{-1} and the maximum azimuthal velocity is 2.4 m s^{-1}.

One can now investigated the mean axial and azimuthal velocity profiles generated by radial swirlers. They are both presented in Fig. 2.7. For the first one, Fig. 2.6 (a), the swirl number is $S = 0.55$ while for the second one in Fig. 2.7 (b), the swirl number is close to 0.65. This can be seen by matching azimuthal

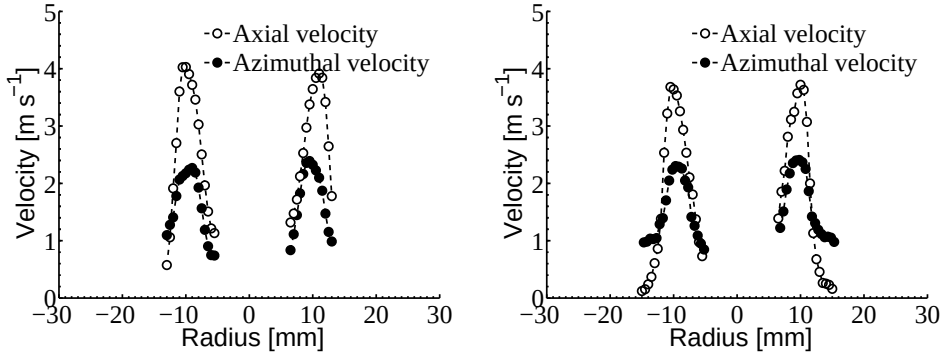

Figure 2.6: Mean velocity profiles of axial and azimuthal components at the injector outlet measured with a laser Doppler velocimeter. The swirl number deduced from these velocity profiles is equal to $S = 0.55$. (a) : Axial swirler (b) : Radial swirler.

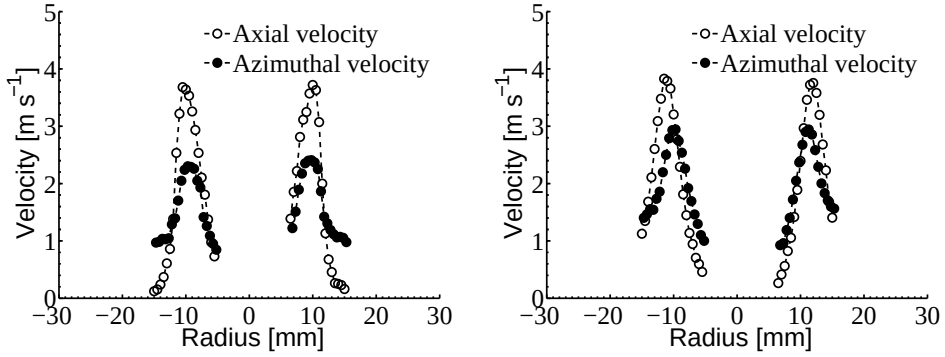

Figure 2.7: Mean velocity profiles of axial and azimuthal components at the injector outlet measured with a Laser Doppler Velocimeter for the radial swirlers. Results give two distincts values for the swirl number. (a) : $S = 0.55$, $h = 6$ mm (b) : $S = 0.65$, $h = 4$ mm.

velocity profiles where it is clear that in the second case, the maximum is 3 m s^{-1} while this maximum is 2.4 m s^{-1} for the first case. In both cases, the maximum axial velocity reach a constant value of 3.8 m s^{-1}. While the axial component of the velocity keep a constant value between both swirlers, the azimuthal component increases which reflects an increase of the swirl number from 0.55 to 0.65.

Abel transform : The flame motion induced by incoming perturbations will be analyzed in chapter 6 using optical imaging techniques to interpret flame describing functions data. This can be achieved by making use of OH PLIF methods as done by Thumuluru *et al.* (2007); Lee *et al.* (2000); Bellows *et al.*

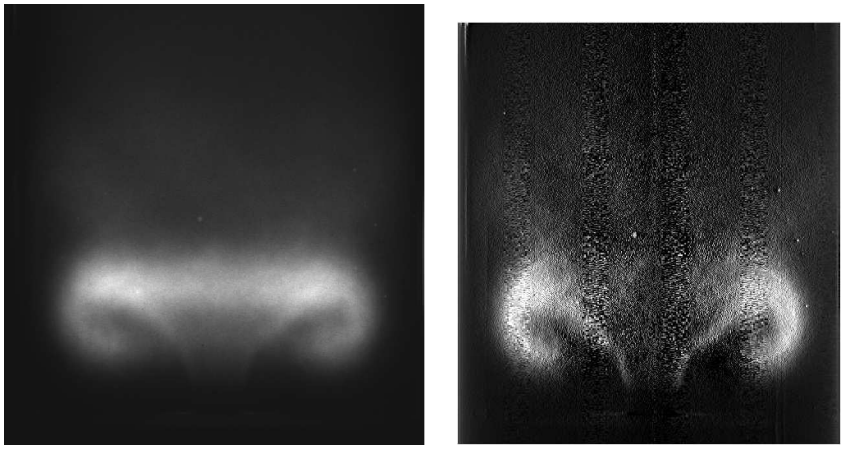

(a) (b)

Figure 2.8: (a) Typical average emission image acquired with the ICCD camera. (b) Abel transform. Configuration : $U_b = 4.13$ m s^{-1}, $f = 100$ Hz and $u'/U_b = 0.5$.

(2007) or by directly recording the flame emission with an ICCD camera as did Külsheimer and Büchner (2002); Schuller *et al.* (2003a); Bellows *et al.* (2007). The method is in fact quite classical and has been used in numerous combustion dynamics studies. Some early emission images from free radicals were obtained for example by Poinsot *et al.* (1987). A direct analysis of instantaneous flame emission images is not suitable because turbulent fluctuations tend to hide the organized motion associated with the periodic motion. It is also important to remember that emission images are formed by integrating flame radiation over the line of sight. It is then more suitable to use a combination of phase conditioned averaging of emission images followed by an Abel transformation. The main objective is to capture the dynamics of the flame at a set of instants in the cycle of oscillation. This is achieved by accumulating one hundred instantaneous images for twelve selected phases in the cycle. The resulting averages are then compressed by binning adjacent pixels of two by two matrices to decrease the image size and augment the signal to noise ratio. An Abel transform is then applied to each binned image to get the two dimensional flame slice. This processing is applied to flames A and B described previously. The Abel transform is illustrated in Fig. 2.8 for an external modulation frequency $f = 100$ Hz. The processed image indicates that combustion is concentrated in a flame brush with a flame edge in the injector near field adjacent to a central core. A special process has been applied to reduce the noise associated with the Abel transform : a Gaussian filter is used to smooth the data on the axis. This does not completely reduce the fluctuations which appear near the axis of symmetry.

The shape of the flame is first examined without modulation for the selected

operating conditions A and B corresponding respectively to mean flow velocities U_b of 2.67 m s^{-1} and 4.13 m s^{-1} at the outlet of the injector tube. Figure 2.9 displays four images of the flame for each operating condition. The first (Fig. 2.9(a)) corresponds to an instantaneous image of the flame region. This shows the highly wrinkled flame pattern formed by the system. The second image (Fig. 2.9(b)) is an ensemble average of a hundred instantaneous images which highlights the mean flame pattern without external perturbations. The third image (Fig. 2.9(c)) is obtained by taking the Abel transform of the average image. This yields a slice through the mean flame. The Abel transform is applicable if the average flame is rotationally symmetric. Images in Fig. 2.9(d) have been scaled in terms of volumetric heat release rate. To do this, one assumes that the relation between chemiluminescence and heat release is linear and essentially depends on the equivalence ratio which is constant in the present experiments. It is usually considered that the dependence with respect to curvature, strain and unsteadiness is less important and that the corresponding variations are small. It is then possible to use a scaling factor β and obtain an estimate of the volumetric heat release rate in W m^{-3}. This is admittedly an approximation but it provides an order of magnitude which can be quite useful. For example the values obtained in this way can be compared with those deduced from calculations thus serving as a guide to modeling. One may then write :

$$\dot{q}(r,x,t) = \beta \times I(r,x,t) \tag{2.3}$$

where $\dot{q}(r,x,t)$ is the local heat release rate and $I(r,x,t)$ the pixel light intensity. The scaling factor β can be determined by integrating the previous expression over the flame volume

$$\dot{Q} = \int \dot{q}(r,x,t) 2\pi r dr dx = \beta \int I(r,x,t) 2\pi r dr dx \tag{2.4}$$

Assuming complete combustion, the global heat release in the flame is given by $\dot{Q} = \dot{m}_f \Delta h$ where $\dot{m}_f$ is the fuel mass flow rate and Δh is the heat released by conversion of a unit mass of fuel. The scaling factor β expressed in W m^{-3} is then equal to :

$$\beta = \frac{\dot{m}_f \Delta h}{\int_0^R \int_0^x I(r,x,t) 2\pi r dr dx} \tag{2.5}$$

This factor can be used to generate distributions of volumetric heat release rate. Results obtained in this way indicate that the flame volume and flame size are larger for flame B. One also finds that the shapes of flames A and B are quite similar, except near the confinement wall for flame B where the flame front is slightly bent in the vicinity of the wall.

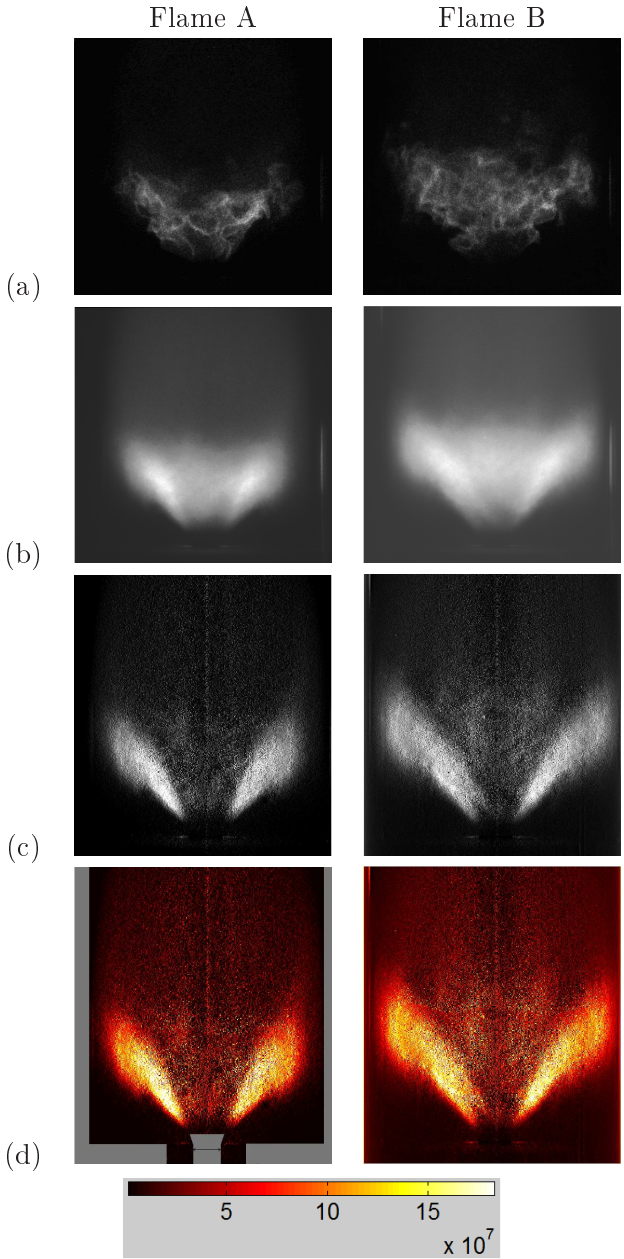

Figure 2.9: From top to bottom : (a) Instantaneous images of the flame, (b) Average of 100 instantaneous images, (c) Abel transform of the average image, (d) Abel transform of the average image providing a two-dimensional slice through the flame scaled in W m^{-3}. Operating point A (left column) $U_b = 2.67$ m s^{-1}. Operating point B (right column) $U_b = 4.13$ m s^{-1}.

Heat release rate : ICCD camera and photomultiplier : It is interesting to examine the heat release rate signal detected by the photomultiplier equipped with an OH* filter collecting light $\lambda = 308$ nm and the light intensity deduced from images acquired with the ICCD camera equipped with a classical glass lens without filter capturing only the visible light of the flame. This is essentially the CH* radiation for a lean methane/air flame. This analysis is carried out for two frequencies. The photomultiplier signal is plotted as solid lines in Fig. 2.10 for the frequencies at $f = 60$ Hz and $f = 90$ Hz for flame A.

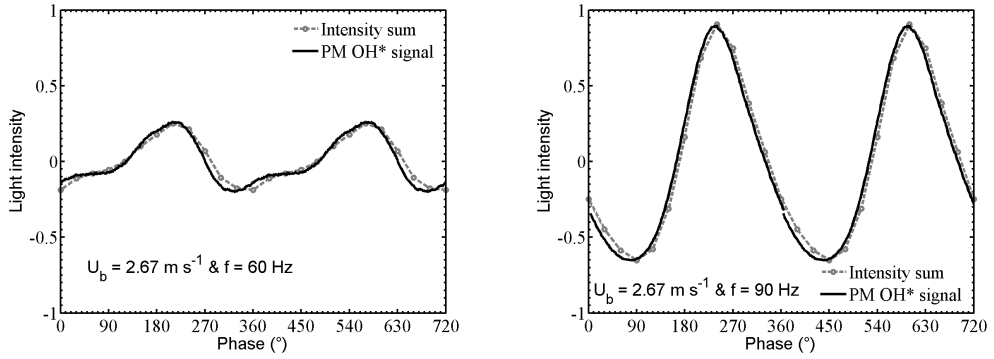

Figure 2.10: Photomultiplier signal and visible light emission signal for flame A, $u'/U_b = 0.5$ and $\phi = 0.7$. (a) $f = 60$ Hz. (b) $f = 90$ Hz. Signals over one period are duplicated for two periods.

The same figure also shows the signal deduced by summing the pixel intensity distribution from the ICCD camera frame. The summation of light intensity over all pixels of the conditioned average images gives a value which is roughly proportional to the heat release rate. These values can be used to synthesize the phase average of unsteady light emission time signal. It is then possible to substract the mean value and divide by this value to obtain a relative light intensity fluctuation. This signal is plotted in Fig. 2.10 as gray dotted lines. These signals and those delivered by the photomultiplier are quite close indicating that the camera images are effectively proportional to the intensity signal recorded by the photomultiplier equipped with the OH* filter. It is then reasonable to consider that these signals are roughly proportionnal to the heat release rate. This confirms that the Abel transformed phase average images can be scaled in terms of volumetric heat release rate as illustrated in Fig. 2.9 (d).

2.5 Conclusion

The main elements used in the experiment are described. The swirlers geometries have been discussed. Systematic experiments are carried out to determine the level of swirl of each swirler configuration. Finally, a method is proposed for the determination of the heat release rate based on the chemiluminescence intensity of images acquired during one cycle of modulation.

Chapter 3

Combustion system acoustics : experiment and theoretical analysis

Abstract : *The acoustic response of multi-elements combustion systems is examined in this chapter. This response is investigated experimentally for each system providing the resonant frequencies. The damping rate is also determined for the various configurations. A theoretical analysis based on coupled cavities is then proposed to predict resonant frequencies and predictions are compared with experimental data. Conditions are examined under which acoustic modes of a chamber filled with hot combustion products can be considered decoupled from the plenum acoustics supplying the fresh reactants through a feeding manifold. It is shown that this is controlled by values of the coupling parameter* $\Xi = (\rho_b c_b)/(\rho_u c_u) S_2/S_3 \simeq (T_u/T_b)^{1/2}(S_2/S_3)$ *where* T_u *and* T_b *are the unburnt and burnt gases temperatures and* S_3/S_2 *is the expansion ratio between the feeding manifold and the chamber cross sections. It is shown that the system acoustics can be analyzed by considering the plenum and the chamber acoustic signatures separately for small values of the parameter* Ξ*. This separation is possible for small values of the chamber outlet impedance when the chamber exhaust is open to atmospheric conditions or for high values of the outlet impedance when the chamber is for example equipped with a sonic nozzle. The case of a plenum featuring a Helmholtz resonance type is investigated in detail when the chamber exhaust impedance is modified. It is shown that self-sustained combustion instabilities develop preferentially around the plenum mode. Exact relations under which the plenum and the chamber modes are decoupled are derived.*

Résumé : *La réponse acoustique du système de cavités couplées est examinée dans ce chapitre. Cette réponse est d'abord étudiée expérimentalement pour chaque système afin de déterminer les fréquences de résonance. Le taux d'amortissement est également obtenu pour les diverses configurations. On traite ensuite des conditions pour lesquelles les modes acoustiques d'une chambre remplie de produits de combustion chauds peuvent être considérées comme découplés de l'acoustique de la partie amont de la chambre de combustion fournissant les réactifs frais. On introduit à cet effet un paramètre de couplage est* $\Xi = (c_b\rho_b)/(\rho_u c_u)S_2/S_3 \simeq (T_u/T_b)^{(1/2)}(S_2/S_3)$ *où* T_u *et* T_b *sont respectivement les températures des gaz frais et des gaz brûlés,* S_3/S_2 *est le rapport des sections entre cavité aval et dispositif d'injection. Il est démontré que l'acoustique du système peut être analysé en découplant les signatures acoustiques de la partie aval de la partie amont pour des petites valeurs du paramètre* Ξ*. Cette séparation est possible pour les petites valeurs de l'impédance de sortie de la chambre, lorsque la sortie de la chambre est ouverte correspondant aux conditions atmosphériques ou pour des fortes valeurs de l'impédance de sortie, lorsque par exemple la chambre est équipée d'une tuyère sonique. Le cas d'une cavité amont caractérisée par une résonance de type Helmholtz est étudié en détail lorsque l'impédance de sortie est modifiée. Il est démontré que les instabilités de combustion auto-entretenues se développent de préférence autour du mode résonant de la cavité amont. Les relations exactes dans lesquelles les modes de la cavité amont et de la cavité aval sont découplés sont obtenues.*

3.1 Introduction

In many practical applications flames are stabilized in a chamber behind a feeding manifold connected to a plenum featuring a large expansion ratio $S_3/S_2 \gg 1$ between the feeding manifold cross section S_2 and the combustion chamber cross section S_3. This is used to create a recirculation of the hot combustion products that help to stabilize the flame. The feeding manifold is eventually also equipped with a swirler to obtain compact lean flames enabling reduced levels of pollutant emissions, see Lefebvre (1998). These configurations are however prone to acoustic induced combustion instabilities which reduce the range of operation of the burner, see Candel (2002); Lieuwen (2005); Culick (2006). In these regimes, self-sustained combustion oscillations develop from initial perturbations and feature a frequency which lies around one of the acoustic modes of the combustor as shown for example by Yu *et al.* (1991); Noiray *et al.* (2008).

In an effort to tackle these problems at the design stage, it is important to have a

good knowledge of the combustor acoustic modes prior to any stability analysis. These modes can often be associated with an eigenfrequency of quarter wave or Helmholtz type mode in simple setups (see among other studies by Schuller *et al.* (2003a); Noiray *et al.* (2006)). In more complex configurations, acoustic modes can be determined experimentally using an internal or an external forcing device. Progress has been made with the use of numerical tools based on acoustic networks of compact elements by Poinsot *et al.* (1987); Dowling and Stow (2003); Sattelmayer and Polifke (2003); Poinsot and Veynante (2001) or more recently of Helmholtz solvers by Nicoud *et al.* (2007) to determine the set of acoustic modes of practical combustors, see for example Selle *et al.* (2006). Recent simulations account for the detailed geometry of the combustor and the temperature field that determines the local sound speed, and may also include acoustic dissipation as ilustrated by Searby *et al.* (2008) or acoustic dampers effects as Oschwald *et al.* (2008). Predictions yield the correct frequencies and shapes of the combustor modes if the acoustic boundary conditions at the domain limits are well known. This raises some difficulties because acoustic impedances at the fuel and air inlets or at the chamber outlet may be influenced by the mean flow, see Janardan *et al.* (1976); Cumpsty and Marble (1977b); Sattelmayer (2003) or by the perturbation amplitude level, see Tran *et al.* (2009). Another issue is that it is often difficult to estimate the impact of modifications of the combustor initial geometry on the modal distribution. Of course, parametric analysis can be undertaken to determine the sensitivity to slight changes of the acoustic boundary conditions or to some geometrical elements, but from an engineering point of view it is also desirable to determine simple rules which would help simplify the problem.

This chapter aims at providing a criterion which can be used to see if elements located upstream of the reaction region can be considered acoustically decoupled from downstream elements of the combustor. Coupled low frequency instabilities involving the propellant feed system and the combustion chamber have been mainly resolved by decoupling these components using large head losses in the injection units, as explained for example by Culick and Yang (1995). This can be obtained in laboratory scale combustors by using sonic nozzles as shown by Bloxsidge *et al.* (1988); Schadow *et al.* (1990); Yu *et al.* (1991); Kendrick *et al.* (1996); Eckstein *et al.* (2006) , but this solution is not recommended for gas turbine combustors where head losses should be minimized between the feeding manifold and the combustion chamber, see Lefebvre (1998). A new criterion is proposed which relies on the geometrical arrangement of the main elements inside the combustor. It may be used (1) On existing configurations to infer if elements of the combustor can be considered acoustically decoupled or (2) At the design stage of new chambers to weaken acoustic coupling between parts of the combustors and to freeze some degrees of freedom for potential ranges of unstable modes.

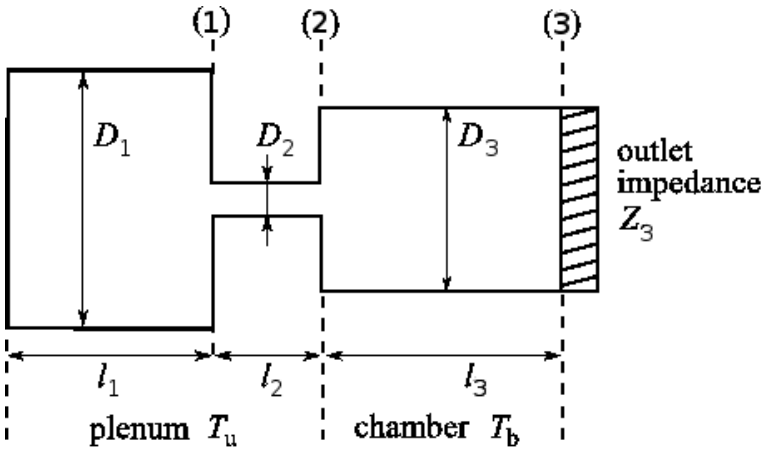

Figure 3.1: Schematic representation of a combustor modeled by three coupled cavities.

Using classical elements of acoustics for plane wave propagation in low Mach flows inside cavities, it is shown that the analysis of the acoustic signatures of many burners can often be simplified into the analysis of the plenum and the combustion chamber acoustics separately. Conditions are examined where this separation is possible for combustors featuring an exhaust open to atmospheric conditions in section 3.2. Effects of the chamber outlet impedance are then presented in section 3.3. The case of a combustor comprising a plenum featuring a Helmholtz resonance (bulk flow oscillation) is investigated in detail throughout the chapter. These theoretical elements are completed in section 3.4 by experimental validations. Section 3.5 is devoted to estimate damping of the system. Section 3.6 compares predictions of pressure distribution.

3.2 Acoustic analysis of three coupled cavities

The objective is to calculate the eigenfrequencies of three coupled cavities, where the two first ones (1) and (2) are filled with fresh reactants at a temperature T_u characterized by the same density ρ_u and sound speed c_u and the last one (3) is filled with hot combustion products at a temperature T_b with a lower density ρ_b and a higher speed of sound c_b (Fig. 3.1). The combustion region, if any, is assumed to be compact in the following developments. Assuming one dimensional harmonic plane waves of the form $u(x,t) = \tilde{u}(x)\exp(-i\omega t)$ where the quantity u denotes the acoustic pressure p or velocity v, the following expressions can be

written in the different cavities (1), (2) and (3) :

$$\begin{aligned}
\tilde{p}_1(x) &= A\exp(ik_u x) + B\exp(-ik_u x) && (3.1)\\
\rho_u c_u \tilde{v}_1(x) &= A\exp(ik_u x) - B\exp(-ik_u x) && (3.2)\\
\tilde{p}_2(x) &= C\exp(ik_u(x-l_1)) + D\exp(-ik_u(x-l_1)) && (3.3)\\
\rho_u c_u \tilde{v}_2(x) &= C\exp(ik_u(x-l_1)) - D\exp(-ik_u(x-l_1)) && (3.4)\\
\tilde{p}_3(x) &= E\exp(ik_b(x-l_1-l_2)) + F\exp(-ik_b(x-l_1-l_2)) && (3.5)\\
\rho_b c_b \tilde{v}_3(x) &= E\exp(ik_b(x-l_1-l_2)) - F\exp(-ik_b(x-l_1-l_2)) && (3.6)
\end{aligned}$$

where the coefficient A, B, C, D, E and F are complex numbers. This set of equations must comply with the following set of continuity and boundary conditions, (similar calculations can be found in mufflers analysis as exemplified by Munjal (1987)) :

$$\begin{aligned}
\tilde{v}_1(0) &= 0 && (3.7)\\
\tilde{p}_1(l_1) &= \tilde{p}_2(l_1) && (3.8)\\
S_1\tilde{v}_1(l_1) &= S_2\tilde{v}_2(l_1) && (3.9)\\
\tilde{p}_2(l_1+l_2) &= \tilde{p}_3(l_1+l_2) && (3.10)\\
S_2\tilde{v}_2(l_1+l_2) &= S_3\tilde{v}_3(l_1+l_2) && (3.11)\\
\tilde{p}_3(l_1+l_2+l_3) &= 0 && (3.12)
\end{aligned}$$

Velocity vanishes at the inlet of the system. Pressure and volume flow rate are continuous at the duct section changes. Pressure vanishes at the system exhaust.

Using Eqs. (3.1) to (3.6) within Eqs. (3.7) to (3.12) yields a system which can be written in a matrix form, $M\,[A\,B\,C\,D\,E\,F\,]^T = 0$, where M is given by :

$$\begin{bmatrix}
1 & -1 & 0 & 0 & 0 & 0\\
e^{(ik_u l_1)} & e^{(-ik_u l_1)} & -1 & -1 & 0 & 0\\
\frac{S_1}{S_2}e^{(ik_u l_1)} & -\frac{S_1}{S_2}e^{(-ik_u l_1)} & -1 & 1 & 0 & 0\\
0 & 0 & e^{(ik_u l_2)} & e^{(-ik_u l_1)} & -1 & -1\\
0 & 0 & \Xi e^{(ik_u l_2)} & -\Xi e^{(-ik_u l_2)} & -1 & 1\\
0 & 0 & 0 & 0 & e^{(ik_b l_3)} & e^{(-ik_b l_3)}
\end{bmatrix} \qquad (3.13)$$

where $\Xi = (\rho_b c_b)/(\rho_u c_u) S_2/S_3 \simeq (T_u/T_b)^{1/2}(S_2/S_3)$. Modes of these three coupled cavities correspond to non trivial solutions of $\det M = 0$.

One may symplify the determinant by decomposition along the last line and then the last column. One is left with :

$$\det M = -2\cos(k_b l_3)\det M_{uu} - 2i\sin(k_b l_3)\det M_{ub} \qquad (3.14)$$

where $\det M_{uu}$ corresponds to the determinant of the two first coupled cavities filled with gases at the same temperature T_u and $\det M_{ub}$ corresponds to a coupling term between cavities separated by the flame. Before specifying the exact

form of theses terms, it is worth noting that this decomposition has yielded an expression where acoustic coupling between cavities filled with gases at different temperatures is isolated in a single term.

Consider first the determinant $\det M_{uu}$ where :

$$M_{uu} = \begin{bmatrix} 1 & -1 & 0 & 0 \\ e^{(ik_u l_1)} & e^{(-ik_u l_1)} & -1 & -1 \\ \frac{S_0}{S_1} e^{(ik_u l_1)} & -\frac{S_0}{S_1} e^{(-ik_u l_1)} & -1 & 1 \\ 0 & 0 & e^{(ik_u l_2)} & e^{(-ik_u l_1)} \end{bmatrix} \tag{3.15}$$

then

$$\det M_{uu} = -4 \left[\cos(k_u l_1) \cos(k_u l_2) - \frac{S_0}{S_1} \sin(k_u l_1) \sin(k_u l_2) \right] \tag{3.16}$$

Modes calculated from $\det M_{uu} = 0$ are associated with the two cavities (1) and (2) traversed by a fresh stream of reactants. The first mode of this system is of Helmholtz type, with a wavelength λ_H large compared to the cavities lengths l_1 and l_2 : $\lambda_H \gg l_1, l_2$. In this case, the following appoximations can be made in Eq. (3.16) :

$$\cos(k_u l_1) \simeq \cos(k_u l_2) = 1 \quad \text{and} \quad \sin(k_u l_1) \simeq k_u l_1 \quad \sin(k_u l_2) \simeq k_u l_2$$

The dispersion relation $\det M_{uu} = 0$ then reduces to :

$$1 - \frac{S_1}{S_2} k_u^2 l_1 l_2 = 0 \tag{3.17}$$

One retrieves the classical Helmholtz angular frequency :

$$\omega_H^2 = \frac{c_u^2 S_2}{S_1 l_1 l_2} = \frac{c_u^2 S_2}{V_1 l_2} \tag{3.18}$$

where $V_1 = S_1 l_1$ is the volume of the first cavity, see Schuller (2003); Poinsot and Veynante (2001).

One should now consider the second determinant $\det M_{ub}$ appearing in Eq. (3.14). This coupling term between the cavities filled with unburnt gases and the flame confinement tube filled with burnt products takes the form :

$$M_{ub} = \begin{bmatrix} 1 & -1 & 0 & 0 \\ e^{(ik_u l_1)} & e^{(-ik_u l_1)} & -1 & -1 \\ \frac{S_1}{S_2} e^{(ik_u l_1)} & -\frac{S_1}{S_2} e^{(-ik_u l_1)} & -1 & 1 \\ 0 & 0 & \Xi e^{(ik_u l_2)} & -\Xi e^{(-ik_u l_1)} \end{bmatrix} \tag{3.19}$$

and

$$\det M_{ub} = -4i\Xi\left[\cos(k_u l_1)\sin(k_u l_2) + \frac{S_1}{S_2}\sin(k_u l_1)\cos(k_u l_2)\right] \tag{3.20}$$

where $\Xi = (S_2/S_3)(\rho_b c_b)/(\rho_u c_u)$ is a dimensionless parameter. It is interesting to note that acoustics coupling between the cavities separated by the flame is controlled by the values of this parameter Ξ.

By combining Eqs. (3.16) and (3.20), the determinant of the three coupled cavities takes an elegant form :

$$\begin{aligned}\det M &= 8\cos(k_b l_3)\left[\cos(k_u l_1)\cos(k_u l_2) - \frac{S_1}{S_2}\sin(k_u l_1)\sin(k_u l_2)\right] \\ &- 8\sin(k_b l_3)\Xi\left[\cos(k_u l_1)\sin(k_u l_2) + \frac{S_1}{S_2}\sin(k_u l_1)\cos(k_u l_2)\right]\end{aligned} \tag{3.21}$$

Note that if Ξ takes vanishingly small values ($\Xi \ll 1$), the contribution from $\det M_{ub}$ in the preceding equation can be neglected and the dispersion relation $\det M = 0$ reduces to :

$$0 = \cos(k_b l_3)\left[\cos(k_u l_1)\cos(k_u l_2) - \frac{S_1}{S_2}\sin(k_u l_1)\sin(k_u l_2)\right] \tag{3.22}$$

This is an important case for combustion systems because (1) The expansion ratio between the chamber and the feeding manifold cross sections is often large ($S_2/S_3 \ll 1$) and (2) the specific impedance between the hot and fresh gases scales approximatively with the square root of the unburnt to burnt temperature ratio $\rho_b c_b/(\rho_u c_u) \simeq (T_u/T_b)^{1/2}$ which also takes small values ($T_u/T_b = 0.15 - 0.40$ in typical applications). This last expression shows that for many combustors the plenum can often be considered acoustically decoupled from the chamber modes. Modes of the coupled cavities {(1), (2), (3)} are then associated either with the plenum injector system or with the chamber separately :

$$\cos(k_b l_3) = 0 \tag{3.23}$$

$$\cos(k_u l_1)\cos(k_u l_2) - \frac{S_1}{S_2}\sin(k_u l_1)\sin(k_u l_2) = 0 \tag{3.24}$$

Solutions of Eq. (3.23) correspond to chamber modes and are of the quarter wave type $f_c^n = (2n+1)c_b/(4l_3)$, where n is an integer. Solutions of Eq. (3.24) correspond to modes associated with the cavities {(1), (2)} filled with fresh reactants. There is no coupling between plenum and chamber modes when the parameter Ξ takes vanishingly small values. This result may be useful to design combustion chambers decoupled from the plenum acoustics which supply the reactants.

It is interesting to examine the case of a plenum with a large volume (1) followed by a narrow channel (2) where a swirler may eventually be installed. This is a

typical case for many practical burners. The dominant resonant mode is then often of Helmholtz type $f_H = \omega_H/(2\pi)$, where $\omega_H^2 = c_u^2 S_1/(V_1 l_2)$, V_1 being the volume of the cavity (1). Consider the general case where the parameter Ξ is not necessary small in Eq. (3.21), the coupled cavities acoustic signature still takes a relatively simple form. Assuming large wavelengths compared to the plenum and the feeding manifold dimensions $\lambda \gg l_1$, l_2 in Eq. (3.21), one obtains the following dispersion relation :

$$\cos(k_b l_3)\left(1 - k_u^2 \frac{S_1 l_1 l_2}{S_2}\right) - \Xi \sin(k_b l_3)\left(1 + \frac{S_1 l_1}{S_2 l_2}\right) k_u l_2 = 0 \tag{3.25}$$

Noting that $k_b = \omega/c_b$, $k_u = \omega/c_u$ and using the fact that in a Helmholtz resonator $V_1 = S_1 l_1 \gg V_2 = S_2 l_2$, the preceding relation simplifies to yield :

$$1 - \left(\frac{\omega}{\omega_H}\right)^2 - \Xi \left(\frac{S_1 l_1}{S_2 l_2}\right)^{1/2} \tan\left(\frac{\omega l_3}{c_b}\right) \frac{\omega}{\omega_H} = 0 \tag{3.26}$$

This expression shows that modes of this system are controlled by three competing parameters :

1. The first is the coupling parameter between the cavities separated by the flame $\Xi = (S_2/S_3)(\rho_u c_u)/(\rho_b c_b) \simeq (S_2/S_3)(T_u/T_b)^{1/2}$,
2. The second is the square root of the plenum cavity volumes $(V_1/V_2)^{1/2}$,
3. The last corresponds to the Helmholtz number $\mathrm{He}_b = \omega l_3/c_b$ of the confinement tube, which can be estimated by replacing the angular frequency ω by the Helmholtz frequency ω_H : $\mathrm{He}_b \simeq \omega_H l_3/c_b$.

The volume ratio V_1/V_2 generally takes high values ($V_1/V_2 \gg 1$), but this is compensated by the two other control parameters which take small values. As already mentioned the parameter Ξ is generally small ($\Xi \ll 1$). The Helmholtz number $\mathrm{He}_b \ll$ is also generally small, because it is desirable to design compact chambers and the sound celerity of the combustion products c_b takes high values. Typical sound celerities in the burnt gases of practical burners ranges from $c_b \simeq 600$ to 900 m s^{-1}. The net effect is that the second term in Eq. (3.26) is in many cases small compared to the other ones, and this contribution can often be discarded when the product $\Xi(V_1/V_2)^{1/2}\mathrm{He}_b \ll 1$ takes small values. This leads to an important result, that the system acoustics is solely controlled by the plenum Helmholtz mode (for chambers with a large expansion ratio). Modifications of the chamber length do not change the system acoustics when the plenum features a Helmholtz resonance. In this acoustical environment, self-sustained longitudinal combustion instabilities may essentially develop around the Helmholtz resonance. In the low frequency range, this indicates the predominance of the acoustics environment upstream from the combustion region compared to modifications of the downstream side of the flame region.

The analysis developed above applies to combustors open to atmospheric conditions and may explain some results observed in laboratory scales experiments, but the validity of this finding is yet limited because practical configurations often feature different downstream impedance conditions. It is then worth investigating effects of a modification of the downstream boundary condition on the modal distribution of three coupled cavities.

3.3 Effects of modification of the downstream boundary

The case of three coupled cavities with an arbitrary boundary condition at the confinement tube outlet can be treated easily using the type of analysis developed in the previous section. Equation (3.12) is now replaced by an impedance condition at the confinement tube outlet. This impedance is represented by Z_3 and the boundary conditions becomes :

$$\tilde{p}_3(l_1+l_2+l_3) = Z_3\tilde{v}_3(l_1+l_2+l_3) \tag{3.27}$$

This leads to a modification of the last line in the matrix M in Eq. (3.13) which should be replaced by the following expression :

$$E(1-\zeta_3)\exp(ik_bl_3) + F(1+\zeta_3)\exp(-ik_bl_3) = 0 \tag{3.28}$$

where $\zeta_3 = Z_3/(\rho_b c_b)$ is the specific impedance at the system outlet. Using the same type of decomposition, one obtains a new expression for the determinant $\det M$ which is slightly modified compared to the case of an open atmospheric condition Eq. (3.14) examined in section 3.2 :

$$\begin{aligned} \det M &= \det M_{uu}\left[(\zeta_3-1)\exp(ik_bl_3) - (\zeta_3+1)\exp(-ik_bl_3)\right] \\ &- \det M_{ub}\left[(\zeta_3-1)\exp(ik_bl_3) + (\zeta_3+1)\exp(-ik_bl_3)\right] \end{aligned} \tag{3.29}$$

One retrieves Eq. (3.14) for an outlet section open to atmospheric conditions when the specific impedance is fixed to $\zeta_3 = 0$. Note that this new expression Eq. (3.29) yields a dispersion relation $\det M = 0$ valid for an arbitrary outlet impedance ζ_3 which has the same general structure as Eq. (3.14) when ζ_2 is set to zero. Coupling between the plenum and the chamber cavity modes is still encompassed in the term $\det M_{ub}$ which is proportional to the parameter Ξ. For vanishingly small values $\Xi \ll 1$, one is thus left with :

$$0 = \det M_{uu}\left[(\zeta_3-1)\exp(ik_bl_3) - (\zeta_3+1)\exp(-ik_bl_3)\right] \tag{3.30}$$

This new dispersion relation shows that the three cavity modes depend on the plenum and the chamber modes independently. Modifications of the system outlet impedance has no effect on the plenum acoustics when Ξ takes vanishingly small

values. This results extends our previous finding to a more general configuration. Practical burners comprising a plenum connected to a flame confinement tube feature no coupled modes between these elements when $\Xi \simeq S_2/S_3(T_u/T_b)^{1/2}$ take small values independently of the outlet impedance. The solution which is often adopted in laboratory facilities is to use sonic nozzles to avoid acoustic interactions between the different cavities from the combustor, as for example to decouple the feeding lines from the chamber. This solution is generally not desirable in practical burners because this also leads to high head losses and increases energy consumption. The solution proposed hereby to decouple cavities is simpler and does not increase head losses.

The analysis conducted above leads a priori to the same type of conclusion as that for a coupled cavity problem with an exhaust open to atmospheric conditions. This is at first glance a surprising result, but it is worth recalling that values of the coupling parameter Ξ were supposed to be vanishingly small. This idealized condition is now examined in more detail by considering the case of a burner featuring a Helmholtz mode.

The particular case of a system equipped with a plenum, a flame confinement tube and a nozzle is now examined. The same type of analysis conducted in section 3.2 is undertaken when the confinement tube is ended by a compact nozzle. This is first carried out without any assumption on values of the parameter Ξ. In the limit of large wavelengths $\lambda \gg l_1, l_2$ compared to the plenum and the feeding manifold dimensions and large volume differences $V_1 \gg V_2$, the dispersion relation Eq. (3.29) takes the form :

$$\begin{aligned} 0 &= \left(1-\frac{\omega^2}{\omega_H^2}\right)\left[\cos(k_b l_3) - i\zeta_3 \sin(k_b l_3)\right] \\ &- \Xi\left(\frac{S_1 l_1}{S_2 l_2}\right)^{1/2} \frac{\omega}{\omega_H}\left[\sin(k_b l_3) + i\zeta_3 \cos(k_b l_3)\right] \end{aligned} \tag{3.31}$$

This expression may also be rewritten by separating terms which depend on ζ_3 :

$$\begin{aligned} 0 &= \left(1-\frac{\omega^2}{\omega_H^2}\right)\cos(k_b l_3) - \Xi\left(\frac{S_1 l_1}{S_2 l_2}\right)^{1/2} \sin(\frac{\omega l_3}{c_b})\frac{\omega}{\omega_H} \\ &- i\zeta_3\left[\left(1-\frac{\omega^2}{\omega_H^2}\right)\sin(k_b l_3) + \Xi\left(\frac{S_1 l_1}{S_2 l_2}\right)^{1/2} \cos(\frac{\omega l_3}{c_b})\frac{\omega}{\omega_H}\right] \end{aligned} \tag{3.32}$$

It is interesting to investigate two limiting cases. First note that when $\zeta_3 = 0$ for a downstream tube open to atmospheric conditions, one effectively retrieves Eq. (3.26). Modes are then associated to the plenum and the manifold system or the confinement tube separately when $\Xi \ll 1$, and in many burners self-sustained longitudinal instabilities may only develop around the plenum Helmholtz frequency as shown in the previous section. Taking the other limiting case when

$\zeta_3 \to \infty$, this would correspond to an acoustically closed confinement flame tube. The dispersion relation now reduces to :

$$0 = \left(1 - \frac{\omega^2}{\omega_H^2}\right) \sin\left(\frac{\omega l_3}{c_b}\right) + \Xi \left(\frac{S_1 l_1}{S_2 l_2}\right)^{1/2} \cos\left(\frac{\omega l_3}{c_b}\right) \frac{\omega}{\omega_H} \tag{3.33}$$

For vanishingly small values of the parameter $\Xi \ll 1$, modes of the three coupled cavities correspond to a combination of the plenum and the flame confinement tube modes calculated separately. The flame tube modes are in this case of half wave type $f_c^n = nc_b/(2l_3)$ because the cavity is acoustically closed at the downstream side. Modes separation is however more difficult to obtain when $\zeta_3 \to \infty$ than when $\zeta_3 = 0$ because the structure of the dispersion relation Eq. (3.33) is slightly different than that of Eq. (3.26). For compact chambers filled with hot products, one can still assume $\mathrm{He}_b = \omega l_3/c_b \ll 1$ and first order approximations of $\sin(\mathrm{He}_b) \simeq \mathrm{He}_b$ and $\cos(\mathrm{He}_b) \simeq 1$ can be used in Eq. (3.33) :

$$0 = \left(1 - \frac{\omega^2}{\omega_H^2}\right) \mathrm{He}_b + \Xi \left(\frac{S_1 l_1}{S_2 l_2}\right)^{1/2} \frac{\omega}{\omega_H} \tag{3.34}$$

The criterion that minimizes interactions between the plenum and chamber acoustic cavities reduces to $\Xi(V_1/V_2)^{1/2} \ll 1$ when the downstream impedance goes to infinity $\zeta_3 \to \infty$. This is a more stringent condition than $\Xi(V_1/V_2)^{1/2}\mathrm{He}_b \ll 1$ obtained for vanishing values of the downstream impedance $\zeta_3 = 0$ (see section 3.2). In summary, regions separated by the flame can be considered decoupled independently of values of the combustion chamber outlet impedance when the coupling parameter Ξ takes vanishingly small values. In practical burners, this coupling parameter takes a small but however a finite value, and one should also pay attention to values of the outlet impedance. For the case of a plenum featuring an Helmholtz mode, it is possible to derive a quantitative criterion. Chamber modes can be considered decoupled when :

- $\Xi(V_1/V_2)^{1/2}\mathrm{He}_b \ll 1$ for $\zeta_3 = 0$, when the exhaust is open to the atmosphere,
- $\Xi(V_1/V_2)^{1/2} \ll 1$ when $\zeta_3 \longrightarrow \infty$, when the exhaust is acoustically closed.

Conditions under which the chamber exhaust impedance approaches that of rigid wall are now examined. Practical chambers feature at their exhaust a distributor before the first stage of the high pressure turbine, see Lefebvre (1998). This distributor is often modeled as a nozzle operating near sonic conditions. Acoustic disturbances through nozzles were analyzed by Cumpsty and Marble (1977b) as a function of the approach Mach number. Neglecting entropy fluctuations convected by the mean flow and assuming a compact nozzle traversed by hot combustion products with a mean approach Mach flow number $\mathrm{M}_b \leq 1$, the specific nozzle impedance then writes :

$$\zeta_3 = \frac{2}{\gamma - 1} \frac{1}{\mathrm{M}_b} \tag{3.35}$$

where γ_b is the specific heat capacity ratio of the burnt gases flowing through the nozzle. This expression shows that $\zeta_3 \to \infty$ is a limiting case reached for small approach Mach numbers $M_b \ll 1$ near the chamber exhaust. The nozzle then acts very much like a solid wall for acoustic waves as indicated by Cumpsty and Marble (1977b). In practical configurations, the exhaust flow is accelerated by the distributor and the approach Mach number has a finite value. Equation (3.33) is a good approximation of the dispersion relation for a combustor equipped with a nozzle when the magnitude of the downstream impedance is larger than 10 : $\zeta_3 \geq 10$. Consider hot combustion products where $\gamma_b \simeq 1.3$, this condition is fulfilled for approach Mach numbers smaller than about $M_b \leq 0.65$.

A modification of the downstream impedance by adding a compact nozzle to the chamber outlet leads to a redistribution of the modes within the combustor. The parameter $\Xi \simeq S_2/S_3(T_u/T_b)^{1/2}$ is still an indicator of the coupling strength between cavities separated by the flame. When this parameter takes vanishingly small values modes of the plenum and the flame tube equipped with the nozzle are decoupled and can be analyzed separately. When the approach Mach number remains lower than 0.65, modes of the flame confinement tube are of half wave type. These modes are decoupled from the plenum Helmholtz mode when $\Xi(V_1/V_2)^{1/2} \ll 1$.

3.4 Experimental validation in a swirled turbulent combustor

Predictions from section 3.2 are compared to experimental data obtained with a swirl burner equipped with a flame confinement tube open to atmospheric conditions (see experimental setup in chapter 2). It was yet not possible to conduct the analysis for a burner equipped with a nozzle at the chamber exhaust because the setup was not designed to sustain operating pressures higher than atmospheric.

The burner comprises a cylindrical body of diameter $D_1 = 65$ mm fed by two inlet ports with a methane air mixture kept at a constant mixture equivalence ratio $\Phi = 0.7$. Three bodies of different lengths $l_1 = 96$, 160 and 224 mm can be used to modify the plenum geometry. This cylindrical piece is followed by a smooth convergent of contraction ratio $\sigma = 3.9$ and length $l = 60$ mm. A small adaptation piece is then used to reduce the outer diameter to $D_2 = 22$ mm. The top of the burner is a straight tube of diameter D_2 with a cylindrical element where a hot wire can be installed to measure the local flow velocity and then a swirler to put the reactive flow mixture in rotation. The cylinder tube of length 117 mm ends in the combustion chamber where the mixture is burnt. A central rod is also used to help to stabilize the lean flame and to avoid flashback within

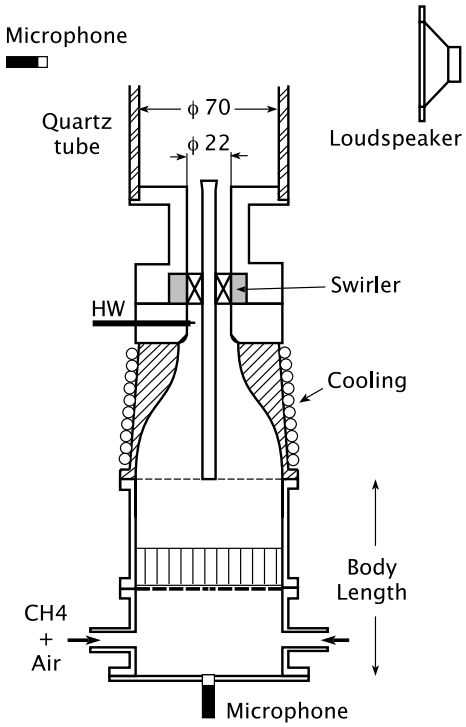

Figure 3.2: Experimental setup comprising a swirl burner with a plenum and a flame confinement tube.

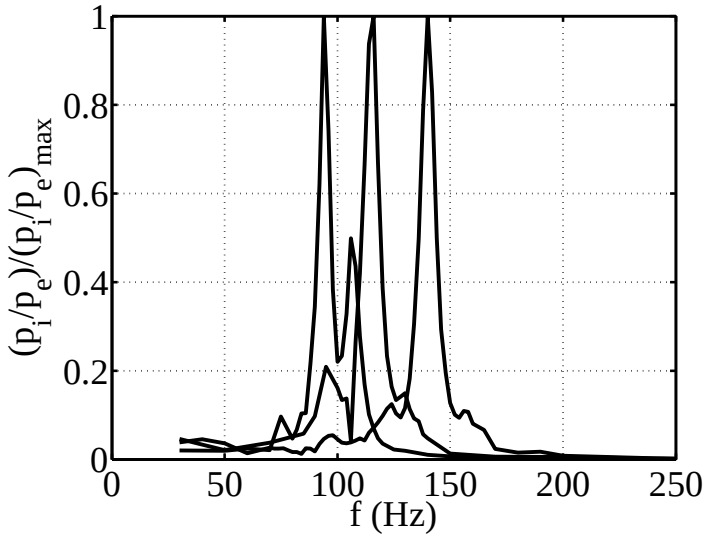

Figure 3.3: Low frequency acoustic response of the feeding manifold without flame confinement tube ($l_3 = 0$). Curve on the left : large body ($l_1 = 224$ mm). Curve at the center : medium body ($l_1 = 160$) mm. Curve on the right : short body ($l_1 = 96$ mm).

Plenum	Short body	Medium body	Large body
l_1 (mm)	96	160	224
f_1 (Hz)	140	116	94/106
f_H (Hz)	142	118	104
Chamber	Short tube	Medium tube	Long tube
l_3 (mm)	100	200	400
f_c (Hz)	635	365	197

Table 3.1: Top lines : Measured (f_1) and estimated (f_H) plenum bulk oscillation frequencies $f_H = c_u/(2\pi)(S_2/V_e l_e)^{1/2}$ as a function of the cylindrical body length l_1 = 96, 160 and 224 mm. Feeding manifold outlet section : S_2 = 352 mm^2. Effective length of the burner feeding manifold : $l_e = \int_1^2 S_2/S(x)dx + \delta_2$ = 106 mm, where $\delta_2 = D_2/2$. Total manifold volume : $V_e = S_0 l_1 + V_1$, where V_1 = 154 mm^3 is the interior volume of the feeding manifold elements comprised between section 0 and 1. Bottom lines : Estimated fundamental oscillation frequency of the chamber confinement tube : $f_c = c_u/[4(l_3 + \delta_2)]$, where $\delta_2 = D_3/2$. The sound speed is taken equal to $c_u^2 = (\gamma_u r T_u)$ = 343 m s^{-1}, with γ_u =1.4, r =287 kg^{-1} K^{-1} and T_u =293 K.

the burner. It has a diameter $d = 3$ mm and extends from the top of the cylindrical body (section 1) to the chamber inlet (section 2). The low frequency acoustic signature of this set of elements constituting the feeding manifold is plotted in figure 3.3. It can be modeled by a Helmholtz resonator as proposed by Durox *et al.* (2002); Schuller *et al.* (2003a) of effective volume V_e corresponding to the total volume of the burner and effective length $l_e = \int_1^2 S_2/S(x)dx + \delta_2 = 106$ mm, where $S(x)$ is the local cross section area at the current axial coordinate comprised between sections 1 and 2, $S_2 = 352$ mm^2 is the final cross section area and $\delta_2 = D_2/2$ is an end correction. The bulk resonant mode of this feeding system is then given by $f_H = c_u/(2\pi)(S_2/V_e l_e)^{1/2}$, see Rienstra and Hirschberg (2005), and can be estimated as a function of the cylindrical body length l_1 in Tab. 3.1. Estimated and measured peak frequencies closely match except with the large body, where experimental data feature a double peak structure at 94 and 106 Hz.

The combustion chamber is a cylindrical tube made of quartz of diameter $D_3 =$ 70 mm where a turbulent swirled flame is stabilized. The swirl number was measured using laser Doppler velocimetry at a distance $z = 2.9$ mm from the chamber floor and a value of $S = 0.55$ was found for the operating conditions envisaged in this study. More information about the burner and detailed characterizations of the flow and flame dynamics can be found in the section devoted to the experimental setup page 36, chapter 1. Three different quartz tubes of lengths $l_3 = 100$, 200 and 400 mm can be used to confine the flame. The estimated fundamental resonant frequencies of quarter-wave type $f_c = c_u/[4(l_3 + \delta_2)]$, where $\delta_2 = D_3/2$ is an end correction, are also indicated in the bottom rows of Tab. 3.1.

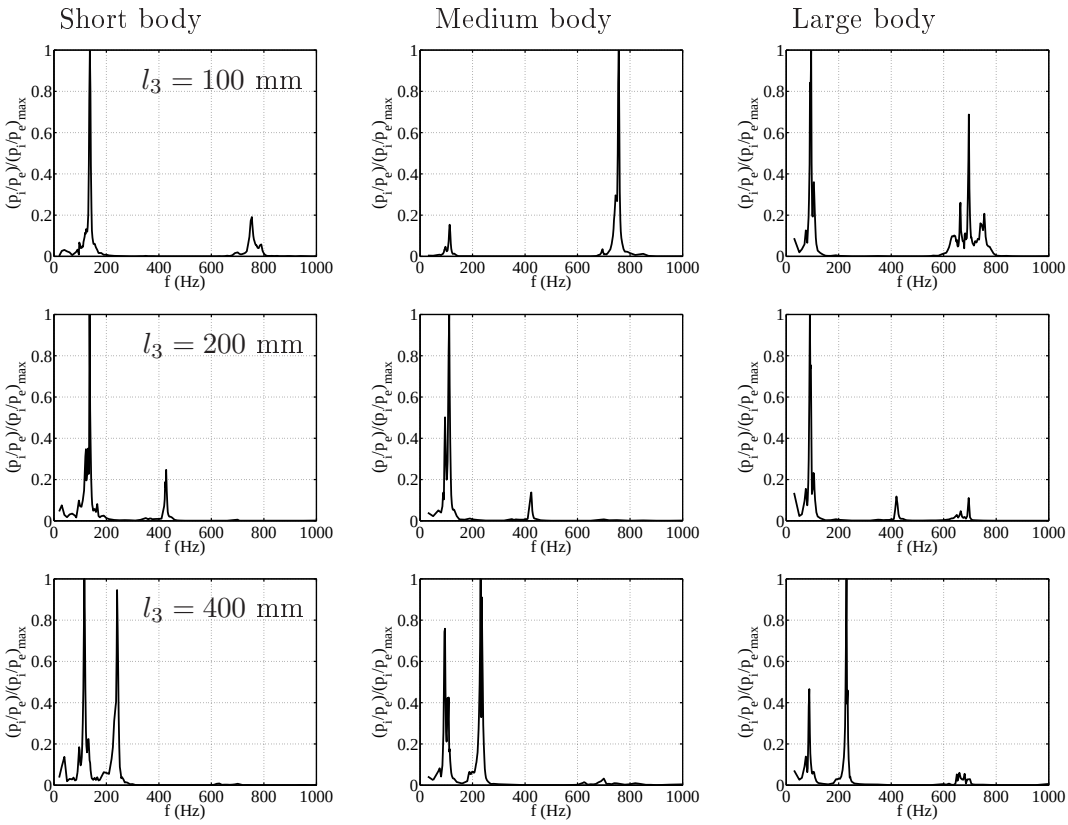

Figure 3.4: Frequency response of the burners submitted to external acoustic modulations. From left to right, the plenum of the burner is equipped with the short ($l_1 = 96$ mm), medium ($l_1 = 160$ mm) and large ($l_1 = 224$ mm) cylindrical bodies. From top to the bottom, the flame confinement tube length is increased from $l_3 = 100$, 200 to 400 mm.

Experiments were first carried out without flames. The acoustic response of this setup was characterized using a loudspeaker, a reference microphone measuring the external pressure p_e in front of the loudspeaker and a second microphone fixed at the bottom of the burner measuring the internal pressure fluctuation p_i resulting from the external modulation. The response $(\tilde{p}_i/\tilde{p}_e)^2$ shows resonant peaks which are functions of the plenum cavity and the confinement tube lengths (Fig. 3.4). Frequencies corresponding to the first two resonant peaks in these figures are gathered at the top of Tab. 3.2 and are indicated by f_1 and f_2 respectively. The frequency f_1 decreases when the manifold body length is augmented from $l_1 = 96$, 160 to 224 mm. For a fixed plenum length, this frequency also slightly decreases when the confinement tube length is increased. This dependence is nonetheless weak compared to modifications of the plenum body length.

Experiments $T_u = T_b = 293$ K	Short body $l_1 = 96$ mm		Medium body $l_1 = 160$ mm		Large body $l_1 = 224$ mm	
Peak frequency (Hz)	f_1		f_1		f_1	
$l_3 = 0$ mm	142		118		104	
Peak frequencies (Hz)	f_1	f_2	f_1	f_2	f_1	f_2
$l_3 = 100$ mm	137	754	113	757	95	696/757
$l_3 = 200$ mm	133	428	111	425	90	420
$l_3 = 400$ mm	117	241	109	231	88	230
Unstable mode	f_1		f_1		f_1	
Peak frequencies (Hz)	135-140		115-128		97-125	

Table 3.2: Top lines : Resonant frequencies measured under cold operating conditions. The two first peak frequencies f_1 and f_2 are indicated in Hz as a function of the plenum body and the flame confinement tube lengths. Bottom line : Peak frequencies detected at limit cycles of unstable combustion modes.

The second peak frequency f_2 decreases significantly when the flame confinement tube length is increased from $l_3 = 100$, 200 to 400 mm, but is almost insensitive to modifications of the plenum body length l_1. It is also found that the peak frequency f_2 evolution follows the same trend as the quarter-wave mode f_c indicated in Tab. 3.1 for confinement tube lengths $l_3 = 100$, 200 and 400 mm. The ratio $f_2/f_c = 0.84 \pm 0.01$ remains essentially constant for the three frequencies explored.

When the mixture is ignited, this setup features unstable regimes characterized by synchronized heat release rate and pressure oscillations within the plenum and the chamber measured by the internal and external microphones in absence of any external perturbations. These unstable modes were characterized for an equivalence ratio $\Phi = 0.7$. Modification of the limit cycle frequency is investigated when the plenum and the flame tube lengths are modified. Results for the instability frequency are gathered at the bottom of Tab. 3.2. When the flame confinement tube length is set to $l_3 = 100$ mm, combustion is found to be always stable and the spectrum measured by the internal of the external microphones remains essentially incoherent. Increasing the flame confinement tube length to $l_3 = 200$ or 400 mm always corresponds to an unstable operation mode for the three cavity bodies tested. The oscillation peak frequency may change from one test to the other depending for example on the thermal history of the burner, but values always lie in the frequency range indicated in the table. These self-sustained peak frequencies are function of the plenum body length l_1, but remain independent of the flame confinement tube length l_3. The oscillation frequency decreases when the plenum body length is increased from $l_1 = 96$, 160 to 224 mm. It is also found that the instability frequency always lies in a frequency bandwidth close to the resonant peak frequency f_1 determined without combustion by external modulation. It is also found that the Helmholtz frequency estimated in

Model $T_b = 300$ K, $\Xi = 0.09$	Short body $l_1 = 96$ mm		Medium body $l_1 = 160$ mm		Large body $l_1 = 224$ mm	
Helmholtz mode (Hz) $l_3 = 0$ mm	f_1 142		f_1 118		f_1 104	
Peak frequencies (Hz)	f_1	f_2	f_1	f_2	f_1	f_2
$l_3 = 100$ mm	140	645	115	648	101	651
$l_3 = 200$ mm	138	375	113	378	99	380
$l_3 = 400$ mm	131	212	107	214	94	215
$T_b = 1600$ K, $\Xi = 0.04$ Peak frequency	f_1 141±1		f_1 117±1		f_1 103±1	

Table 3.3: Top lines : Predicted resonant frequencies under cold operating conditions. The two first peak frequencies f_1 and f_2 are indicated in Hz as a function of the plenum body and the flame confinement tube lengths. Bottom line : Predicted resonant frequencies under hot operating conditions.

Tab. 3.1 closely matches the peak frequency f_1 in the absence of a confinement tube ($l_3 = 0$ in Tab. 3.2)

These results can easily be interpreted using the theoretical analysis developed in section 3.2. First note that the wavelength associated with the instability frequency is always very large compared to the plenum dimensions. The oscillation frequencies in the last column of Tab. 3.2 closely match the corresponding plenum Helmholtz frequencies determined in Tab. 3.1. By comparing these predictions with the observed instability oscillation frequencies, this clearly shows that the instability peak is always locked on the Helmholtz resonance frequency of the plenum and is essentially unaffected by modifications of the downstream confinement tube length. It is then interesting to investigate why the fundamental acoustic mode of the system features a weak dependence when increasing the downstream confinement tube length without combustion and remains unchanged with combustion. This can be done by examining values of the cavity coupling parameter Ξ between the plenum and the flame tube. This parameter is calculated for the nonreactive cases at room temperature and the reactive cases at the hot combustion products temperature. One respectively finds $\Xi = 0.09$ for $T_b = T_u = 293$ K and $\Xi = 0.04$ for $T_u = 293$ K and $T_b = 1600$ K. This parameter is thus weaker the in the presence of combustion. One should however pay attention that in the case of a plenum featuring a Helmholtz mode the exact coupling parameter between the upstream and the downstream regions separating the flame is the product of Ξ, the volume ratio $(V_1/V_2)^{1/2}$ and the Helmholtz number $\mathrm{He}_b = \omega l_3/c_b$. When replacing the angular frequency by $\omega \simeq \omega_H$ one can estimate the chamber Helmholtz number and values of the exact coupling

parameter :

$$\Xi_* = \Xi \left(\frac{V_1}{V_2}\right)^{1/2} \frac{\omega_H l_3}{c_b} \tag{3.36}$$

Results are gathered in Tab. 3.3 for the different cases explored. It is found that Ξ_* ranges from 0.10 to 0.32 under cold conditions when the geometrical parameters are varied, but takes much values under hot conditions $\Xi_* = 0.02$ to 0.06. Solutions of Eq. (3.26) indeed yield precise estimates of the fundamental peak frequencies under cold forced experiments and hot self-sustained unstable regimes. Due to the high temperature of the hot products Ξ_* takes vanishingly small values in the presence of combustion, the plenum and the flame tube are then essentially decoupled. Under cold conditions, there is a weak coupling between the plenum and the confinement tube because Ξ_* is not so small.

3.5 Damping

One can also estimate the damping associated to frequency response of the burner submitted to external acoustic modulation. To determine the damping factor it is interesting to assume that the system behaves like a second order system with a force term. If this assumption is made one may deduce the damping of this system from a measurement of the quality factor. It is here worth recalling that the resonant system defined by the following second order differential equation :

$$\ddot{x} + 2\xi\omega_0\dot{x} + \omega_0^2 x = F\cos(\omega t) \tag{3.37}$$

has a quality factor Q defined by :

$$Q = \frac{f_0}{\Delta f} \tag{3.38}$$

where Δf is the frequency width of the resonance curve taken at half height of the peak when the square of the amplitude is plotted with respect to frequency. It is easy to show that :

$$Q = \frac{1}{2\xi} \tag{3.39}$$

Now one may recall that $x \simeq Ae^{-\xi\omega_0 t}\cos[\omega_0(1-\xi^2)^{1/2} + \Phi]$, where Φ is the phase between the response of the system and the force term.

The damping coefficient defined by $\alpha = \xi\omega_0$ takes the form :

$$\alpha = 2\pi\xi f_0 = \frac{\pi f_0}{Q} \tag{3.40}$$

Flame tube (mm) :	**0**	**100**	**200**	**400**
Short burner				
Δf *(Hz)*	8	7.4	7.5	7.6
Damping α (s^{-1})	25	23.3	23.6	23.9
Medium burner				
Δf *(Hz)*	8.5	5.8	7	7.5
Damping α (s^{-1})	26.8	18.2	22	23.6
Long burner				
Δf *(Hz)*	6.6	6	6.7	5.2
Damping α (s^{-1})	20.8	19	21.1	16.4

Table 3.4: Damping coefficient α in s^{-1} for the different geometrical configurations.

from which one finally obtains :

$$\alpha = \frac{\pi f_0 \Delta f}{f_0} = \pi \Delta f \tag{3.41}$$

The damping coefficient is directly proportional to the frequency bandwidth Δf:

$$\alpha = \pi \, \Delta f \tag{3.42}$$

The rate of decay of energy is :

$$\frac{1}{E}\frac{dE}{dt} = -2\alpha = -\Delta\omega \tag{3.43}$$

From Eq. (3.42) and from results of burner acoustic responses plotted in Fig. 3.4, one can determine the damping coefficient of each configuration. Results are listed in Table. 3.4.

From the previous results, one may conclude that the damping coefficient in the various configurations is of the order of 20 s^{-1}. A general observation is that increasing the flame tube length or the upstream manifold size tends to not change the damping coefficient.

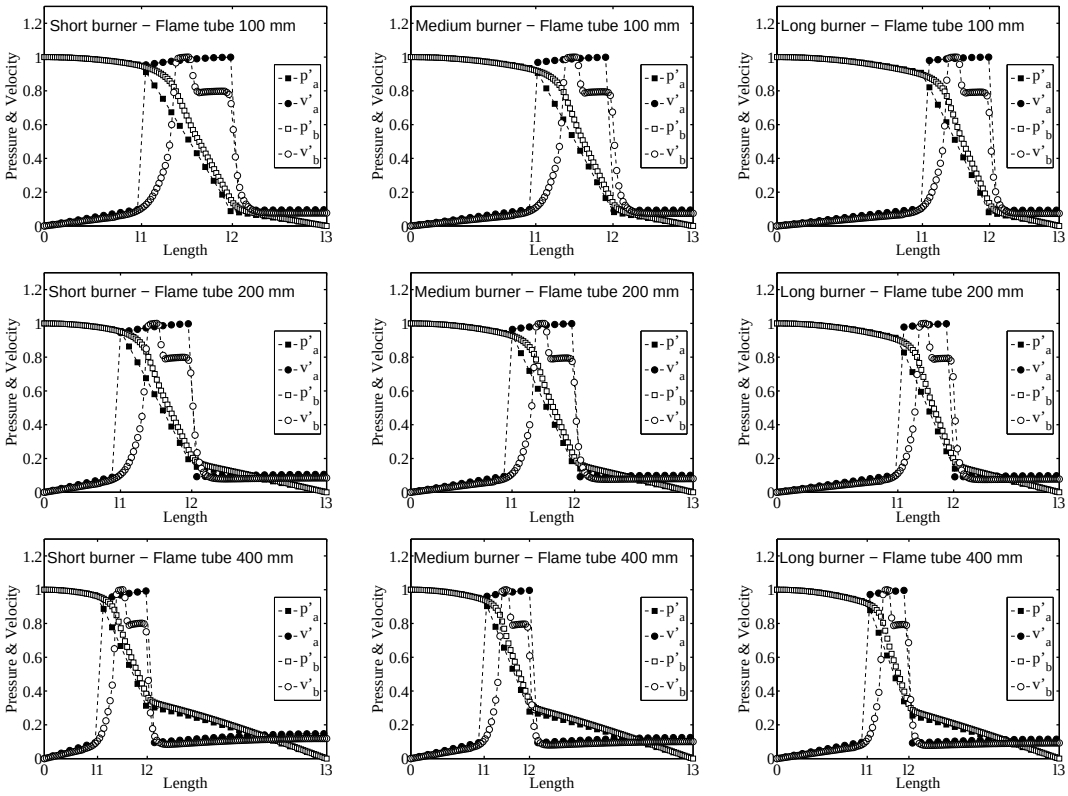

Figure 3.5: Pressure and velocity fluctuations profiles for all geometrical configurations. Black symbols are obtained from the multi-element coupled model. Open symbols are from a direct solution of the Helmholtz equation.

3.6 Comparisons between predictions and measurements

It is interesting to compare the pressure and velocity fluctuations profiles from the multi-element coupled cavity approach developped in section 3.2 of the present chapter and from a direct solution of the Helmholtz equation in the exact geometry of the system. This direct solution is obtained with Comsol (Numerical simulation have been carried out by Geoff Searby from IRPHE, Marseille). Results are exhaustively give in Fig.3.5 for all configurations. This comparison indicates that it is reasonable to make use a of multi-element coupled cavity model to predict the eigenfrequencies and mode shapes for combustion systems used in the present investigation.

3.7 Conclusion

It has been shown that acoustic interactions between the combustion chamber and the feeding manifold system with the plenum can often be neglected when the coupling parameter Ξ between theses cavities takes small values. This criterion can be used to simplify analysis of modal distribution of existing facilities or to design new chambers with reduced interactions between the feeding manifold and the combustion chamber cavities. It has also be shown that the threshold level under which acoustic uncoupling is ensured depends on values of the downstream impedance at the chamber exhaust. For a given configuration, this criterion should thus be completed by more detailed calculations or experiments to obtain the exact distribution of the modes within the combustor.

Exact conditions leading to decoupled plenum and chamber acoustic signatures were derived for systems featuring a bulk oscillation mode (Helmholtz mode) when the outlet impedance is modified. It has been shown that low frequency instabilities preferentially lock on the plenum mode and are independent of geometrical modifications of the chamber. This shows the predominance of the acoustics environment upstream from the combustion region compared to modifications on the downstream side of the flame region for low frequency combustion instabilities in chambers featuring a large expansion ratio.

Damping coefficient are determined from experimental frequency responses of the burner submitted to external acoustic modulations. It is shown that the damping coefficient in the various configuration is of the order of 20 s^{-1}. Pressure and velocity fluctuations profiles for all geometrical configurations determined with the multi-element coupled cavity approach and from a direct solution of the Helmholtz equation in the exact geometry confirms that is reasonable to make use of a multi-element approach to predict eigenfrequencies and mode shapes.

Part II

Flow and combustion dynamics

Chapter 4

Mode conversion processes over cascades and in swirling flows

Abstract : *When an acoustic wave impinges on an airfoil cascade a convective vorticity mode is generated giving rise to transverse velocity perturbations. This mode conversion process is investigated to explain the flow dynamics observed when swirlers are submitted to incident acoustic disturbances. The phenomenon is first studied in the case of a two dimensional airfoil cascade using a model derived from an actuator disk theory. The model is simplified to deal with low Mach number flows. The velocity field on the downstream side of the cascade features two components, an axial perturbation associated with the transmitted acoustic wave and a transverse disturbance corresponding to the vorticity wave generated at the cascade trailing edge. The model provides the amplitude of both components and defines their phase shift. Numerical simulations are carried out in a second stage to validate this model in the case of a cascade operating at a low Reynolds number Re = 2 700 based on the chord length. Space-time diagrams of velocity perturbations deduced from these simulations are used to retrieve the two types of modes. Experiments are then carried out in the case of an axial swirler placed in a cylindrical duct and submitted to plane acoustic waves emitted on the upstream side of the swirler. The amplitude and phase of the two velocity components measured in the axial and azimuthal directions are found to be in good agreement with theoretical estimates and with numerical calculations. This analysis is motivated by combustion dynamics observed in flames stabilized by aerodynamic swirlers in continuous combustors.*

Résumé : *Quand une onde acoustique interagit avec une grille d'aubes, un mode tourbillonnaire est généré et il en résulte des perturbations de vitesses transversales. Ce processus de conversion de mode est étudié pour expliquer la dynamique des écoulements observés lorsque des vrilles (swirlers) sont soumises à des perturbations acoustiques incidentes. Le phénomène est d'abord etudié dans le cas d'une grille dans une configuration bidimensionnelle au moyen d'une analyse théorique fondée sur le modèle du disque actuateur. Ce modèle est simplifié pour tenir compte du faible nombre de Mach de l'écoulement. Le champ de vitesse en aval de la grille possède deux composantes, une perturbation axiale associée à l'onde acoustique transmise et une perturbation transversale correspondant à l'onde tourbillonnaire générée aux bords de fuite de la grille. Le modèle fournit l'amplitude des deux composantes et définit leur déphasage. Des simulations numériques sont réalisées dans une deuxième étape pour valider ce modèle dans le cas d'un faible nombre de Reynolds : Re = 2 700 basé sur la longueur de corde des aubes. Des diagrammes spatio-temporels des perturbations de vitesses déduits de ces simulations sont utilisés pour mettre en évidence les deux types de modes. Les expériences sont ensuite effectuées dans le cas d'une vrille (swirler) axiale placé dans une conduite cylindrique et soumise à des ondes acoustiques planes émises en amont. Les amplitudes et phases des deux composantes de vitesse mesurée dans les directions axiale et azimutale sont en bon accord avec les estimations théoriques et avec les calculs numériques.*

4.1 Introduction

Mode conversion is a mechanism where one type of propagating disturbance generates another type of wave. This involves convective modes (entropy and vorticity) and acoustic modes and takes place in many situations in fluid dynamics. The present investigation is concerned with one such mechanism whereby an acoustic wave is incident on an airfoil cascade producing a vorticity wave in the downstream flow. At this point, it is worth putting this problem in perspective by reviewing configurations of fundamental and practical interest where mode conversion is important. In Fig. 4.1(a) entropy waves, generally hot spots, convected through a nozzle generate acoustic pressure waves which are radiated to the far field. This mechanism designated as "entropy noise" or indirect combustion noise initially considered by Candel (1972) and Marble and Candel (1977) has been examined extensively in relation with aeroacoustic applications by Morfey (1973a), Ffwocs-Williams and Howe (1975), Howe (1975), Bake *et al.* (2009) and Leyko *et al.* (2009). A related problem considered by Cumpsty and Marble (1977b) is that of entropy waves impinging on a blade row sketched in Fig. 4.1(b).

The cascade acts like a nozzle and the incident entropy waves are accelerated in the flow generating acoustic waves propagating in the upstream and downstream directions. This again constitutes a source of core noise in gas turbines studied by Cumpsty and Marble (1977a). In the third configuration shown in Fig. 4.1(c) the coupling results from vortices shed from the upstream side of a cavity exposed to a uniform flow. The vortices impinge on the downstream cavity lip and generate acoustic waves which in turn synchronize the vortex shedding mechanism at the leading edge cavity (see for example the review by Rockwell and Naudascher (1979)). Characteristic frequencies can be estimated with an expression due to Rossiter (1964). A related problem found in solid propellant rocket engines is shown in Fig. 4.1(d). Here vortices are shed from baffles separating the propellant segments and protruding in the gas stream or from the edge of the propellant bloc as exemplified in this subfigure. The vortices impinge on the nozzle radiating an acoustic wave which may couple with the vortex shedding mechanism giving rise to self sustained oscillations. In solid rocket engines this mechanism is responsible for troublesome thrust oscillations augmenting the vibrational levels on the payload as studied by Dotson *et al.* (1997). A simplified version of the previous case is shown in Fig. 4.1(e) where a diaphragm blocks the flow in a channel. When an acoustic wave impinges on this constriction vortices are generated. The mode conversion process taking place in this geometry is studied in a recent article by Noiray *et al.* (2009). Another situation of interest is that of a jet exhausted from a nozzle or a channel into a quiescent atmosphere as shown in Fig. 4.1(f). An acoustic wave propagating in the upstream flow and interacting with a channel exhaust produces a convective mode in the free jet when the Strouhal number is sufficiently low meaning that the oscillation is in the low frequency range. This process has received considerable attention in the past and is the subject of a classical article by Crow and Champagne (1971). Birbaud *et al.* (2007) provide many additional references and map the various modes of interactions in a diagram. A related process takes place in a flame stabilized on a burner equipped with a driver unit as in Fig. 4.1(g). In the low frequency range the acoustic wave is transformed in a convective mode which modulates the flame. This type of mode conversion has been studied for example by De Soete (1964), Boyer and Quinard (1990a), Baillot *et al.* (1992), Bourhela and Baillot (1998), Schuller *et al.* (2003a), Birbaud *et al.* (2006), Kornilov *et al.* (2007) and Shanbhogue *et al.* (2009).

The present chapter is concerned with the problem shown in Fig. 4.2(a) and (b). An acoustic wave impinges on an airfoil cascade or a swirler placed in a duct. The motivation of this analysis lies in the domain of combustion dynamics. In many combustors operating in a continuous mode the flame is stabilized in a swirling flow generated by axial or radial vanes. Typical gas turbine combustors rely on radial swirlers which impart rotation to the incoming air producing an inner recirculation zone filled with hot gases and anchoring the flame in the vicinity of the

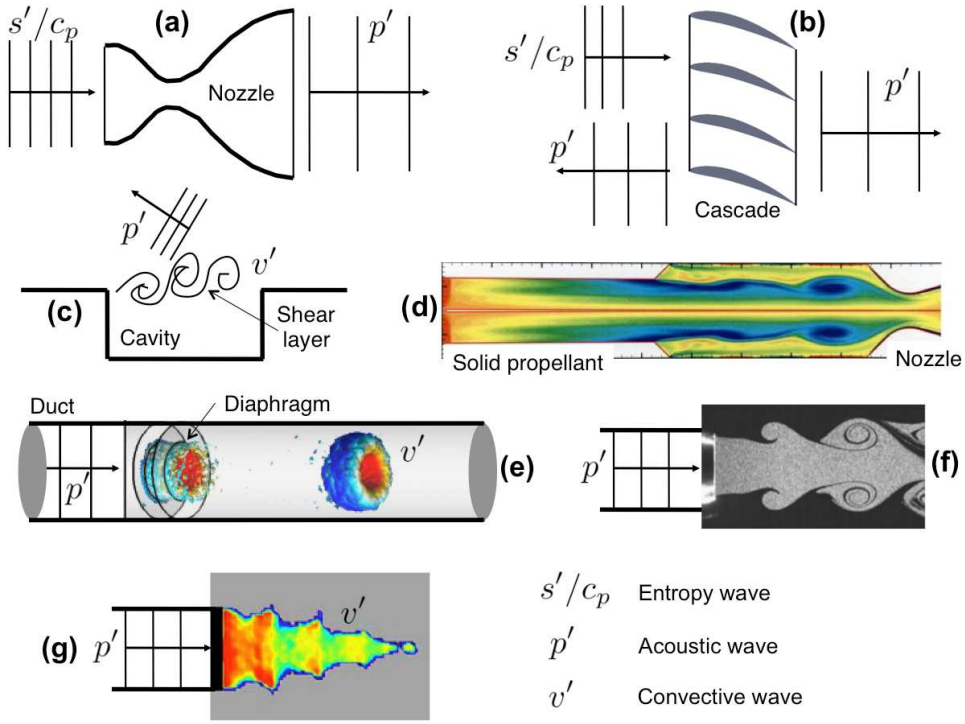

Figure 4.1: Review of mode conversion mechanisms. (a) : entropy waves, generally hot spots, convected through a nozzle generate acoustic pressure waves which are radiated to the far field. (b) : entropy waves impinging on a blade row. (c) : vortices shed from the upstream side of a cavity exposed to a uniform flow. (d) : vortices shed from baffles separating the propellant segments and protruding in the gas stream or from the edge of the propellant bloc. (e) : acoustic waves are impinging the diaphragm and vortices are then generated. (f) : modulated jet exhausted from a nozzle or a channel into a quiescent atmosphere. (g) : conical flame submitted to acoustic modulations.

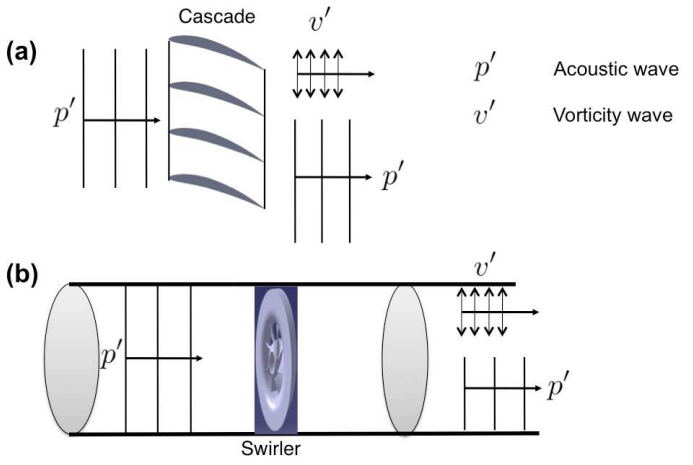

Figure 4.2: Mode conversion mechanisms study in the present work. (a) : acoustic waves impinging on an airfoil cascade. (b) : acoustic waves impinging on a swirler in a duct.

injection plane. Under unstable operation coupling acoustics and combustion, the swirlers are submitted to incident acoustic perturbations. It is interesting to examine this situation and specifically analyze the possible generation of a vorticity wave and the associated velocity perturbations on the downstream side of the swirler. At this point it is worth briefly reviewing the literature dealing with the interaction of perturbations with blade rows. This problem covered in the classical textbooks of Horlock (1978) and Greitzer *et al.* (2004) has been extensively investigated in the domain of turbomachinery for example by Kaji and Okazaki (1970), Koch (1971) and Morfey (1973b) in early works and more recently by Peake and Kerschen (1997) and Glegg (1999). It is important because such interactions induce fluctuating forces on the blades generating noise and undesirable vibrations. Conversion of entropy fluctuations by a cascade has been worked out analytically by Cumpsty and Marble (1977b) and was pursued by Cumpsty (1979). It is shown that the interaction gives rise to acoustic pressure waves. These studies are used as starting points of the model developed in the present chapter. Most of these studies consider high Mach number flows found in axial compressors or turbines, the case of low Mach flows is less well documented.

The response of a cascade to unsteady perturbations can be studied with numerical simulations as exemplified by Paynter (1997). The case of swirlers interacting with acoustic perturbations has recently been examined by Wang and Yang (2005) using LES. Consequences on the dynamics of swirling flames are discussed in a recent review by Huang and Yang (2009). It is deduced from simulations that axial and azimuthal velocity disturbances propagate at different velocities on the downstream side of the swirler. This is also inferred by Hirsch *et al.*

(2005) and Komarek and Polifke (2010). While the presence of the convective component is recognized by these authors, there are no direct measurements of the axial and azimuthal velocity components which support this conclusion and no theoretical attempt is made to estimate the respective levels of the various perturbations, except perhaps in a study carried out by Sajben and Said (2001) where the strength of the vorticity wave is estimated.

This chapter is organized as follows. A theoretical formulation is first derived from the analysis of Cumpsty and Marble (1977b) to deal with situations where the Mach number is low corresponding to standard operation of swirlers (section 5.2). The blade row is assumed to operate in the low velocity range and interacts with an incident acoustic wave giving rise to a perturbed velocity field downstream of the cascade. Amplitudes of the downstream perturbations are determined. The model is derived in 2D a standard assumption used in turbomachinery analysis where the flow is described on a median cylindrical surface located at equal distances from hub and tip. The underlying equations are based on an actuator disk description. Numerical simulations are carried out with a Navier-Stokes unsteady flow solver (section 5.3). Simulations are performed in a 2D cascade which is consistent with the two dimensional theory. The modulation free flow established in a group of airfoils is obtained in a first step. In this simulation the wakes formed at the airfoil trailing edges give rise to a shear layer instability which develop into a Karman street of vortices. The flow is then modulated by an axial acoustic wave which propagates towards the cascade. Two modulation frequencies are considered $f = 60$ Hz and $f = 100$ Hz corresponding to two Strouhal numbers based on the chord length respectively equal to 0.15 and 0.25 for two amplitudes of the inlet velocity fluctuation $u'_\infty = 0.1$ m s^{-1} and $u'_\infty = 1$ m s^{-1}. These simulations are used to extract the velocity components amplitudes. Space-time diagrams are plotted highlighting the axial and azimuthal modes of propagation. The problem is then examined experimentally by making use of a ducted swirler submitted to a plane acoustic wave (section 5.4). This axisymmetric geometry is easier to consider for the experiments. The situation is close to that found in turbomachinery analysis where calculations are carried out in 2D cascade configurations while the real geometry has a rotational symmetry. The objective is not so much to reproduce simulations through an experiment but to reveal a mechanism and for this one may use the geometry which is easiest to explore. The perturbed velocity field on the downstream side of the swirler is characterized and these data are compared with theoretical estimates and numerical calculations (section 5.5).

4.2 Theoretical model

This analysis is concerned with the interaction taking place between a swirler and incident acoustic perturbations. This problem is easier to tackle theoretically by considering the two dimensional geometry of a cascade as plotted in Fig. 4.3. The incoming flow velocity $\overline{w}_1$ is oriented in the axial direction while the outgoing flow $\overline{w}_2$ makes an angle $\overline{\theta}_2$ with respect to the axis. One assumes that the flow velocities remain in the low Mach number range. The characteristic size of the cascade (the blade chord) is small compared to the acoustic wavelengths considered. The ratio is typically of the order of 0.01. One may then consider that it is compact with respect to the incident wave field and use an actuator disk to represent the blade row. The swirler can then be treated as a discontinuity for these perturbations and operates like an actuator disk.

To relate perturbations on the upstream and downstream sides of this cascade one may use jump conditions provided by Cumpsty and Marble (1977b) which are adapted to a low Mach number flow :

$$s'_1 = s'_2 \tag{4.1}$$

$$\frac{\rho'_1}{\overline{\rho}_1} + \frac{w'_1}{\overline{w}_1} - \theta'_1 \tan\overline{\theta}_1 = \frac{\rho'_2}{\overline{\rho}_2} + \frac{w'_2}{\overline{w}_2} - \theta'_2 \tan\overline{\theta}_2 \tag{4.2}$$

$$\frac{p'_1}{\gamma\overline{p}_1} + \frac{s'_1}{(\gamma-1)c_p} = \frac{p'_2}{\gamma\overline{p}_2} + \frac{s'_2}{(\gamma-1)c_p} \tag{4.3}$$

where s' is the entropy fluctuation and $\rho'/\overline{\rho}$ the relative density fluctuation. Subscripts 1 and 2 refer to inlet and outlet of the cascade vanes. The ratios $w'_1/\overline{w}_1$ and $w'_2/\overline{w}_2$ are the relative velocity fluctuations on each side of the cascade, θ'_1 is the fluctuation of the angle of incidence θ_1, θ'_2 is the fluctuation of the angle

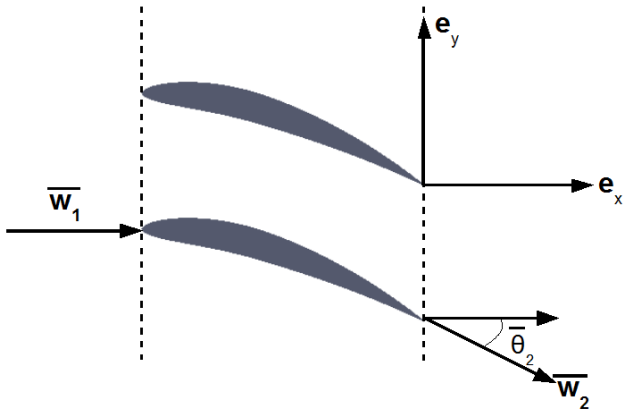

Figure 4.3: Geometry of the airfoils cascade.

θ_2 at the trailing edge, p' refers to the fluctuation in pressure, γ is the specific heat ratio and c_p is the specific heat of the working fluid. At the trailing edge the Kutta condition implies that the flow should leave the blade in a direction tangent to the mean camber line so that the perturbation angle vanishes $\theta'_2 = 0$. In region 1, the pressure field is formed by incident and reflected acoustic waves which are taken as plane waves propagating in the axial direction :

$$p'_1 = A \exp i(kx - \omega t) + AR \exp i(-kx - \omega t) \tag{4.4}$$

where A is the amplitude of the incident acoustic wave, R is the reflection coefficient of this wave and $k = \omega/c$ designates the acoustic wave number. The velocity fluctuation corresponding to this field is expressed as :

$$u'_1 = \frac{A}{\rho_1 c_1} \exp i(kx - \omega t) - \frac{AR}{\rho_1 c_1} \exp i(-kx - \omega t) \tag{4.5}$$

where ρ_1 and c_1 are the density and the speed of sound in region 1. It is assumed in the present analysis that the mean density and speed of sound are the same on both sides of the swirler : $\rho_1 = \rho_2 = \overline{\rho}$ and $c_1 = c_2 = \overline{c}$. In region 2, the transmitted acoustic pressure also propagating in the axial direction writes :

$$p'_2 = AT \exp i(kx - \omega t) \tag{4.6}$$

where T is the transmission coefficient and the corresponding acoustic velocity component is (subscript a) :

$$(u'_2)_a = \frac{AT}{\overline{\rho}\,\overline{c}} \exp i(kx - \omega t) \tag{4.7}$$

A vorticity wave (subscript v) is also generated at the swirler. This is required to satisfy the set of jump conditions. The incident acoustic field has a wavevector which is perpendicular to the actuator disk. This field of plane waves and those corresponding to the reflected and transmitted acoustic waves have a zero wavevector projection in the transverse direction. As a consequence, the vorticity wave must also have a zero wavevector projection in the transverse direction to be compatible with the other wave fields. The vorticity wave corresponds to a convective velocity fluctuation which is transverse to the direction of propagation. There are no velocity perturbations in the x-direction to satisfy conservation of mass. The vorticity wave must then have a zero wave number in the transverse direction y and it is convected by the mean flow in the x direction with a velocity $\overline{u}_2 = \overline{w}_2 \cos\overline{\theta}_2$ which is also equivalent to $\overline{v}_2 = \overline{u}_2 \tan\overline{\theta}_2$. This wave comprises a single velocity component of amplitude B in the transverse direction :

$$(v'_2)_v = B \exp i\left[\frac{\omega x}{\overline{w}_2 \cos\overline{\theta}_2} - \omega t\right] \tag{4.8}$$

Velocity perturbations on the downstream side of the swirler have the following components :

$$\boldsymbol{w}'_2 = (u'_2)_a\, \boldsymbol{e}_x + (v'_2)_v\, \boldsymbol{e}_y \tag{4.9}$$

In what follows one may drop indices a and v but it is important to remember that the axial and transverse velocity components respectively correspond to an acoustic wave propagating at the speed of sound $\overline{c}$ and to a vorticity wave convected at the flow velocity $\overline{u}_2 = \overline{w}_2 \cos\overline{\theta}_2$ in the axial direction. It is interesting to determine fluctuations in the modulus of the downstream flow velocity $\boldsymbol{w}'_2 = u'_2 \boldsymbol{e}_x + v'_2 \boldsymbol{e}_y$ and in the angle θ'_2. We begin with :

$$\overline{w}_2 + w'_2 = [(\overline{u}_2 + u'_2)^2 + (\overline{v}_2 + v'_2)^2]^{\frac{1}{2}} \tag{4.10}$$

Neglecting second order terms this last expression can be written as :

$$\overline{w}_2 + w'_2 = (\overline{u}_2^2 + \overline{v}_2^2)^{\frac{1}{2}} \left[1 + 2\frac{(\overline{u}_2 u'_2 + \overline{v}_2 v'_2)}{\overline{u}_2^2 + \overline{v}_2^2}\right]^{\frac{1}{2}} \tag{4.11}$$

Expanding the square root to first order one finds :

$$\overline{w}_2 + w'_2 = \overline{w}_2 \left[1 + \frac{(\overline{u}_2 u'_2 + \overline{v}_2 v'_2)}{\overline{w}_2^2}\right] \tag{4.12}$$

and the fluctuation in modulus may be written as :

$$w'_2 = \frac{\overline{u}_2}{\overline{w}_2} u'_2 + \frac{\overline{v}_2}{\overline{w}_2} v'_2 \tag{4.13}$$

This can be cast in the following form for w'_2 :

$$w'_2 = \cos\overline{\theta}_2 u'_2 + \sin\overline{\theta}_2 v'_2 \tag{4.14}$$

Some straightforward calculations also lead to :

$$\theta'_2 = \sin\overline{\theta}_2 \cos\overline{\theta}_2 \left[\frac{v'_2}{\overline{v}_2} - \frac{u'_2}{\overline{u}_2}\right] \tag{4.15}$$

Noting that the change in pressure and density across the swirler is small ($\overline{p}_1 \simeq \overline{p}_2$, $\overline{\rho}_1 \simeq \overline{\rho}_2$) one easily deduces from the previous set of jump conditions that :

$$p'_1 = p'_2 \tag{4.16}$$

$$\frac{w'_1}{\overline{w}_1} - \theta'_1 \tan\overline{\theta}_1 = \frac{w'_2}{\overline{w}_2} - \theta'_2 \tan\overline{\theta}_2 \tag{4.17}$$

Now the fluctuation in angle on the downstream side of the swirler must vanish to satisfy the unsteady Kutta condition $\theta'_2 = 0$. Since fluctuations on the upstream side are only axial $w'_1 = u'_1$ one deduces that there are no angular fluctuations at the leading edge $\theta'_1 = 0$. The jump conditions for the perturbations simplify :

$$p'_1 = p'_2 \tag{4.18}$$

$$\frac{u'_1}{\overline{w}_1} = \frac{u'_2 \cos\overline{\theta}_2 + v'_2 \sin\overline{\theta}_2}{\overline{w}_2} \tag{4.19}$$

Inserting Eqs. (4.4) to (4.8) in these last expressions, one obtains :

$$A(1+R) = T \tag{4.20}$$

$$\frac{A}{\overline{\rho}\,\overline{c}}\frac{1}{\overline{w}_1}(1-R) = \frac{AT}{\overline{\rho}\,\overline{c}}\frac{1}{\overline{w}_2}\cos\overline{\theta}_2 + \frac{B\sin\overline{\theta}_2}{\overline{w}_2} \tag{4.21}$$

Noting that the steady state mass balance requires that $\overline{w}_1 = \overline{w}_2\cos\overline{\theta}_2$, the previous expression becomes :

$$A(1-R) = \cos^2\overline{\theta}_2 AT + \overline{\rho c}\sin\overline{\theta}_2\cos\overline{\theta}_2 B \tag{4.22}$$

From the Kutta condition $\theta_2' = 0$ (Eq. (4.15)), one also deduces that $v_2' = u_2'\tan\overline{\theta}_2$ which yields :

$$B = \frac{AT}{\overline{\rho}\,\overline{c}}\tan\overline{\theta}_2 \tag{4.23}$$

Inserting this expression in Eq. (4.22), one obtains :

$$A(1-R) = AT \tag{4.24}$$

This relation combined with Eq. (8.7) finally yields :

$$R = 0 \qquad \text{and} \qquad T = 1 \tag{4.25}$$

Assumptions of equality of mean pressure and density on the two sides of the swirler lead to a zero reflection coefficient and to a unit value for the transmission coefficient. One also finds from this analysis that the transverse velocity is directly proportional to the axial acoustic velocity component and that $\tan\overline{\theta}_2$ defines the proportionality between these two components. This result is in agreement with previous findings by Sajben and Said (2001). It is thus possible to write the velocity components on the downstream side of the swirler under the following form :

$$u_2' = \frac{A}{\overline{\rho}\,\overline{c}}\exp i\left[\frac{\omega}{\overline{c}}x - \omega t\right] \tag{4.26}$$

$$v_2' = \frac{A}{\overline{\rho}\,\overline{c}}\tan\overline{\theta}_2\exp i\left[\frac{\omega}{\overline{u}_2}x - \omega t\right] \tag{4.27}$$

The axial velocity perturbation propagates at the speed of sound while the transverse velocity component is convected at the local flow velocity $\overline{u}_2 = \overline{w}_2\cos\overline{\theta}_2$ in the axial direction. The previous calculations indicate that the swirler acts as a mode converter. When it is submitted to axial acoustic waves it generates a vorticity wave which is convected by the flow in the axial direction. This convective wave is characterized by a velocity component in the transverse direction. The relative amplitude of this component is equal to the relative amplitude of the axial velocity perturbation $v_2'/\overline{v}_2 \simeq u_2'/\overline{u}_2$. These conclusions were obtained from a two dimensional actuator disk theory because it provides essential results

without the complications encountered in a 3D configuration. Such 2D analysis are found in turbomachinery flow investigations, see for example Cumpsty and Marble (1977b). The reasoning is easy to follow in 2D because the algebra is simplified by using a well established actuator disk framework. The analysis in 3D is more complex because of the radial velocity component. However 3D numerical simulations carried out recently (see chapter 7) indicate that the mode conversion is confirmed and that the amplitude of the radial component is less important by an order of magnitude than the axial and azimuthal components. It is then reasonable to apply the previous results to a swirler and consider that the azimuthal velocity fluctuation can be approximately identified to the transverse component determined previously.

The previous analysis relies on a 2D actuator disk theory because it provides essential results without the complications encountered in a 3D configuration. Such 2D analysis are found in turbomachinery flow investigations. The reasoning is easy to follow in 2D because the algebra is simplified by using the well established actuator disk framework. The analysis in 3D is more complex because of the radial velocity component. However 3D numerical simulations presented in chapter 7 indicate that the mode conversion is confirmed and that the amplitude of the radial component is less important by an order of magnitude than the axial and azimuthal components.

4.3 Numerical simulation

Simulation is now used to examine the unsteady flow interaction with a cascade. It is convenient to examine the process with 2D configurations. The computational requirements are reduced and calculations can be repeated. Simulations are carried out with the AVBP code (Schönfeld and Rudgyard (1999)), a compressible Navier-Stokes flow solver operating on structured and unstructured meshes. AVBP solves the laminar and turbulent compressible Navier-Stokes equations in two or three space dimensions. The last effort on this code was put on modeling unsteady turbulent reactive flows motivated by activities in the field of unsteady turbulent combustion as reported by Selle *et al.* (2006) or Staffelbach *et al.* (2009). This code is used in the present context because it has a good degree of precision with a third order in space and in time discretization and suitably describes acoustics flow interactions. The filtered compressible equations exhibit subgrid scale tensors and vectors describing the interaction between the resolved and subgrid motions.

The filtered quantity $\overline{f}$ is resolved in the numerical simulation whereas $f' = f - \overline{f}$ is the subgrid scale part due to the unresolved flow motion. For variable density

ρ, a mass-weighted Favre filtering is introduced such as :

$$\overline{\rho}\widetilde{f} = \overline{\rho f} \tag{4.28}$$

The balance equations for Large Eddy Simulations (LES) are obtained by filtering the instantaneous balance equations and give :

$$\frac{\partial \overline{\rho}\,\widetilde{u_i}}{\partial t} + \frac{\partial}{\partial x_j}(\overline{\rho}\,\widetilde{u_i}\,\widetilde{u_j}) = -\frac{\partial}{\partial x_j}[\overline{P}\,\delta_{ij} - \overline{\tau_{ij}} - \overline{\tau_{ij}}^t], \tag{4.29}$$

where ρ refers to the density, u to the velocity, p to the pressure, δ the Kronecker symbol and $\overline{\tau_{ij}}$ and $\overline{\tau_{ij}}^t$ are respectively the laminar and turbulent filtered stress tensors. Subscripts i, j and l refer to the three spatial dimensions while t denotes for turbulence.

$$\frac{\partial \overline{\rho}\,\widetilde{E}}{\partial t} + \frac{\partial}{\partial x_j}(\overline{\rho}\,\widetilde{E}\,\widetilde{u_j}) = -\frac{\partial}{\partial x_j}[\overline{u_i\,(P\,\delta_{ij} - \tau_{ij})} + \overline{q_j} + \overline{q_j}^t] + \overline{\dot{\omega}_T} + \overline{Q_r} \tag{4.30}$$

In this equation, E denotes for the total energy per unit mass, $\overline{q_j}$ and $\overline{q_j}^t$ are respectively the resolved filtered and the subgrid scale heat flux vectors. $\overline{\dot{\omega}_T}$ is the chemical source term and $\overline{Q_r}$ the radiative source term.

$$\frac{\partial \overline{\rho}\,\widetilde{Y_k}}{\partial t} + \frac{\partial}{\partial x_j}(\overline{\rho}\,\widetilde{Y_k}\,\widetilde{u_j}) = -\frac{\partial}{\partial x_j}[\overline{J_{j,k}} + \overline{J_{j,k}}^t] + \overline{\dot{\omega}_k}, \tag{4.31}$$

where Y is the mass fraction of the species k. $\overline{J_{j,k}}$ and $\overline{J_{j,k}}^t$ are respectively the diffusive species and the subgrid scale diffusive flux vectors. Finally, $\dot{\omega}_k$ refers to the reaction rate of each species computed with the Arrhenius law.
In Eqs. (4.29), (4.30) and (4.31), one recognizes standard resolved parts including laminar stress and flux terms and an unresolved part featuring turbulent stresses and fluxes. The resolved parts are the same as those found in DNS but they are expressed in terms of filtered variables. In large eddy simulations the unresolved part has to be modeled. In the limiting case where the unresolved stresses and fluxes vanish, the code provides quasi-DNS solutions of the Navier-Stokes equations.

In the present analysis, the code is used in this quasi-DNS limit because the cell size in the region of interest is very small and the Reynolds number based on the chord length is low ($\mathrm{Re}_c = 2700$). It has also been verified that standard boundary layer structures are well retrieved. Under these circumstances the physical viscosity is much larger than the subgrid scale viscosity. It has been checked that in the cascade and its nearfield (at distances of up to 4 chords) the laminar viscosity is two orders of magnitude larger than the subgrid scale viscosity. The subgrid scale stresses are only used in the present context to dissipate the vortices convected by the flow towards the outlet of the domain. This can be

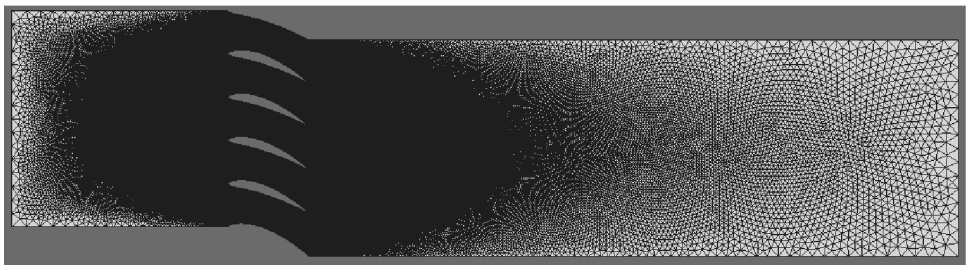

Figure 4.4: Mesh used for numerical simulations.

accomplished with a Smagorinsky model, which is used here to avoid problems linked with the passage of vortices through the downstream boundary. When the cell size is increased dissipation by this model is augmented and the perturbations are damped in this way. The downstream part of the domain serves as a "sponge layer" and is not used in the analysis. The acoustic motion is also well represented with the third order in space and time precision of the code. The element sizes are much smaller than the wavelength and the size of the domain of interest is much smaller than the wavelength. Under these conditions, the system is compact with respect to the wavelength, the acoustic motion then corresponds to a bulk fluctuation of the flow variables and the level of dissipation and dispersion are minimal in the region of interest.

A group of five airfoils is used to represent the cascade together with periodic boundary conditions on the upper and lower sides of the domain. The mesh shown in Fig. 4.4 comprises 450 000 cells. The total length of the computational domain is 13 centimeters while the transverse size is 3.1 centimeters corresponding respectively to 13 and 3.1 chord lengths. Airfoils are separated by 6 millimeters in the transverse direction. Several previous investigations have been carried out with the AVBP code in which tetrahedral grids have been used. Acoustic propagation is suitably described because the precision is third order and the typical grid size is quite small compared to the wavelength so that the system is compact with respect to the wavelength. Under these circumstances one expects little dispersion and dissipation. Considering the growth of a laminar boundary layer over a thin flat plane, standard expressions give a thickness of nearly one millimeter at the trailing edge. Each side of the airfoil is refined with 200 mesh points so that at least 20 points lie in the boundary layer at the trailing edge. The mesh is sufficiently refined to capture the boundary layers on the airfoils suction and pressure sides. The minimum cell size is 0.03 mm and the typical average cell size is 0.045 mm. Time integration is explicit with a fixed time step equal to 4.5×10^{-8} s.

The air flow velocity at the numerical domain inlet is fixed to $u_\infty = 4\ \mathrm{m\ s^{-1}}$. This

flow impinges on the cascade. Each airfoil features a NACA 8411 profile which is also used to design the swirler considered in section 4. The trailing edges make an angle $\theta_2 = 25°$ with the horizontal axis. The chord length of the airfoil is $l_c =$ 10 mm. No slip boundary conditions are used on the airfoils and the upper and lower sides of the domain are periodic. Non-reflecting boundary conditions for Navier-Stokes equations are used at the computational domain inlet and outlet and this allows an easy modulation of the flow at the inlet. The outlet then behaves as a non-reflecting subsonic condition.

We first investigate the dynamics of the modulation free flow through the cascade. There are no incident perturbations and the dynamics observed in this reference case corresponds to the transient leading to the establishment of the flow in the airfoil cascade and in the downstream domain. It is interesting to examine the vorticity field in the downstream flow shown in Fig. 4.5 in the form of successive maps. The flow is initialized with an axial velocity equal to 4 m s^{-1} everywhere in the computational domain. This does not satisfy the boundary conditions in the cascade and there is an initial adjustment of the flowfield during a short period of time. A starting vortex is then shed from the trailing edges to satisfy Kelvin's theorem. The circulation in each vortex is opposite to that which develops around each blade. This can be seen at $t = 0.45$ ms in Fig. 4.5. One distinguishes a vortex shed at the extremity of each trailing edge. This intense starting vortex is generated to satisfy the conservation of circulation in the flow as expected from Kelvin's theorem. From $t = 2.25$ ms to $t = 11.25$ ms, this primary vortex is convected in the downstream direction and the wake behind each airfoil expands in both axial and transverse directions. The starting vortex intensity is progressively reduced by viscous dissipation. This vortex is also dissipated by numerical viscosity which is low but non-negligible when the mesh size increases near the domain outlet. Shear layer instability becomes visible at $t = 13.5$ ms. The instability grows up to $t = 18$ ms. The flow then approaches a state which satisfies the Navier-Stokes equations and boundary conditions on the blades and computational domain boundaries. The amplitude of oscillation saturates for larger times $t > 20.25$ ms giving rise to well established Karman vortex streets defining a pattern of counter-rotating vortices.

These simulations are carried out at a modest flow velocity and the flow while unsteady remains laminar but features a periodic pattern of vortices generated by wake instability. The mode conversion process is also operating under turbulent flow conditions a point which is currently investigated with fully 3D simulations of the flow through a swirler. To obtain a fully turbulent wake downstream the cascade, the inlet velocity should be augmented but this is out of the scope of this study. To make sure that the flow remains laminar the calculation were carried out for the modulation free flow over a long period of 50 ms. It was found that

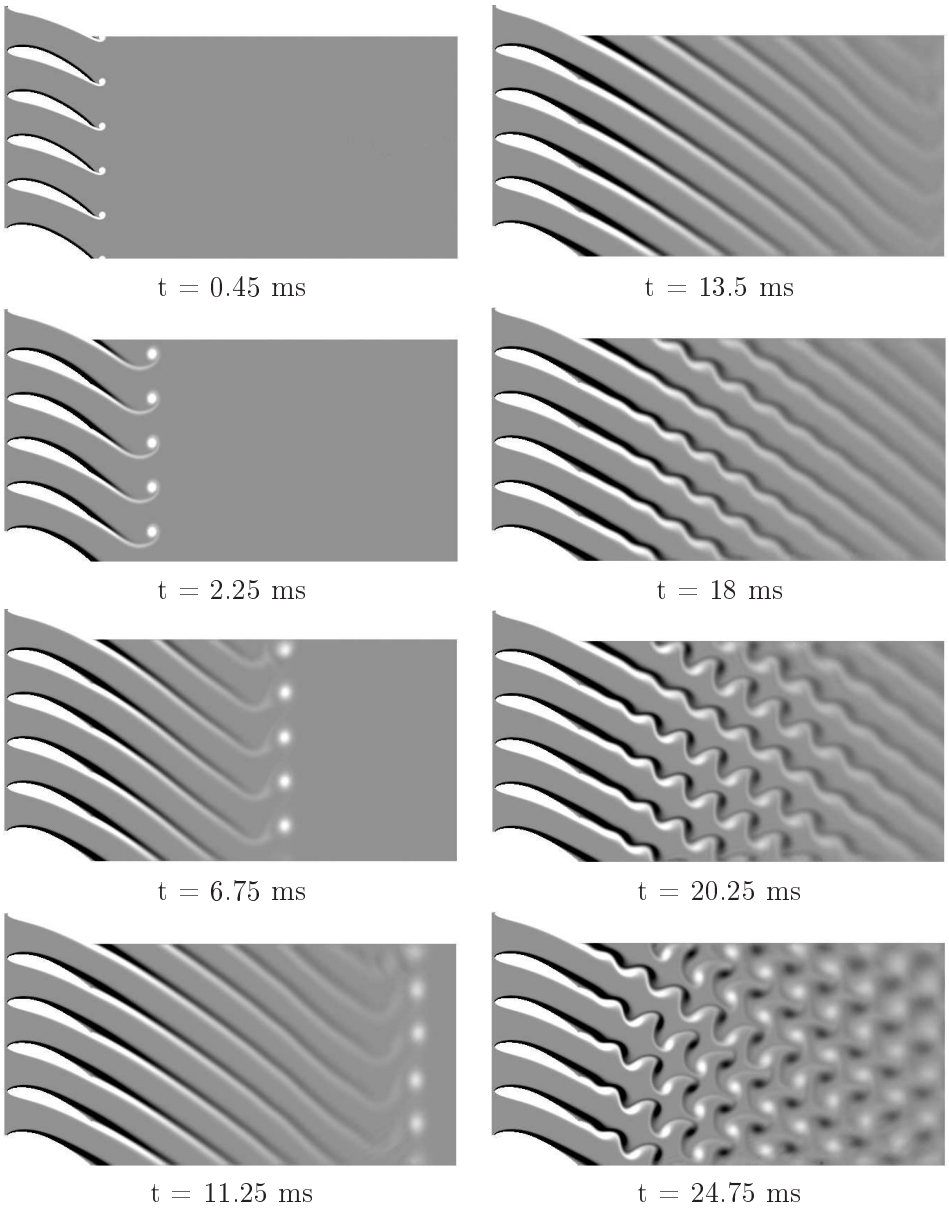

Figure 4.5: Vorticity fields of the flow in the absence of acoustic modulation. The maximum level of vorticity 5000 s^{-1} is in black while the minimum level -5000 s^{-1} is in white. The time instant of each simulation is given below each field in ms. The flow dynamics goes through three stages : (1) emission of a vortex from the airfoils trailing edges, (2) Destabilization of the wake caused by shear layer instability, (3) Fully developed Karman vortex street.

the flow did not transition to a turbulent state but continuously featured distinct vortex patterns like those shown in Fig. 4.5.

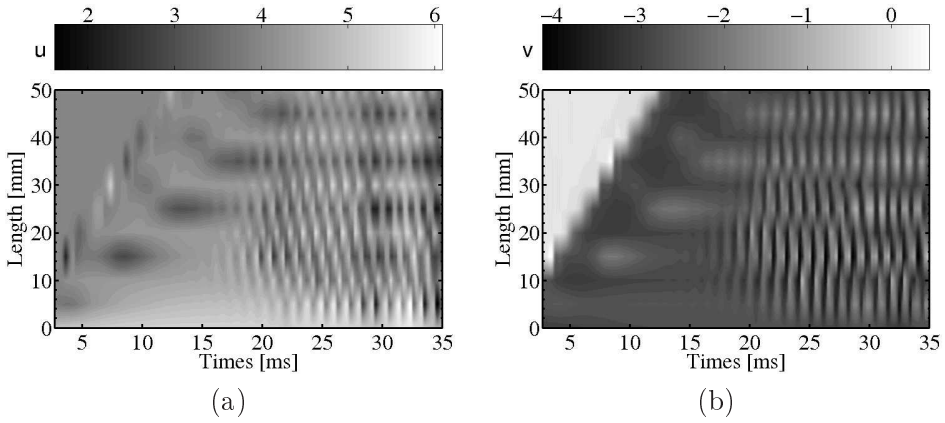

(a) (b)

Figure 4.6: Space-time diagrams of velocity components beyond the airfoils cascade. Theses diagrams are obtained with raw velocity signals extracted from numerical simulations along straight lines downstream the cascade. (a) : u velocity component. (b) : v velocity component.

This dynamics is now studied with space-time diagrams describing the temporal evolution of both axial and transverse velocity components u and v along straight lines in the axial direction. Data were recorded at points separated by a distance $\Delta x = 5$ mm over a distance of 50 mm corresponding to five chord lengths and over a time duration of 35 ms. The aim of the space-time diagrams is to highlight the behavior of the flow on the downstream side of the cascade. Figure 4.6 shows the space-time diagram corresponding to Fig. 4.5. The axial and transverse velocity signals are analyzed as a function of time in the diagram appearing in Fig. 4.6. Figures 4.6 (a) and (b) respectively display the axial u(x,t) and transverse v(x,t) velocity components along this line. From $t = 0$ to about $t = 20$ ms, one observes in Fig. 4.6 (a) a periodic pattern of alternating high and low velocities convected by the mean flow and corresponding to the shedding and convection of the starting vortex described previously. The second pattern observed is the trace of the wake with a velocity defect as expected. Finally, at $t = 18$ ms, a periodic pattern is formed reflecting the convection of vortices in the Karman streets. The same description applies to the velocity component v displayed in Fig. 4.6 (b). The first pattern is now superposed on a zero velocity region where no transverse velocity exists before the flow is established in the cascade. The second pattern in this figure corresponds to the trace of the wake and is characterized by a low velocity region. Beyond $t = 18$ ms, one observes a regular pattern associated with the Karman vortices at a frequency $f = 905$ Hz corresponding to a Strouhal number $\mathrm{St} = f l_b / u_\infty = 0.25$ based on the blade maximum thickness $l_b = 1.1$ mm and the inlet velocity $u_\infty = 4$ m s^{-1}.

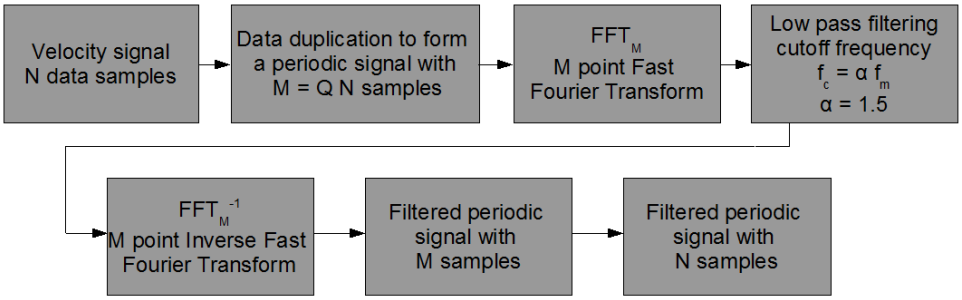

Figure 4.7: Block-diagram detailing the filtering procedure of velocity signals.

4.3.1 Data analysis for modulated cases

The analysis is now carried out both for low and high amplitudes of modulation. The objective is to investigate signal amplitudes and acoustic or convective modes. Some data processing is needed to extract the periodic signals corresponding to the perturbed motion from the complete velocity signal. This can be done by noting that the modulation frequency is well separated from the natural vortex shedding frequency. One may then extract the required information by filtering out the velocity data. The procedure is detailed in the block-diagram in Fig. 4.7 and consists in applying a FFT algorithm to the perturbed velocity fields u' and v'. The signal comprising N samples corresponding to three periods is first duplicated Q times to form a longer sequence of M = Q N samples. This sequence is then used to get the Fourier transform with a Fast Fourier Transform (FFT) algorithm. The duplication operation applied to the data is used to artificially increase the spectral resolution. The elementary filter size Δf is reduced by a factor $1/Q$. Spectral components corresponding to frequencies exceeding a cut-off value $f_c = \alpha f_m$, f_m being the modulation frequency ($\alpha = 1.5$), are then eliminated. This procedure filters out high frequency components corresponding to vortex shedding in the airfoil wakes. An inverse FFT is then applied to the result. This process corresponds to a rectangular window in the frequency domain. The transition band is sharp but the rejection level is moderate. However, by suitably choosing α one can essentially eliminate the signals associated with vortex shedding yielding the low pass filtered velocity disturbances. One can then investigate the evolution of the phase shift between both perturbed velocity signals u' and v'.

This is obtained by calculating the cross power spectral densities of the filtered velocity signals at discrete points separated by regular intervals of 5 mm along a line perpendicular to the cascade. The phase difference between the signals is deduced from the complex value of the cross power spectral density calculated at the driving frequency f_m. The reference used to establish this phase evolution is the axial velocity signal u' measured at the cascade trailing edge located at $x =$

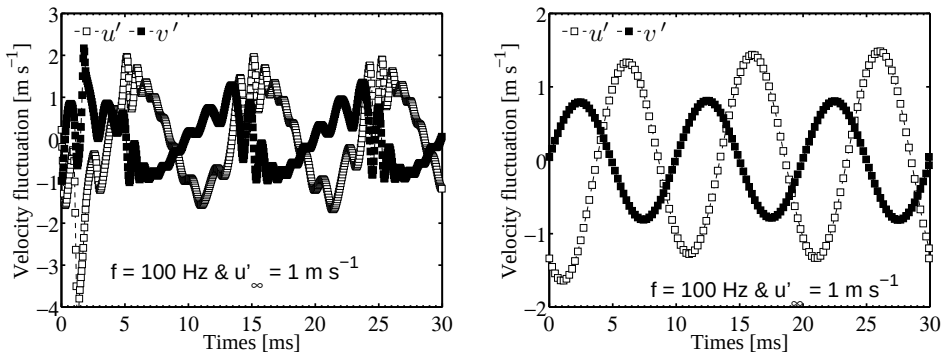

(a) (b)

Figure 4.8: Amplitudes of perturbed velocity signals extracted at a distance of one chord from the cascade back end in the computational domain. Data are obtained for an inlet velocity modulation $u'_\infty = 0.1$ m s^{-1} with $f = 100$ Hz. (a) : raw signal. (b) : after low pass filtering.

0 mm.

The starting point of the acoustically modulated cases is a mean flow consisting of the flow over an airfoil with a well established Karman vortex street. The flow is unsteady and laminar. After an initial transient of about one period, it is well established and periodic as can be checked by recording signals at various points in the domain. The first period in the numerical simulation is not taken into account in the analysis because the flow is transient. After this initial period results can be analyzed. The mean flow can then be obtained by summing over time to eliminate oscillations associated with vortex shedding from the blade trailing edges.

Typical axial and azimuthal velocity signals are displayed in Fig. 4.8. These signals feature a high frequency component corresponding to the periodic fluctuation associated with alternating vortices in the wakes and a low frequency component induced by the flow modulation. This last component is extracted by the low pass filtering method described in Fig. 4.7.

4.3.2 Low amplitude modulation

Two frequencies of modulation are investigated $f = 60$ Hz and $f = 100$ Hz at a low forcing amplitude. This is used to validate the theoretical model derived in the linear approximation. The amplitude of the signals and the phase relation between axial and transverse velocity perturbations are specifically considered.

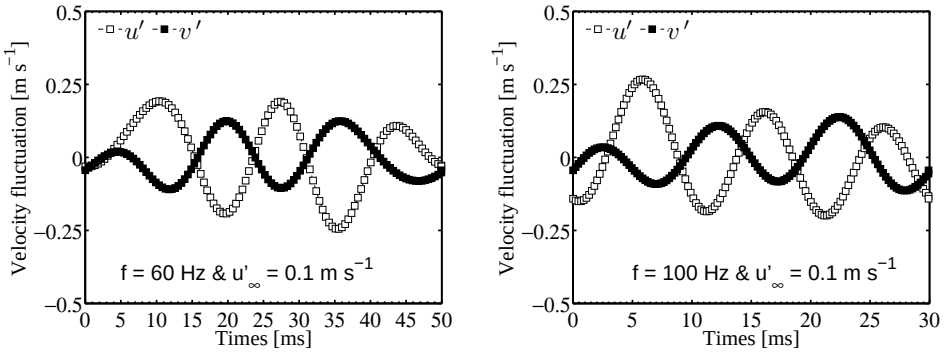

Figure 4.9: Filtered amplitudes of perturbed velocity signals extracted at a distance of one chord from the cascade back end in the computational domain. Data are obtained for an inlet velocity modulation $u'_\infty = 0.1$ m s^{-1}. (a) : $f = 60$ Hz. (b) : $f = 100$ Hz.

Signal amplitudes Figure 4.9 displays amplitudes of velocity perturbations u' and v' at a distance of one chord from the cascade back plane. Subfigures (a) and (b) respectively correspond to modulations at $f = 60$ Hz and $f = 100$ Hz. In both cases the amplitude of the relative transverse velocity fluctuation v' is slightly lower than the relative axial velocity disturbance u'. This is close to what was predicted analytically. One also finds that the amplitudes of the two signals vary as a function of time indicating that a certain amount of reflection takes place at the computational domain outlet.

Acoustic and convective mode The analysis of vorticity fields is carried out by examining Fig. 4.10 presented for $f = 100$ Hz and for two phases in the cycle 0° and 180°. Over one cycle of modulation, one finds that fully developed Karman vortices streets are established in the airfoil wakes. The global behavior is identical for each phase of the cycle : the thickness of the boundary layers around the airfoil remains almost constant with very small variations, the frequency of vortex-shedding is also constant. It is difficult to identify a periodic pattern corresponding to the imposed modulation frequency $f = 100$ Hz for an input level equal to $u'_\infty = 0.1$ m s^{-1}. These results indicate that with a low input level, it is not possible to detect the vortical mode associated to the modulation frequency because the amplitude of this mode is too low compared to the amplitude of the high frequency Karman vortices formed in the blade row wakes.

Results of the data filtering are plotted in Fig. 4.11 for two modulation frequencies $f = 60$ Hz and $f = 100$ Hz and for a small perturbation level $u'_\infty = 0.1$ m s^{-1}. The figure gathers the phases determined with signals extracted from numerical simulations at 60 Hz and 100 Hz respectively in (a) and (b). It serves to identify

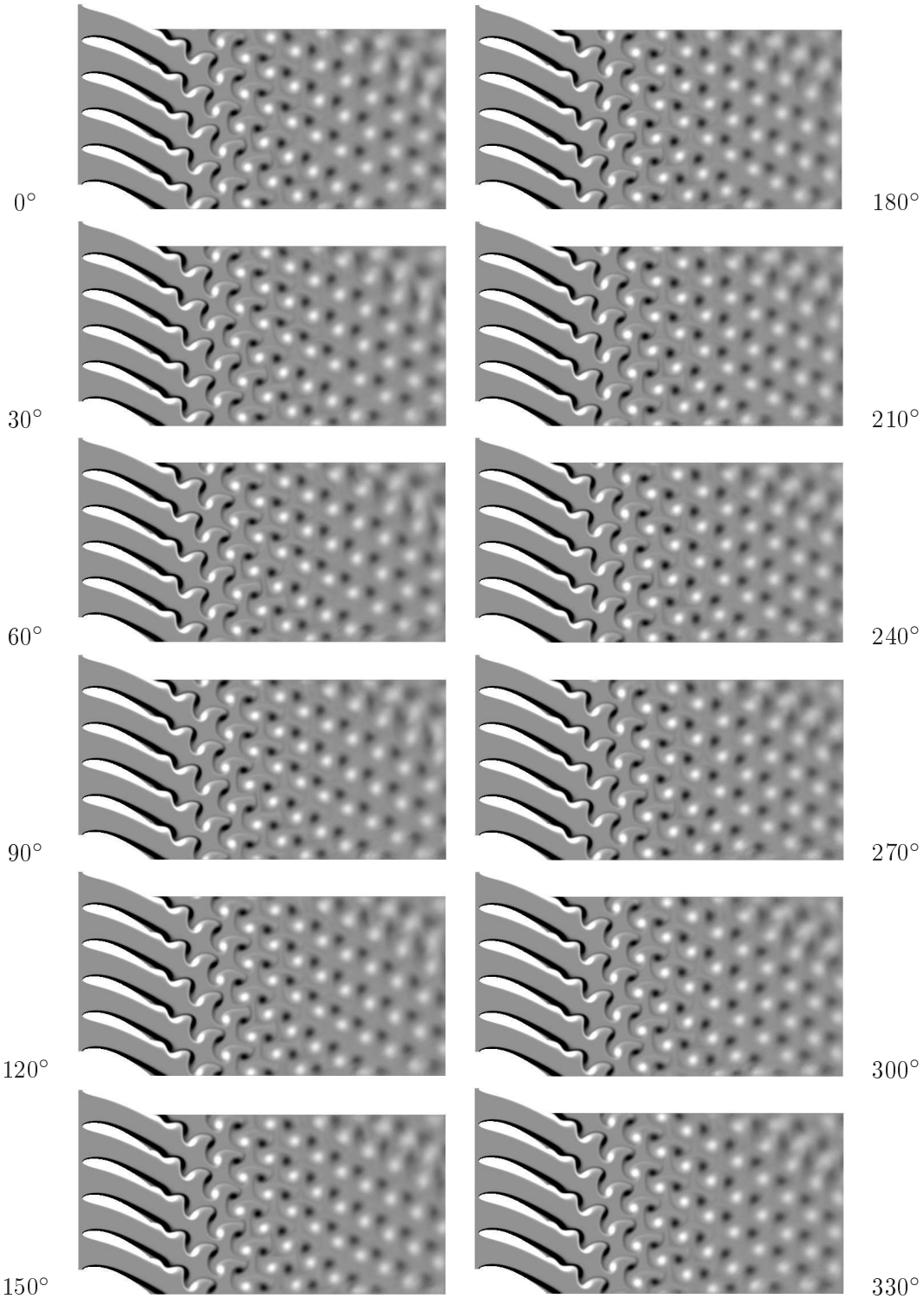

Figure 4.10: Vorticity fields of the flow with an acoustic modulation of amplitude u'_∞ = 0.1 m s^{-1} at the inlet and for a frequency f = 100 Hz. The maximum level of vorticity 5000 s^{-1} is in black while the minimum level -5000 s^{-1} is in white.

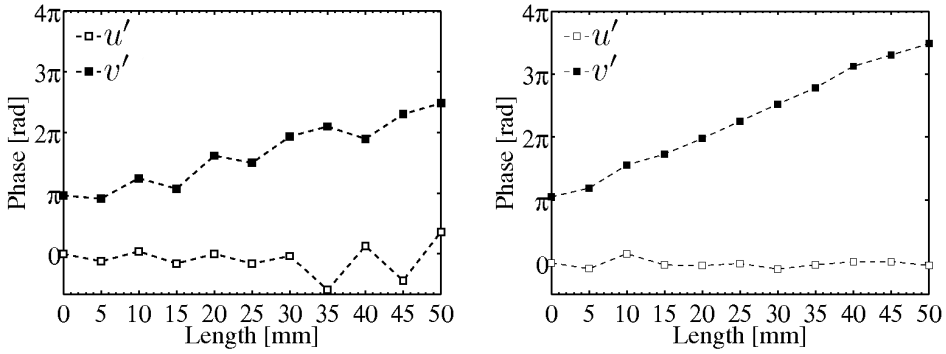

Figure 4.11: Evolution of the phase shift between relative fluctuations of velocity u' and v' in the linear regime. Data are extracted from numerical simulations for a modulation amplitude equal to $u'_\infty = 0.1$ m s^{-1}. (a) : $f = 60$ Hz. (b) : $f = 100$ Hz.

the two types of waves propagating in the downstream flow. The axial velocity disturbance has an essentially constant phase and it is acoustic. The phase shift is negligible because this wave propagates on a small distance at the speed of sound. One can also say that the phase shift is small because the distance is a small fraction of the wavelength. The transverse disturbance is convective as the phase shift increases linearly with distance and frequency and is inversely proportional to the mean axial flow velocity : $\Delta\varphi = 2\pi f x/\overline{u}$.

The transverse perturbations v' are out of phase with axial velocity fluctuations u' at the trailing edge location as expected from linear theory $v'_2 = \tan\overline{\theta}_2 u'_2$ (here $\tan\overline{\theta}_2$ is negative). Results obtained at $f = 60$ Hz feature some spurious oscillations which are less visible at $f = 100$ Hz. This may be attributed to the filtering procedure which does not fully eliminate the high frequency components. As the relative forcing amplitude is weak ($u'_\infty/u_\infty = 0.025$), the perturbation signal is low and it is affected by residual high frequency fluctuations. Oscillations are more visible on the acoustic velocity component near the computational domain outlet where some reflections have already been mentioned. These differences do not however scramble the general trend. It will be seen below that results can significantly be improved by increasing the modulation level.

4.3.3 High amplitude modulation

We now examine the dynamics of the modulated flow induced by an intense acoustic wave with an amplitude $u'_\infty = 1$ m s^{-1} at the inlet of the domain. This case is explored for the same modulation frequencies $f = 60$ Hz and $f = 100$ Hz. Amplitudes of velocity components u' and v' are investigated and the acoustic to

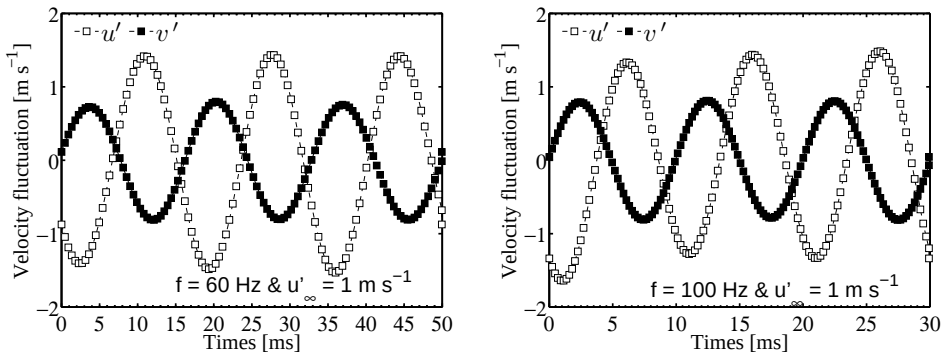

Figure 4.12: Filtered velocity signals extracted from the simulations at one chord length downstream of the airfoil trailing edge ($x = 0$ mm) for an inlet velocity modulation $u'_\infty = 1$ m s^{-1}. (a) : $f = 60$ Hz. (b) : $f = 100$ Hz.

convective mode conversion mechanism is highlighted with space-time diagrams.

Signal amplitudes The amplitude of velocity signals in the downstream flow are extracted from the numerical fields of u and v. The mean velocity is subtracted to get the fluctuations u' and v'. The low pass filtering procedure described previously is used to separate the periodic coherent motion due to the modulation. This process is first applied at a point located at a distance of one chord from the cascade back plane. Signals are plotted in Fig. 4.12 for the two modulation frequencies. One finds that the ratio of amplitudes $|v'|/|u'|$ is close to 0.5 for both frequencies. This is in agreement with analytical predictions obtained in section 2 which give a value $|v'|/|u'| = |\tan\overline{\theta}_2| = 0.47$ for a trailing edge angle $\theta_2 = 25°$.

It is also found that the fluctuation amplitude $u' \simeq 1.2$ m s^{-1} is greater than that of the incident wave amplitude $u'_\infty = 1$ m s^{-1}. This is because the axial flow is accelerated due to the presence of the wakes in which the axial velocity is reduced.

Acoustic and convective modes The dynamics of the flow field is now investigated by examining the vorticity fields over one cycle of excitation shown in Fig. 4.13. The first phase at 0° shows the classical vortex-shedding beyond the airfoil followed by an intense vortex pairs. These two vortices are then convected by the mean flow. At 60°, a new vortex pair is formed at the trailing edge of each airfoil. This induces an increase of the boundary layer thickness on the suction side near the trailing edge. At 180°, this pair is shed and convected by

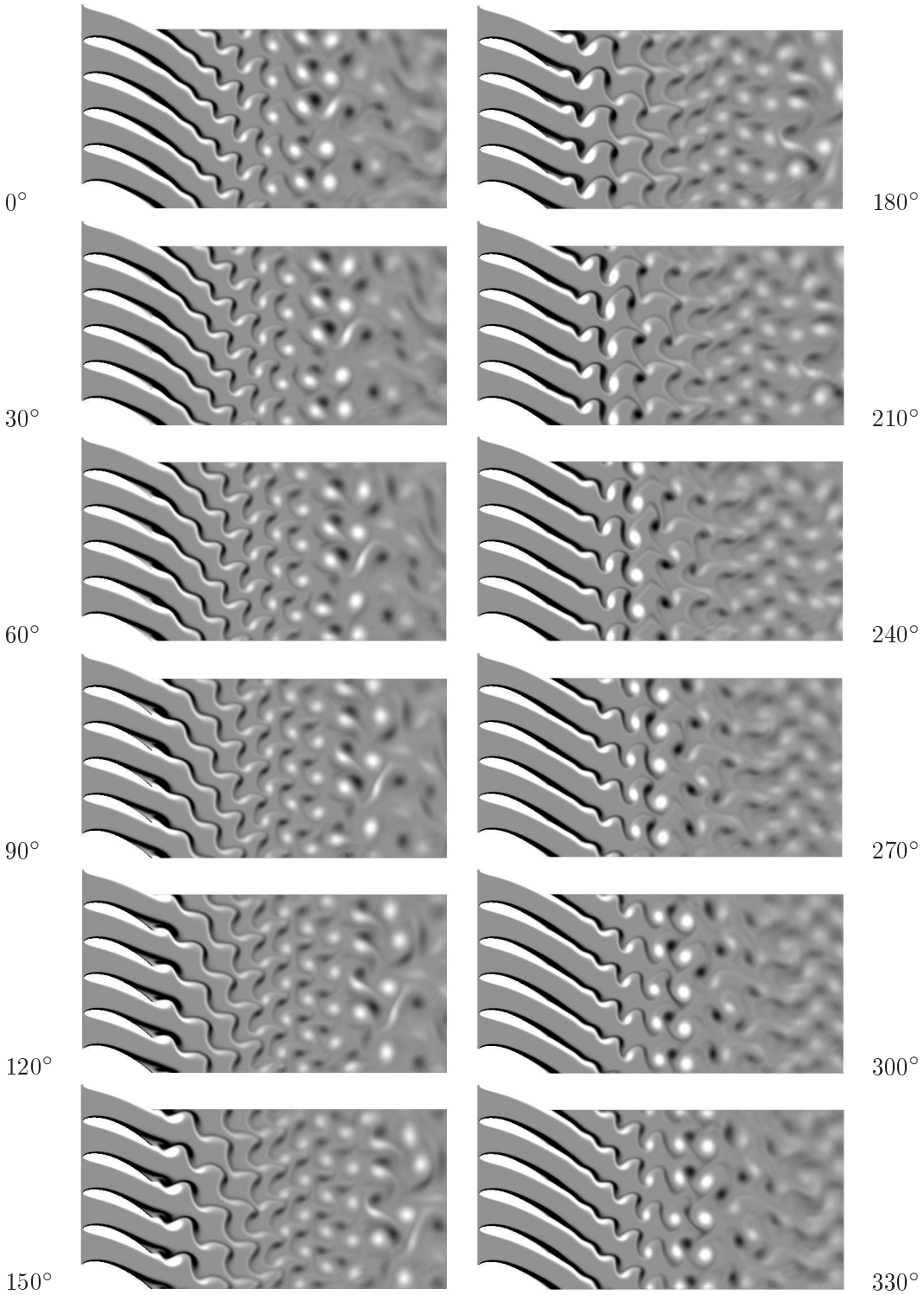

Figure 4.13: Vorticity fields of the flow with an acoustic modulation of amplitude u'_∞ = 1 m s^{-1} at the inlet and for a frequency f = 100 Hz. The maximum level of vorticity 5000 s^{-1} is in black while the minimum level -5000 s^{-1} is in white.

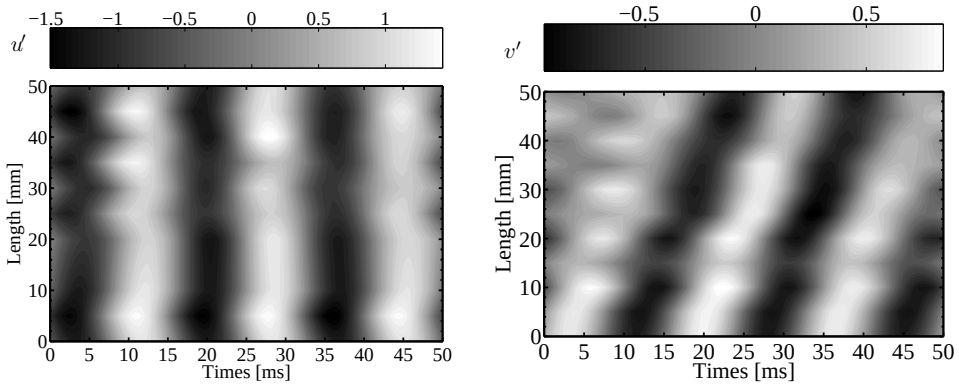

(a) (b)

Figure 4.14: Space-time diagrams of fluctuating velocity components beyond the airfoils cascade for a modulation frequency $f = 60$ Hz and an amplitude equal to $u'_\infty = 1$ m s^{-1}. Theses diagrams are obtained by filtering raw velocity signals extracted from numerical simulations along a straight line downstream the cascade and each 5 mm over three time periods. (a) : axial fluctuation u'. (b) : transverse fluctuation v'.

the mean flow. In the remaining part of the cycle, the classical high frequency vortex shedding also present in the non modulated case prevails.

One can now investigate the flow dynamics with space-time diagrams. It is again necessary to filter out velocity components corresponding to the vortices formed in the airfoil wakes. This is accomplished by applying the method described previously. Because the frequency associated to the Karman vortices is much larger than the modulation frequency, the corresponding velocity components can be filtered out. It is then possible to extract the coherent motion corresponding to the modulation frequency. Space-time diagrams are obtained for three time periods for both frequencies such that the total time observed is 50 ms at $f = 60$ Hz and 30 ms at $f = 100$ Hz.

For the modulation frequency $f = 60$ Hz, the space-time diagram is shown in Fig. 4.14. The axial velocity fluctuation u' is plotted in Fig. 4.14(a) while the transverse fluctuation velocity v' is displayed in Fig. 4.14(b). For the axial velocity, one finds a pattern of alternating black and white vertical stripes. This means that the propagation of axial velocity perturbations is nearly instantaneous indicating that propagation takes place at the speed of sound. For the transverse velocity component the white and dark stripes are inclined indicating that this component is convected by the flow. It it interesting to extract the convective velocity u_{cv} which can be deduced by estimating the slope of the stripes $a = \Delta l/\Delta t \simeq 3.7$m s^{-1}. This value is close to the flow velocity $u_\infty = 4$ m s^{-1} imposed at the numerical domain inlet. These space-time diagrams confirm that

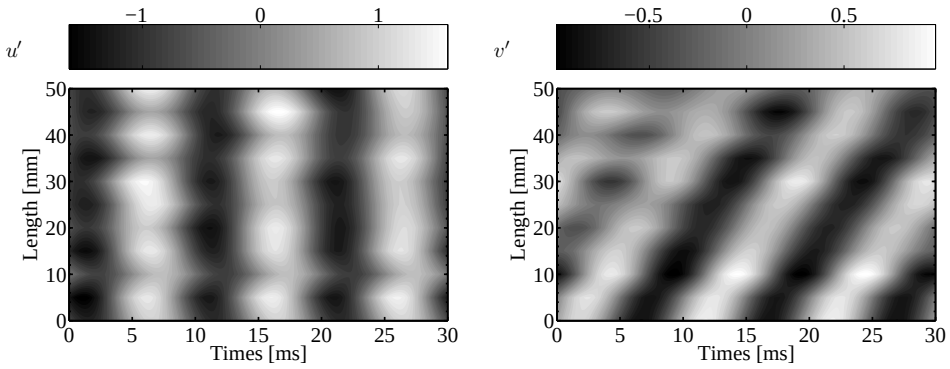

(a) (b)

Figure 4.15: Space-time diagrams of fluctuating velocity components on the downstream side of the cascade for a modulation frequency $f = 100$ Hz and an amplitude equal to $u'_\infty = 1$ m s^{-1}. Theses diagrams are obtained by filtering raw velocity signals extracted from numerical simulations on a straight line downstream the cascade and each 5 mm over three time periods. (a) : axial fluctuation u'. (b) : transverse fluctuation v'.

axial and transverse velocity perturbations respectively propagate at the speed of sound and at a convective velocity as predicted by the analytical model derived in Section 2.

A similar analysis can be carried out for a modulation frequency $f = 100$ Hz. The corresponding space-time diagrams given in Fig. 4.15 are quite similar to those examined previously. Note that the time scale in Fig. 4.14 and Fig. 4.15 is slightly different. One can also determine the convective velocity of transverse velocity perturbations with $a = \Delta l/\Delta t = 4$ m s^{-1} which is again equal to the inlet flow velocity u_∞. The phase shift between the two velocity components is shown in Fig. 7.15. In this case too, the phase evolves in a nearly linear fashion with respect to distance and is essentially proportional to the modulation frequency and inversely proportional to the convection velocity. At the origin, the phase shift is equal to π as expected for a situation where the trailing edge angle $\overline{\theta}_2$ is negative.

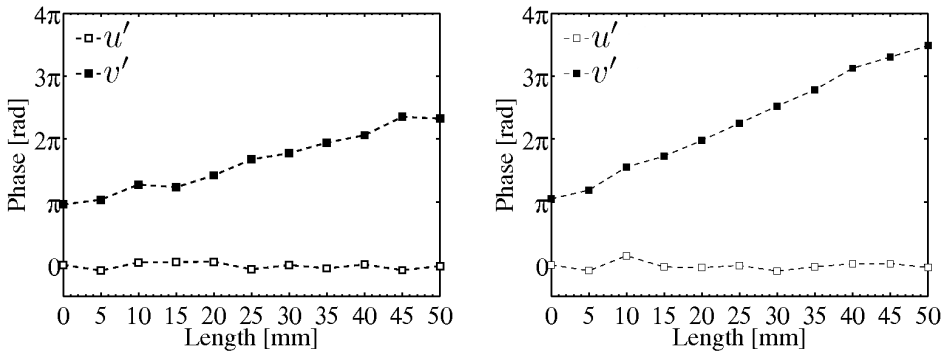

Figure 4.16: Evolution of the phase between axial and transverse velocity perturbations u' and v'. Data are extracted from numerical simulations for a modulation amplitude equal to $u'_\infty = 1$ m s^{-1}. (a) : $f = 60$ Hz. (b) : $f = 100$ Hz.

4.4 Experiments on a ducted swirler

It is now interesting to see if the previous features can be retrieved experimentally. This is accomplished in a cylindrical configuration where the flow is set in rotation by an axial swirler. This choice is made because experiments are easier to perform in an axisymmetric system. Admittedly a cascade experiment might have been more consistent with the numerical simulation. However since we intend to characterize a mechanism the change in configuration is reasonable.

4.4.1 Experimental setup

The experimental setup is sketched in Fig. 4.17. The system comprises three elements : a loudspeaker, a convergent unit and a tube containing a swirler. The flow injected at the base of the convergent unit from two orifices diametrically opposed traverses a honeycomb to break the largest turbulent scales and produce a laminar flat velocity flow profile on the upstream side of the swirler. The gas is convected through the swirler

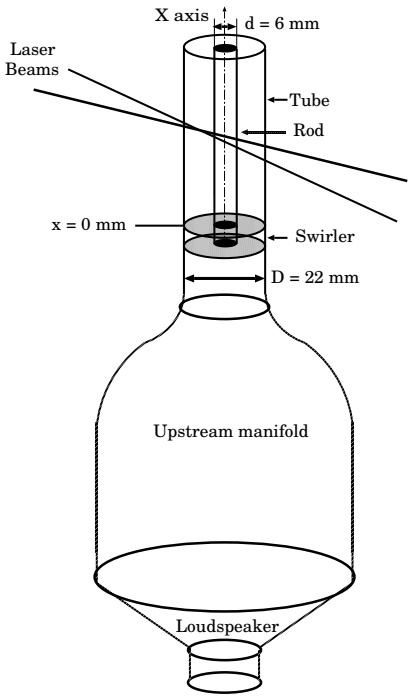

Figure 4.17: Experimental setup used to determine velocity signals behind a swirler. Laser

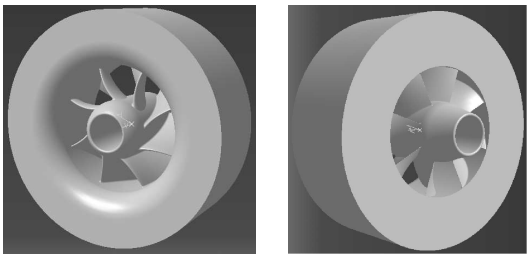

(a) (b)

Figure 4.18: Swirler geometry used in the experiment. (a) upstream side. (b) : downstream side.

which imparts a rotating motion to the flow. The swirling flow obtained in this way evolves in an annular tube made of quartz. A rod is located at the center of the tube in this experiment.

The swirler comprises eight vanes periodically spaced. The blades are formed by NACA 8411 profiles and their stagger angle with respect to the axial direction is 45°. Upstream and downstream views of the swirler are displayed in Fig. 4.18.

A laser Doppler velocimeter is used to measure the velocity signals in the axial and azimuthal directions. The data are recorded at 5 mm intervals on a vertical line located in the middle of the section between the tube and the rod. This set up was also used in experiments on combustion dynamics reported in chapter 2. The bulk velocity in the tube is $U_b = 2.67$ m s^{-1} and the fluctuation level of the axial velocity disturbance was measured downstream the swirler, at a distance of 17 mm from the swirler backplane, and it is equal to $u'_{rms}/U_b = 0.5$.

4.4.2 Results

Results gathered from measurements are plotted in Fig. 4.19 in the form of phase evolutions for the velocity signals $u(x,t)$ and $v(x,t)$ for two modulation frequen-

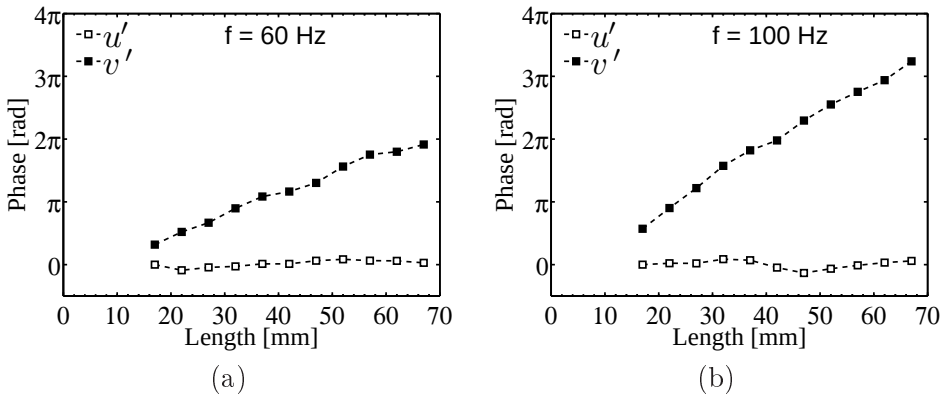

Figure 4.19: Experimental phase shift evolution of axial and azimuthal velocity components u' and v' for two modulation frequencies. Data are recorded from 17 mm to 67 mm due to limitations in optical access downstream of the swirler. The swirler backplane is located at $x = 0$ mm. (a) : $f = 60$ Hz. (b) : $f = 100$ Hz.

cies $f = 60$ Hz and $f = 100$ Hz. One immediately observes that the phase of the axial velocity signal u' is nearly constant when the distance from the swirler increases. This indicates that axial disturbances propagate at a high phase velocity which can only be the speed of sound. An azimuthal component is detected by the laser Doppler velocimeter and this velocity component v' features a phase which varies linearly with distance from the swirler. This reflects the convective character of azimuthal perturbations originating from the swirler blades trailing edges. Using the slope of the phase function it is possible to determine the convection velocity which is found to be $u_{cv} = 3.05$ m s^{-1} for $f = 60$ Hz and $u_{cv} = 3.19$ m s^{-1} for $f = 100$ Hz. These two values are of the order of the bulk velocity in the channel indicating that azimuthal perturbations created at the swirler are essentially transported by the flow. It is also worth noting that the phase difference at the airfoil trailing edges $x = 0$ mm coincides with the theoretical prediction $\Delta\varphi \simeq 0$ by extrapolating the phase curve (black square symbols) to zero.

4.5 Comparison between theory, numerical simulations and experiments

Analytical results, numerical simulations and experiments are now compared in Fig. 4.20. Black symbols correspond to experiments while open markers pertain to numerical predictions. The horizontal axis indicates the distance from the swirler backplane where velocity signals are analyzed to determine the phase shift. Measurements are carried out at points separated by an interval of five millimeters. The evolution of the phase shift between u' and v' is specifically

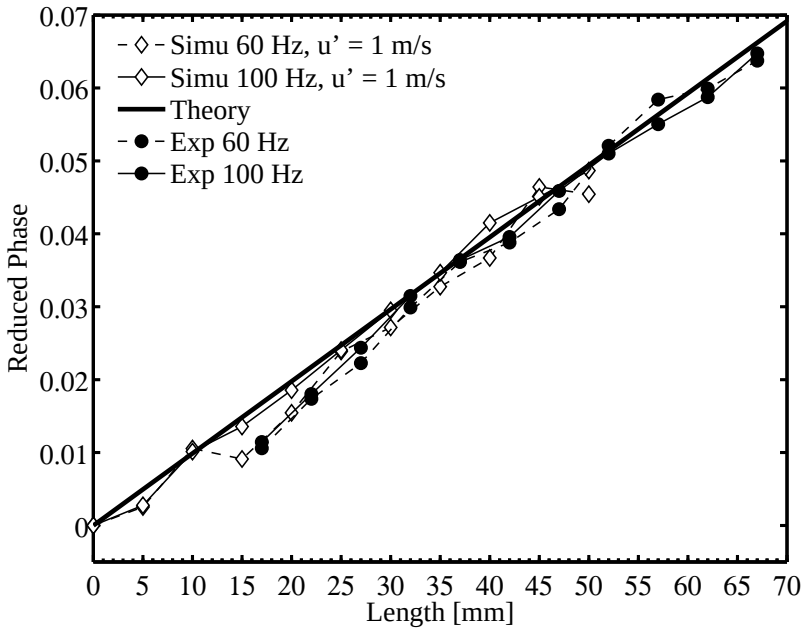

Figure 4.20: Comparison of simulations, theory and experiments with the reduced phase as a function of the length. Results of simulations indicate that the phase shift at the cascade trailing edge plane $\varphi_0 = \pi$ because of the negative value of the blade trailing edge angle. Results of experiments indicate that $\varphi_0 \simeq 0$ at the swirler backplane.

examined. It is interesting to introduce a reduced phase to collapse the experimental data and numerical results and compare with theory. This can be accomplished by multiplying the phase by the convection velocity u_{cv} and dividing by the frequency f :

$$\varphi^* = (\varphi - \varphi_0)\frac{u_{cv}}{2\pi f} \tag{4.32}$$

where φ_0 is the phase between axial and azimuthal velocity signals at the cascade backplane in 2D or at the swirler in 3D and is respectively equal to $\varphi_0 = \pi$ and $\varphi_0 = 0$. The reduced quantity is plotted in Fig. 4.20 as a function of distance from the cascade (simulations) and from the swirler backplane (experiments). One finds that numerical simulations and experimental data closely match theory confirming that the transverse perturbation are well described by the model. Experimental results are in agreement with simulations in that the phase is found to be proportional to frequency and distance and inversely proportional to a convection velocity. The convective velocity is close to the mean flow velocity. Numerical simulations also agree with theoretical predictions of this phase shift. There are however minors differences in the phase determined experimentally which are most probably due to the fact that the swirler blades have a variable angle at the trailing edge. This result can be used to predict the phase of the transverse or azimuthal velocity perturbations with respect to incident acoustic disturbances but this requires an estimate of u_{cv} which can be taken equal to the mean flow velocity.

4.6 Conclusion

The major point of this study is that swirler units used to set a flow in rotation act as mode conversion element. When acoustic waves impinge on a swirler unit they generate an azimuthal velocity perturbation. When the flow is acoustically perturbed, interactions with a swirler or an airfoil cascade generates an azimuthal velocity disturbance (in the swirler case) or a transverse velocity disturbance (in the 2D cascade configuration). The main characteristics of this disturbance are documented in this chapter. Theory, simulation and experiments are used to show that this wave is convected by the flow. The theoretical model based on actuator disk theory provides an estimate of the amplitude of this wave and links its relative level to the relative axial velocity disturbance. It is then demonstrated that this mode conversion process is retrieved from numerical simulations of the flow in a two dimensional cascade and that the azimuthal velocity disturbance is observed in experiments on an axisymmetric configuration. It can be concluded that the conversion process will have a profound effect on the dynamics of the flow downstream of the swirler and that the combination of axial and azimuthal

velocity perturbations will modulate the rate of rotation of the flow. This in turn will affect the downstream flow by changing the rate of rotation of the flow. Now it is known that most practical combustors like those found in jet engines or gas turbines use swirlers to stabilize combustion. The dynamics of the flow will be influenced by the process described in the present chapter. It has been shown in a recent study of swirling flame dynamics that the upstream flow dynamics plays a central role. The present study focuses on this point and documents this fundamental process with a combination of theory, numerical simulation and experimentation.

Chapter 5

Combined dynamics of swirler and turbulent swirling flames

Abstract : *The dynamics of premixed confined swirling flames is investigated by examining their response to incident velocity perturbations. A generalized transfer function designated as the flame describing function (FDF) is determined from 0 to 400 Hz and for a velocity fluctuation level between 0 and 72% of the bulk velocity. The unsteady heat release rate is deduced from the emission intensity of OH^* radicals. This global information is complemented by phase conditioned Abel transformed emission images. By assuming that the light intensity from these images is proportional to the heat release rate, it is possible to deduce the distribution of unsteady heat release rate in $W\,m^{-3}$ and see how it evolves with time during the modulation cycle and for different forcing frequencies. It is found from experiments and demonstrated analytically that a swirler submitted to axial acoustic waves originating from the upstream manifold generates a vorticity wave on its downstream side. The flame is then submitted to a transmitted axial acoustic perturbation which propagates at the speed of sound and to an azimuthal velocity perturbation which is convected at the flow velocity. The net result is that the dynamical response and unsteady heat release are determined by the combined effects of these axial and induced azimuthal velocity perturbations. The former disturbance induces a shedding of vortices from the injector lip which roll-up the flame extremity while the latter effectively perturbs the swirl number which results in an angular oscillation of the flame root. The phase between incident perturbations is controlled by the convective time delay between the swirler and the injector. The constructive or destructive interference between the different perturbations is shown to yield the low and high gains observed for certain frequencies.*

Résumé : *La dynamique de flammes prémélangées swirlées est étudiée en analysant leur réponse aux perturbations de vitesses incidentes. Une fonction de transfert généralisée est déterminée en balayant une gamme de fréquences allant de 0 à 400 Hz et en changeant la fluctuation de vitesse entre 0 et 72 % de la vitesse débitante. Le taux de dégagement de chaleur instationnaire est déduit de l'intensité d' émissions du radical OH^*. Cette information globale est complétée par des transformées d'Abel d'images formées par moyenne synchronisée par la phase. On obtient ainsi la distribution d'émission lumineuse. En supposant que l'intensité lumineuse est proportionnelle au taux de dégagement de chaleur, il est possible de déduire la distribution des taux de dégagement de chaleur instationnaires en $W\ m^{-3}$ et observer l'évolution de la distribution spatiale de cette quantité au cours du cycle de modulation et pour différentes fréquences de forçage. Ces données peuvent être utiles pour la détermination des régimes d'instabilité mais aussi donnent des indications sur les mécanismes qui contrôlent la dynamique des flammes swirlées. Il est montré expérimentalement et analytiquement que le swirler soumis à des ondes acoustiques provenant de l'amont génère une onde tourbillonnaire en aval. La flamme est donc soumise à une perturbation acoustique axiale transmise au travers de la vrille qui se propage à la vitesse du son et à une perturbation de vitesse azimutale qui est convectée par l'écoulement. Il en résulte que la réponse de la flamme est déterminée par les effets combinés de ces perturbations de vitesse axiale et azimutale. Les perturbations axiales provoquent l'enroulement d'un tourbillon à l'extrémité de flamme tandis que les perturbations de vitesses azimutales génèrent une oscillation angulaire de la base de la flamme. La phase entre les perturbations incidentes est contrôlée par le délai de convection des perturbations entre la sortie du swirler et la base de la flamme. L'interférence constructive ou destructive entre les différentes perturbations provoque respectivement des forts ou faibles gains dans la réponse de la flamme. On peut ainsi expliquer les caractéristiques principales de la fonction de transfert des flammes swirlées.*

5.1 Introduction

Reduction of NO_x emissions while keeping other pollutants like CO at a low level has given rise to difficult challenges. Much of the effort in the gas turbine industry has focused on advanced combustion systems in which reactants are injected in premixed form at a relatively lean equivalence ratio. This lean premixed mode (LPM) of operation has many advantages but raises combustion dynamics problems. Lean premixed flames are sensitive to flow perturbations and premixed

operation near the lean blowout limit can lead to oscillations, flashback or extinction Plee and Mellor (1978); Culick (2001); Candel (2002); Lieuwen and Yang (2005).

In most practical LPM combustors the flame is stabilized by a swirling injector. Combustion is established around a hot kernel formed by the swirling flow. The gas rotation induces a lower pressure zone in the central region generating an internal recirculation of burnt gases anchoring the flame. When the rate of swirl exceeds a threshold the inner recirculation zone (IRZ) becomes hydrodynamically unstable and its development is intimately associated with a vortex breakdown process Lilley (1977); Syred (2006); Huang and Yang (2009). The intensity and shape of the IRZ mainly depend on the rate of rotation induced by swirl and on the combustor geometry. The rate of rotation is characterized by the swirl number S (see for example Gupta *et al.* (1984)) defined as the ratio of the tangential to axial momentum flux :

$$S = \frac{\int_0^R \rho\, u\, v\, 2\,\pi\, r^2\, dr}{R \int_0^R \rho\, u^2\, 2\,\pi\, r\, dr} \tag{5.1}$$

where ρ is the fluid density, u the axial, v the azimuthal velocity components, r the radius and R a characteristic outer radius. In this expression, the pressure term in the axial momentum flux has been neglected. It is known that the inner recirculation zone is well defined for swirl numbers exceeding 0.6. In typical industrial combustors, the swirl number is generally chosen close to this value. A second stabilization mechanism is linked to an outer recirculation zone (ORZ) Lilley (1977); Syred (2006); Thumuluru *et al.* (2007) which is formed by recirculation of hot gases trapped between the flame, the combustor walls and the combustor backplane.

The swirling flow configuration used in LPM combustors in combination with the highly resonant flame tube geometry employed in these systems gives rise to various kinds of combustion instabilities, a problem which has received considerable attention and is investigated in a large number of articles and papers Broda *et al.* (1998); Lee *et al.* (2000); Lawn (2000); Fritsche *et al.* (2007); Meier *et al.* (2007); Kang *et al.* (2007); Schuermans *et al.* (2009). A comprehensive review of many issues is due to Huang and Yang Huang and Yang (2009). The source of instability is the resonant coupling between unsteady fluctuations of heat release rate and the pressure oscillation in the chamber. This coupling is however indirect and one important element is the sensitivity and dynamical response of swirling flames to incoming disturbances. This central aspect is envisaged in the present article which specifically focuses on the dynamical response of the flame to incoming acoustic perturbations. Our objectives are (1) to provide systematic measurements of the flame describing function (a transfer function depending on

frequency and amplitude of incident perturbations), (2) obtain spatial distributions of heat release perturbations during the cycle of oscillation and (3) explain the observed response of the flame to incident perturbations. It is shown that the flame dynamics cannot be understood without considering the response of the swirler to incoming acoustic perturbations and it is demonstrated analytically and experimentally that the swirler generates a vorticity wave which is manifested in azimuthal velocity perturbations having the same order of magnitude as the incoming acoustic disturbances. The flame is then submitted to a combination of axial and azimuthal disturbances which in turn induce different motions and heat release perturbations. It is shown that these elements can be used to explain the observed dynamical response.

At this point, it is worth examining the existing literature and reviewing what is already available on the previous aspects. It is first important to remember that perturbations of various types need to be considered. One class is formed by velocity fluctuations which accompany pressure oscillations Poinsot *et al.* (1987); Yu *et al.* (1991); Paschereit *et al.* (2000). Another type of perturbation consists in equivalence ratio disturbances, which can be created by the differential response of fuel and air injectors to pressure waves generated by unstable combustion Keller (1995); Lieuwen and Zinn (1998); Sengissen *et al.* (2007).

In general, flame dynamics issues can be treated by examining the flame response to well controlled externally imposed disturbances. This aspect is already covered by some articles which consider the dynamics of swirling flames experimentally Bellows *et al.* (2007); Bellows *et al.* (2007); Weigand *et al.* (2006); Külsheimer and Büchner (2002); Kim *et al.* (2010) or numerically through RANS Mongia (2004); Armitage *et al.* (2006) or through the more advanced LES approach Roux *et al.* (2005); Grinstein and Fureby (2005); Huang and Yang (2005); Freitag and Janicka (2007). Simulations are now widely used to optimize the steady state performance of swirling injectors but the validation of unsteady numerical calculations in well controlled configurations is still a research issue. Some of the previous studies show that it is essential to take into account the frequency dependence and the nonlinearities associated with the flame and combustor responses. Experimental work indicates that the IRZ is a sensitive region and that its intensity and location can be influenced by incoming perturbations Thumuluru *et al.* (2007); Bellows *et al.* (2007); Bellows *et al.* (2007). Previous studies also indicate that the dynamics of swirling flames are linked to vortex roll-up processes taking place in the injection region and involving the flame tip Huang and Yang (2009); Kang *et al.* (2007); Bellows *et al.* (2007); Külsheimer and Büchner (2002). This phenomenon is similar to the roll-up motion observed at the tip of laminar and turbulent "V" flames Durox *et al.* (2005); Balachandran *et al.* (2005). Vortices are shed from the injector nozzle lip in response to the flow pulsations and roll-up the flame edge resulting in large heat release rate fluctuations. When the flow is rotating, one direct effect of the swirl number is to

change the flame spreading angle modifying the distance between the nozzle and the flame front. In an unconfined flame study Külsheimer and Büchner (2002) it is concluded that at large swirl numbers (0.79) the flame is more susceptible to instabilities, and that its response can amplify the perturbation. When the flame is unconfined only the IRZ stabilizes the combustion because ambient air is entrained and it is difficult to extend the results obtained to confined cases where the ORZ is also present. In a confined swirled burner submitted to velocity modulations with mixtures kept at a fixed equivalence ratio, Kim *et al.* Kim *et al.* (2010) have shown that the flame length is reduced as the modulation frequency increases. In the linear regime and for a fixed perturbation level, they were able to reduce their data obtained for flame transfer functions at different lean operating conditions into a single curve using a Strouhal number based on the relative length scales ratio of the flame length to the convective length scale of inlet velocity fluctuation. As the magnitude of the inlet velocity fluctuation increases a saturation appears, due to nonlinear effects, and the gain of the flame transfer functions decreases. The amplitude of the perturbation where this saturation arises, depends on the frequency. In this case, saturation appears faster when the frequency is lower but the phase remains almost unaffected for relative perturbation levels lower than 0.2. Other authors Thumuluru *et al.* (2007); Bellows *et al.* (2007) also evoke the nonlinear behaviour of swirling flames submitted to increasing levels of mass flow fluctuations. It is shown that the unsteady shape of the flame is a strong function of the mass flow rate fluctuation level as also observed for non swirling flames Balachandran *et al.* (2005); Durox *et al.* (2009). The main conclusions are that the flame response saturates when the mass flow rate fluctuation is augmented, and that it is not easy to determine a time delay between flow rate fluctuations and resulting perturbations in heat release rate. Furthermore, flame transfer functions are often not complete or limited to linear perturbations Borghesi *et al.* (2009), with the exception of references Thumuluru *et al.* (2007); Kim *et al.* (2010); Bellows *et al.* (2003). But theses results are limited and it is necessary to collect more data to understand the dynamics of swirling flames.

Some previous investigations have concerned the influence of the swirler design on flame transfer functions (see for example Gentemann *et al.* (2004); Hirsch *et al.* (2005)). It is found that the transfer functions of radial and axial swirlers feature the same behaviour at moderate and high frequency but slight differences are observed in the low frequency range.

A number of articles Thumuluru *et al.* (2007); Bellows *et al.* (2007); Külsheimer and Büchner (2002); Kim *et al.* (2010); Kim *et al.* (2009) deal with the effect of flow modulations on the dynamics of confined swirling flames and provide some of the data needed to predict thermo-acoustic instabilities and limit cycles in combustion chambers. In Kim *et al.* (2009), the laboratory-scale gas turbine

combustor used to measure flame transfer functions and predict instability frequencies is mainly used in the linear regime. Flame transfer functions measured with this type of burner indicate that the Strouhal number constitutes a relevant dimensionless parameter Kim *et al.* (2010). The present article tries to fill the need for a nonlinear description of the flame dynamics by making use of transfer functions for increasing perturbation levels up to amplitudes approaching reverse flow conditions. Another aspect which is not well understood is how flow perturbations created at the swirler outlet modify the flame dynamics. This issue is discussed in a few recent studies Huang and Yang (2009); Stone and Menon (2002); Wang and Yang (2005); Komarek and Polifke (2010). It is concluded from LES calculations Huang and Yang (2009); Wang and Yang (2005) and indirectly from transfer function measurements by Komareck and Polifke Komarek and Polifke (2010) that on the downstream side of the swirler the perturbation comprises an acoustic and a convective component. While the presence of this convective component is recognized Huang and Yang (2009); Wang and Yang (2005); Komarek and Polifke (2010) there are no direct measurements of the axial and azimuthal velocity components which support this conclusion and no theoretical attempt is made to obtain an estimate of the respective levels of perturbation. The impact of the acoustic and convective perturbations on the flame dynamics is also not fully discussed. It is known that modulated flames can be influenced by interferences between different types of perturbations propagating at different velocities Schuller *et al.* (2003b); Preetham *et al.* (2008); Shanbhogue *et al.* (2009). The present paper emphasizes the combined effects of the swirler and flame.

The chapter is organized to deal with the previous issues. The flame response to axial velocity modulations is described in section 5.2. Transfer functions are measured for different levels of incoming perturbations. This family of transfer functions forms a "flame describing function" (FDF) which depends on frequency and amplitude of the incident disturbances. Two sets of results corresponding to different mass flow rates are reported. Flame describing functions are determined using two methods by measuring axial velocity fluctuations on the two sides of the swirler. This global analysis of the flame response is completed in section 5.3 by a detailed examination of phase conditioned images of the flame patterns during the modulation cycle. Distributions of heat release are obtained by taking the Abel transform of phase conditioned emission data. These images provide a slice through the flame and determine the evolution of the reaction region as a function of time. Space-time diagrams of heat release rate fluctuations are then used to understand the global response of the flames at different forcing frequencies. Section 5.4 discusses physical mechanisms driving the observed response. This requires a detailed examination of the perturbations on the downstream side of the swirler. This analysis is then used in section 5.5 to interpret the signals observed for two characteristic frequencies of the flame describing function cor-

responding to low and high gains.

5.2 Flame Describing Functions

It has been shown recently by Noiray *et al.* (2008), that the Flame Describing Function gives access to nonlinear features of combustion dynamics. The FDF is determined for a range of frequencies and for different levels of incoming velocity perturbations. It can be defined by :

$$\mathcal{F}(\omega, u') = \frac{\dot{Q}'/\overline{\dot{Q}}}{u'/\overline{u}} \tag{5.2}$$

The heat release rate is generally estimated by recording the global emission signals of excited radicals like CH* or OH* using a photomultiplier detecting the whole light radiated by the flame. In the present study, the heat release rate is deduced from OH* emission and the axial velocity disturbance is measured with a LDV system or a hot wire. One can then write this flame describing function as a function of the OH* chemiluminescence signal :

$$\mathcal{F}(\omega, u') = \frac{\dot{Q}'/\overline{\dot{Q}}}{u'/\overline{u}} \simeq \frac{I'_{\mathrm{OH}^*}/\overline{I}_{\mathrm{OH}^*}}{u'/\overline{u}} \tag{5.3}$$

This FDF can be expressed as a complex number in terms of a gain G and a phase difference Φ which depend on the frequency and the incoming perturbation level. The classical flame transfer function (FTF) then corresponds to the flame describing function (FDF) obtained for a fixed perturbation level :

$$\mathcal{F}(\omega, u') = G(\omega, u')\, e^{i\Phi(\omega, u')} \tag{5.4}$$

The gain G reflects the level of response while the phase Φ defines the time delay between velocity and emission signals.

The FDF is here determined in two ways which differ by the location where axial velocity disturbances u' are measured. In the first case, this velocity component is obtained by laser Doppler velocimetry at $x = 2.9$ mm above the backplane of the confinement tube and at a radial distance $r = 8$ mm from the axis. This defines a small measurement volume on the downstream side of the swirler in the turbulent swirling flow, close to the reaction region. In the second case, the axial velocity fluctuation is measured with a hot wire set in a small cylindrical piece (20 mm in height) placed on the upstream side of the swirler. The calibration of this device is made by using a premixture at an equivalence ratio $\phi = 0.7$.

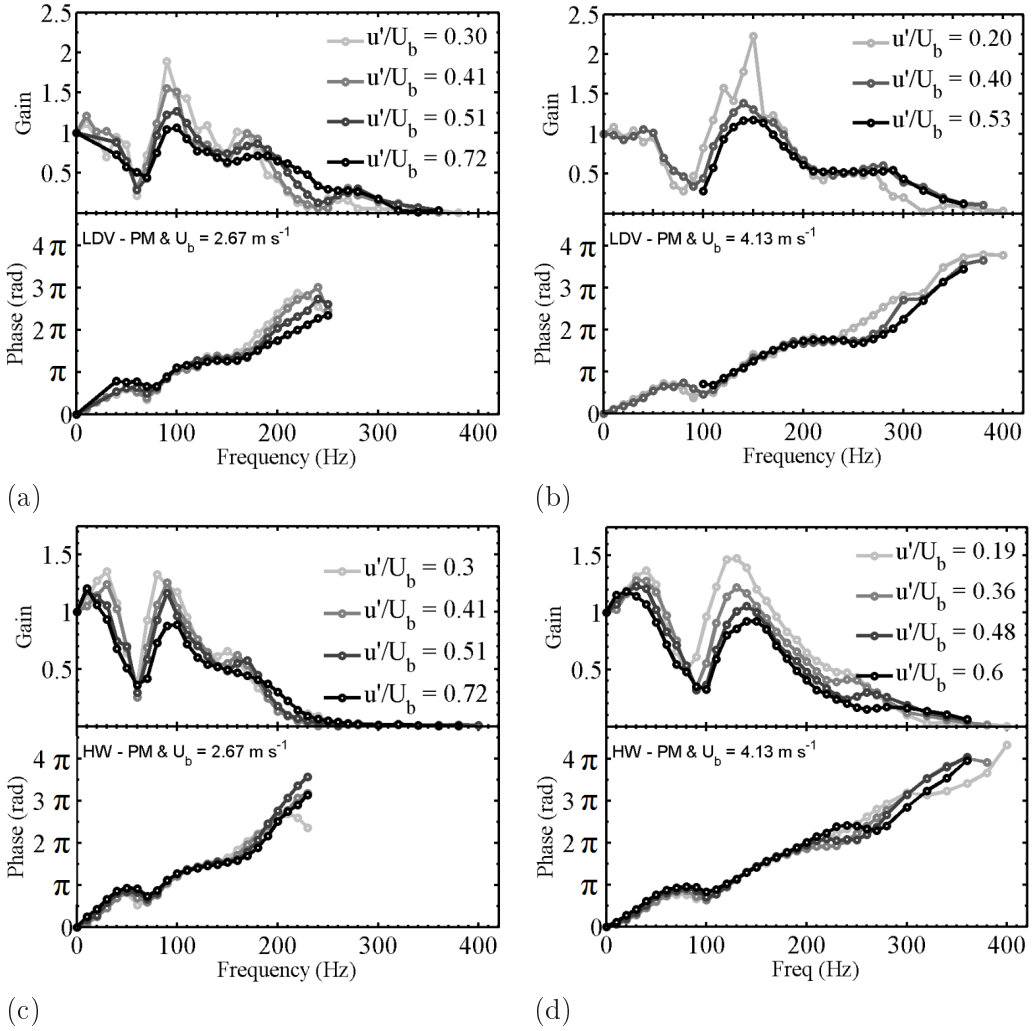

Figure 5.1: Flame describing function based on LDV measurement for flame A (a) and flame B (b). Flame describing function based on hot wire anemometry for flame A (c) and flame B (d).

The flame response is determined first by using velocity measured with the laser Doppler velocimeter (LDV). The FDF obtained for case A presented in Fig. 5.1 (a) pertains to a flow with a bulk velocity $U_b = 2.67$ m s^{-1} over a frequency range extending from 0 to 400 Hz and to four velocity modulation levels $u'/U_b = 0.3$, 0.41, 0.51 and 0.72 where u' corresponds to the rms perturbation level determined at $x = 2.9$ mm from the injector outlet and at $r = 8$ mm from the axis. The gain approaches one in the low frequency limit. It decreases in a first range between 0 and 60 Hz to a value of less than 0.5. From 60 to 100 Hz, each curve features a peak. For all velocity disturbance levels, this peak is the maximum in the frequency range of interest. At 100 Hz, the flame response is highest. Beyond

100 Hz and until 150 Hz, the gain drops again and reaches a value of 0.75 for most of the transfer function curves. From 150 Hz to 180 Hz, the gain increases but reaches a local maximum of about 1 (for the smallest modulation level) and 0.75 (for the highest modulation level). Beyond 180 Hz the gain decreases in all cases and reaches a value which falls below 0.25. An increase of the level of the perturbation generates a decrease of the gain, especially in the range 60 Hz - 180 Hz. The phase, Fig. 5.1 (a), increases nearly continuously with frequency from 0 to 250 Hz. Beyond 250 Hz, the phase is less smooth due to the low value of the gain in that frequency range. Under these conditions phase estimates become less reliable. The phase signal can be used to determine a global delay of the dynamical interaction between the incoming velocity modulation and the resulting heat release rate perturbation. If the phase varies in an approximately linear way with respect to frequency, it is possible to write $\Phi = \omega\tau_{cv}$ where $\omega = 2\pi f$ and determine the delay which is in this case associated to a convective time. One finds $\tau_{cv} = 5$ ms which corresponds to the time required by a disturbance to be convected to the flame and reach the flame edge. This can be seen by calculating this delay for the flame geometry under investigation : $\tau_d \simeq L/U_b$ where L is a characteristic length of the flame under unsteady operation and U_b is the bulk velocity. In this particular case, $L \simeq 1.5$ cm and U_b is 2.67 m s^{-1}. The associated delay is 5.6 ms which is close to the characteristic delay deduced from the transfer function phase. While the phase evolution is roughly linear, there are also ripples and a slight decrease around 70 Hz where the gain is small. But whatever the amplitude levels, phase curves collapse well.

The describing function shown in Fig. 5.1 (b) obtained for flame B corresponds to a larger flow velocity of 4.13 m s^{-1}. This FDF was also measured with the LDV system. The response is determined in the same frequency range, but only three velocity disturbance levels u'/U_b : 0.2, 0.4 and 0.53 are considered. Data are lacking for the highest velocity disturbance level in the range 0-100 Hz because the flame flashes back into the burner when forced by the loudspeaker. From 0 to 60 Hz, the gain is constant and close to a value of one. From 60 to 100 Hz, the gain diminishes and reaches a low value of 0.3. From 100 to 150 Hz, the gain increases and reaches a local maximum for the three curves. From 150 to 200 Hz, the gain decreases and reaches a value of 0.6. This value remains constant in the frequency range 200-280 Hz. For the frequencies exceeding 280 Hz and up to 400 Hz, the gain decreases finally taking values below 0.2. The general trend for the phase is quasi-linear from 0 to 400 Hz but there are undulations. The different curves composing the FDF collapse well up to 250 Hz.

To evaluate the influence of the velocity measurement point, one may compare the previous data with FDFs based on hot wire velocity measurements. With this comparaison, it is possible to see if the swirler adds a time delay to the flame

response. The resulting FDFs are plotted in Fig. 5.1 (c) and (d) for flame A and B respectively. The modulation levels indicated in these figures now correspond to the rms perturbation level determined at the hot wire location.

For flames A and B results are close to those obtained previously with the LDV system. It is interesting to discuss the main differences between the two kinds of measured FDF. All FDF measured with the LDV or the hot wire have the same global shape. The minimum and the maximum gains are located at the same frequency independently of the measurement technique. The main difference is found in the low frequency range where the gain is slightly higher in the hot wire case than in the LDV case for both flames. Furthermore, peaks obtained with the LDV take higher values than those observed with the hot wire system as can be seen by comparising (a) and (b) versus (c) and (d) in Fig. 5.1. As deduced from measurements obtained with the LDV system, the gain decreases for high amplitude perturbations. The phase is roughly linear with a few undulations for both measurements methods. There are small differences in the slopes determined with the two methods. For the hot wire FDF, slope of the phase curves is slightly higher than the slope of the phase obtained with LDV. This is due to the fact that the velocity perturbation is measured with the LDV system at 2.9 mm from the base of the cone and not exactly in the outlet plane. Then the time delay determined with the LDV system is shorter than the time delay determined with the hot wire. From results presented in Fig. 5.1, it can be concluded that the swirler does not induce an additional time delay. And this difference is close to the time delay obtained by dividing the distance 2.9 mm by the bulk velocity. Finally, measurements are smoother with the hot wire system.

A central issue in studying dynamics is to identify characteristic dimensionless numbers. In the case of swirled flames submitted to incoming velocity disturbances in constant equivalence ratio mixture, the Strouhal number mainly describes the flame response to velocity perturbations of constant level, see Kim *et al.* (2010). It is then natural to transform previous data by using this dimensionless group based on the flow velocity and defined as : $\mathrm{St} = fD/U_b$ where f is the frequency, D the injector outer diameter and U_b the bulk velocity. Results are presented in Fig. 5.2 where the first plot, marked (a) shows flame transfer functions for flames A and B determined for a disturbance level u'/U_b of 0.5 measured at the injector outlet with the LDV system. The second plot, marked (b), shows the same functions but determined for a disturbance level of 0.5 inside the burner upstream the swirler. Some data are missing in the top plot in the low frequency range but it is interesting to note that the gain and phase curves collapse well from 0 up to 0.7 in terms of Strouhal number. Beyond this value, the two curves are distinct but the difference remains small and the general trend is the same. This is also verified for the other relative velocity amplitudes. The

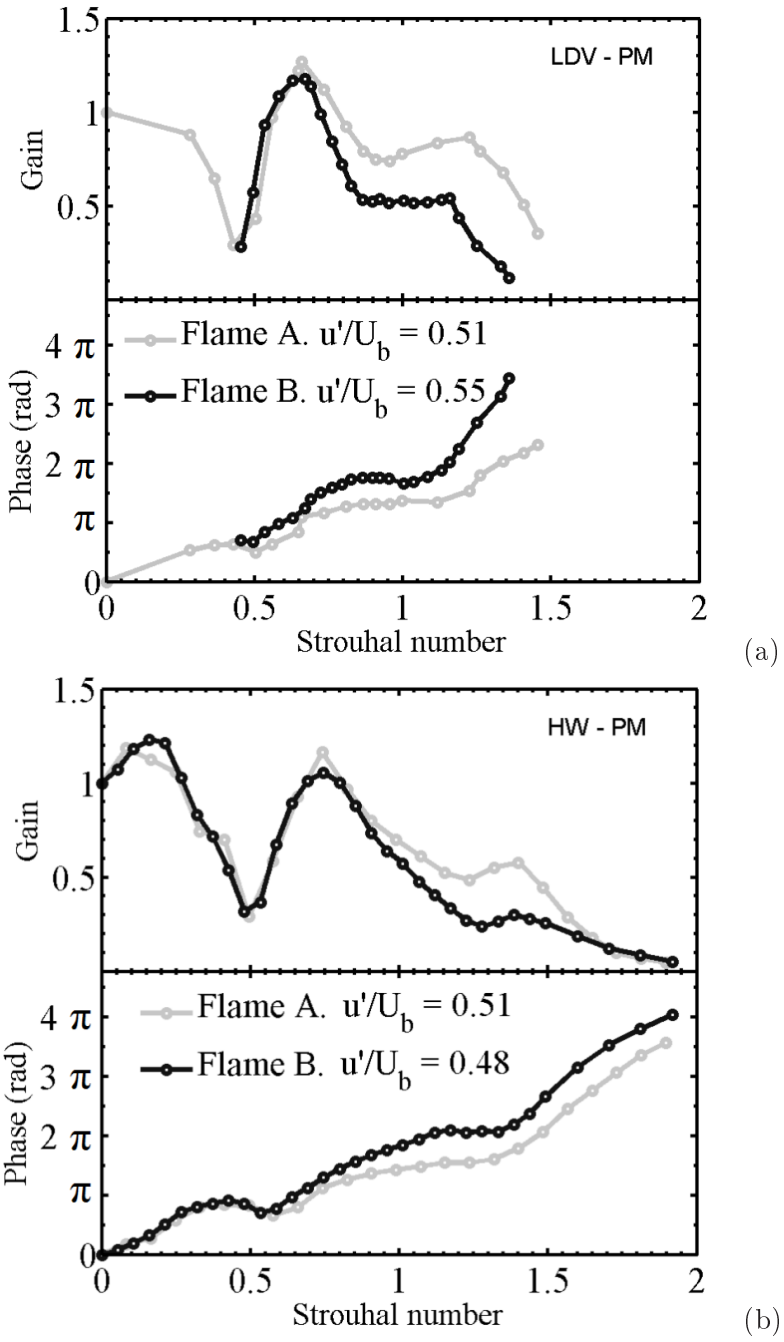

Figure 5.2: Strouhal number (St = fD/U_b) dependency for FDF issued from two different measurement methods. Results obtained in (a) are based on LDV measurement and in (b) are based on hot wire anemometry.

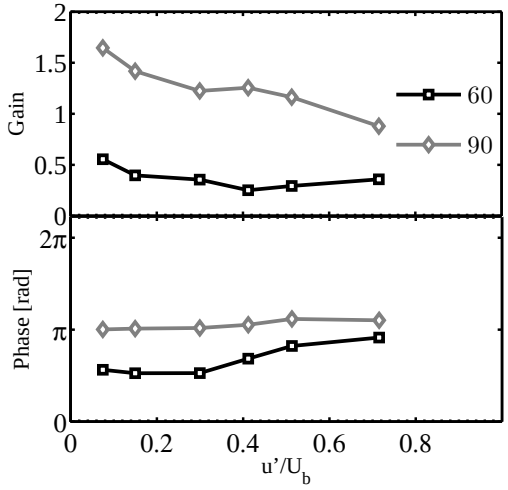

Figure 5.3: Gain and phase of the flame describing function for flame A plotted as a function of the input velocity u'/U_b.

Strouhal number can then be used to predict the transfer function behaviour for a given geometry confirming previous findings from Kim *et al.* (2010). The collapse is imperfect probably because, as suggested by a reviewer the Reynolds number also changes with the bulk flow velocity.

Some general trends can be mentioned for these FDFs. The gain can be higher than unity indicating that the system behaves as an amplifier. This feature may favor combustion instabilities. Beyond a Strouhal number of 1.5 - 2, the gain is small, indicating that perturbations at high frequencies are less favor to trig such combustion instabilities. By increasing the perturbation amplitude, the gain regularly decreases. This nonlinearity in the flame response is crucial to the prediction of limit cycle oscillations. The gain curves also feature also a local minimum for a Strouhal number around 0.5 which will be examined later in the paper. With this burner, the phase slope does not depend on the perturbation level and then the time delay is always the same at a given frequency. It is not fully independent of the frequency but the scatter around a mean value is relatively small.

It is interesting to plot the gain and the phase versus the input velocity fluctuations u'/U_b for two characteristics frequencies $f = 60$ Hz and $f = 90$ Hz respectively black and gray curves in Fig. 5.3. These plots obtained for flame A show that there is a change in gain and phase as the relative amplitude of the velocity inlet increases and reflects the nonlinearity of the system.

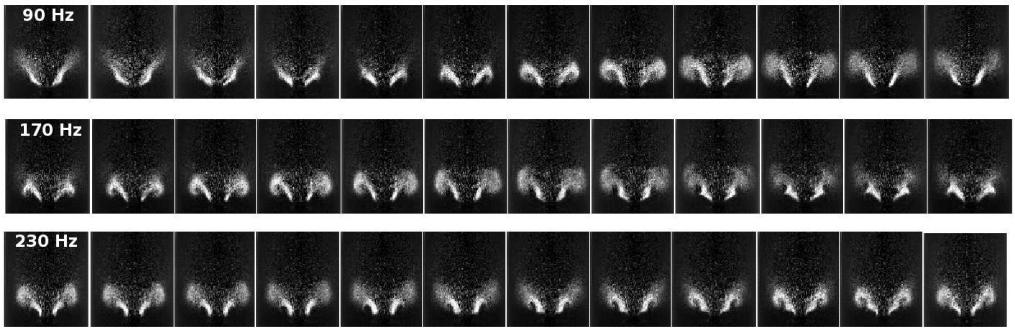

Figure 5.4: Abel transform for flame A at low amplitude $u'/U_b \simeq 0.3$.

5.3 Unsteady flame dynamics at low modulation amplitude

Flame A Dynamics of flame A is investigated with a low level of modulation corresponding to a velocity fluctuation in the injector tube of $u'/U_b \simeq 0.3$ and for three frequencies $f = 90$ Hz, $f = 170$ Hz and $f = 230$ Hz. Results are presented in Fig. 5.4. This is achieved by accumulating one hundred instantaneous images for twelve selected phases in the cycle. The resulting averages are then compressed by binning adjacent pixels of two by two matrices to decrease the image size and augment the signal to noise ratio. An Abel transform is then applied to each binned image to get the two dimensional flame slice. This processing is applied to flame A described previously.

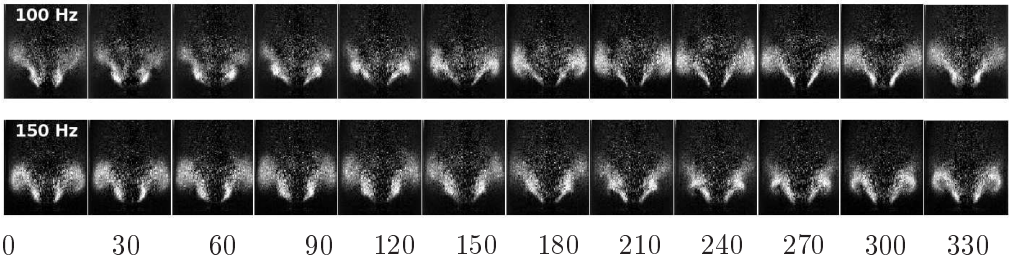

Figure 5.5: Abel transform for flame B at low amplitude $u'/U_b \simeq 0.2$.

Flame B Dynamics of flame B is investigated with a low level of modulation corresponding to a velocity fluctuation in the injector tube of $u'/U_b \simeq 0.2$ and for two frequencies $f = 100$ Hz and $f = 150$ Hz. Results are presented in Fig. 5.5

5.4 Unsteady flame dynamics at high modulation amplitude

The flame motion induced by incoming perturbations is analyzed in this section using optical imaging techniques to interpret flame describing functions data. This can be achieved by making use of OH PLIF methods as done by Thumuluru *et al.* (2007); Lee *et al.* (2000); Bellows *et al.* (2007) or by directly recording the flame emission with an ICCD camera as by Bellows *et al.* (2007); Külsheimer and Büchner (2002). A direct analysis of instantaneous flame emission images is not suitable because turbulent fluctuations tend to hide the organized motion associated with the periodic motion. It is also important to remember that emission images are formed by integrating flame radiation over the line of sight. It is then more suitable to use a combination of phase conditioned averaging of emission images followed by an Abel transformation. The main objective is to capture the dynamics of the flame at each instant in the cycle during the oscillation. This is achieved by accumulating one hundred instantaneous images for twelve selected phases in the cycle. The resulting averages are then compressed by binning adjacent pixels of two by two matrices to decrease the image size and augment the signal to noise ratio. An Abel transform is then applied to each binned image to get the two dimensional flame slice. This processing is applied to flames A and B described previously. The Abel transform is illustrated in Fig. 2.8 on page 45 for an external modulation frequency $f = 100$ Hz. The processed image indicates that combustion is concentrated in a flame brush with a flame edge in the injector near field adjacent to a central core and reduce the noise associated with the Abel transform. A Gaussian filter is used to smooth the data. This does not completely reduce the fluctuations which appear near the axis of symmetry.

Phase conditioned Abel transformed images are now used to analyze the dynamics of flames A and B. Case A is illustrated with the dynamics observed for the modulation level $u'/U_b = 0.5$ selected for the transfer function comparison carried out previously. The flame patterns over a full cycle of oscillation are shown in Fig. 5.6. Data correspond to four different forcing frequencies $f = 20$, 60, 90 and 230 Hz which are characteristic points in the transfer function represented in Fig. 9.2. In these figures, results are displayed as a function of time expressed in degrees of phase. These data can be used to examine the evolution of the flame surface area by assuming that the volumetric rate of reaction is a product of the local heat release rate per unit surface multiplied by the surface per unit volume. If the rate per unit surface does not change, then the Abel transformed images can be interpreted in terms of phase average surface densities. Consider first the case where the flame response is modulated at $f = 20$ Hz. This corresponds to a gain of about unity (on the left plot in Fig. 9.2). The flame surface is decreasing from 0° to 180° and increasing from 180° to 300°. The flame motion essentially

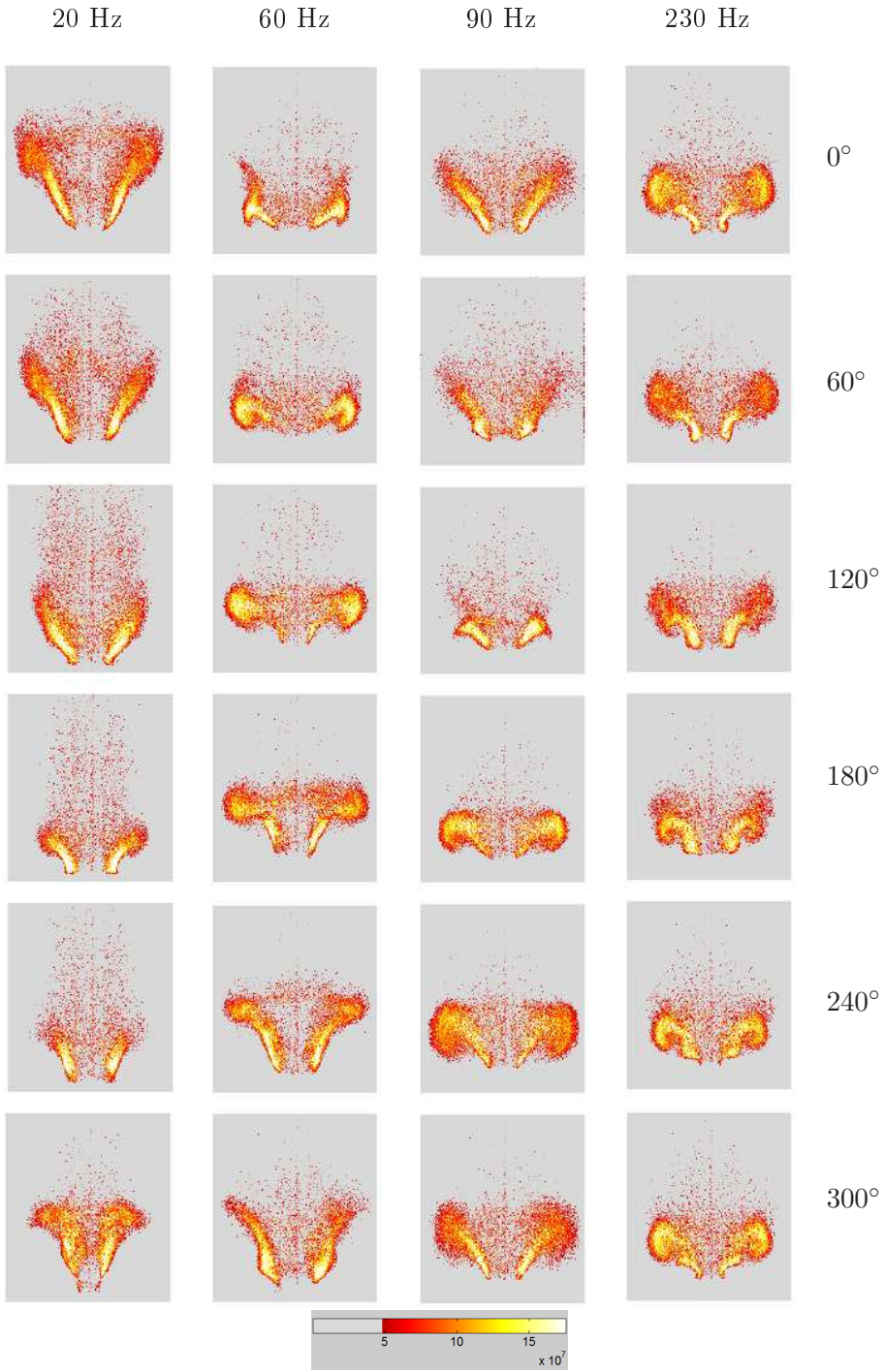

Figure 5.6: Flame slice images obtained by phase averaging and Abel transformation of emission images recorded by an ICCD. Flame A - $u'/U_b \simeq 0.5$ and $\phi = 0.7$. Images are scaled in W m^{-3}.

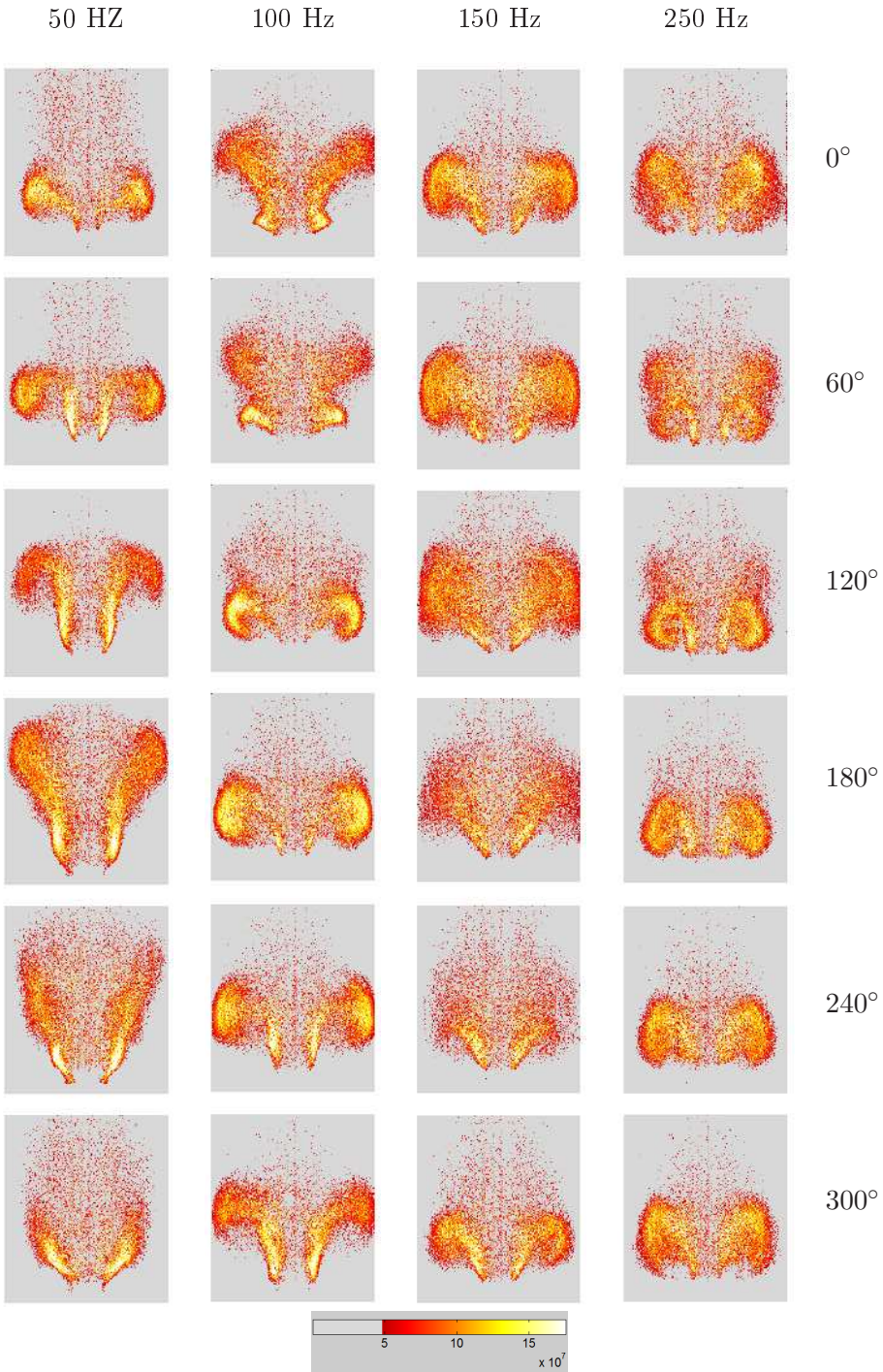

Figure 5.7: Flame slice images obtained by phase averaging and Abel transformation of emission images recorded by an ICCD. Images are scaled in W m^{-3}. Flame B - $u'/U_b \simeq 0.5$.

corresponds to that of a bulk oscillation, with minor flame roll-up at the flame tip. It is also found that from 60° to 240° flashback takes place and the flame is seen to slightly move into the burner. It is now worth examining a case at f = 60 Hz presented in Fig. 5.6, where the gain of the transfer function takes a small value (0.25, on the left plot in Fig. 9.2). The flame is now subjected to a convective roll-up motion between 0° to 120°, but the flame surface does not change significantly during the cycle. From 120° to 240° the convective motion is still present but the flame surface is affected and increases slightly. After 240° and up to 300°, the flame surface is decreasing. For a modulation frequency of f = 90 Hz, the gain of the FDF slightly exceeds unity ($G \simeq 1.25$). The flame surface now features large variations. The flame surface decreases from 240° to 120° and then increases in the remainder of the cycle. Images in Fig. 5.6 show that vortex roll-up acts on the flame and specifically on its tips from 120° to about 240°. At higher modulation frequencies, as for example in images presented in the right part of Fig. 5.6 for $f = 230$ Hz, one finds that the main vortex roll-up occurs at the flame tips from 0° to 120°. After that, the main vortex roll-up progressively disappears while a second roll-up wrinkles the flame base from 180° to 240°. From 240° to 300°, the second vortex becomes dominant and propagates along the flame. It should be noted that during the cycle, the shape of the flame is changing but the surface area remains nearly constant. The gain found in this situation approaches $G \simeq 0.2$.

Effects of the mean flow velocity are now examined with data obtained for flame B and for a modulation level $u'/U_b = 0.5$ which nearly coincides with that used for flame A. The flame patterns are shown in Fig. 5.7 for four frequencies f = 50, 100, 150 and 250 Hz corresponding to characteristic points in the gain of the transfer function presented on the right plot in Fig. 9.2. Similar dynamics is observed for flame B and Flame A. The main difference is in the interaction of the flame with the walls of the flame tube. Results reported in this section give an indication on the flame motion induced by incoming perturbations and on the different response types which can be observed when the frequency is varied. These data complement the describing function measurements and they constitute a database for future comparisons with unsteady simulations. One question which cannot be answered with the present chapter is that of the possible influence of a precessing vortex core (PVC). This requires further experiments and large eddy simulations carried out in chapter 13. It is generally believed that the PVC is weaker under hot fire conditions. Its impact on the flame response is not fully documented.

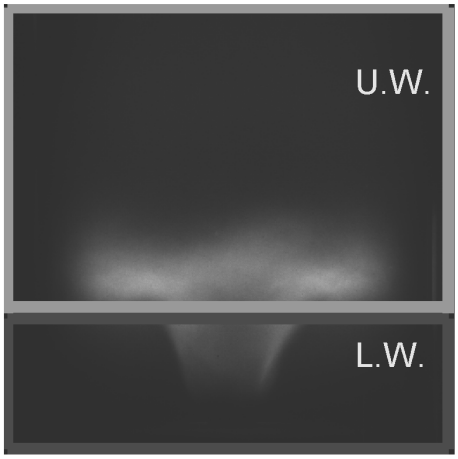

(a)

Figure 5.8: View of the two interrogation windows superimposed on flame A at 60 Hz. UW and LW respectively designate the upper and lower windows.

5.5 Discussion

The underlying mechanisms leading to different flame dynamics are now examined by analyzing emission images. This is achieved by defining two interrogation windows, an upper window noted UW and a lower window noted LW as indicated in Fig. 5.8 for flame A. In this figure, the light intensity radiated by flame A modulated at $f = 60$ Hz is detected separately in the two windows. The cutting line separates an upper region where 70% of the heat is released from a lower region where 30% of the heat is deposited. With this choice, the relative fluctuations in these two regions have the same order of magnitude : $\dot{Q}'_{lw}/\overline{\dot{Q}}_{lw} \simeq \dot{Q}'_{uw}/\overline{\dot{Q}}_{uw}$. For the higher forcing frequency $f = 90$ Hz for flame A and $f = 150$ Hz for flame B the cutting line defines upper and lower regions where 63% and 37% of heat is released. It is thus possible to deduce the contribution to the heat release rate signal from the light emission detected in each of the previous windows. This is obtained by summing the pixels in the two windows for each phase-locked image. This process is repeated for $f = 60$ Hz and $f = 90$ Hz for flame A and for $f = 100$ Hz and $f = 150$ Hz for flame B. It is important to remember that these values correspond to characteristic points where the gain of the FDF are respectively minimum and maximum. Results are displayed in Fig. 5.9 (a) and (b) for flame A and in Fig. 5.9 (c) and (d) for flame B.

For flame A and for a modulation frequency $f = 60$ Hz, the signals detected in the two windows are essentially out of phase and the sum of these signals is smaller than its upper and lower components. The global response of the flame is low because the lower and upper parts of the flame respond in opposition. In other words the process leads to a cancelation of their respective contributions.

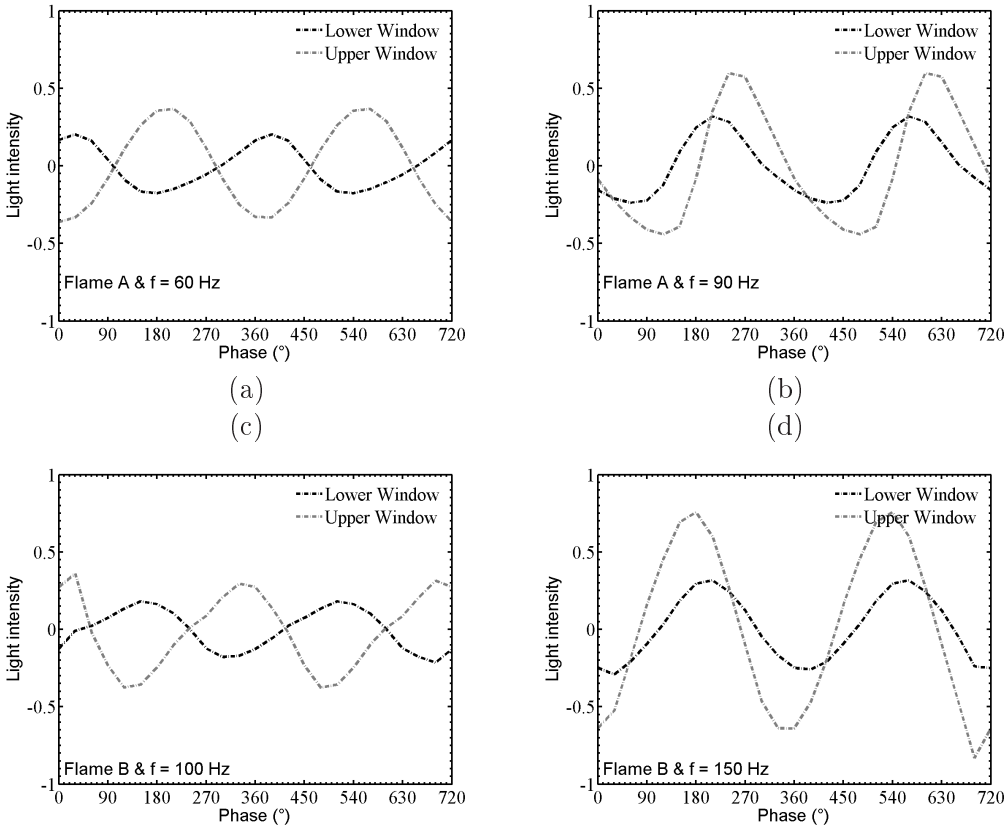

Figure 5.9: Heat release rate signals reconstructed from the light emission detected in the upper and lower windows. (a) $f = 60$ Hz, flame A. (b) $f = 90$ Hz, flame A. (c) $f = 100$ Hz, flame B, (d) $f = 150$ Hz, flame B.

At $f = 90$ Hz, the situation is quite different. The signals from the lower and upper parts of the flame are nearly in phase and the whole flame contributes coherently to the fluctuation in heat release rate. The same observations can be made for flame B. At $f = 100$ Hz, the signals from the lower and upper windows are out of phase while at $f = 150$ Hz, emissions from these two windows are nearly in phase. The main result is that the flame response is a strong function of the response of each part of the flame. These observations indicate that the gain of the flame is linked to the timing of the heat release perturbations in the flame. When this timing corresponds to an out of phase motion, the gain is low. When the sum of the light intensity in both windows is in phase, the gain is high.

It is also interesting to examine these data by plotting phase-space diagrams. One uses a reference frame where the vertical axis is the phase and the horizontal axis corresponds to the axial coordinate in the flame. Space-phase diagrams corresponding to modulations at $f = 60$ and $f = 90$ Hz are plotted in Fig. 5.10 (a) and (b) respectively for flame A. These diagrams are formed by summing emission over the pixels in each line of the phase average images. For a given phase ψ one starts from the phase average image like Fig. 5.8 acquired with the ICCD camera. Let $I(j, l, \psi)$, $j = 1, ..., 512$, $l = 1, ..., 512$ be the local pixel intensity on the CCD screen. One forms a transversally averaged emission signal $< I > (j, \psi)$ and then subtracts the time average intensity from this signal. The result is then divided by this average to obtain a relative intensity fluctuation $(< I > (j, \psi) - \overline{< I >})/\overline{< I >}$. For a given phase ψ, this quantity defines the spatial distribution of relative emission which may be interpreted as the spatial distribution of transversally integrated heat release rate. This operation is repeated for a set of phases and results are gathered in the form of contours. In Fig. 5.10, the vertical gray line indicates the border of the two windows LW and UW defined in the previous section.

An examination of the diagram in Fig. 5.10 (a) corresponding to flame A under a modulation at $f = 60$ Hz indicates the presence of alternate positive and negative fluctuations. For a given phase one finds a region in the flame where the fluctuation is positive while in another region the fluctuation is negative. These regions are convected downstream and the process is repeated periodically. This explains observations made previously where the two regions located in the LW and UW operate in phase opposition when the flame is modulated at $f = 60$ Hz. When this takes place the total heat release fluctuation in the flame is low. For $f = 90$ Hz shown in Fig. 5.10 (b), both sides of the gray line are nearly in phase and both contribute positively or negatively to the heat release fluctuation. Under these circumstances the global level of heat release fluctuation is high. For flame B, similar trends are observed for $f = 100$ Hz and $f = 150$ Hz. From this analysis it becomes clear that the flame response can be weak when two regions

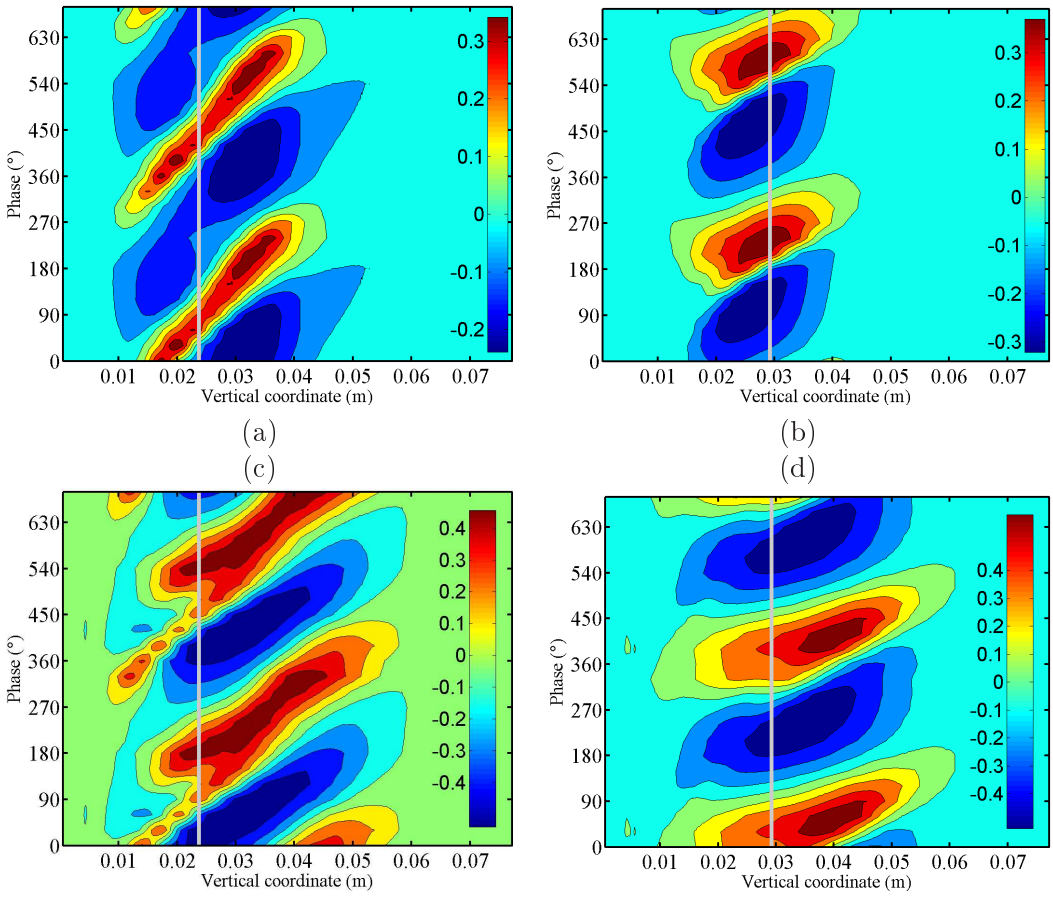

Figure 5.10: Space-time distributions of light emission. (a) : flame A modulated at f = 60 Hz. (b) : flame A modulated at f = 90 Hz. (c) : flame B modulated at f = 100 Hz. (d) : flame B modulated at f = 150 Hz. These diagrams are formed by summing emission over the pixels in each line of the phase average images. For a given phase this quantity defines the spatial distribution of relative emission which can be interpreted as the spatial distribution of transversally integrated heat release. The gray line indicates the limit used to split both windows.

in the flame operate sequentially and give rise to a destructive interference of their heat release rates. Furthermore, the patten orientation in these maps are different suggesting that the response is determined by a combination of perturbations. In Fig. 5.10 (a) and (c), convective propagation is clearly visible while in Fig. 5.10 (b) and (d), the motion is close to a bulk mode.

5.6 Physical mechanisms driving the response

It is now interesting to consider the physical mechanisms defining the flame response and examine more specifically the mechanism which gives rise to the local minimum and maximum in the FDF gain curve. This requires an analysis of perturbations on the downstream side of the swirler. It is known from chapter 7 that a blade row interacting with an incident acoustic wave generates reflected and transmitted acoustic waves as well as a vorticity wave in the downstream region. This last wave features velocity components in the axial and transverse directions which are convected by the flow. The same mechanism operates when a swirler is impinged by acoustic waves inducing a vorticity wave on its downstream side. It is useful to develop an analysis of the mode conversion process taking place at this component. This can be accomplished by employing an actuator disk description of this device and using the work of Cumpsty and Marble (1977b) to start the analysis. In the geometry shown in Fig. 4.3, page 81, the swirler is represented by a two dimensional cascade. The incoming flow velocity $\overline{w}_1$ is oriented in the axial direction while the outgoing flow $\overline{w}_2$ makes an angle $\overline{\theta}_2$ with respect to the axis. To relate perturbations on the upstream (index 1) and downstream (index 2) sides of this cascade one may use jump conditions provided in Cumpsty and Marble (1977b) and adapted to a small Mach number flow.

It is thus possible to write the velocity components on the downstream side of the swirler in the following form :

$$u'_2 = \frac{A}{\overline{\rho}\,\overline{c}} \exp i\left(\frac{\omega}{\overline{c}}x - \omega t\right) \tag{5.5}$$

$$v'_2 = \frac{A}{\overline{\rho}\,\overline{c}} \tan\overline{\theta}_2 \exp i\left(\frac{\omega}{\overline{u}_2}x - \omega t\right) \tag{5.6}$$

The axial velocity component propagates at the speed of sound while the transverse velocity component is convected at the local flow velocity $\overline{u}_2 = \overline{w}_2 \cos\overline{\theta}_2$ in the axial direction. The previous calculations indicate that the swirler acts as a mode converter. When it is submitted to axial acoustic waves it generates a vorticity wave which is convected by the flow in the axial direction. This convective wave is characterized by a velocity component in the transverse direction. These conclusions were obtained from a two dimensional cascade model. The application to a typical swirler is only approximate but sufficient for the present

purpose. It is then possible to consider that the azimuthal velocity fluctuation can be identified to the transverse component determined previously.

Since the flow leaving the swirler is rotating around the x-axis, the presence of fluctuations in the radial and azimuthal directions will have an effect on the instantaneous swirl number. In principle, the swirl number is defined by assuming that the flow is steady. It is however informative to calculate this number by expressing the velocity components in terms of a mean value and a small fluctuation $u = \overline{u} + u'$ and $v = \overline{v} + v'$. If one assumes for simplicity that the relative fluctuations are uniform over the flow and that their amplitude is small, one may expand the swirl number given in Eq. (6.1) to first order. This yields :

$$S = \overline{S}\left[1 + \frac{v_2'}{\overline{v}_2} - \frac{u_2'}{\overline{u}_2}\right] \tag{5.7}$$

where $\overline{S}$ is the mean value in the absence of fluctuations. This expression indicates that fluctuations in swirl number are due to the difference between the relative fluctuations of azimuthal and axial velocities. Using expressions Eq. (5.6) and substituting in Eq. (5.7), one obtains :

$$\frac{S - \overline{S}}{\overline{S}} = \frac{S'}{\overline{S}} = a\left[\exp i\left(\frac{\omega}{\overline{u}_2}x\right) - \exp i\left(\frac{\omega}{\overline{c}}x\right)\right]\exp(-i\omega t) \tag{5.8}$$

where a designates the modulus of incoming relative fluctuations in axial velocity downstream the swirler.

The axial and azimuthal fluctuations propagate at significantly different phase velocities, the first being acoustic in nature while the second is convective. This has the consequence that these two components will interact with the flame constructively or destructively depending on the distance between the swirler and the injector exhaust as can be seen by examining expression Eq. (8.13). The influence of this distance was indeed noticed previously by Huang and Yang (2009); Gentemann *et al.* (2004); Wang and Yang (2005); Komarek and Polifke (2010) and the resulting effect was attributed to swirl number fluctuations but the present calculations provide estimates of these fluctuations around its mean value and indicate that the amplitude of these fluctuations is governed by the combination of incident axial perturbations with azimuthal velocity perturbations induced by the swirler.

This analysis indicates that the vortical mode generated on the downstream side of the swirler gives rise to azimuthal velocity fluctuations which are convected by the flow. These fluctuations combine with perturbations in axial velocity. The impact of this disturbed field on the flame response depends on the phase shift.

This differs in nature from mechanisms invoking the PVC.

It is worth noting that the present two-dimensional model only approximates conditions prevailing near the swirler hub in the axial case. Radial swirlers are well represented by a cascade. In addition, fully three dimensional calculations not shown here confirm that the same mode conversion mechanism is at work.

5.7 Data interpretation

The entire set of data corresponding to the FDF have provided the important information that all transfer functions composing the FDF feature the local minimum and maximum and that the mechanisms producing these gains operate for all levels of perturbation. The following analysis is carried out for a single level of perturbation but is equally valid for others values. It turns out that the mode conversion process taking place at the swirler is essentially linear. It is then reasonable to use the highest modulation level to get the best signal to noise ratio.

It is now possible to interpret the flame describing function measurements and specifically consider the minimum and maximum gain of this function. This analysis is carried out for flame A, which features a minimum and a maximum gain at $f = 60$ and $f = 90$ Hz respectively but similar results are found for flame B. It is already shown in the previous subsection that the perturbed velocity field comprises an axial and an azimuthal component. It is also known from previous studies that when the axial velocity perturbation reaches a maximum a vortex is shed from the injector lips. This vortex is convected by the flow and eventually rolls up the flame tip. This is a first mechanism of unsteady heat release which induces large flame surface area fluctuations which mainly operate near the end of the flame and produces most of the heat release fluctuation detected in the upper window UW defined in section 6.4. The second mechanism is here associated with the combined axial and azimuthal velocity perturbations. This induces fluctuations in swirl number as expressed in the linearized form by Eq. (5.7) or more explicitly by Eq. (8.14) which in return give rise to a breathing motion of the central recirculation region resulting in an angular deflection of the flame. The flame angle changes in response to the incoming perturbations of axial and azimuthal velocity components. It is interesting to estimate the relative angular fluctuation induced by this mechanism. This can be done by describing the normal propagation of the flame in terms of a turbulent burning velocity S_T. The flame angle α is then defined by :

$$\sin \alpha = \frac{S_T}{u} \tag{5.9}$$

This expression can be linearized around the mean state assuming small variations of the fluctuating quantities :

$$\sin(\overline{\alpha}+\alpha') = \frac{\overline{S}_T + S'_T}{\overline{u}+u'} \tag{5.10}$$

After some simple calculations in which one only retains first order terms, one finds the following relation :

$$\frac{\alpha'}{\overline{\alpha}} \simeq \frac{\tan\overline{\alpha}}{\overline{\alpha}}\left[\frac{S'_T}{\overline{S}_T} - \frac{u'}{\overline{u}}\right] \tag{5.11}$$

It is reasonable to assume that the fluctuations in turbulent burning velocity ($S_T \sim v_{max}$, see Ishizuka *et al.* (1998)) are linked to the axial and azimuthal velocity perturbations. A first order expansion consists in assimilating S'_T/S_T to the weighted sum of relative fluctuations in azimuthal and axial velocities :

$$\frac{S'_T}{\overline{S}_T} = \chi\frac{v'}{\overline{v}} + \zeta\frac{u'}{\overline{u}} \tag{5.12}$$

The relative fluctuation of flame angle then becomes :

$$\frac{\alpha'}{\overline{\alpha}} \simeq \frac{\tan\overline{\alpha}}{\overline{\alpha}}\left[\chi\frac{v'}{\overline{v}} + (\zeta-1)\frac{u'}{\overline{u}}\right] \tag{5.13}$$

To use the previous model one has to fix the coefficients defining the relative perturbations in turbulent burning velocity in Eq. (5.12). This information is admittedly not easy to obtain. We use the following values : $\chi = -0.4$ and $\zeta = 0.4$ deduced from a trial and error process. These values are also obtained from a separate analysis of the theoretical transfer function of swirling flames, see chapter 8. The present choice corresponds to a trade-off.

One expects from the previous analysis that swirl number fluctuations will be reflected in flame angle fluctuations. Also, the fluctuations in burning velocity and flame angle will directly translate into fluctuations in heat release rate. It is then possible to consider the mechanism which defines the heat release perturbation near the root of the flame, in the lower window and link these perturbations to fluctuations of flame angle α and burning velocity S_T. The heat released by the flame in the lower window is proportional to the burning velocity and flame surface area :

$$\dot{Q}_{lw} = \rho S_T A_f \Delta h Y_{FO} \tag{5.14}$$

where ρ is the density of the fresh stream, A_f is the flame surface, Δh is the heat release per unit mass of fuel (50 MJ kg^{-1}) and Y_{FO} is the mass fraction of

fuel in the premixed stream. Near the flame anchor point the surface may be assimilated to a truncated cone :

$$A_f = \frac{\pi(r_2^2 - r_1^2)}{\sin\alpha} \tag{5.15}$$

where r_2 is the radius of the flame at the top of the lower window, at a distance d_{lw} from the central rod and r_1 is the radius of the rod. Now, $r_2 = d_{lw}\tan\alpha$ and $r_1 << r_2$ so that A_f is proportional to $\sin\alpha/\cos^2\alpha$. The heat release fluctuation in the lower region $\dot{Q}'_{lw}$, may be obtained by expanding Eq. (8.31) :

$$\dot{Q}'_{lw} = \rho\Delta h Y_{FO}(S'_T A_f + S_T A'_f) \tag{5.16}$$

and the relative fluctuation in heat release is then determined by :

$$\frac{\dot{Q}'_{lw}}{\overline{\dot{Q}}_{lw}} = \frac{S'_T}{\overline{S}_T} + \alpha'\frac{1+\sin^2\overline{\alpha}}{\cos\overline{\alpha}\sin\overline{\alpha}} \tag{5.17}$$

To allow a comparison with experimental data, it is convenient to obtain the ratio of the heat release rate perturbation in the lower window to the total heat release in the flame. This is obtained from the previous expression :

$$\frac{\dot{Q}'_{lw}}{\overline{\dot{Q}}} = \eta\left[\frac{S'_T}{\overline{S}_T} + \alpha'\frac{1+\sin^2\overline{\alpha}}{\cos\overline{\alpha}\sin\overline{\alpha}}\right] \tag{5.18}$$

Here $\eta = \overline{\dot{Q}}_{lw}/\overline{\dot{Q}}$ represents the ratio of mean heat release in the lower window to the total mean heat release in the flame and its value is approximately equal to $\eta = 0.3$ for flame A. Expression Eq. (8.23) together with Eq. (5.12) and Eq. (5.13) fully determine the heat release fluctuations detected in the lower window (LW). The combination of these fluctuations with those induced at the flame tip determines the flame response to incident perturbations.

This scenario may now be verified by examining signals detected in the experiments and comparing these data to theoretical estimates based on the previous expression. For this analysis one considers the following signals : $v'/\overline{v}$, $u'/\overline{u}$, $\alpha'/\overline{\alpha}$, $\dot{Q}'_{lw}/\overline{\dot{Q}}$, $\dot{Q}'_{uw}/\overline{\dot{Q}}$ and $\dot{Q}'/\overline{\dot{Q}}$. All these signals are obtained from measurements. Radial profiles of axial velocity fluctuations were not measured but previous experiments in other configurations indicate that the perturbation level is approximately constant except near the boundaries where it diminishes. Then the measured level at a median point is representative of the state of modulation. In addition, it is also worth plotting the swirl number fluctuations $S'/\overline{S}$ deduced by subtracting the axial velocity fluctuation from the azimuthal velocity fluctuation Eq. (5.7) and theoretical estimates of α'/α deduced from expression Eq. (5.13) and $\dot{Q}'_{lw}/\overline{\dot{Q}}$ obtained from Eq. (8.23). The signals corresponding to flame A are plotted in Fig. 5.11 and Fig. 5.12 which respectively correspond to a

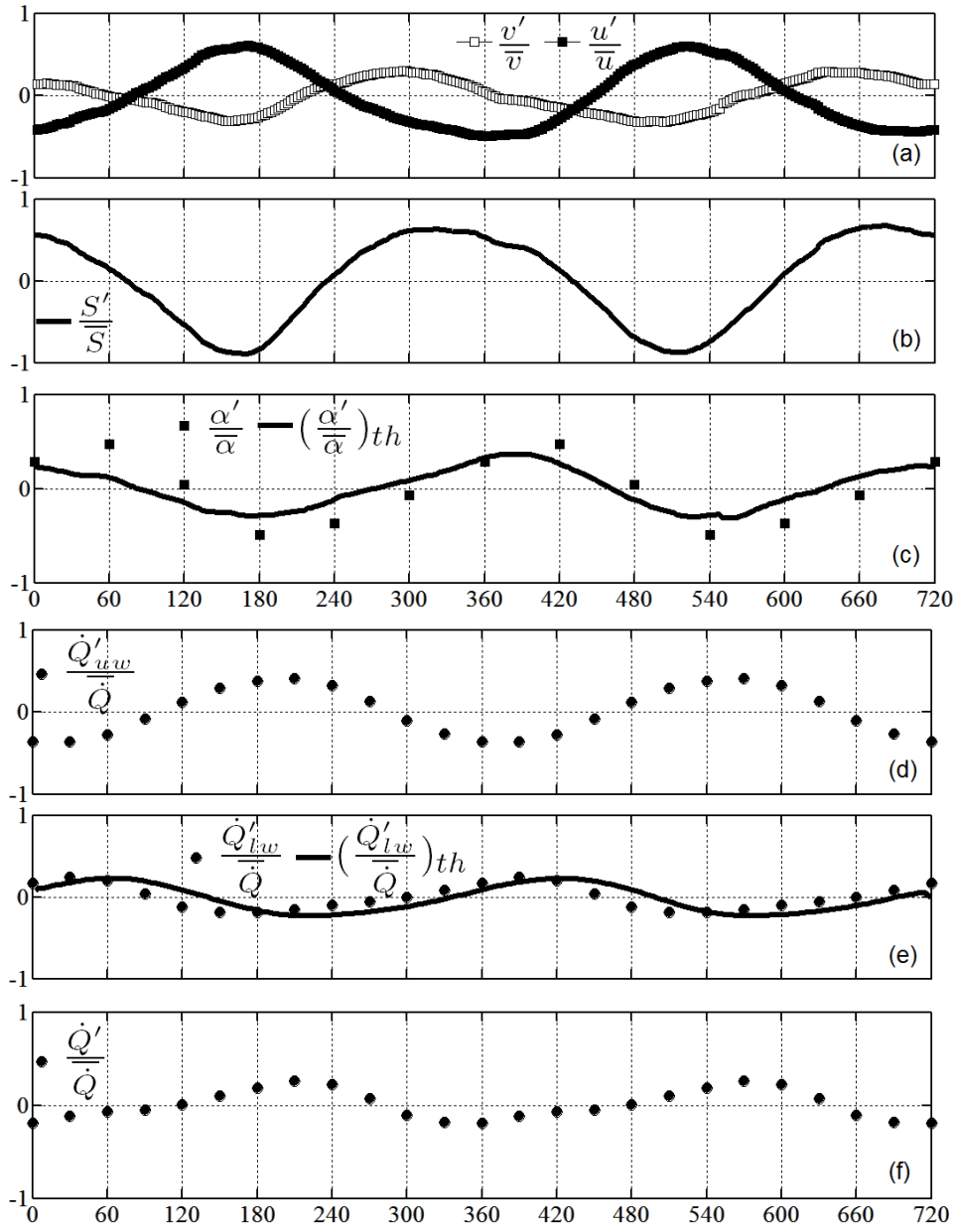

Figure 5.11: Characteristic signals describing the response of the flame A at $f = 60$ Hz versus phase (in degrees) during two cycles. Reconstructed signals are plotted as solid lines while experimental data are represented by symbols. (a) Relative velocity fluctuations. Open squares : $v'/\overline{v}$, dark squares : $u'/\overline{u}$. (b) Relative swirl number fluctuations $S'/\overline{S}$ deduced from the velocity signals. (c) Angular fluctuations $\alpha'/\overline{\alpha}$. Squares : experiment. Solid line : prediction. (d) Relative heat release rate in the upper window $\dot{Q}'_{uw}/\overline{\dot{Q}}$. (e) Relative heat release rate in the lower window $\dot{Q}'_{lw}/\overline{\dot{Q}}$ symbols : experiment, solid line : prediction. (f) Relative total heat release rate fluctuation in the flame $\dot{Q}'/\overline{\dot{Q}}$.

minimum and a maximum response of the flame at $f = 60$ and $f = 90$ Hz.

We first examine signals at 60 Hz plotted in Fig. 5.11. The relative velocity fluctuations displayed in the top subfigure have the same order of magnitude ($|v'|/\overline{v} \simeq |u'|/\overline{u}$) in agreement with the actuator disk theory derived previously. The two signals are nearly in phase opposition. Measurements of the phase between the two velocity components over a range of frequencies indicate that this quantity evolves linearly with frequency $\varphi = \omega\tau_c + \varphi_0$ as predicted theoretically. There is however a phase offset φ_0 which does not appear in the model. For flame A one finds $\tau_c = 12$ ms and $\varphi_0 = -1$ rad. The phase between $u'/\overline{u}$ and $v'/\overline{v}$ reflects the delay induced by convection of azimuthal perturbations v'. This convection takes place at a velocity which is close to the maximum axial velocity in the injection channel. For flame A this corresponds to 3.8 m s^{-1}. The swirl number fluctuations $S'/\overline{S}$ estimated from expression Eq. (5.7) in terms of the relative velocity fluctuations are in this case quite large (Fig. 5.11 (b)). These fluctuations are almost in phase with the flame angle fluctuations displayed in Fig. 5.11 (c). The flame angle α defined between the flame sheet and the vertical axis increases when the swirl number increases. The next three subfigures display relative heat release fluctuations. The heat release rate fluctuation in the upper window $\dot{Q}'_{uw}/\overline{\dot{Q}}$ (Fig. 5.11 (d)) is delayed with respect to the axial velocity signal measured at the base of the flame and displayed in Fig. 5.11 (a), black square symbol. The phase difference $\Delta\varphi \simeq 60°$ between these two signals corresponds to a delay $\tau \simeq 3$ ms. This delay is that required for convection of a vortex from the injector lip to the flame tip. The heat release in the lower window follows the flame angle fluctuation $\dot{Q}'_{lw}/\overline{\dot{Q}} \simeq \alpha'/\overline{\alpha}$. When the flame angle is decreasing, the heat release rate observed in the lower window also decreases. The inverse mechanism occurs when the flame angle increases (Fig. 5.11 (e)). The theoretical signal $\dot{Q}'_{lw}/\overline{\dot{Q}}$ deduced from expression Eq. (8.23) and plotted as a solid line in Fig. 5.11 (e) is in good agreement with experimental data shown as black symbols. The total heat release rate shown in Fig. 5.11 (f) is the sum of heat release rates measured in the lower and upper interrogation windows as discussed in section 4. In the present case for a modulation frequency $f = 60$ Hz, the two velocity signals at the flame base are out of phase and their combination has a relatively low amplitude and one may conclude that the two mechanisms perturbing the flame interfere to reduce the total response thus yielding a low gain.

The signals corresponding to $f = 90$ Hz for flame A are displayed in Fig. 5.12. The relative axial and azimuthal velocity fluctuations are still of the same order of magnitude as expected from the actuator disk theory but the signals are now nearly in phase. The swirl number fluctuations deduced from experimental velocity signals are much weaker than at 60 Hz Fig. 5.12 (b). The flame angle is

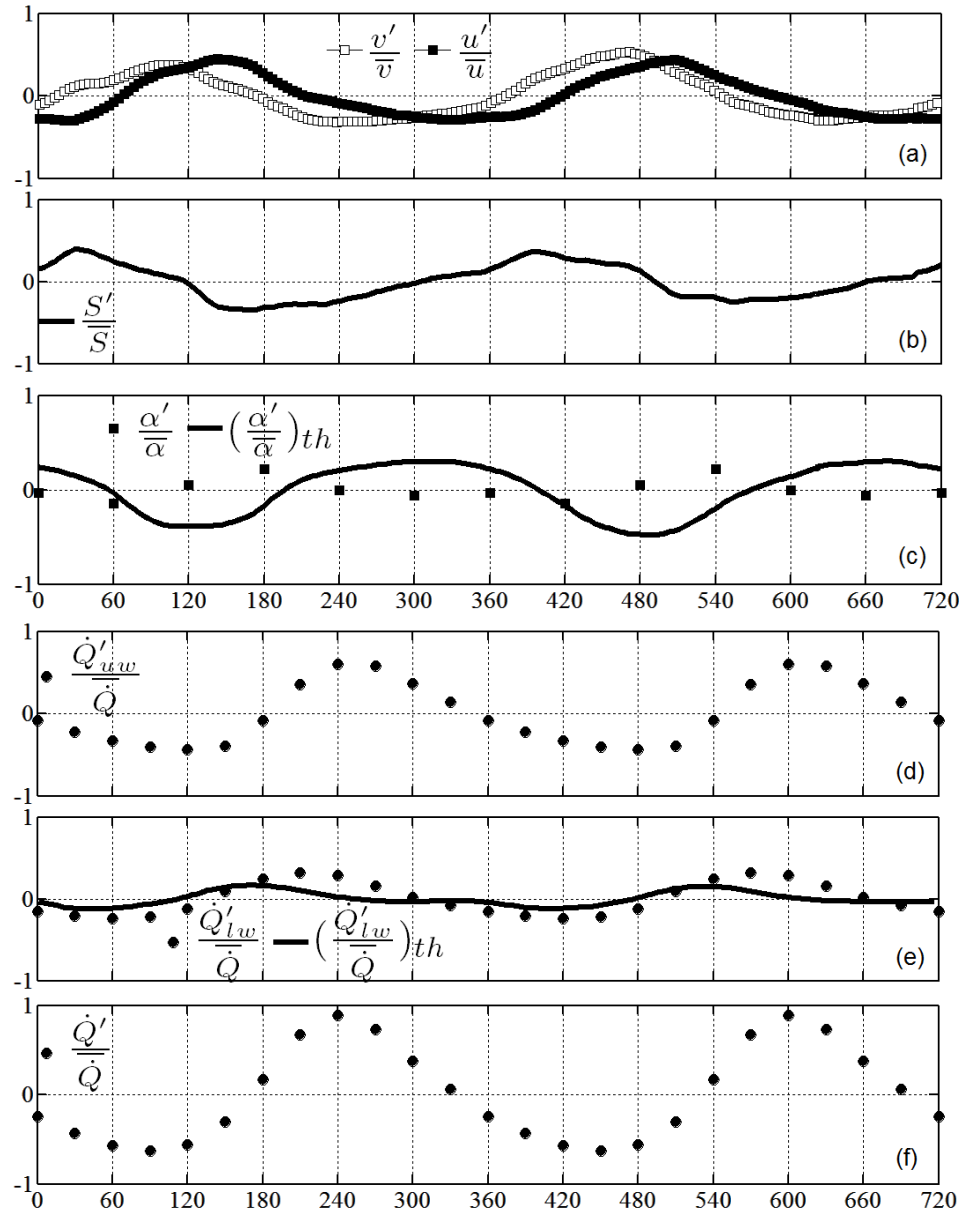

Figure 5.12: Characteristic signals describing the response of the flame A at $f = 90$ Hz versus phase (in degrees) during two cycles. Reconstructed signals are plotted as solid lines while experimental points are represented by symbols. (a) Relative velocity fluctuations. Open squares : $v'/\overline{v}$, dark squares : $u'/\overline{u}$. (b) Relative swirl number fluctuations $S'/\overline{S}$ deduced from the velocity signals. (c) Angular fluctuations $\alpha'/\overline{\alpha}$. Squares : experiment. Solid line : prediction. (d) Relative heat release rate in the upper window $\dot{Q}'_{uw}/\overline{\dot{Q}}$. (e) Relative heat release rate in the lower window $\dot{Q}'_{lw}/\overline{\dot{Q}}$ symbols : experiment, solid line : prediction. (f) Relative total heat release rate fluctuation in the flame $\dot{Q}'/\overline{\dot{Q}}$.

also weakly perturbed by these fluctuations Fig. 5.12 (c). The calculated flame angle fluctuation Eq. (5.13) is larger than expected and out of phase compared to experimental data. Concerning the heat release rate in the upper window, the mechanism involving flame surface fluctuation is present in this case and one can define a time delay between the upper window heat release signal $\dot{Q}_{uw}/\overline{\dot{Q}}$ and the axial velocity signal $u'/\overline{u}$ at the flame base. The phase difference $\Delta\varphi \simeq 90°$ yields a delay $\tau \simeq 3$ ms which nearly coincides with that found at 60 Hz. A comparison between Fig. 5.12 (c) and (e) indicates that when the flame angle increases, the heat release rate in the lower window increases like in the 60 Hz case. The calculated heat release fluctuation in the lower window has the right order of magnitude but the phase is less well reproduced. The experimental signals $\dot{Q}'_{lw}/\overline{\dot{Q}}$ and $\dot{Q}'_{uw}/\overline{\dot{Q}}$ are nearly in phase yielding a maximum response in terms of total heat release rate fluctuation.

The previous theory provides some suitable estimates of the experimental signals. It confirms the existence of two processes of unsteady heat release associated with two types of velocity perturbations. While results are quite satisfactory at the minimum of the transfer function gain, some improvement is needed at the point of maximum response.

It is probable that the mechanism described in this article will be equally important in lean premixed injectors operating at higher bulk velocities. As the FDF can be scaled in terms of Strouhal numbers one deduces that frequencies will follow Strouhal scaling rules. An increase in bulk velocity by a factor of 10 will multiply the characteristic frequencies by the same factor if geometrical dimensions are kept constant.

5.8 Conclusion

The dynamics of swirled premixed flames is considered in this chapter leading to the followings results :

1. The flame response is determined in terms of families of transfer functions which constitute a flame describing function (FDF). The FDF depends on the frequency and amplitude of the incoming perturbation and can be used in nonlinear analysis of instabilities involving this type of flame. Two methods employed for the FDF determination yield similar values. Data indicate that the transfer function gain depends on the input level most notably in frequency ranges where this gain reaches an extremum. The phase is less dependent on the input level and features a quasi linear behaviour with

respect to frequency indicating that the flame responds with a delay to the incoming perturbations.

2. It is found that transfer functions can be collapsed for a fixed value of the modulation amplitude at least in the low frequency range in terms of a Strouhal number confirming previous findings.

3. Systematic experiments indicate that the flame response is controlled by two types of fluctuations, the first being related to azimuthal velocity perturbations generated by the swirler and convected by the flow, the second being associated to axial velocity perturbations propagating to the injector exhaust. Fluctuations in the swirl number are generated and may combine with vortex roll-up inducing large variations in flame surface area.

4. An estimate of induced azimuthal velocity perturbations obtained from an actuator disk analysis is found to agree well with laser Doppler measurements of these components.

5. At the frequency corresponding to a local minimum in the FDF gain, it is shown that the initial and downstream regions of the flame operate in phase opposition giving rise to heat release components which interfere destructively and yield a low level for the global heat release signal. At the frequency corresponding to a local maximum in gain, the heat release signals induced by the two types of perturbations are in phase and their combination yields a maximum level.

Chapter 6

Swirler geometry and swirl number effects on FDF

Abstract : *This chapter deals with the response of swirling flames submitted to acoustic velocity disturbances when the rotation of the flow is produced by an axial or a radial swirler. The objective is to compare responses obtained in these two cases. The response is characterized in term of the flame describing function (FDF) which generalizes the classical flame transfer function concept by considering not only the frequency but also the amplitude of the velocity disturbances. The FDF been shown to be relevant in studies of combustion instabilities coupled by acoustics. Results indicate that for both types of swirlers, the dynamics is essentially similar for the gains and the phases of the flame describing functions. It is also found that the swirl number value markedly influences the gain response. The characteristic shape of the FDF, with a local minimum and maximum are found in both cases and these features correspond to the mechanisms described previously (swirl number fluctuations and vortex roll-up of the flame. Swirl number fluctuations are induced by the interaction of the incident acoustic disturbances with the swirler. This generates in the two cases a transmitted acoustic wave and a convective vorticity wave. This last wave is characterized by azimuthal velocity perturbations. The mode conversion process giving rise to the latter type of disturbance was already demonstrated in the case of an axial swirler. It is here examined in the radial swirler geometry. It is shown that the mode conversion processes in the two geometries are quite similar and that they produce similar effects on the flame dynamics and response.*

Résumé : *Ce chapitre traite de la réponse des flammes swirlées soumises à des perturbations de vitesses acoustiques lorsque la rotation de l'écoulement est produite par un swirler axial ou radial. L'objectif est de comparer les réponses obtenues dans ces deux cas. La réponse est caractérisée en terme de fonction de transfert généralisée, qui élargit la fonction de transfert de flamme en considérant non seulement la fréquence mais aussi l'amplitude des perturbations de vitesses. Cet outil a montré sa pertinence dans l'étude des instabilités de combustion couplées par l'acoustique. Les résultats indiquent que pour les deux types de swirlers, la dynamique est essentiellement similaire pour les gains et les phases de la réponse. Il est également constaté que la valeur du nombre de swirl influence fortement la réponse en terme de gain. La forme caractéristique de la fonction de transfert généralisée, avec un minimum et un maximum local, se retrouve pour les deux cas de swirlers. Cette réponse caractéristique correspond à des mécanismes décrits précédemment (fluctuations du nombre de swirl et enroulement d'un tourbillon à l'extrémité de la flamme). Les fluctuations du nombre de swirl sont induites par l'interaction des perturbations acoustiques incidentes avec le swirler. Cela génère dans les deux cas (axial et radial) une onde transmise acoustique et une onde tourbillonnaire convectée. Cette dernière est caractérisée par des perturbations de vitesses azimutales. Le processus de conversion de mode à l'origine de ce dernier type de perturbation a déjà été démontré dans le cas d'une vrille axiale. Il est ici étudié dans la géométrie radiale. Il est montré que le processus de conversion de mode pour les deux géométries est très similaire et qu'il produit des effets identiques sur la dynamique de flamme et donc sur la réponse.*

6.1 Introduction

It has been shown in some recent studies that the response of flames to velocity perturbations can be suitably characterized by making use of the flame describing function (FDF). This generalizes the flame transfer function by taking into account the effect of the modulation frequency and of the amplitude of the incoming velocity disturbances as did Noiray *et al.* (2008); Durox *et al.* (2009). The FDF may be included in an acoustic network analysis of combustion systems to predict regions of instability and estimate frequencies and amplitudes of limit cycle oscillations. This analysis has been carried out for a set of conical flames anchored to a perforated plate, see Noiray *et al.* (2008) and to a swirling flame, see Kulkarni and Nicoud (2010) and chapter 9 of the present manuscript. The flame dynamics and response plays a central role in this framework.

In the case of non-swirling flames, the main physical mechanisms controlling the shape of the flame transfer function have been widely analyzed. For conical flames, the acoustic modulation produces wrinkles convected along the flame front resulting in a high response at low frequency. The gain of the flame transfer function approaches unity as the frequency is reduced and the cut-off frequency is reached when one convective wavelength sets along the flame front, see Ducruix *et al.* (2000). It was also shown that the same type of response can be obtained by modifying the dynamics of the flame root, see Kornilov *et al.* (2007) and Preetham *et al.* (2008). "V" flames are more receptive to flow perturbations and convective effects result in a gain exceeding unity, see Schuller *et al.* (2003b). The flame response then results from convected wrinkles along the flame front, see Boyer and Quinard (1990b) also interfering with large vortices shed from the burner lips and synchronized by the acoustic forcing, see Durox *et al.* (2005). This latter mechanism is responsible for vortex rollup at the flame tip producing large flame extinctions and peak values of the gain at characteristic frequencies. It has also been shown that the dynamics of the anchoring points of "V" flames may strongly modify their response, see Perterson and Emmons (1961), Dowling (1999) and Shanbhogue *et al.* (2009). The transfer function of premixed non-swirling flames submitted to velocity perturbations is then mainly determined by three competing mechanisms (a) flame front wrinkling, (b) attachment point dynamics and (c) interaction with coherent structures, which may interfere constructively or destructively. These mechanisms also operate for swirling flames, see Thumuluru and Lieuwen (2009). There are indications in Straub and Richards (1999) and more recently in Hirsch *et al.* (2005) that the swirler has an influence on the dynamics of the flame when it is submitted to incident acoustic perturbations. For example Straub and Richards (1999) show that the axial position of the swirler in the injector element changes the instability characteristics of the system. It is indicated by Hirsch *et al.* (2005) that the swirling jet dynamics are defined by generation and stretching associated with convective effects if the swirler is located upstream. However this article did not provide an estimate of the respective levels of axial and azimuthal perturbations producing fluctuations in swirl strength.

It is shown more recently (chapter 4) that the interaction between an axial swirler and incident acoustic disturbances generates a vorticity wave convected by the flow. This mode conversion process plays a major role because it gives rise to azimuthal velocity disturbances which are convected by the flow and influence the flame dynamics. It is then natural to inquire whether this will also occur in a radial swirler configuration and if the same unsteady flow and flame response features can be found in the radial configuration. This issue is already addressed in a previous paper from Hirsch *et al.* (2005). This article does not provide a theoretical estimate of the conversion process taking place in the swirler. This study was also carried out in the linear regime or at least for a single level of

modulation. As in the present investigation, the equivalence ratio was not the same for both swirler types due to flame stabilization difficulties. It was set to 0.71 for the radial system and to 0.63 for the axial one. The swirl number was not explicitly given but it has been kept equal for both swirlers types and one previous study on the radial swirler indicates a value $S = 0.73$ by Gentemann *et al.* (2004) for the same combustor. Results of this study indicate that phases of the flame transfer function are quite similar for both swirlers while amplitudes differ markedly in the low frequency range. Specifically, the gain curve presents a peak around 100 Hz for the axial swirler whereas the radial one exhibits two distinct maximum values at 40 Hz and 110 Hz. It is however worth noting that the axial and radial swirlers are not located at the same distance from the dump plane in this analysis. In the present study, we show that the two swirler geometries yield the same response when they are placed at the same distance from the dump plane and that the mode conversion process taking place in the two geometries are also quite similar.

At this point it is worth briefly reviewing the literature concerning flame transfer functions of swirling flames generated by axial swirlers. It is abondant, see for example Külsheimer and Büchner (2002), Bellows *et al.* (2007) and chapters 5 and 8 of the present manuscript. These studies consider the combustion dynamics of swirling flames and characterize the role of vortex roll-up on the flame response. Radial swirlers are less well documented except the study from Gentemann *et al.* (2004) where the flame transfer function is experimentally measured and reconstructed by postprocessing data from numerical simulations. The numerical simulations retrieve the shape of the swirling flame gain and phase response.

The swirl number is recognized as a fundamental parameter defining the dynamics of flow and flame as shown in the extensive review from Huang and Yang (2009). In the absence of combustion, the dynamics of a turbulent swirling jet submitted to an acoustic forcing is considered by Alekseenko *et al.* (2008). It is found that an increase of the swirl intensity leads to a higher value of the turbulent kinetic energy. When acoustic forcing amplitude is increased the turbulent kinetic energy increases enhancing mixing. The influence of the swirl number S on the unsteady dynamics of the flow in a swirl injector is considered by Wang *et al.* (2005) who show that the size of the vortex breakdown region is strongly augmented when S takes higher values. The dynamics of two swirling flames respectively with swirl numbers equal to $S = 0.44$ and $S = 1.1$ is simulated by Huang and Yang (2005). It is shown that when the swirl number is increased the flow features a larger inner recirculation zone which moves upstream merging with the recirculation zone of the central bluff body. This specific feature is also examined experimentally in Vanierschot and Van den Bulck (2008) for different

levels of swirl. Another aspect discussed by Huang and Yang (2005) is that an increase in the swirl number strength diminishes the flame length. It appears that a single reference contains experimental data on the influence of the swirl number on the flame transfer function, see Külsheimer and Büchner (2002). It is shown that an increase in the swirl number leads to an augmented flame response when the frequency is fixed. This is at variance with our own conclusions on the influence of the swirl number. But their analysis is concerned with unconfined flames whereas our work focuses on confined swirling flames. In the case of unconfined flames, vortex rings develop in the shear layer between the combustible mixture and ambient air, their interaction with the flame front takes place at the flame tip where fresh ambient air is entrained within the reaction zone. In the case of confined flames, hot gases are entrained within the reaction zone, thus modifying the flame vortex rollup.

It has been recently shown that mode conversion occurring in swirl injectors is fundamental in the understanding of flame dynamics, see chapter 5. Straub and Richards (1999) analyzed the influence of the axial swirler vane location on the flame response and showed that this could be used to suppress self-sustained oscillations. The mechanism of mode conversion was evoked but only partially investigated. This process is identified by Wang and Yang (2005), where large eddy simulations describe effects of an external excitation on the swirling flow dynamics. It is shown that two different propagation modes are involved in swirl injectors : the flow oscillation in the axial direction travelling acoustically while the oscillation in the azimuthal direction propagates at the local flow velocity. Perturbations created at the swirler outlet which modify the flame dynamics are discussed in a few recent studies from Huang and Yang (2009); Wang and Yang (2005); Komarek and Polifke (2010). It is concluded indirectly from transfer function measurements by Komarek and Polifke (2010) that on the downstream side of the swirler the perturbation comprises an acoustic and a convective component. While the presence of this convective component is recognized there are no direct measurements of the axial and azimuthal velocity disturbances. The relative levels of the different perturbations propagating on the downstream side of the swirler are not estimated in these previous references. This is analyzed more recently in chapter 5 for an axial swirler. It is then useful to pursue this analysis by comparing radial and axial swirlers and by measuring the respective velocity disturbances in the injector tube.

This chapter is organized as follows. The swirl-stabilized burner is first described and the axial and radial geometry are given. The velocity profiles measured with a laser Doppler velocimeter are reported and the swirl number of each configuration is calculated. In a second section, swirling flames describing functions are compared in the axial and radial geometries. Another point which deserves

attention is the effect of the mean swirl number on the flame response. This aspect is also considered in that section.

6.2 Experimental configuration

6.2.1 Combustor

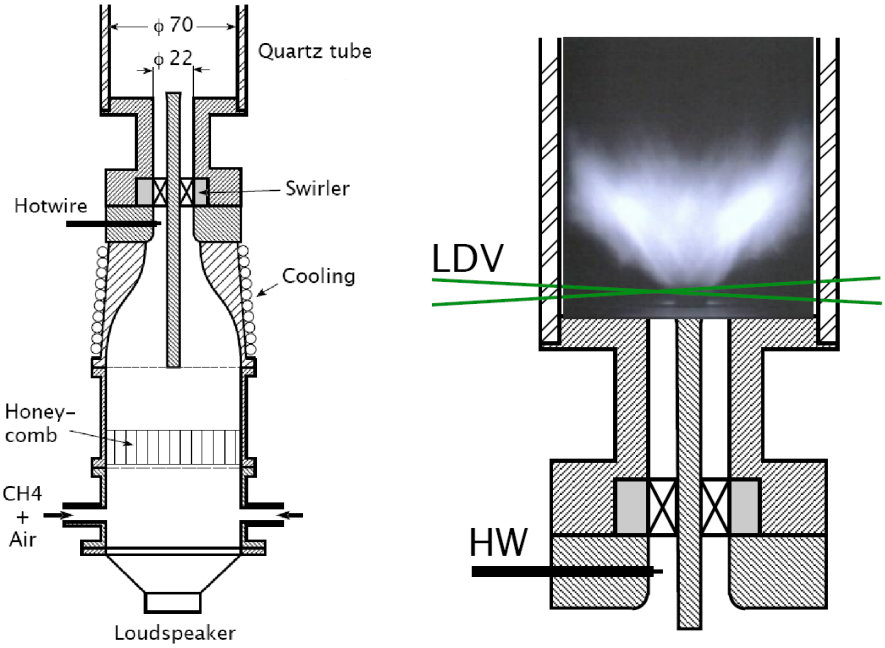

(a) (b)

Figure 6.1: Swirl-stabilized combustor with the axial swirler. The experimental setup is the same with the radial swirler. (a) : Global experimental setup with the loudspeaker generating velocity fluctuations in the flow and located at the base of the burner. The hotwire probe used to measure FDF is located upstream the swirler. (b) : Close-up view of the flame tube with laser beams used to measure the velocity profiles just downstream the injector.

The combustor consists in three sections : an upstream manifold, an injector and a combustion chamber or flame tube as sketched in Fig. 6.1. A methane/air flow enters through two diametrically opposed apertures at the base of the upstream manifold and then flows through a honeycomb piece which breaks the largest turbulent eddies in fine scale fluctuations. The bulk velocity in the injector is $U_b = 2.67$ m s^{-1}. The swirler device induces the rotating motion to the mixture and a swirling flame is anchored to a conical bluff-body stabilizing the flame in the combustion chamber.

To compare the influence of the geometry and swirl number on the flame describing functions, it is natural to try to work at a constant equivalence ratio. For the axial swirler and the first radial swirler ($S = 0.55$), this parameter was set to 0.7 while for the second radial swirler ($S = 0.65$) we use an equivalence ratio of 0.62 as the flame was not well stabilized inside the burner. This small difference is not fundamental as some previous studies indicate that the influence of the equivalence ratio does not significantly influence the flame transfer function (see for example Kang *et al.* (2007)).

To measure the flame describing function, a loudspeaker generates the acoustic velocity disturbances in the flow for a range of frequency from 0 up to 400 Hz and a photomultiplier captures the light radiated by the flame and When the flame is submitted to a velocity fluctuation u' the heat release fluctuates by an amount Q' deduced from the light intensity fluctuation I'. It is assumed as in many previous studies that $Q'/\overline{Q} = I'/\overline{I}$. The laser Doppler velocimeter (LDV) provides the mean and root mean square velocity profiles near the outlet of the injector as sketched in Fig. 6.1 (b).

6.2.2 Axial and radial swirlers

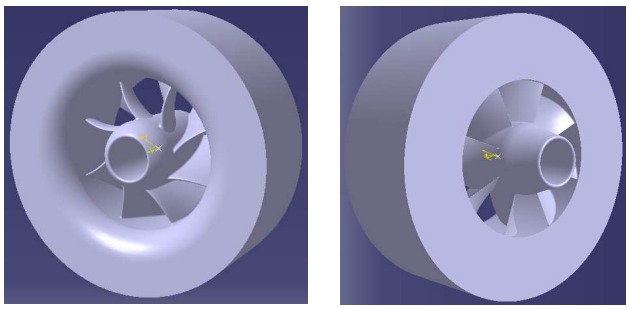

(a) (b)

Figure 6.2: Axial swirler geometry. (a) : upstream side. (b) : downstream side.

Three swirler geometries are considered in this chapter : an axial and two radial swirlers which differ by their swirl numbers. The axial swirler is sketched in Fig. 6.2 while the radial swirlers with $S = 0.55$ is sketched in Fig 6.3. Both geometries are widely used in industrial applications like gas turbines or jet engines and in research studies.

The axial swirler comprises eight vanes periodically spaced by 45°. Vanes are made of NACA 8411 airfoils profiles and the angle of each vane changes with the

radius : the inner vane angle is 30° while the outer vane angle is 58°.

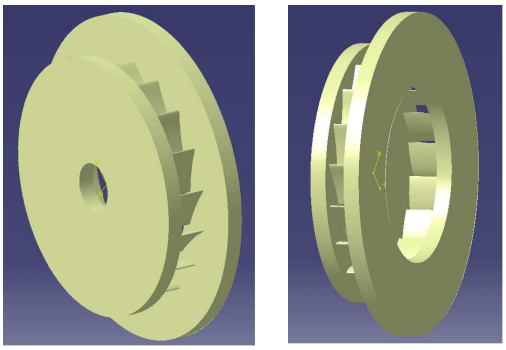

(a) (b)

Figure 6.3: Radial swirler geometry. (a) : upstream side. (b) : downstream side.

The radial swirlers are made of eighteen vanes periodically spaced by 20°. Vanes are made of NACA 8411 airfoils profiles. Two parameters characterize the radial geometry : the thickness of the circular inlet section of the swirler and the vanes trailing edge angle. The trailing edge angle is equal to 58° for the first geometry RS_1 and 72° for the second one (RS_2). The thickness of the circular inlet section is 6 mm for the first swirler and 4 mm for the second one.

6.2.3 Swirl numbers

Mean velocity profiles measured by LDV at the outlet of the injector for the three geometries are now investigated. The swirl number calculation is done according to the following formulae Gupta *et al.* (1984). This is applied to the right side of the velocity profiles :

$$S = \frac{\int_0^R \rho\, u\, v\, 2\,\pi\, r^2\, dr}{R \int_0^R \rho\, u^2\, 2\,\pi\, r\, dr} \tag{6.1}$$

where ρ is the fluid density, u and v respectively the axial and azimuthal velocity components, r the radius and R the characteristic outer radius.

The comparison is first achieve between the axial and the radial swirlers and results of measurements are sketched in Fig. 6.4. The calculated swirl numbers are close to $S = 0.55$ for both swirlers. For the axial swirler, Fig. 6.4 (a), it is found that velocity profiles are not perfectly symmetric and this is probably due to the vane wakes behind the swirler. The maximum of axial velocity is close to 4.1 m s^{-1} while the maximum of azimuthal velocity is near 2.4 m s^{-1}. For the radial swirler RS_1, Fig. 6.4 (b), one also distinguishes slight differences in the

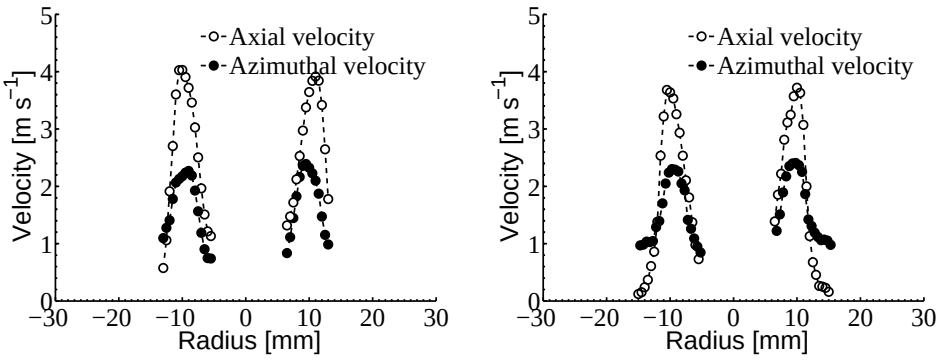

Figure 6.4: Mean velocity profiles of axial and azimuthal components at the injector outlet measured with a laser Doppler velocimeter for $S = 0.55$. (a) : Axial swirler (b) : Radial swirler RS_1.

symmetry of the profiles. In this case, the maximum axial velocity is close to 3.8 m s^{-1} and the maximum azimuthal velocity is 2.4 m s^{-1}.

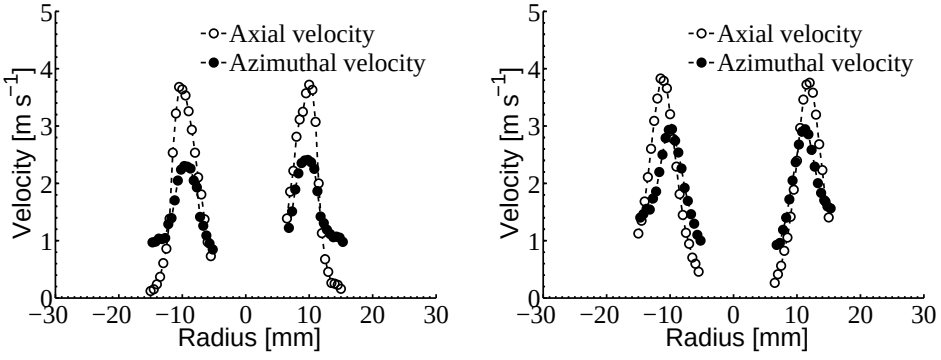

Figure 6.5: Mean velocity profiles of axial and azimuthal components at the injector outlet measured with a Laser Doppler Velocimeter for the radial swirlers. (a) Radial swirler RS_1 : $S = 0.55$ (b) Radial swirler RS_2 : $S = 0.65$

One can now investigate the mean axial and azimuthal velocity profiles generated by the radial swirlers. They are both presented in Fig. 6.5. For RS_1 (Fig. 6.4 (a)), the swirl number is $S = 0.55$ while for the second system RS_2 (Fig. 6.5 (b)) the swirl number is close to 0.65. This can be seen by comparing azimuthal velocity profiles where it is clear that in the RS_2 case, the maximum is 3 m s^{-1} while this maximum is 2.4 m s^{-1} for RS_1. In both cases, the maximum axial velocity reaches a constant value of 3.8 m s^{-1}. While the axial component of the velocity keeps a constant value, the azimuthal component increases reflecting an

increase in swirl number from 0.55 to 0.65.

6.3 Swirling flames describing functions

Experimental swirling flames describing functions are now investigated by first comparing geometrical effects at constant swirl number and then considering swirl number effects for the same radial geometry. All FDFs are presented for a frequency range extending from 0 to 400 Hz and for four acoustic velocity fluctuation amplitudes u'/U_b close to 0.075, 0.15, 0.3 and 0.4. These FDF are defined as the ratio of the relative heat release rate fluctuation $\dot{Q}'/\overline{\dot{Q}}$ to the relative velocity amplitude disturbance $u'/\overline{u}$ so that :

$$\mathcal{F}(\omega, u') = \frac{\dot{Q}'/\overline{\dot{Q}}}{u'/\overline{u}} \tag{6.2}$$

These FDFs can also be written as a complex number highlighting a gain G and a phase Φ :

$$\mathcal{F}(\omega, u') = G(\omega, u')\, e^{i\Phi(\omega,u')} \tag{6.3}$$

The gain G reflects the level of response while the phase Φ defines the time delay between velocity input and heat release rate output signals.

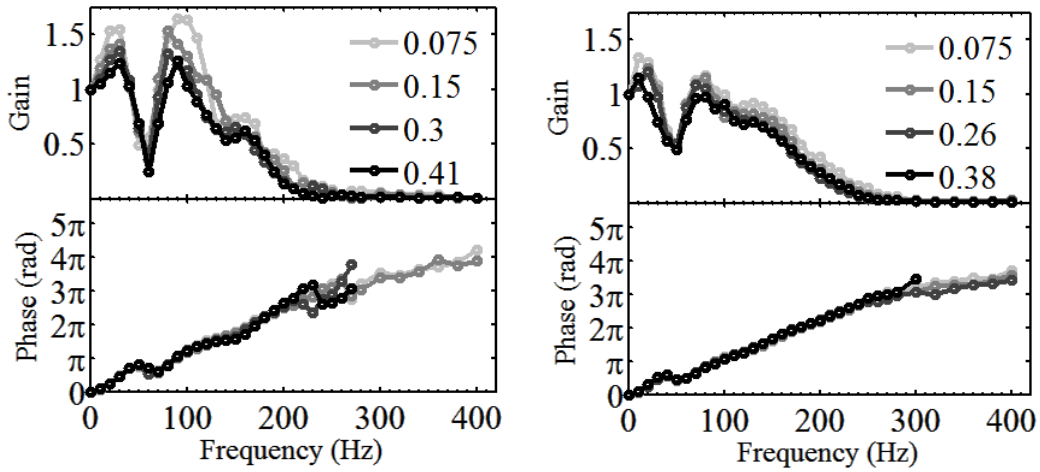

Figure 6.6: Flame describing functions for the axial swirler at $S = 0.55$. Gain G and phase Φ of the FDF are presented for a frequency range from 0 to 400 Hz. Four distinct amplitudes of the velocity disturbances are investigated. (a) : Axial swirler. (b) : Radial swirler.

Flame describing functions obtained with the axial and radial swirlers are respectively presented in Fig. 6.6 (a) and (b) for a constant swirl number equal to $S = 0.55$.

One can start by comparing the gain G of both responses at low relative velocity modulation amplitude $u'/U_b = 0.075$. For the axial swirler in Fig. 6.6 (a), the response presents a peak at 20 Hz where G exceeds 1.5 and then decreases to 0.5 at 55 Hz. Then the gain increases and reaches a second peak at 90 Hz where the response is maximum over the whole frequency range and G equals 1.7. Beyond this frequency value, the gain decreases continuously with slight undulations and above 250 Hz, the flame response to acoustic modulation essentially vanishes. This type of response characterized by a minimum gain followed by a maximum can be predicted by a kinematic description of the flame front motion which combines the effects of flame speed fluctuations resulting from swirl number fluctuations with the transport of convected disturbances, see previous chapters. These two mechanisms prevail and interfere to determine the flame response level. For the radial swirler in Fig. 6.6 (b), the gain highlights the same global behavior with a less intense response. A peak is still present at 20 Hz, but its value is close to 1.3, then the gain decreases and reaches a minimum located at the same frequency as the axial swirler ($f_{min} = 55$ Hz). Beyond this frequency, the gain increases reaching a second peak at about 80 Hz but its intensity is not as strong as in the axial case with a value for G of 1.2. Then the response diminishes continuously and it essentially vanishes beyond 250 Hz. To conclude, both minimum and maximum responses take place at the same frequencies but intensities of theses responses are stronger in the axial swirler case. It is finally important to note that the gain of the flame response decreases when the relative velocity modulation level is increased. This is a key feature of the nonlinear response of such flames.

The case of the axial swirler in Fig. 6.6 (a) highlights the fact that for all amplitudes of velocity disturbances, the phase Φ is almost the same from 0 up to 210 Hz where some slight differences are observed. It is also found that some undulations in the curves are present around 60 Hz. Concerning the radial swirler in Fig. 6.6 (b), the curves are superimposed showing that the phase is not a function of the amplitude of the velocity disturbance. Here also, some undulations are visible around 60 Hz. To conclude, one may say that phase evolutions are very similar and that propagation of perturbations are following the same mechanisms for the two swirler geometries.

Considering next the radial swirler geometry, one may investigate the influence of the swirl number on the flame describing function. For this we compare two radial swirlers with a swirl number respectively equal to $S = 0.55$ and $S = 0.65$.

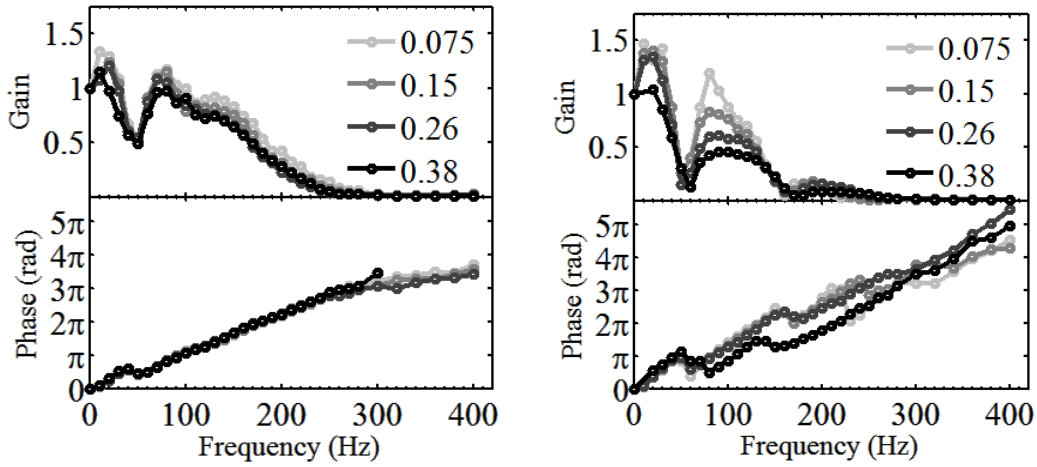

Figure 6.7: Flame describing functions for radial swirler. Gain G and phase Φ of the FDF are presented for a frequency range from 0 to 400 Hz. Four distinct amplitudes of the velocity disturbances are investigated. (a) : Swirl number $S = 0.55$ (b) : Swirl number $S = 0.65$

Results are respectively displayed in Fig. 6.7 (a) and (b). The response of the radial swirler RS_1 with $S = 0.55$ is already described in the previous section. The comparison is now made with results obtained for RS_2 corresponding to $S = 0.65$ for an acoustic velocity disturbance amplitude $u'/U_b = 0.075$. The gain G, now reaches a maximum value at 10 Hz, with a value equal to 1.5. Then, as in the RS_1 case ($S = 0.55$), the gain drops reaching a minimum value of 0.25 at 50 Hz. After that, the gain increases and passes through a local maximum at 80 Hz with a value of 1.2. The gain then continuously decreases with respect to the frequency up to 160 Hz where a characteristic second minimum is recorded which is only observed in the RS_2 case ($S = 0.65$). Beyond 160 Hz, the flame response is weak. To conclude, the dynamics is similar to that found in the RS_1 case for a lower swirl number but intensities of minimum and maximum are stronger in the RS_2 and a second minimum is recorded for the second case. One may also discuss about the influence of the amplitude of the velocity disturbances u'/U_b. Here also, an increase in amplitude implies a decrease of the response but the effect is stronger in the of RS_2 case an less pronounced in the RS_1 case.

The phase evolution highlights a specific behavior : for a threshold value of the ratio u'/U_b close to 0.3, a shift is observed and phase differs significantly from that recorded for the radial swirler RS_1. In both cases, some undulations are seen in the phase, in regions where the gain response features minimum values.

6.4 Mode conversion process

The response of swirling flames formed by an axial swirler is examined in chapter 6 in terms of gain and phase of the FDF. It was specifically shown that the gain curves are the consequence of a combination of processes which can be designated as vortex roll-up of the flame and perturbations induced by swirl number fluctuations. The interference of these two mechanisms was shown to be responsible for the weak and strong response of the flame. This provided an explanation of the low gain value observed at $f = 60$ Hz and the high gain value at $f = 90$ Hz for flame A. This analysis is now extended to the radial swirler geometry. One can still assume that the first mechanism involving vortex roll-up acts at the tip of the flame due to the acoustic wave transmitted downstream the swirler. It is however necessary to confirm that mode conversion also takes place in the radial case giving rise to inducing swirl number fluctuation. This is deduced in what follows from experimental measurements.

We specifically consider the conversion taking place at the swirler when an acoustic wave impinges on this device. We already know from the axial swirl experiments (see chapters 5, 6 and 7) that this gives rise to a transmitted acoustic wave propagating at the speed of sound and to azimuthal velocity perturbations convected by the flow. A phase shift exists between the axial u' and the azimuthal v' velocity fluctuations leading to swirl number fluctuations.
This frequency shift is now examined by recording axial and azimuthal velocity fluctuations in a tube mounted on the downstream side of the swirler. Measurements are carried out with an LDV system. To allow comparisons, results are presented in Fig. 6.8 for the axial swirler at two frequencies of interest $f = 60$ Hz and $f = 90$ Hz for the case where the swirl number is $S = 0.55$. The same measurements are carried out for the radial swirler RS_1 in Fig. 6.9. Due to limitation in the optical access, measurements cannot be carried out between 0 and 59 mm, where 0 mm corresponds to the swirler outlet. It is found from these results that in all cases, the axial velocity fluctuation is acoustic as the phase does not change as a function of the location in the tube while the phase of the azimuthal velocity fluctuation is continuously increasing as a function of the measurement location.

One can also extract from these data the convection velocity of the azimuthal disturbance. Calculations from the slope of the curves leads to the results gathered in Table. 7.1. The convective velocities range between 3.5 and 3.8 m s^{-1}. These data suggest that the convective velocity u_{cv} of the azimuthal disturbances is slightly higher than the bulk velocity in the injector which is $U_b = 2.67$ m s^{-1}. Specifically, the convective velocity of azimuthal disturbances is close to the maximum velocity (4.1 m s^{-1}) determined at the measurement point with LDV. The previous measurements clearly indicate that mode conversion takes place in the

Table 6.1: Convective velocities of azimuthal disturbances expressed in m s^{-1}

Axial swirler f = *60 Hz*	$u_{cv} = 3.7$
Axial swirler f = *90 Hz*	$u_{cv} = 3.8$
Radial swirler f = *60 Hz*	$u_{cv} = 3.5$
Radial swirler f = *90 Hz*	$u_{cv} = 3.6$

radial swirler case and that one may expect the same effects on the flame dynamics as those found in the axial case. This can be further analyzed by comparing these results to those obtained by previous authors using a different swirler and flow conditions. To do so, a Strouhal number $\mathrm{St} = fL/u_{cv}$ can be defined based on the frequency of the minimum flame response, the convective velocity u_{cv} of azimuthal disturbances and the distance L between the swirler outlet and the combustor dump plane. One finds here $\mathrm{St} = 0.67$ for $f = 55$ Hz, $L = 0.043$ m and $u_{cv} = 3.5$ m s^{-1} in the case of the radial swirler (RS_1). The same type of analysis carried out on the configuration explored by Hirsch *et al.* (2005) yields a value $\mathrm{St} = 0.66$ for a different radial swirler operated under different flow conditions corresponding to $L/u_{cv} = 8.8$ ms. These results obtained for different burners, swirler geometries, swirler locations and operating conditions confirm the mechanisms taking place downstream the swirler, where convective and acoustic waves interfere to determine the swirling flame response.

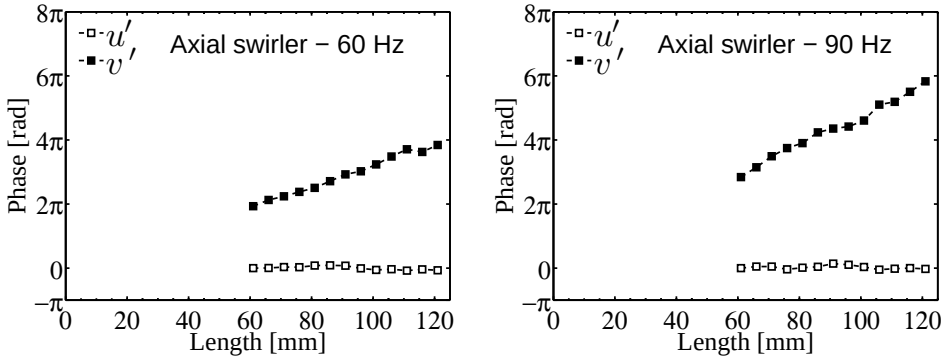

(a) (b)

Figure 6.8: Experimental phase evolution as a function of the tube length at $S = 0.55$ for the axial swirler. (a) : $f = 60$ Hz. (b) : $f = 90$ Hz.

6.5 Conclusion

This chapter focuses on the influence of the swirler geometry and swirl number effects on the response of swirling flames. The first conclusion is that the axial or radial swirler geometry lead to the same characteristic response. Slight differences

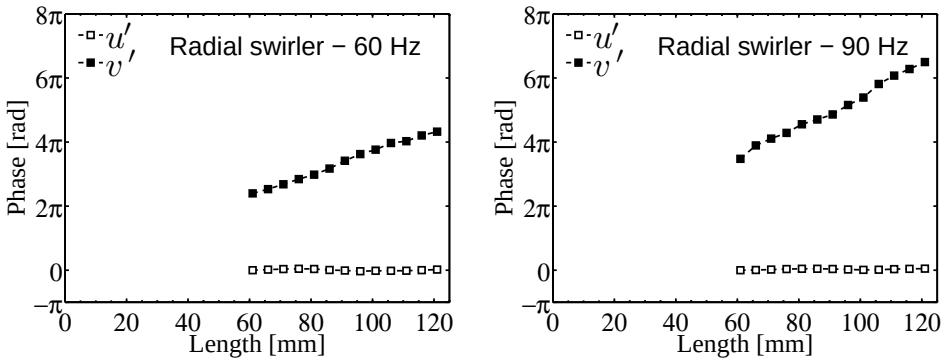

Figure 6.9: Experimental phase evolution as a function of the tube length at $S = 0.55$ for the radial swirler. (a) : $f = 60$ Hz. (b) : $f = 90$ Hz.

are found in the maximum and minimum levels in gain which are slightly lower in the radial geometry. Concerning the swirl number, it is shown here that a moderate increase in the swirl number $S = 0.55$ to $S = 0.65$ leads to strong effects in the amplitude of the flame describing function. For the second swirl number, there is a second peak which is significantly affected by the amplitude of the inlet disturbance u'/U_b and the gain decreases substantially when the relative velocity disturbance level is augmented. This may possibly reflect a modification in the relative importance of the mechanisms controlling the flame response. Another important conclusion is that the minimum of the gain in the response is still located at the same frequency for both axial and radial swirlers confirming the fact that mode conversion is also at work in the radial geometry. This is confirmed by measurements of the phase between the axial and azimuthal velocity fluctuations. This result is of importance in the design of gas turbine combustors and can be used to define improved swirling injectors.

Chapter 7

Large Eddy Simulations of perturbed swirling flames

Abstract : *The dynamics of a turbulent premixed confined swirling flame is investigated using large eddy simulation. The flame response is determined by introducing an external acoustic forcing at two modulation frequencies corresponding to characteristic values of the flame transfer function obtained experimentally. The underlying physical mechanisms identified experimentally are investigated numerically. Simulations confirm that swirl number fluctuations and vortex roll-up govern the flame response. It is also confirmed that the first mechanism is associated with a mode conversion process taking place when acoustic waves impinge on the swirler unit. The axial acoustic velocity disturbance on the upstream side of the swirler generates an axial acoustic wave and an azimuthal convective disturbance in the downstream flow. These combined disturbances are retrieved in the simulation and their effect on the swirl number is extracted. Calculations also indicate that vortex shedding synchronized by the acoustic forcing takes place at the injector lip outlet. Vortices originating from this region are convected in the jet shear layer, impinge on the flame and roll-up the flame tip. This process interferes with oscillations in the flame angle induced by swirl number fluctuations. Phasing of the flame angle with respect to the instant of vortex shedding from the injector lips determines the lifetime of the vortex before interaction with the flame and controls the strength of this interaction. When this lifetime is reduced, the vortex cannot fully develop and the flame response remains weak. For larger lifetimes, the vortex can fully develop and produce larger heat release rate perturbations. This process depends on the forcing frequency which determines the phasing between swirl number fluctuations and vortices generation.*

Résumé : *La dynamique d'une flamme swirlée prémélangée turbulente est étudiée au moyen de la simulation numérique aux grandes échelles. La réponse de la flamme est déterminée en introduisant un forçage acoustique externe à deux fréquences de modulation correspondant à des valeurs caractéristiques de la fonction de transfert de flamme obtenues expérimentalement. Ces valeurs caractéristiques de la réponse diffèrent en terme de gain. Les mécanismes physiques sous-jacents identifiés expérimentalement sont étudiés numériquement. Les simulations confirment que les fluctuations du nombre de swirl et que le vortex rollup régissent la réponse de la flamme. Il est également confirmé que le premier mécanisme est associé à un processus de conversion de mode qui a lieu lorsque les ondes acoustiques impactent le swirler. La perturbation de vitesse axiale acoustique sur le côté en amont du swirler génère une onde acoustique axiale et une perturbation convective azimutale en aval de celui-ci. Ces mécanismes sont restitués par les simulations numériques. Les calculs indiquent également que les tourbillons responsables du rollup sont synchronisés par le forçage acoustique à la sortie des lèvres de l'injecteur. Ces tourbillons sont ensuite convectés dans la couche de cisaillement du jet et interagissent sur la flamme en provoquant le roll-up de l'extrémité de la flamme. Ce processus interfère avec les oscillations de l'angle de la flamme induite par les fluctuations du nombre de swirl. La phase entre l'angle de la flamme et la formation des tourbillons au bord de l'injecteur détermine la durée de vie du tourbillon avant son interaction avec la flamme et contrôle l'intensité de cette interaction. Lorsque cette durée de vie est réduite, le tourbillon ne peut pas se développer pleinement et la réponse de la flamme reste faible. Pour les plus longues durées de vie, le tourbillon peut se développer pleinement et produire de plus grandes perturbations du taux de dégagement de chaleur. Ce processus dépend de la fréquence qui détermine la phase entre les fluctuations du nombre de swirl et la génération des tourbillons.*

7.1 Introduction

The study is motivated by the dynamical problems encountered in practical combustors and in particular in devices using lean premixed combustion where flashback (see for example Plee and Mellor (1978)), flame blowout and self-sustained oscillations (see Candel (2002); Lieuwen and Yang (2005)) may develop. In this combustion mode, the flame is often stabilized in swirling flows featuring complex unsteady interactions between the flame and the flow. The aim of this chapter is to enhance the physical understanding of the processes which determine the flame response to incident disturbances. This is accomplished by suitably com-

bining Large Eddy Simulations (LES) and analysis to retrieve the fundamental mechanisms identified in some recent experiments. The present work is focused on swirling flames perturbed by acoustic disturbances travelling in the upstream flow. It specifically considers the processes taking place when these waves cross the swirler unit and reach the injector exhaust section. This gives rise to different types of disturbances traveling in the downstream flow direction and produce competing flow interactions perturbating the flame response and generating heat release fluctuations. These mechanisms are investigated with LES. Results obtained numerically are compared with well controlled experiments carried out previously.

Many elementary mechanisms can be responsible for heat release rate perturbations and have been the subject of different reviews from Candel (2002); Ducruix *et al.* (2003); Lieuwen and Yang (2005). These mechanisms eventually operate simultaneously and it is difficult to sort the dominant ones for swirling flames, see Thumuluru *et al.* (2007). Scenarios have however been proposed to explain some of the key elements and parts of the global flame response. These different contributions are examined below and are combined to put in light two competing mechanisms determining the response of weakly turbulent swirling flames. This analysis extends a work carried out in chapter 4 and 5 where it is shown that acoustic disturbances impinging on the swirler generate transverse velocity perturbations which are convected by the flow. The flow downstream the swirler features then axial and azimuthal velocity perturbations propagating at different speeds. They induce swirl number fluctuations at the burner outlet and as a result the flame executes a breathing motion with oscillation of the flame root angle. Vortex roll-up takes also place when the axial perturbations reach the injector exhaust section. These vortices are convected by the flow and interact with the flame rolling up its tips. Vortex rollup and flame root angle fluctuations combine constructively or destructively depending on the forcing frequency of the incoming velocity perturbations leading to a low or a strong response of the swirling flame, see chapter 5. Conditions under which these flame responses can be obtained were not fully investigated yet and this is the purpose of the present study. It is now worth reviewing the different contributing mechanisms.

The impact of swirling strength fluctuation on the flame transfer function was first envisaged by Hirsch *et al.* (2005). This was used to explain some experimental observations for the flame transfer function which features amplitudes exceeding unity and different behaviours for radial or axial swirler types. The scenario proposed is based on fluctuations of the flowrate and of the circulation induced by the swirling flow inside the burner. It is shown that these latter perturbations are converted at the burner outlet into azimuthal vorticity fluctuations which are then transported along a streamsurface of the swirling jet downstream the annular exit. It is assumed that the azimuthal vorticity component is con-

vected along a diverging conical shell of constant angle α. The vorticity strength increases with the relative distance from the burner caused by the diverging jet and is superimposed with growing oscillations. This creates additional velocity fluctuations via the Biot-Savart law impinging on the flame. In this scenario, the flame response then results from direct velocity perturbations due to flowrate fluctuations at the burner outlet and vortex induced additional velocity perturbations. Using this model it is shown that the flame transfer function mainly depends on the location of the swirler and less on the type of swirler used. The possibility of swirl angle fluctuations is however not evoked in this study and the relation between the different velocity components at the burner outlet is determined heuristically using a convective time lag. In a recent analysis, it is concluded indirectly from transfer function measurements in Komarek and Polifke (2010) that on the downstream side of the swirler the perturbation comprises an acoustic and a convective component but the impact of the acoustic and convective perturbations on the flame dynamics is not fully discussed.

Dynamics of swirling flames was recently reviewed by Huang and Yang (2009). The influence of the swirl number on the flame dynamics is discussed by Huang and Yang (2005) for two swirling flames characterized by very different swirl numbers and respectively equal to $S = 0.44$ and 1.1. Simulations indicate that an increase in this number results in a larger inner recirculation zone which moves upstream to merge with the recirculation zone of the central bluff-body. It is also found that an increase in swirl strength strongly reduces the flame length. The swirl number also influences the unsteady dynamics of the flow and the vortex breakdown region is enhanced with a higher value of this number, see Wang *et al.* (2005). The case of acoustic perturbations impinging swirlers has also been examined in Wang and Yang (2005). It is deduced from LES that axial and azimuthal velocity disturbances propagate at different velocities on the downstream side of the swirler.

Many contributions also concern the possible interferences between different types of perturbations. Indeed, different parts of the perturbed flame may enhance or cancel out local heat release fluctuations from other parts, see Shanbhogue *et al.* (2009); Shin *et al.* (2008), producing maximum and minimum responses in the global transfer function, see Preetham *et al.* (2008), depending on the phase relationship of the different effects. It is specifically shown that interference phenomena both in the distribution of heat release and in the global transfer function arise because the flame is excited by multiple disturbances propagating at different speeds.

Experiments reported by Kim *et al.* (2009); Kim *et al.* (2010) deal with the effect of flow modulations on the dynamics of confined swirling flames and provide some

Table 7.1: Experimental parameters

Equivalence ratio	0.7
Injector bulk velocity [m s^{-1}]	2.67
Swirl number	0.55
Reynolds number	3 500
Acoustic modulation level u'/U_b	0.51
Flame tube diameter [mm]	70
Injector diameter [mm]	22

of the transfer function data needed to predict thermo-acoustic instabilities and limit cycles in combustion chambers. A laboratory-scale gas turbine combustor is used to measure flame transfer functions and predict instability frequencies mainly in the linear regime, see Kim *et al.* (2009). Flame transfer functions measured with this type of burner indicate that the Strouhal number constitutes a relevant dimensionless parameter and data show the effect of the flame angle, see Kim *et al.* (2010).

Simulations reported in the present chapter are carried out to examine premixed swirling flame dynamics in a well controlled experimental configuration with three objectives : (1) Compare numerical predictions with experimental data to validate the numerical approach; (2) Examine the mechanisms identified experimentally and see if they can be retrieved numerically; (3) Complement the available data with additional information generated by the simulation and provide a simple mechanism explaining strong and low swirling flame response to incoming perturbations. The experimental geometry is briefly presented in section 2 together with a typical flame transfer function. The main features of the Navier-Stokes LES flow solver are reviewed in section 3 and initial results are obtained for the flame in absence of modulation. Unsteady flame dynamics is considered in section 4. The last section is focused on the mechanisms of mode conversion at the swirler and on the flame / vortex interactions. Effects of swirl number fluctuations and vortex roll-up are described and their interference is investigated.

7.2 Experimental conditions

7.2.1 Setup

The experimental setup sketched in Fig. 7.1 consists of four elements: (1) An upstream manifold; (2) An injector equipped with a swirler; (3) A quartz tube

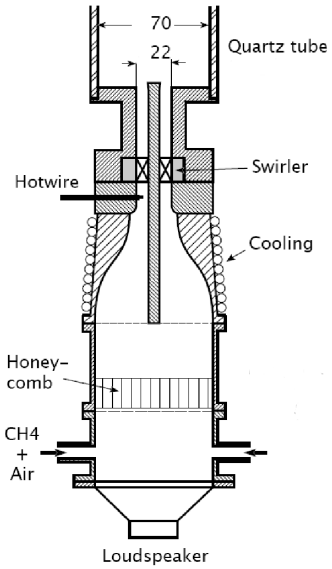

Figure 7.1: Experimental setup with sizes in millimeters. It consists in a upstream manifold, a swirler, an injector and a flame tube in quartz.

confining the flame; (4) A loudspeaker located at the bottom of the system. A premixed flow of air and methane with an equivalence ratio equal to 0.7 is introduced at the base of the upstream manifold through two diametrally opposed apertures. In order to break the largest turbulent eddies, this flow passes through a grid and a honeycomb layer. The flow then traverses a convergent unit decreasing the boundary layer thickness and defining a flat velocity profile at the swirler inlet. The swirler imparts a rotating motion to the flow. It is made of eight NACA airfoil vanes periodically spaced. More details on the experimental setup can be found in chapter 2.

7.2.2 Flame transfer function

The flame transfer function defined as the ratio of relative heat release rate to velocity fluctuation is here used to characterize the response of the flame to incident velocity disturbances : $\dot{Q}'/\overline{\dot{Q}} = G\exp(i\varphi)u'/U_b$, where u' is measured at the burner outlet and U_b correspond the bulk velocity in the injector. This leads to a gain G and a phase φ as a function of the frequency. This response plotted in Fig. 7.2 for a relative velocity modulation equal to $u'/U_b = 0.51$ shows two distinct behaviors at $f = 60$ Hz and $f = 90$ Hz, which respectively correspond to low and high values of the gain. It is of interest to understand the underlying dynamics defining these very different flame responses.

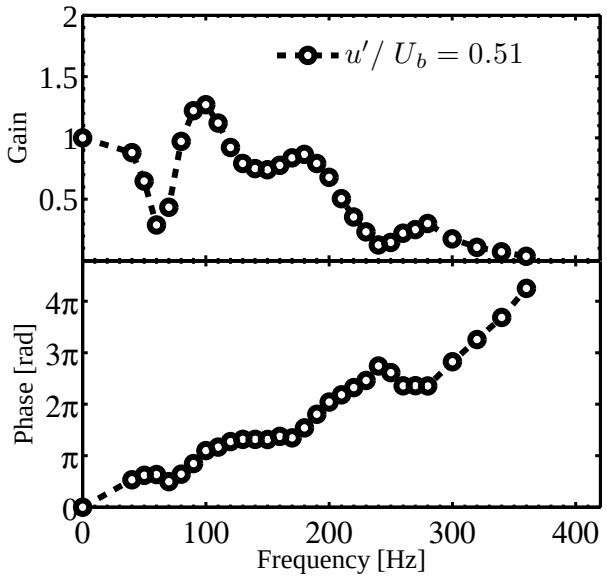

Figure 7.2: Flame transfer function determined experimentally for a frequency range of 0 to 400 Hz at a relative velocity modulation $u'/U_b = 0.51$ where U_b is the bulk velocity in the injector duct and u' the rms velocity fluctuation level. The gain is plotted in the top figure while the phase between the velocity signal and the heat release rate signal is plotted in the bottom figure.

It is first worth examining time traces of relative heat release rate signals determined experimentally to reveal the differences between the flame response at the two characteristic frequencies and get some insight on the nonlinearity of this response. The signals plotted in Fig. 7.9 indicate that with a modulation frequency $f = 90$ Hz, the amplitude of the relative heat release rate signal $\dot{Q}'/\overline{\dot{Q}}$ is much higher than that observed at $f = 60$ Hz. The amplitude of the velocity modulation was kept constant at the two forcing frequencies and it is essentially sinusoidal with a very little harmonic content, but the two heat release rate rate signals are nonlinear. The waveform determined at 60 Hz is markedly different from a sinusoid.

7.3 Numerical simulations

7.3.1 Large Eddy Simulation code

Simulations are carried out with AVBP, a code developed at Cerfacs (see Schönfeld and Rudgyard (1999); Staffelbach *et al.* (2009)) to solve the laminar or turbulent compressible Navier-Stokes equations in three space dimensions. In the turbulent case, the LES balance equations for mass, momentum and energy are solved by

the code. The filtered quantity $\overline{f}$ is determined while the subgrid scale fluctuation $f' = f - \overline{f}$ is modeled. As the density is variable, a mass-weighted Favre filtering is adopted so that $\overline{\rho}\widetilde{f} = \overline{\rho f}$. One important difficulty in reactive flows lies in the representation of the filtered reaction rates. It is shown in many previous studies that a suitable model for fully premixed laminar flames is obtained by artificially thickening the reaction layers, see Colin *et al.* (2000). In practice and in order to resolve the flame on the relatively coarse mesh as used in LES, the flame front is thickened by modifying the preexponential factor and changing the transport coefficients but the local burning velocity is conserved. In the case of turbulent reacting LES, the Thickened Flame Model (TFM) introduces modifications in the interaction of turbulence with the flame front. It is thus necessary to compensate this missing distorsion by introducing a sub-grid scale wrinkling model. This is done with an efficiency function determined from direct numerical simulations. This efficiency function describes effects of the sub-grid scale wrinkling as a function of the local sub-grid turbulence velocity u' and spatial filter size Δ. After closure, one obtains the following set of filtered modeled equations:

- Momentum

$$\frac{\partial \overline{\rho}\widetilde{u}_i}{\partial t} + \frac{\partial}{\partial x_j}(\overline{\rho}\widetilde{u}_i\widetilde{u}_j) = -\frac{\partial}{\partial x_j}\left[\overline{p}\delta_{ij} - 2(\overline{\mu}+\mu_t)(\widetilde{S}_{ij} - \frac{1}{3}\widetilde{S}_{ll}\delta_{ij})\right], \tag{7.1}$$

  where ρ refers to the density, u to the velocity, p to the pressure, μ to the dynamic viscosity of the gas and S_{ij} is the strain rate tensor. Subscripts i, j and l refer to the three spatial dimensions while t denotes turbulence. The sub-grid scale turbulent viscosity μ_t is modeled through the WALE model (see Ducros *et al.* (1998)) which provides a suitable description of the sub-grid scale dynamics in free shear flows and also recovers the scaling laws in wall regions.

- Energy

$$\begin{aligned}
&\frac{\partial \overline{\rho}\widetilde{E}}{\partial t} + \frac{\partial}{\partial x_j}(\overline{\rho}\widetilde{E}\widetilde{u}_j) = -\frac{\partial}{\partial x_j}\left[\widetilde{u}_i\overline{p}\delta_{ij} - 2\overline{\mu}\widetilde{u}_i(\widetilde{S}_{ij} - \frac{1}{3}\widetilde{S}_{ll}\delta_{ij})\right] \\
&+ \frac{\partial}{\partial x_j}\left[c_p\mathcal{E}\mathcal{F}\frac{\overline{\mu}}{Pr}\frac{\partial \widetilde{T}}{\partial x_j}\right] \\
&+ \frac{\partial}{\partial x_j}\left[\sum_{k=1}^{N}\left(\mathcal{E}\mathcal{F}\frac{\overline{\mu}}{S_{c,k}}\frac{W_k}{W}\frac{\partial \widetilde{X}_k}{\partial x_j} - \overline{\rho}\widetilde{Y}_k(\widetilde{V}_j^c + \widetilde{V}_j^{c,t})\right)\widetilde{h}_{s,k}\right] \\
&+ \frac{\mathcal{E}\dot{\omega}_T}{\mathcal{F}}.
\end{aligned} \tag{7.2}$$

In this equation, E denotes the total energy per unit mass, $\mathcal{E}$ is the efficiency function, $\mathcal{F}$ is a flame thickening factor ($\mathcal{F} = 3.3$ in the present simulations), T is the temperature and c_p the specific heat of the working fluid. The quantity W indicates the mean molecular weight of the mixture, X and Y are the species molar and mass fractions respectively. The vectors $\widetilde{V}_j^c + \widetilde{V}_j^{c,t}$ are the diffusion velocities, the scalars $h_{s,k}$ correspond to the sensible enthalpies per unit mass and $\dot{\omega}_T$ refers to the reaction rate defined by an Arrhenius expression.

- Species

$$\frac{\partial \overline{\rho}\widetilde{Y}_k}{\partial t} + \frac{\partial}{\partial x_j}(\overline{\rho}\widetilde{Y}_k\widetilde{u}_j) = \frac{\partial}{\partial x_j}\left[\mathcal{E}\mathcal{F}\frac{\overline{\mu}}{S_{c,k}}\frac{W_k}{W}\frac{\partial \widetilde{X}_k}{\partial x_j} - \overline{\rho}\widetilde{Y}_k(\widetilde{V}_j^c + \widetilde{V}_j^{c,t})\right] + \frac{\mathcal{E}\dot{\omega}_k}{\mathcal{F}}. \tag{7.3}$$

where $\dot{\omega}_k$ refers to the reaction rate of each species computed with the Arrhenius law.

The finite rate chemistry is modeled by a single step global reaction involving four species and a diluent CH_4, O_2, CO_2, H_2O and N_2 :

$$CH_4 + 2O_2 \rightarrow CO_2 + 2H_2O \tag{7.4}$$

The volumetric reaction rate of this single step reaction $\dot{\omega}_0$ given in mol m^{-3} s^{-1} is defined by an Arrhenius law :

$$\dot{\omega}_0 = A\left[\frac{\rho Y_{CH_4}}{W_{CH_4}}\right]^{n_{CH_4}}\left[\frac{\rho Y_{O_2}}{W_{O_2}}\right]^{n_{O_2}}\exp(-E_a/RT) \tag{7.5}$$

where the pre-exponential factor A is equal to 6.98×10^9 S.I. units, the activation energy E_a is 20 000 kJ mol^{-1}, n_{CH_4} is 1.0 and n_{O_2} is 0.5. These values were adjusted to yield a laminar burning velocity which coincides with that determined experimentally, see Martin *et al.* (2006).

7.3.2 Mesh and boundary conditions

A fully unstructured mesh is used in the present calculations because it is well adapted to the complex experimental geometry. A part of this mesh is represented in Fig. 7.3. The choice was made to discretize the complete burner from the upstream manifold to the end of the flame tube. The mesh is made of 6 millions tetrahedral cells and the minimum cell volume is 3.73×10^{-12} m^3. Time integration is third order in time, see Coli and Rudgyard (2000), explicit and with

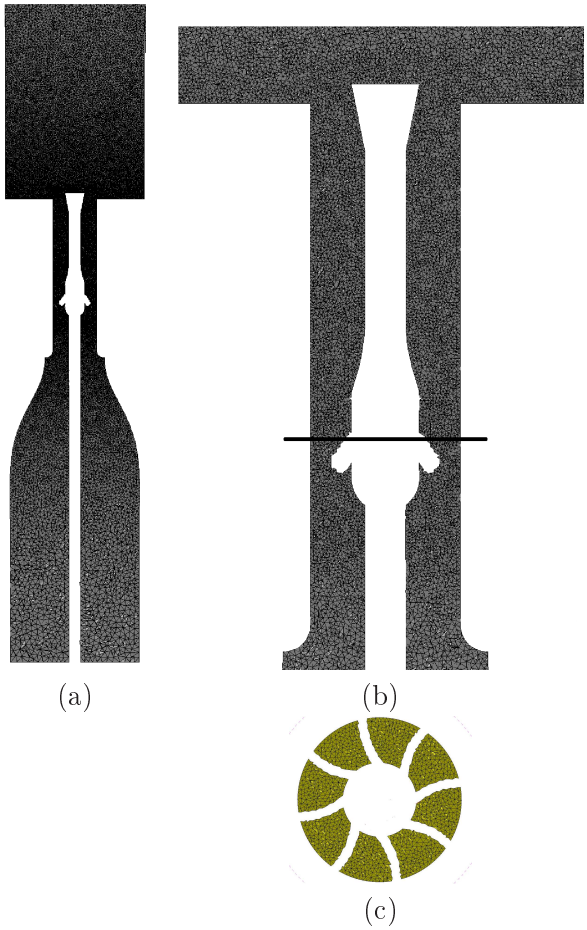

Figure 7.3: (a): View of a longitudinal cut in the mesh used to represent the burner, injection duct and flame tube. (b): Close-up view of the mesh with the cutting line in black where (c) is obtained. Note that a very large volume is used to simulate the ambient atmosphere and connects to the flame tube (not shown in this figure). (c) : transversal cut of the mesh at the center of the swirler indicating cells around the eight vanes.

a fixed time step equal to $1.25\,10^{-7}$ s. All walls are treated as no-slip boundary conditions. A very large volume is used to simulate the ambient atmosphere so that the flow and waves are suitably exhausted from the flame tube. On the large volume downstream side, the boundary condition is non-reflecting. This is also the case for the system inlet allowing an easy modulation using an incoming characteristic wave condition, see Poinsot and Lele (1992); Kauffmann *et al.* (2002). The flame tube walls are adiabatic while the backplane and the central rod are isothermal with temperatures respectively fixed at 600 and 650 K.

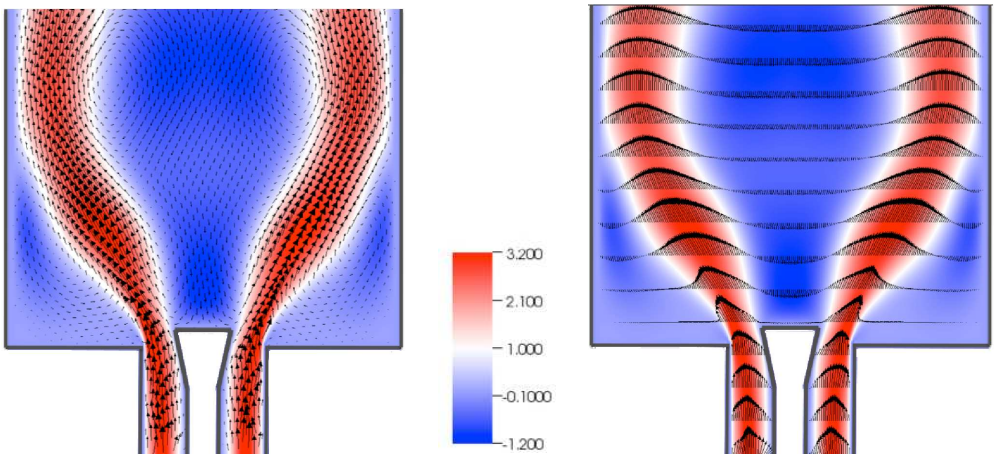

Figure 7.4: Time and azimuthal averages of the axial velocity field plotted on a color scale. The superimposed average velocity vectors correspond to an axial slice through the system.

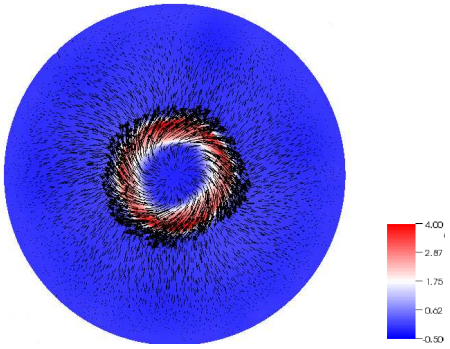

Figure 7.5: Top view of the time average axial velocity field. Instantaneous velocity vectors are superimposed.

7.3.3 Modulation free flame

It is natural to first consider the modulation free flame. A general view of the mean flow in the system determined from the simualtion is given in Figs. 7.4 and 7.5. The annular jet flow is diverging at the burner outlet separating an outer recirculation zone from a central inner recirculation zone. The highest shear stresses are found on the external jet branches as indicated by the velocity profiles in right part of Fig. 7.4. The top view in Fig. 7.5 indicates that the geometrical axis of the flame tube and the center of the vortex breakdown region are identical which confirms that no precessing vortex core is at work in the present experiment.

One may now compare results of simulation and measurements by examining

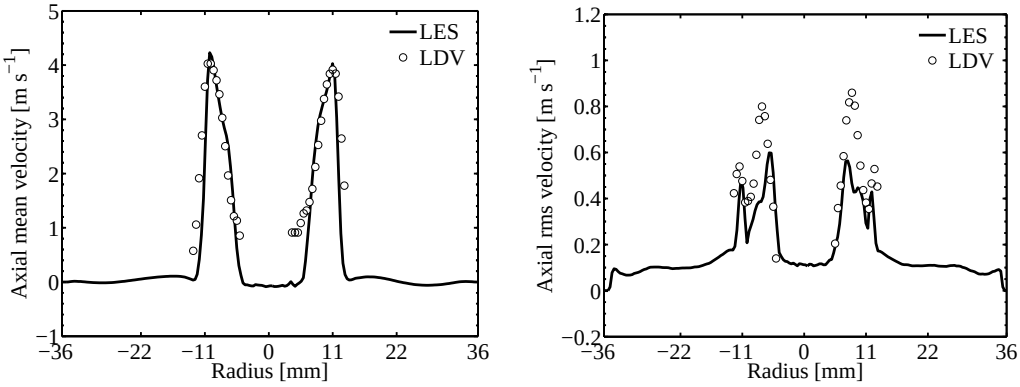

Figure 7.6: Radial profiles of time average and rms axial velocity component u in a section located at 4 mm downstream of the injector outlet.

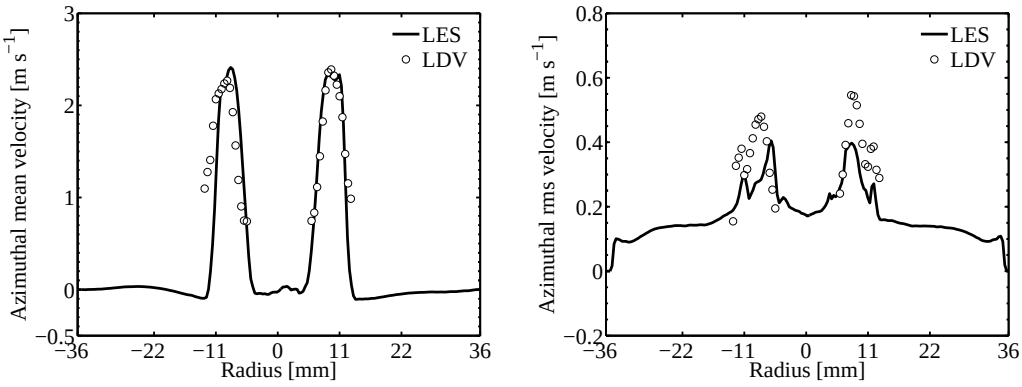

Figure 7.7: Radial profile of time average and rms azimuthal velocity component v_θ in a section located at 4 mm downstream of the injector outlet.

the mean and rms profiles of axial and azimuthal velocities plotted in Fig. 7.6 and Fig. 7.7 respectively. One finds that the simulation provides fairly accurate mean velocity profiles but that the rms distributions are slightly underestimated with LES. One explanation is that the calculated rms profiles do not account for the subgrid scale fluctuations. In addition, in the experimental setup, the flow is introduced through orifices and the corresponding fluctuations are not completely eliminated by the honeycomb grid. This geometric specificity of the apparatus is not modeled in the calculation. As a consequence the flow in the injector features a higher level of fluctuations than in the simulation. The grid size used in the simulation is also perhaps too coarse to fully account for the wakes formed by the trailing edges of the swirler blades. It is also useful to examine the experimental and numerical rates of swirl. This may be quantified in terms of a swirl number

$$S = \frac{\int_{r_1}^{r_2} \rho\, u\, v_\theta\, 2\,\pi\, r^2\, dr}{r_2 \int_{r_1}^{r_2} \rho\, u^2\, 2\,\pi\, r\, dr} \tag{7.6}$$

The swirl number measured in the experiment is 0.55 and the simulation yields a value of 0.58 which is quite close. Another important variable in reacting flows is the distribution of volumetric heat release rate. Experimental values of this quantity are deduced from images of light emission from free radicals like OH* and CH*. Average emission images are Abel transformed to obtain a slice through the flame and a special procedure (see chapter 2) is used to scale the result in W m^{-3}. Experimental data plotted in Fig. 7.8 features a certain amount of noise associated with the Abel transform. If compared to LES, one finds that the distributions of volumetric heat release rate are similar. The flame brush is slightly thicker in the experiment and the maximum rates are in agreement reaching in both cases a value close to 180 MW m^{-3} which is quite typical of atmospheric premixed hydrocarbon flames at a moderate Reynolds number and an equivalence ratio of 0.7. One also remarks that the left part of the flame is more intense both in the experiments and in the simulations. Flame angle and flame brush thickness are also in good general agreement. The main difference is found at the extremity of the flame where the simulated flame shape is between a "V" and an "M" flame and corresponds not strictly to a "V" flame as in the experiment. These differences may be explained in various ways. It is also possible that the boundary conditions used in the simulation do not quite match the experimental values. The flame tube is treated as an adiabatic wall in the calculation which it is not the case in the experiment. The difference is however minor and one may conclude that the natural flame is well represented in the simulation.

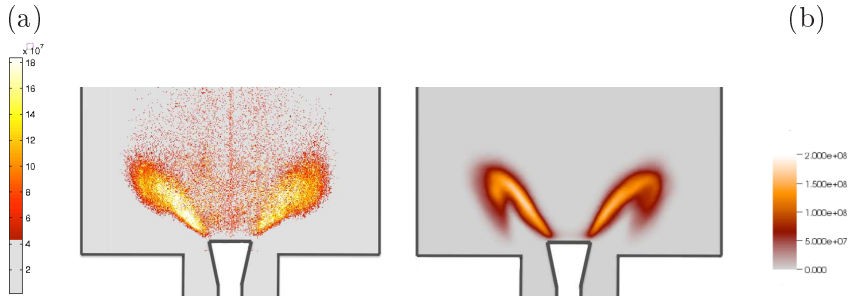

Figure 7.8: Volumetric heat release rate distribution in W m^{-3}. Experimental data on the left are obtained by averaging chemiluminescence emission images, taking an Abel transform and scaling the result in terms of volumetric heat release rate. Numerical simulations on the right are obtained by taking axial cuts through the flame and calculating time average distributions of volumetric heat release rate.

7.4 Perturbed flame dynamics

7.4.1 Retrieving experimental signals

The flow is now modulated by a sinusoidal axial velocity perturbation introduced at the bottom of the burner. This produces fluctuations in heat release rate which are plotted in Fig. 7.9. Results of simulations are obtained by phase averaging the

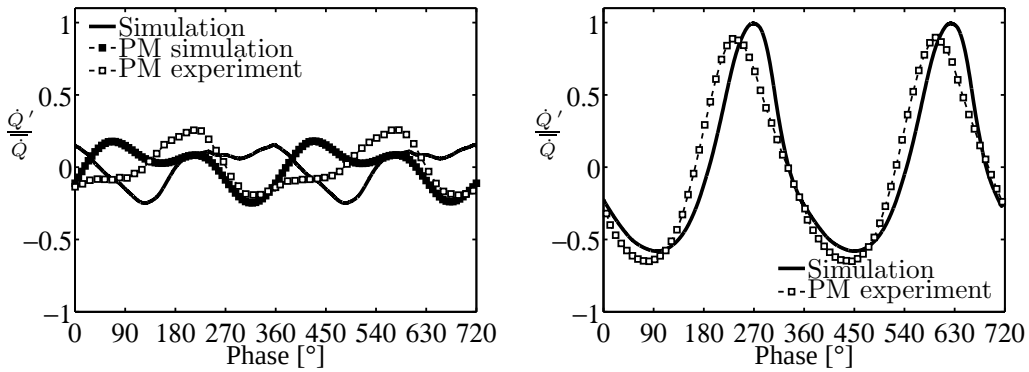

Figure 7.9: Heat release rate signals $\dot{Q}'/\overline{\dot{Q}}$. Solid lines correspond to simulation results and are obtained by phase averaging over nine periods of modulation. Black square curve is obtained by integrating the heat release rate in a window which captures the signal that would be recorded by a photomultiplier like in the experiment. This window excludes points located inside the injector and does not account for heat release associated with the part of the flame which flashes back. Open square curve is obtained experimentally with a photomultiplier capturing the light radiated by the flame but not that originating from the flame inside the injector. (a) $f = 60$ Hz. (b) $f = 90$ Hz.

Table 7.2: Flame transfer function

	$f = 60$ Hz	$f = 90$ Hz
Experimental Gain	0.29	1.22
Experimental Phase [rad]	1.98	2.66
Numerical Gain	0.30	1.05
Numerical Phase [rad]	–	2.05

instantaneous signal over nine periods. The relative fluctuation $\dot{Q}'/\overline{\dot{Q}}$ is shown as a function of phase angle during two periods for the characteristic frequencies $f = 60$ Hz and $f = 90$ Hz. Before comparing these results with experimental data, it is important to note that the photomultiplier measuring heat release rate signals in the experiment does not capture the whole light radiated by the flame if the flame travels into the injector. This actually takes place at $f = 60$ Hz. It is then necessary to extract the signal which would be recorded by a photomultiplier. This consists in limiting the integration of heat release to a window similar to the experimental observation window (i.e. excluding the injection duct). Results are plotted as black square symbols. These data can then be compared with the experimentally determined heat release rate signals also plotted in Fig. 7.9 (a) and (b). At $f = 60$ Hz, both experimental and numerical results agree in terms of signal amplitudes. The maximum and minimum responses are also found at the same phase in the cycle. The shape of the signal is however not perfectly reproduced by the numerical simulation. One can also conclude that flashback has no effect on the amplitude of the heat release rate by comparing both signals at $f = 60$ Hz but a strong effect on the phase of these signals. At $f = 90$ Hz, the amplitude of experimental and numerical signals agree well with only a slight shift in phase. The shape of the signal is accurately reproduced by the numerical simulation.

From both numerical simulations performed in this chapter at respectively $f = 60$ Hz and $f = 90$ Hz, it is possible to retrieve signals determined experimentally. This can be used to obtain estimates of the flame transfer function and compare the values obtained with those given in Fig. 7.2. The velocity signals are determined at the location used in the experimental setup and are used as inputs of the flame transfer function while the global heat release rate signals are used as outputs of the flame transfer function to determine the numerical flame response. Results are gathered in Table 7.2 which compares data for the gain and the phase of the flame transfer function determined experimentally and numerically. At the modulation frequency of 60 Hz the global heat release rate signal is calculated in the region which can be observed experimentally with the photomultiplier. This excludes locations inside the duct which are swept by the flame during a small part of the cycle. A reasonable agreement is obtained but the phases are less well predicted than the gains.

7.4.2 Combustion dynamics

The dynamics is now examined by considering the evolution of the volumetric heat release rate distribution during a modulation cycle. Experiments were previously carried out by generating a plane acoustic wave with a loudspeaker located at the base of the burner. Light emission by the flame was recorded with an ICCD camera. Six phase-locked images were recorded during an oscillation cycle to define the motion of the flame at the modulation frequency. Each image, separated by a phase angle of 60°, was formed by accumulating one hundred instantaneous images. An Abel transform was then applied to each image to get the two-dimensional flame slice. The final images are scaled in terms of volumetric heat release rate and the levels are given in W m^{-3}. Results are plotted in Fig. 7.10.

Numerical simulations are also phase averaged by calculating the dynamics over nine periods and by spatially averaging the results over thirty two axial slices around the axis. Results are plotted in Fig. 7.11 for the two modulation frequencies. Comparison between experiments and numerical results indicate that the dynamics is well retrieved by LES and for both frequencies. Specifically, the flame motion combining large flame angle fluctuation at the flame root and vortex rollup is accurately captured at $f = 60$ Hz. At $f = 90$ Hz, the numerical simulation retrieves previous experimental results where oscillations in the flame angle are reduced during the modulation cycle and the larger roll-up observed experimentally is also well captured.

These results characterize the flame dynamics and can be used to interpret the heat release rate signals plotted in Fig. 7.9. The case modulated at $f = 60$ Hz is first considered (Fig. HR3). From about 240° to 300° the flame angle α, defined between the flame sheet and the vertical axis, increases suddenly while its root penetrates within the burner. This corresponds to a sudden drop in heat release rate indicated by the continuous decrease of the ratio $\dot{Q}'/\overline{\dot{Q}}$ in Fig. 7.9(a) (square symbols, PM experiment). The flame root is then pushed outside the injection tube and reattaches to the anchoring central rod for a phase corresponding to nearly 0°. This instant also corresponds to the maximum flame angle α_m and one can identify the beginning of a roll-up process at the flame tip. This roll-up process lasts from about 0° to a phase comprised between 180° and 240° and corresponds to an increase of the flame surface area as indicated by Fig. 7.9 with the regular augmentation of $\dot{Q}'/\overline{\dot{Q}}$. When this mechanism ends the flame retracts rapidly and begins to travel back into the burner. This is accompanied by a sudden drop of the heat release rate which reaches its minimum value at 300°. The net output of these combined mechanisms examined over one cycle of oscillation is that the flame front exhibits a complex motion with some flashback,

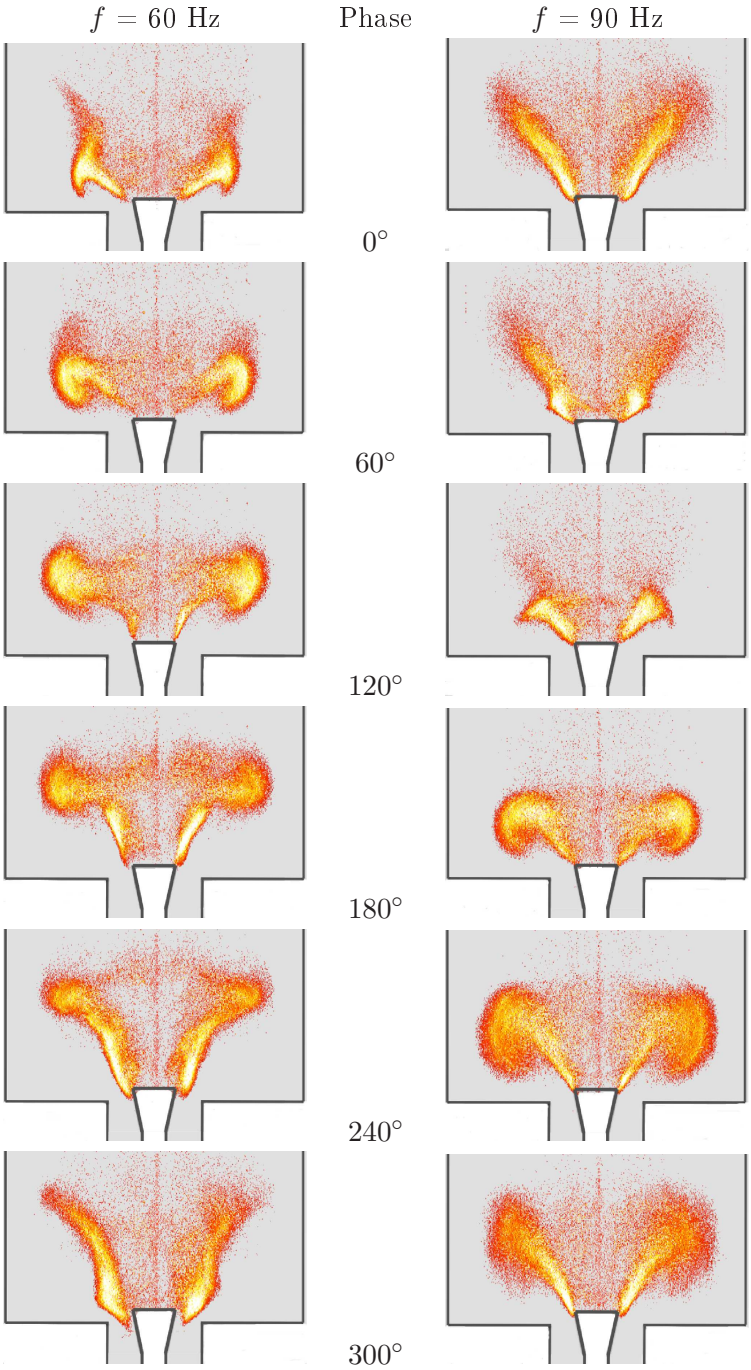

Figure 7.10: Phase conditioned average heat release rate distribution in W m^{-3} obtained experimentally. Left : $f = 60$ Hz. Right : $f = 90$ Hz. The colorbar is the same as in Fig. 7.8(a)

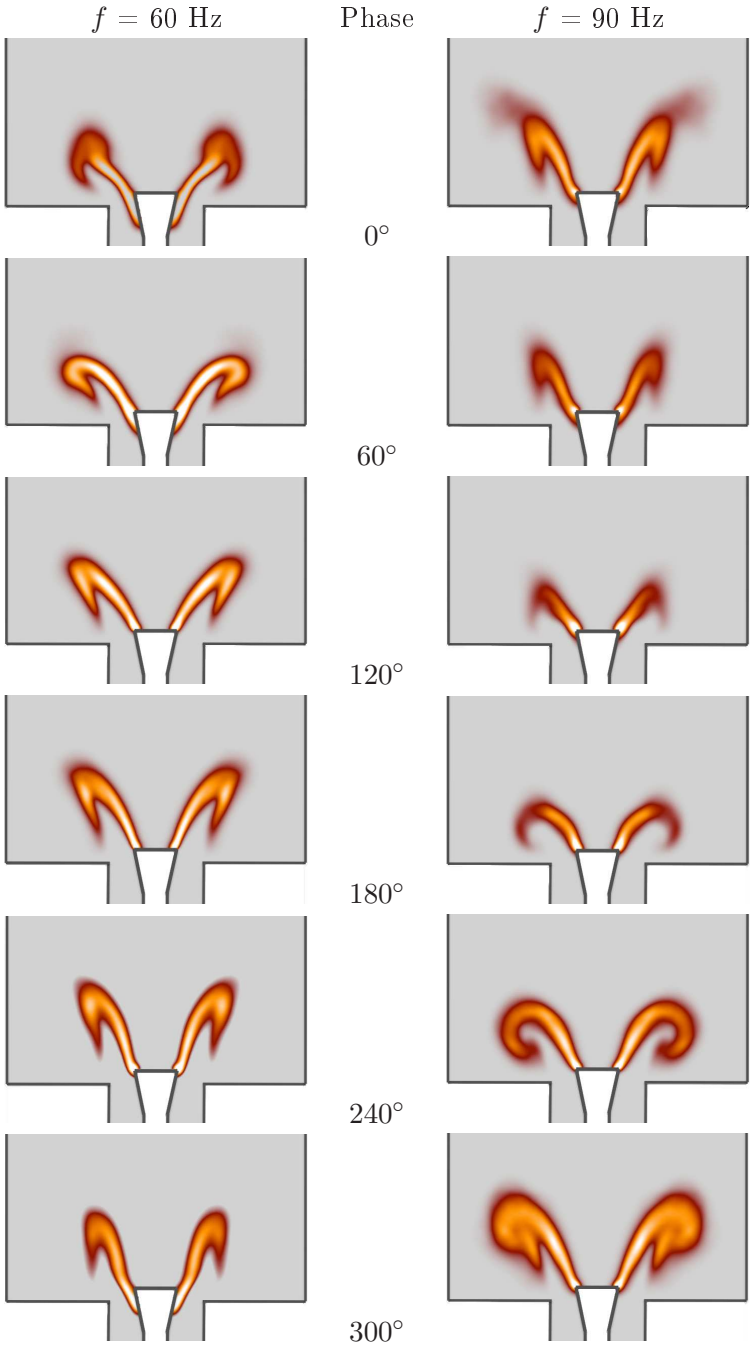

Figure 7.11: Phase conditioned average heat release rate distribution in W m^{-3} obtained with LES. Left : $f = 60$ Hz. Right : $f = 90$ Hz. The colorbar is the same as in Fig. 7.8(b)

a strong flame angle change and roll-up of the flame tips which interfere destruc-

tively to hinder heat release fluctuations. For a modulation at $f = 90$ Hz the situation is different. From 90° to 270°, the ratio $\dot{Q}'/\overline{\dot{Q}}$ increases continuously in Fig. 7.9(b) (square symbols, PM experiment). During this period the flame tip is progressively roll-up at the extremity while the angle at the flame root reduces regularly but with a limited variation compared to its maximal value α_m reached for a phase comprised between 60° and 120° (Fig. 7.10). The remaining part of the cycle, the flame surface area reduces regularly while the distribution of heat release rate takes a compact shape. No flashback occurs during the cycle and the flame remains attached to the anchoring device. In this case, the flame angle features a reduced oscillation over a modulation cycle and the flame dynamics is essentially controlled by the roll-up mechanism at the flame tip with large heat release fluctuations.

One can conclude this section by underlining two points concerning the swirling flame dynamics. At $f = 60$ Hz, the flame features strong fluctuations in the flame angle and roll-up at the flame tip while at $f = 90$ Hz, variations of the flame angle remain limited and the tip roll-up determines the dynamics of the flame front inducing large variations in the heat release rate. The distinct responses observed at these two frequencies can be attributed to the interference between two processes. The first, responsible for the flame angle variations, may be caused by fluctuations in swirl number. The second corresponds to flame tip roll-up and subsequent acceleration of burning of reactants.

7.5 Mode conversion at the swirler

7.5.1 Theoretical modeling

Before examining two key processes influencing the flame dynamics, it is worth recalling theoretical results obtained previously in chapter 4 in an analysis of mode conversion taking place when an acoustic wave impinges on a swirler. The analysis relies on actuator disk theory and on jump conditions derived by Cumpsty and Marble (1977b) which link flow variables upstream and downstream of a blade row cascade. One considers that on the upstream side of the cascade the axial velocity is determined by an acoustic wave at an angular frequency ω.

$$u(x,t) = \overline{u} + u' \exp(ikx - i\omega t) \tag{7.7}$$

When the jump conditions at the actuator disk are specified for a low Mach flow one finds that on the downstream side of the cascade, the velocity field has two components, an axial acoustic velocity perturbation propagating at the speed of

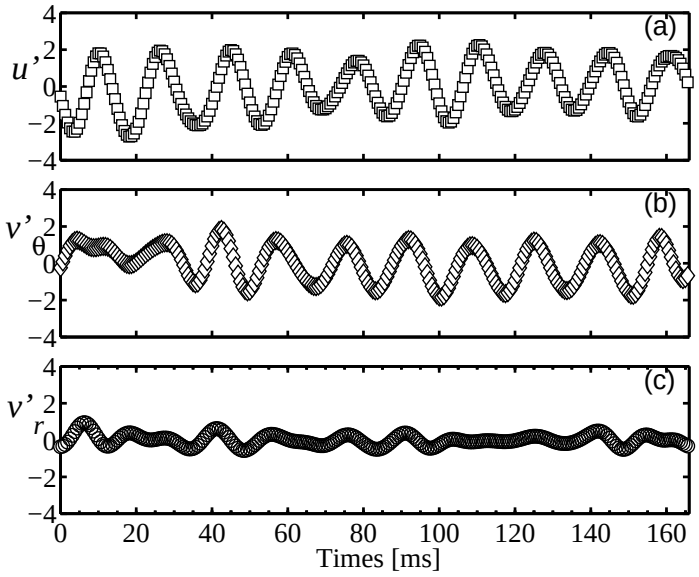

Figure 7.12: Velocity fluctuation signals recorded at 28 mm downstream of the swirler and at a radial distance of 5.7 mm from the axis. Modulation at $f = 60$ Hz.

sound with the same amplitude as in the upstream flow and a transverse velocity component convected by the flow.

$$u(x,t) = \overline{u} + u' \exp(ikx - i\omega t) \tag{7.8}$$

$$v(x,t) = \overline{v}_\theta + v'_\theta \exp(i\frac{\omega x}{\overline{u}} - i\omega t) \tag{7.9}$$

The amplitude of the transverse velocity perturbation is directly related to that of the axial wave:

$$v'_\theta = u' \tan\theta_2 \tag{7.10}$$

where θ_2 is the blade trailing edge angle with respect to the axial direction. Noting that $\overline{v}_\theta = \tan\theta_2 \overline{u}$ this condition may also be cast in the form:

$$v'_\theta / \overline{v}_\theta = u' / \overline{u} \tag{7.11}$$

The axial velocity disturbance corresponds to the transmitted acoustic wave and its amplitude remains unchanged. The transverse velocity perturbation travels at the flow velocity $\overline{u}$. This perturbation is associated with a vorticity wave

generated at the blade row trailing edges when the cascade is submitted to axial perturbations. Velocity disturbances on the downstream side of the swirler propagate at different velocities because a vortical mode with an azimuthal component and a transmitted axial acoustic wave are generated when the swirler is impinged by an axial acoustic wave. This mode conversion mechanism taking place at the swirler outlet generates swirl number fluctuations that should be taken into account in the analysis of the response of the flame. In a non-swirling jet a "V" flame would be rolled up by the vortex generated by the acoustic-vortical conversion at the outlet of the injector. In the present study, the swirling jet will be submitted to two key processes: the classical vortex roll-up and effect of the swirl number fluctuation.

7.5.2 Signal analysis

From analytical modeling derived previously in chapter 4, it is possible to compare the amplitude of velocity signals in the downstream flow with predictions. Figure 7.12 and Fig. 7.13 display velocity fluctuation signals obtained for the two modulation frequencies $f = 60$ Hz and $f = 90$ Hz. The perturbed axial u', azimuthal v'_θ and radial v'_r velocity fields are recorded at a probing point located 28 mm from the swirler and at a radial distance of 5.7 mm from the axis. It is first interesting to note that the radial velocity fluctuation is relatively small compared to axial and azimuthal components. One finds that the amplitude predicted theoretically Eq. (7.10) is in agreement with numerical results if one takes

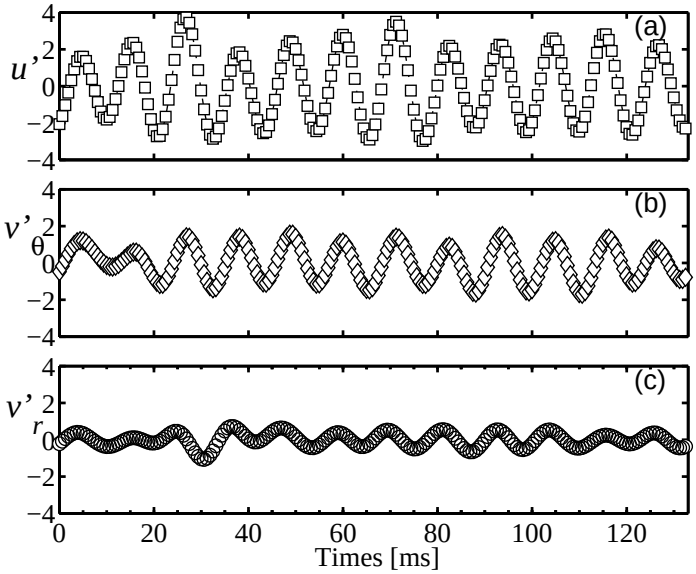

Figure 7.13: Velocity fluctuation signals recorded at 28 mm downstream of the swirler and at a radial distance of 5.7 mm from the axis. Modulation at $f = 90$ Hz.

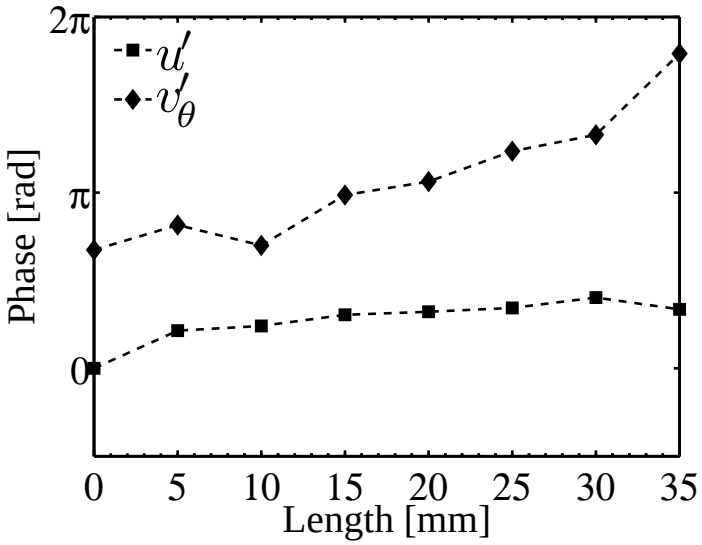

Figure 7.14: Axial evolution of phase shift between relative velocity fluctuations $u'/\overline{u}$ and $v'_\theta/\overline{v}_\theta$ with respect to the axial velocity fluctuation at the swirler outlet at $x = 0$. Modulation at $f = 60$ Hz.

θ_2 equal to 30°.

Figure 7.14 and Fig. 7.15, corresponding to $f = 60$ Hz and $f = 90$ Hz respec-

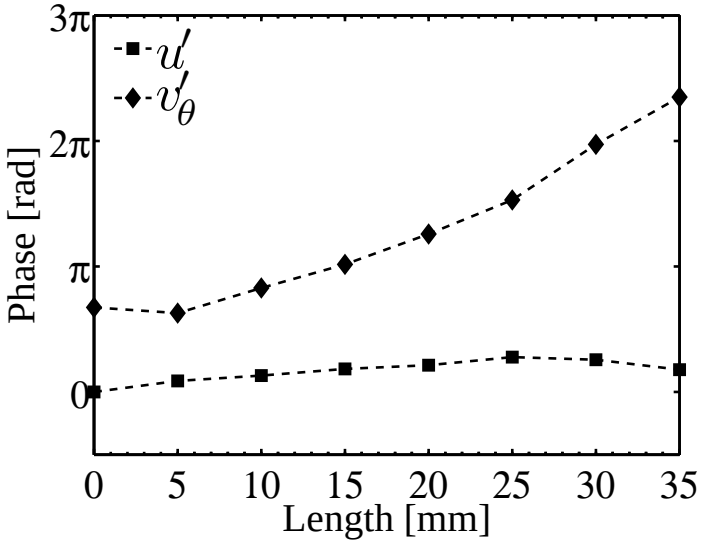

Figure 7.15: Axial evolution of phase shift between relative velocity fluctuations $u'/\overline{u}$ and $v'_\theta/\overline{v}_\theta$ with respect to the axial velocity fluctuation at the swirler outlet at $x = 0$. Modulation at $f = 90$ Hz.

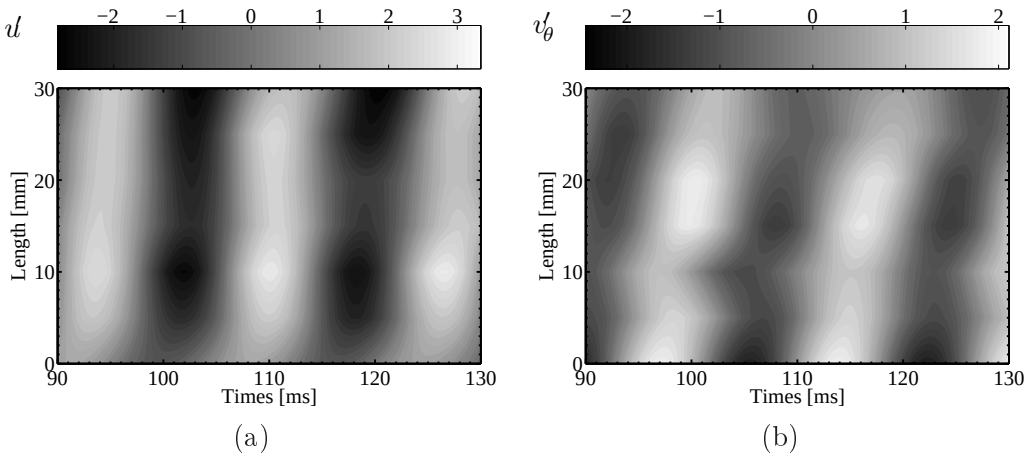

Figure 7.16: Space-time diagrams of velocity signals recorded on the downstream side of the swirler. These diagrams are obtained by low pass filtering signals on a sideline parallel to the burner axis at points separated by 5 mm. Modulation at $f = 60$ Hz. (a) : u'. (b) : v'_θ.

tively, show the evolution of the phase shift between axial u' and azimuthal v'_θ velocity fluctuations. These curves are obtained by low pass filtering the velocity data obtained from the simulation. The procedure consists in applying a FFT algorithm to the velocity fields u' and v'_θ. This is used to filter out higher frequency components corresponding to vortex shedding in the swirler wakes. An inverse FFT is then applied to the result. This process provides the filtered fluctuating velocities. One can then investigate the evolution of the phase shift between the perturbed velocity signals u' and v'_θ with respect to the axial velocity signal u' measured at the swirler trailing edge $x = 0$ mm. The phase shift is obtained by calculating cross power spectral densities of the filtered velocity signals at discrete points separated by a distance of 5 mm and located on a sideline in the downstream flow. The phase shift between filtered velocity perturbation signals is deduced from the complex value of the cross power spectral density at the driving frequency. For both modulation frequencies $f = 60$ and 90 Hz shown in Fig. 7.14 and Fig. 7.15, one finds that the phase shift of u' is nearly constant indicating that this component propagates at a high velocity which is that of an acoustic wave. Results differ for the transverse velocity component v'_θ. In Fig. 7.14, the phase shift increases roughly linearly with the distance to the swirler and reaches a value a bit lower than 2π at $x = 35$ mm for a modulation frequency $f = 60$ Hz. The value π taken at the swirler trailing edge $x = 0$ simply indicates that the the blade is inclined with a negative angle with respect to the axial direction ($\theta_2 = -30^o$). For a higher modulation frequency $f = 90$ Hz, the phase shift also increases linearly with the distance from the swirler but reaches a larger value than 2π at $x = 35$ mm (Fig. 7.15). The slope is proportional to the frequency and the transverse velocity component v'_θ travels at the flow velocity $\overline{u}$.

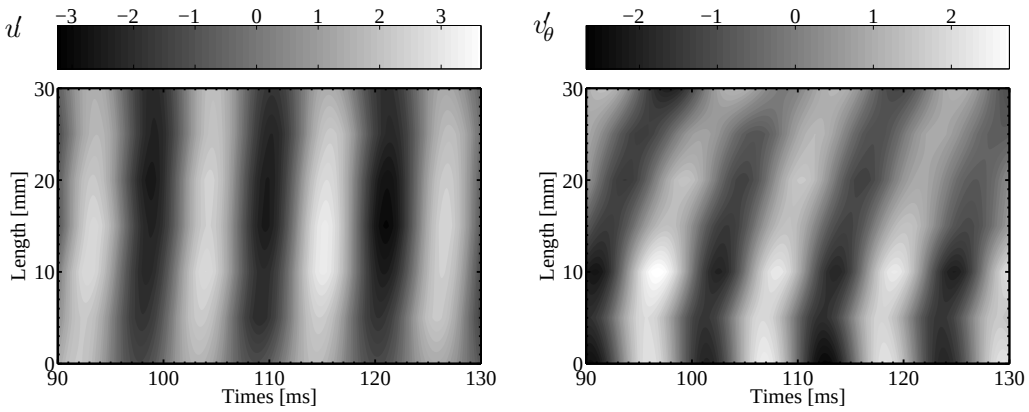

Figure 7.17: Space-time diagrams of velocity signals recorded on the downstream side of the swirler. These diagrams are obtained by low pass filtering signals on a sideline parallel to the burner axis at points separated by 5 mm. Modulation at $f = 90$ Hz. (a) : u'. (b) : v'_θ.

It is now interesting to use space-time diagrams to investigate the mode conversion taking place at the swirler. Such diagrams are plotted in Fig. 7.16 and Fig. 7.17 for the two characteristic frequencies $f = 60$ and 90 Hz. The space-time diagrams describe the temporal evolution of axial and azimuthal velocity fluctuations u' and v'_θ on a straight line parallel to the swirler axis at a radial distance of 5.7 mm. Data are recorded at points separated by $\Delta x = 5$ mm over a distance $x = 30$ mm and for a time period of 40 ms. Figures 7.16 and 7.17 (a) show the axial velocity component u'. One observes a periodic pattern of alternating high and low velocity stripes which are near to perpendicular to the time axis and reflect the acoustic nature of this perturbation. Figures 7.16 and 7.17 (b) display the azimuthal fluctuating component. One finds that the space-time diagram is well defined and the pattern is inclined forming oblique stripes. The slope can be used to estimate the convection velocity of $u_{cv} = 3.3$ m s^{-1} of the transverse component v'_θ.

These diagrams clearly demonstrate that the velocity fluctuations travelling in the injection duct behind the swirler differ in nature. The axial perturbation is acoustic while the transverse component is convected by the mean flow with a velocity $u_{cv} \simeq 3.3$ m s^{-1}.

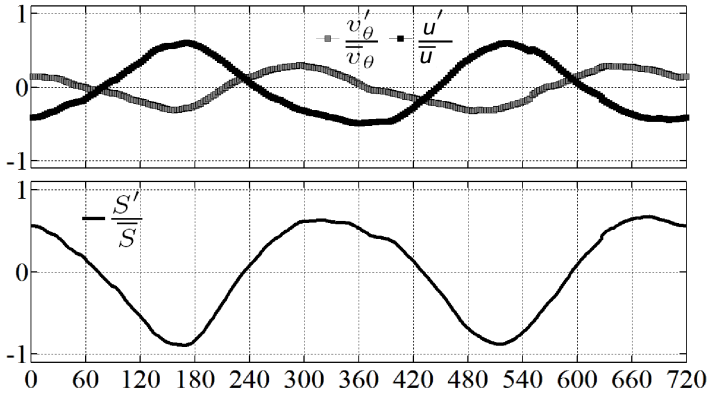

Figure 7.18: Experimental velocity signals and linearized swirl number fluctuation $S'/\overline{S}$ at the base of the flame. $f = 60$ Hz.

7.6 Contributing mechanisms

7.6.1 Swirl number fluctuations

The velocity field characterized in the previous sections induces swirl number fluctuations. These variations may be determined directly by calculating instantaneous values of the swirl number S using expression Eq. 7.6 or a linearized version of this expression :

$$\frac{S'}{\overline{S}} = \frac{v'_\theta}{\overline{v}_\theta} - \frac{u'}{\overline{u}} \tag{7.12}$$

This form is approximate but easy to use and more physical. It was already

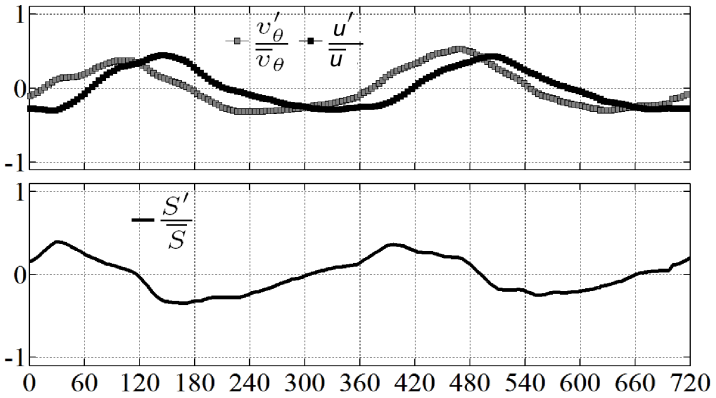

Figure 7.19: Experimental velocity signals and linearized swirl number fluctuation $S'/\overline{S}$ at the base of the flame. $f = 90$ Hz.

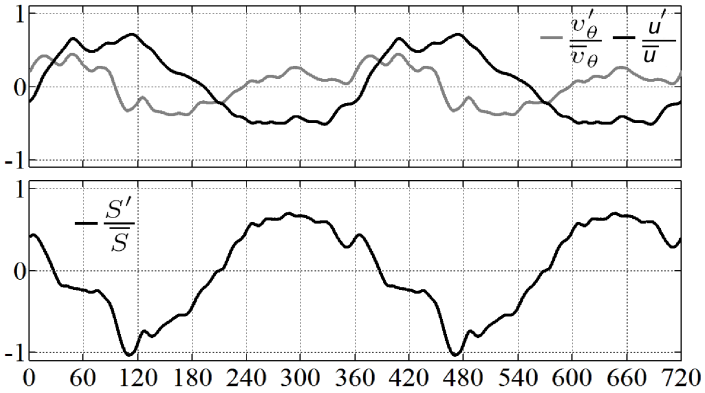

Figure 7.20: Numerical velocity signals and linearized swirl number fluctuation $S'/\overline{S}$ at the base of the flame. $f = 60$ Hz.

employed in the experimental analysis in chapter 5. The axial and azimuthal velocity signals at the base of the flame are now used to determine the level of swirl. The point where the velocity signals are determined is located at 4.3 mm from the combustor backplane and at one half of the injector diameter ($r =$ 8 mm). Experimental swirl number fluctuations are plotted in Fig. 7.18 for $f = 60$ Hz and in Fig. 7.19 for $f = 90$ Hz. Results deduced from numerical simulations are displayed in Fig. 7.20 for $f = 60$ Hz and in Fig. 7.21 for $f = 90$ Hz. These diagrams indicate that the numerical simulation suitably captures the swirl number fluctuations observed experimentally. The match is not perfect but the velocity signals and resulting swirl number oscillations are reasonably well retrieved. The previous data confirms that the pulsating velocity field induces swirl number fluctuations. These variations are found in the experiments and the simulations larger for a modulation at 60 Hz than at 90 Hz. This in turn produces larger flame angle fluctuations at 60 Hz than at 90 Hz as it was observed

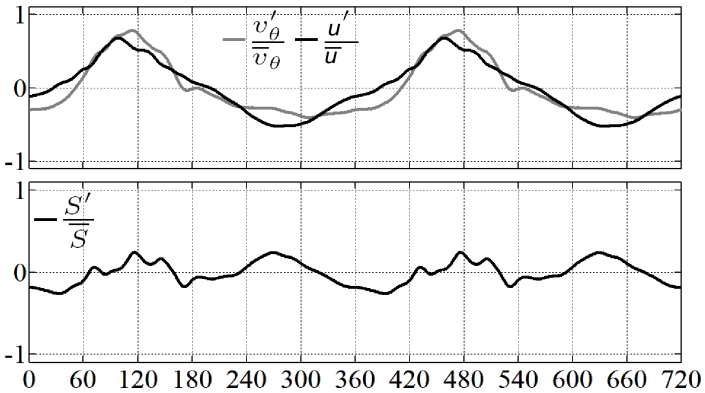

Figure 7.21: Numerical velocity signals and linearized swirl number fluctuation $S'/\overline{S}$ at the base of the flame. $f = 90$ Hz.

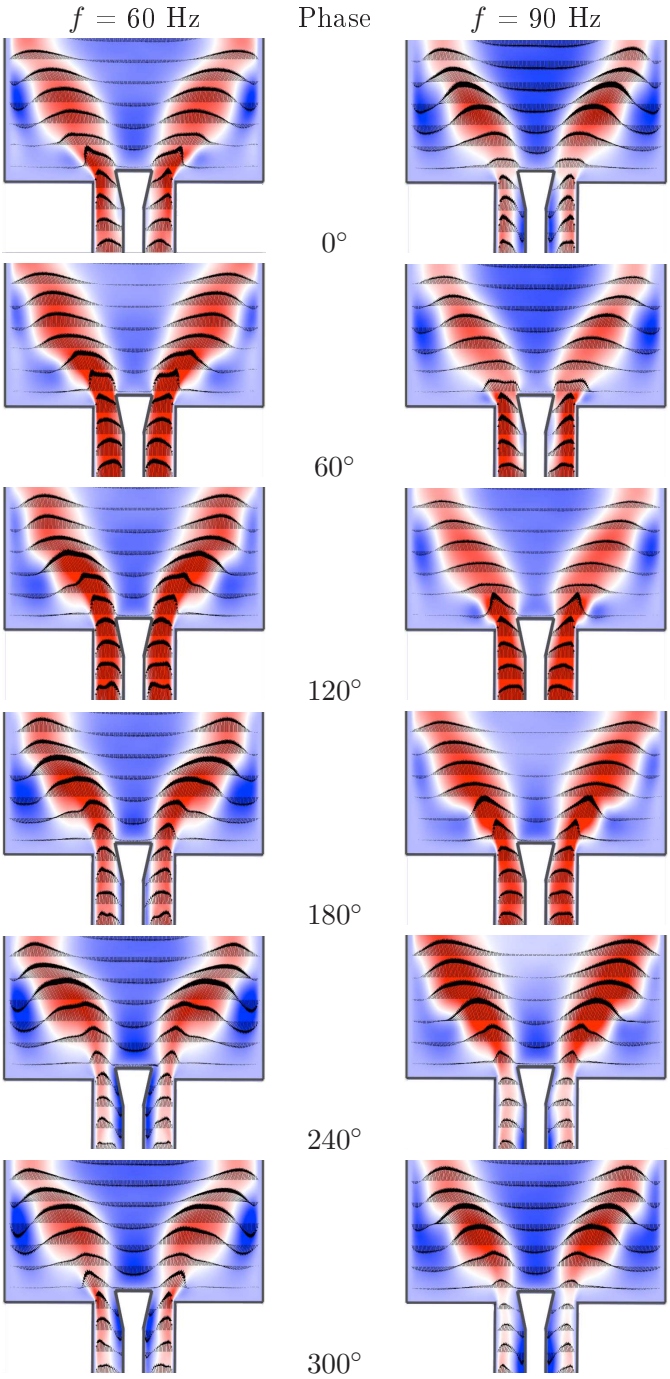

Figure 7.22: Axial velocity and velocity vectors: on the left, $f = 60$ Hz; on the right, $f = 90$ Hz. The maximum velocity is 4 m s^{-1} and colored in red while the minimum velocity is -2 m s^{-1} and colored in blue.

in Fig. 7.10 and Fig. 7.11.

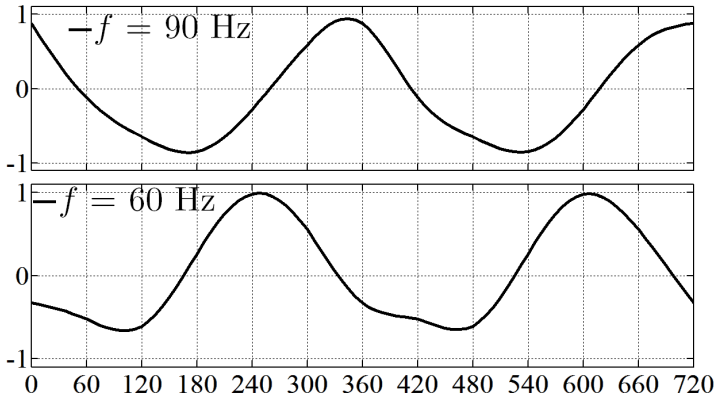

Figure 7.23: Axial velocity fluctuation $u'/\overline{u}$ extracted from LES on the burner symmetry axis and 4.3 mm downstream the backplane of the combustor.

It is next interesting to examine the processes which determine the flame response. The first identified mechanism is linked to the motion and strength of the Inner Recirculation Zone (IRZ) which is controlled by the swirl number and defines in turn the flame angle with respect to the axial direction. The second process is related to vortex shedding from the injector outer lip. To examine the dynamics of the IRZ and the influence of the fluctuating swirling flow, one may rely on LES and plot the axial velocity fields and velocity profiles during one cycle of modulation. Figure 7.22 shows the flow configuration at six phases during a cycle for the two modulation frequencies $f = 60$ and 90 Hz. For both frequencies, one observes a well defined central inner recirculation zone where velocity vectors indicate a reverse flow. The strength of this IRZ changes during the cycle. When the rotation rate is low, the IRZ is essentially formed by the bluff body and the negative axial flow velocities are low. When the rotation level is high the IRZ is strong and the reverse flow is more intense. This is in agreement with previous experimental studies from Vanierschot and Van den Bulck (2008) in which the swirl number is varied continuously.

At $f = 60$ Hz, the maximum backward velocity is reached for a phase comprised between 240° and 300° while at $f = 90$ Hz, this maximum is reached between 300° and 0°. These phases nearly match with maximum of the swirl number as indicated in Fig. 7.20 and Fig. 7.21. The velocity vectors plotted in Fig. 7.22 indicate that similar levels of fluctuation of reverse flow occur during a cycle of modulation near the anchoring rod. This is better shown in Fig. 7.23 where the relative axial velocity fluctuation ratio $u'/\overline{u}$ takes about the same level for both modulation frequencies in the vicinity of the central bluff body. It can however be noted that the motion of the IRZ takes place at a different phase with respect to the incident axial velocity fluctuations. The unsteady flow around the rod also changes significantly for the two modulation frequencies. A large reversal flow

takes place along the central rod for phases comprised between 180° and 300° at $f = 60$ Hz while this phenomenon remains very limited between 240° and 0° at $f = 90$ Hz. This may indicate that a certain swirl number fluctuation level must be reached to induce flashback along the central bluff body.

7.6.2 Interfering mechanisms

One may now try to see how the two dynamical processes examined previously combine to define the flame response to incident velocity perturbations. It is found from previous experimental work that the flame motion is governed by a mechanism where the swirl number is perturbed inducing variations in flame angle and a mechanism where vortices shed from the injector lip interact with the flame inducing changes in the flame surface area. These mechanisms were found to act constructively or destructively depending on the modulation frequency.

To examine the vortex shedding process taking place at the injector lip and rolling up the flame, one may first locate the vortex structures in the flow at various instants during a modulation cycle. The identification of vortex structures is conveniently achieved by post-processing the LES and calculating a phase average Q-criterion fields. This quantity is defined by Hunt *et al.* (1988) as :

$$Q = \frac{1}{2}\left(\|\Omega\|^2 - \|S\|^2\right), \tag{7.13}$$

where S is the symmetric component of the velocity gradient while Ω is the antisymmetric part. Q-criterion fields are plotted in Fig. 7.24 together with phase average flame contours shown as black solid lines at each phase of the cycle separated by 60°. These results are obtained by taking an average over nine cycles. It is also possible to improve the result by taking azimuthal averages because the phase average is rotationally symmetric. The colorbar for the Q-criterion is set from 2.10^6 s^{-2} in red to -2.10^6 s^{-2} in blue. The description of the dynamics can be analyzed by examining vortex patterns in the flow and their interactions with the flame front. Heat release rate contours are also used to track the flame front dynamics during one modulation cycle. For the modulation frequency $f = 60$ Hz, one finds that a vortex is shed from the injector external lip near 300°. The corresponding swirl number determined at the base of the flame is also close to its maximal value (Fig. 7.20) and this induces a flashback along the anchoring rod due to the high value of the rotation rate. The flame angle α is also large because of the high rotation rate (Fig. 7.11). In these conditions, the vortex generated at the injector lip cannot fully developed and rapidly interacts with the flame tip for a phase near 0°. Its size and strength remain thus limited and the resulting flame roll-up is weak during the remaining part of the cycle. At

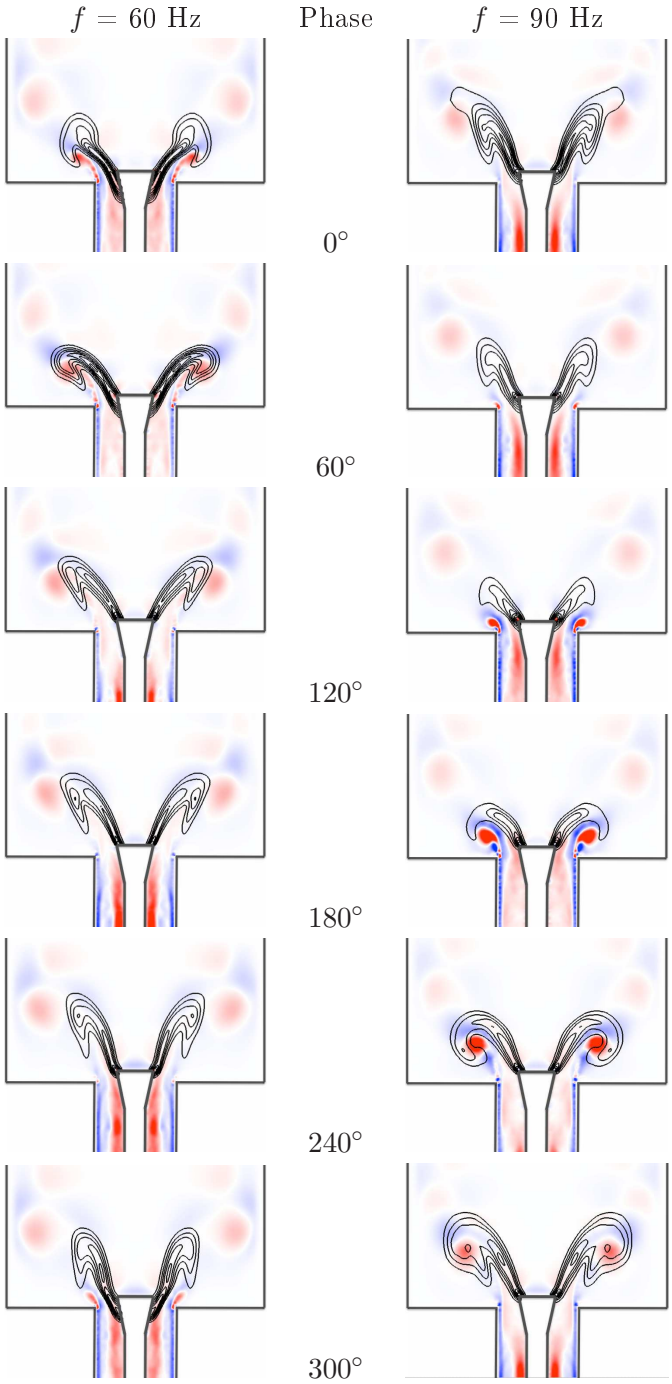

Figure 7.24: Q criterion contour in color: the colorbar is set from $2\,10^6$ s^{-2} in red to $-2\,10^6$ s^{-2} in blue. Heat release rate contours in black are used to track the flame front during one cycle of modulation. Left : $f = 60$ Hz. Right : $f = 90$ Hz.

$f = 90$ Hz and for a phase corresponding to 60°, an annular vortex is shed from the injector external lip. The corresponding flame angle α at that instant in the modulation cycle is significantly smaller than at $f = 60$ Hz because swirl number fluctuations are substantially reduced in this case (Fig. 7.21). This vortex is thus convected by the flow and increases in size and strength before interacting with the flame for a phase of about 180°. At this instant in the cycle, it is strong enough to roll-up the flame tip from 180° to 300° thereby increasing the flame surface area. Finally, during the next part of the cycle, the vortex is dissipated, the flame front extremities collapse and the flame spreads over a broad area and one observes the formation of a new vortex pattern in the duct due to the mode conversion process taking place at the swirler.

The previous results indicate that a strong vortex rolls up the flame at $f = 90$ Hz which is confirmed by the experiments (Fig. 7.10). It is also found that vortex shedding is significantly less important at $f = 60$ Hz. The formation of the vortex is canceled by the important swirl number at $f = 60$ Hz while at $f = 90$ Hz, its formation takes place in a quasi non-swirling jet. This clearly shows that the rate of rotation of the flow has an impact on the annular vortex shedding. The present calculations also indicate that the flame motion is determined by the relative phasing between the IRZ strength fluctuations controlling the flame angle and the incident axial velocity fluctuations. At 60 Hz, the phasing is such that the flame angle changes significantly and the vortex created by the axial velocity fluctuation rapidly interacts with the flame without possibility to gain in size and strength. At 90 Hz, the IRZ dynamics combined with the axial velocity fluctuations keep the flame angle at an essentially constant value and this let time for the vortex generated by the axial velocity fluctuation to fully developed and gain in strength before interacting with the flame. These interfering mechanisms can only be explained by taking into account the mode conversion mechanism at the swirler outlet which is at the origin of swirl number fluctuations and thus flame root angle fluctuations.

7.7 Conclusion

The dynamics of a swirling flame submitted to incident acoustic velocity perturbations is investigated numerically. The incoming wave is initiated on the upstream side of a swirler unit. It is first confirmed that mode conversion takes place at the swirler and that this gives rise to azimuthal velocity fluctuations which are convected by the flow. The numerical results also agree with theoretical results obtained previously by making use of an actuator disk theory to evaluate the levels of fluctuation in the flow on the downstream side of a blade row cascade. The combination of axial and azimuthal velocity perturbations in-

duce variations in swirl number confirming previous experimental observations of this process. The calculations also indicate that vortex shedding taking place at the injector lips can induce flame roll-up and subsequently large variations in flame surface area. The two mechanisms of rotation rate fluctuations and vortex roll-up combine in one case and lead to an intense fluctuation in heat release. In a second case, these mechanisms interfere destructively inducing a low level of heat release rate fluctuations. The outcome depends on the inlet acoustic wave frequency. Simulations indicate that vortex roll-up is strong when fluctuations of the rotation rate are limited and the inner recirculation zone strength is weak. In contrast, the shedding and roll-up process is less intense when the IRZ strength features large fluctuations and the rotation rate is high.

Chapter 8

Modeling of flame transfer functions

Abstract : *An analytical model is derived for the linear response of swirling flames submitted to velocity disturbances. The flame dynamics is represented by a linearized version of the G-equation. Turbulent fluctuations are first averaged in time to obtain a kinematic equation in which the flame is represented by a wrinkled sheet. The variables are then phase averaged to describe acoustic perturbations and obtain a perturbed G-equation. It is first concluded that the flame motion results from the combined effects of axial and azimuthal velocity perturbations. The latter disturbances formed at the swirler when this element is submitted to axial velocity fluctuations are convected by the flow and impinge on the flame. In this disturbance field the swirl number is perturbed and this is effectively modeled by assuming that the turbulent burning velocity is modulated by the axial and azimuthal velocity perturbations. It is then shown that the response of swirling flames can be deduced from the transfer function of inverted conical flames submitted to axial velocity perturbations. It is however important to account for the phase shift resulting from the propagation of axial and azimuthal disturbances on the downstream side of the swirler. This phase shift, due to the difference in propagation velocity of acoustic and convective perturbations, is determined experimentally. Theoretical transfer functions are compared with measurements corresponding to two bulk velocities at a constant swirl number $S = 0.55$. A good agreement is obtained. It is shown in particular that minima and maxima of the flame response are suitably retrieved and the Strouhal number can be used to collapse the data.*

Résumé : *Un modèle analytique est établi pour la réponse linéaire de flammes swirlées soumises à des perturbations de vitesses. La dynamique de la flamme est représentée par une version linéarisée de l'équation pour une variable de champ G. Les fluctuations turbulentes sont d'abord moyennées pour obtenir une équation cinématique pour le champ moyen. Une moyenne de phase est ensuite appliquée aux perturbations acoustiques pour obtenir une équation pour le champ G perturbée. Il est d'abord conclu que le mouvement de flamme est dû aux effets combinés des perturbations de vitesses axiales et azimutales. Les fluctuations du nombre de swirl sont modélisées en supposant que la vitesse de combustion turbulente est modulée par ces perturbations de vitesses. Il est ensuite montré que la réponse des flammes swirlées peut être déduite de la fonction de transfert des flammes en "V" soumises à des perturbations de vitesses axiales. Il est toutefois important de tenir compte de la différence de phase résultant de la propagation des perturbations axiales et azimutales. Cette différence de phase, résultant de la différence des vitesses de propagation des perturbations acoustiques et convectives, est déterminée expérimentalement. Les fonctions de transfert théoriques sont comparées aux mesures pour deux vitesses débitantes différentes et pour un nombre de swirl fixé $S = 0.55$. Un bon accord est obtenu. On montre en particulier que le gain minimal obtenu pour un nombre de Strouhal de 0.5 est bien reproduit par le modèle théorique.*

8.1 Introduction

A suitable description of flame dynamics and combustion response to incident perturbations is one important element for the prediction of combustion instabilities. It is convenient to use a description based on the transfer function to represent this response in a compact form. Theory, experiments and simulations have been widely used to deal with this problem in various geometries. Results are available for simple flames but the case of swirling flames is less well documented. It is our goal to show that the dynamics of premixed swirling flames submitted to incoming velocity disturbances results from a complex interaction involving initial axial velocity perturbations in combination with azimuthal disturbances induced by the swirler. By accounting for these two types of perturbations, it is shown that one can deduce a model for the swirling flame response which exhibits the main features of experimentally determined transfer functions.

Flame transfer functions have been extensively studied in laminar configurations like conical flames by Baillot *et al.* (1992), inverted conical flames by Durox *et al.* (2005) and multiple conical flames by Kornilov *et al.* (2009). These data can be

used to guide and validate the theoretical modeling but they also provide an understanding of the physical mechanisms controlling the combustion response. The flame transfer function gain of conical flames behaves like that of a low pass filter. For "V" flames, the gain can exceed unity for a range of frequencies indicating that this flame geometry is more sensitive to incident perturbations. Vortex roll-up has been associated to this overshoot in the gain and depends on frequency for swirling flames Lohrmann *et al.* (2003). The phase evolves in a nearly linear fashion with frequency indicating that velocity disturbances are convected from the outlet of the injector to the flame. Turbulent "V" flame configurations are also considered by Balachandran *et al.* (2005); Armitage *et al.* (2006) and some studies also focus on swirling flames as Bellows *et al.* (2007); Thumuluru *et al.* (2007); Borghesi *et al.* (2009). Flame transfer functions measured with a swirl-stabilized burner indicate that the Strouhal number is the relevant dimensionless group, see Kim *et al.* (2010).

The transfer function may also be determined from simulations. In principle, this requires an unsteady flow solver and broadband modulations of the incoming flow. The transfer function is then derived by post-processing results of these time dependent calculations. This is exemplified by Gentemann *et al.* (2004); Kopitz and Polifke (2008) with Unsteady Reynolds Average Navier-Stokes codes. It is probably more adequate to use LES methods as illustrated in a number of recent investigations from Borghesi *et al.* (2009); Kaufmann *et al.* (2002); Chang *et al.* (2009). The numerical approach however does not yield analytical expressions and tends to hide the underlying mechanisms.

The theoretical modeling of flame transfer functions (FTF) has also been pursued in laminar or turbulent configurations by Preetham *et al.* (2007). Most derivations rely on the kinematic G-equation in which the flame front is represented by a surface $G = G_0$ separating fresh gases $G < G_0$ from burnt gases $G > G_0$. This is used for example by Fleifil *et al.* (1996); Schuller *et al.* (2003b); Lieuwen (2005). A unified framework carried out by Schuller *et al.* (2003b) deals with conical and "V" flames submitted to uniform or convective disturbances. The motion of the flame anchor point is also considered for a ducted flame by Dowling (1999). It is also shown in Preetham *et al.* (2008) that these transfer functions can be very sensitive to the vortex convection velocity. In the case of "V" flames it is found that the transfer function gain is a strong function of the amplitude of the velocity perturbation. Modeling has been extended to turbulent configurations to study the nonlinear response of premixed flames, see Lieuwen (2005). Turbulent flame speed effects on flame transfer function for such "V" flames have also been investigated Lipatnikov and Sathiah (2005); Sathiah and Lipatnikov (2007) but effects are significant only for long flames. The FTF of conical flames is close to that found in the linear regime but the response of "V"

flames is influenced by the amplitude of oscillation, see Schuller *et al.* (2003b). Turbulent flame speed effects on flame transfer function for such "V" flames have also been investigated by Lipatnikov and Sathiah (2005). Theoretical transfer functions of swirling flames are less common and do not fully reproduce characteristic features of the flame response, see You *et al.* (2005); Borghesi *et al.* (2009); Komarek and Polifke (2010) even if a fitting is suggested by Komarek and Polifke (2010). There are multiple sources of convecting vortices in the arrangement of our present study. The main contributing mechanisms are those generating large vortex structures. They can be produced by the swirler, the backward facing step and the centerbody and are all synchronized by the modulation frequency. Detailed characterizations of the flow dynamics however show that in this setup the main contributing mechanism is that due to the swirler. Studies from You *et al.* (2005); Borghesi *et al.* (2009) do not account for the presence of an azimuthal velocity disturbance convected by the flow in addition to the initial axial component propagating at the speed of sound a feature which is reported in some recent investigations by Wang and Yang (2005); Komarek and Polifke (2010); Huang and Yang (2009). The effect of this convective mode is however not included in most of these studies with the exception of Komarek and Polifke (2010) which provides a phenomenological representation of the FTF. The presence on the downstream side of the swirler of a perturbation featuring acoustic and convective components is documented in previous sections in which the azimuthal disturbance velocity is fully characterized from experiments and also by considering the theoretical response of a blade row submitted to incident axial perturbations. It is necessary to represent this complex perturbed flow field if one wishes to determine the FTF of swirling flames.

The present study attempts to improve the modeling of the swirling flame transfer function by suitably accounting for the perturbed flow field induced by the swirler. It relies on a G-equation derived by first taking an ensemble average with respect to the turbulent fluctuations. This equation is then separated into steady and phase average components corresponding to imposed flow modulations, a process leading to a perturbed G-equation. It is then shown that the response of swirling flames results from the direct effect of axial velocity perturbations and from the combined effects of axial and azimuthal velocity components. The latter are taken into account by considering that the turbulent flame velocity is perturbed by these disturbances. It is shown that the transfer function of swirling flames can be deduced from the transfer function of "V" flames submitted to convective flow disturbances. This is accomplished by taking into account the relative level of axial and azimuthal disturbances and the phase shift between these two components. This last quantity can be estimated theoretically or deduced from measurements of the axial and azimuthal velocity signals.

The geometry of the problem is described in section 8.2. The perturbed G-equation is derived in section 8.3. A theoretical expression is deduced for the transfer function in section 8.4. The modeling of incident velocity components is envisaged in section 8.5 including measurements of the phase difference between axial and azimuthal velocity perturbations. Comparisons between predictions and experimental data are also carried out in this section.

8.2 Experimental configuration and problem geometry

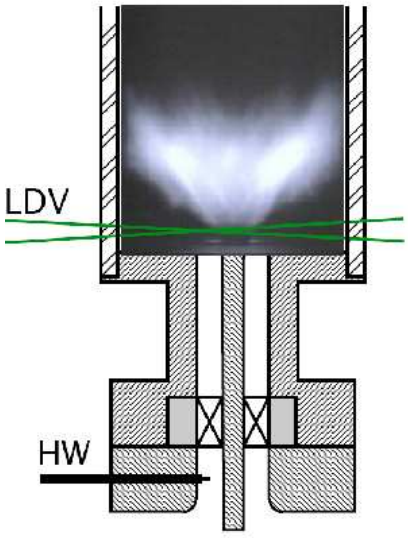

Figure 8.1: Injector and flame tube scheme. The flame is anchored at a cone ending a rod. Flame visualization is achieved by a long time exposure without any excitation in order to capture the mean flame front.

It is interesting to first examine the experimental configuration. The burner comprises three elements : an upstream manifold, an injector and a flame tube made of quartz. A premixed methane/air stream (equivalence ratio 0.7) is introduced through the burner base and passes through a 2 cm thick honeycomb layer to break the largest turbulent scales. The burner body is terminated by a convergent section which is fitted to the cylindrical injection tube. The swirler placed in this tube defines the rate of rotation of the flow. A central rod terminated by a small cone is used to anchor the flame and avoid flashback as shown in Fig. 8.1. The swirler represented in Fig. 8.2 comprises eight blades formed by NACA 8411 airfoil sections. The vanes are periodically spaced with a stagger angle of 45°. The vanes are twisted radially, so that the angle at the trailing edge evolves linearly from 30° at the hub to a value of 58° at the vane tip. The measured swirl

number is $S = 0.55$.

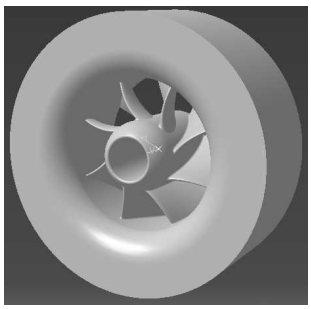

Figure 8.2: Axial swirler with eight vanes. The inner diameter d of the swirler is equal to the diameter of the injector tube (22 mm). The rod passes through the center hole of the swirler (6 mm in diameter).

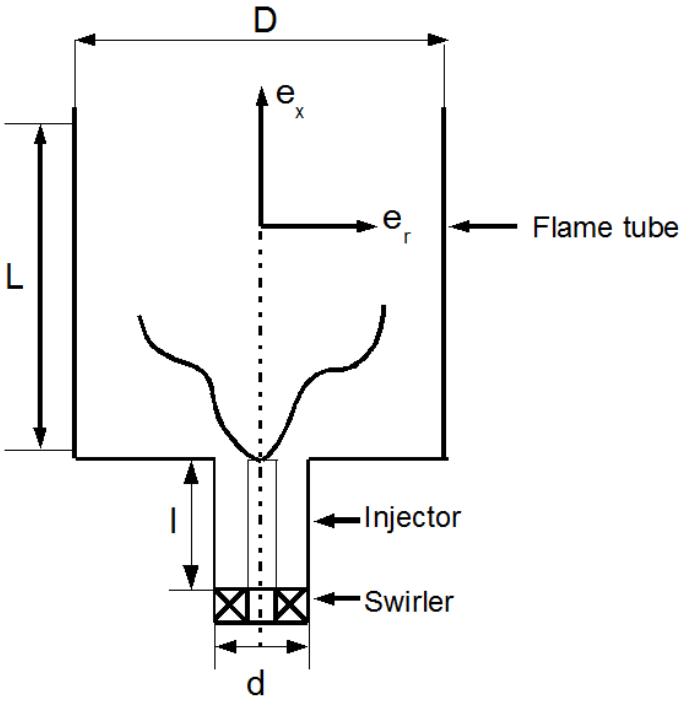

Figure 8.3: Geometrical view of the configuration : swirler (d = 22), injector (d = 22, l = 43) and flame tube (D = 70, L = 100). All dimensions are given in millimeters.

The problem geometry is an idealized version of the previous configuration shown schematically in Fig. 8.3. It is assumed for simplicity that the flame is anchored at the center of the rod on the vertical axis. In the experiment, the flame transfer function is determined by measuring the axial velocity disturbances u' generated

by a loudspeaker placed at the burner base and the total heat release rate perturbation $\dot{Q}'$ of the flame. The velocity fluctuation is obtained by laser Doppler velocimetry at $x = 2.9$ mm above the backplane of the confinement tube and at a radial distance of $r = 8$ mm from the axis. This defines a small measurement volume on the downstream side of the swirler in the turbulent swirling flow, close to the reaction region. Heat release rate fluctuations are estimated by recording the global emission signals of excited radicals OH^* using a photomultiplier collecting the light emitted by the flame. The experimental flame transfer function $\mathcal{F}^s_{\text{exp}}$ is then obtained by taking the ratio of relative heat release rate fluctuations and relative axial velocity fluctuations :

$$\mathcal{F}^s_{\text{exp}}(\omega) = \frac{\dot{Q}'_s/\overline{\dot{Q}}_s}{v'_x/\overline{v}_x} \tag{8.1}$$

8.3 Derivation of the perturbed G-equation

The theoretical swirling flame transfer function is defined as :

$$\mathcal{F}^s_{\text{th}}(\omega) = \frac{A'/\overline{A}}{v'_x/\overline{v}_x} \tag{8.2}$$

Where A is related to the flame surface area and assuming that for a lean premixed flame the ratio $\dot{Q}'/\overline{\dot{Q}}$ is equivalent to $A'/\overline{A}$.
To start this analysis it is assumed that the flame is instantaneously described as a surface defined by a kinematic G-equation :

$$\frac{\partial G}{\partial t} + \boldsymbol{v}\cdot\boldsymbol{\nabla} G = S_D|\boldsymbol{\nabla} G| \tag{8.3}$$

where one of the contours of G defines the flame front location, $\boldsymbol{v}$ is the local flow velocity and S_D designates the displacement velocity of the flame surface propagating normal to itself. To obtain the equation governing the perturbed flame front position one has to deal with two types of velocity disturbances. It is natural to distinguish turbulent fluctuations which wrinkle the front in a random fashion and organized perturbations associated to the modulations imposed to the flow. It is then convenient to begin by taking an ensemble average of the G-equation to derive a Reynolds average equation. This equation is decomposed in a second step by separating the mean field from the phase average field. This yields a perturbed G-equation.

In the first step one uses an ensemble average and turbulent fluctuations around this average. Each variable a is written as a sum of a mean value $\overline{a}(\boldsymbol{x}, t)$ and of

a turbulent fluctuation $a'(\boldsymbol{x},t)$:

$$G(\boldsymbol{x},t) = \overline{G}(\boldsymbol{x},t) + G'(\boldsymbol{x},t) \tag{8.4}$$

$$\boldsymbol{v}(\boldsymbol{x},t) = \overline{\boldsymbol{v}}(\boldsymbol{x},t) + \boldsymbol{v}'(\boldsymbol{x},t) \tag{8.5}$$

Inserting this decomposition in Eq. (8.3) one obtains :

$$\frac{\partial}{\partial t}(\overline{G}+G') + (\overline{\boldsymbol{v}}+\boldsymbol{v}')\cdot\boldsymbol{\nabla}(\overline{G}+G') = S_D|\boldsymbol{\nabla}(\overline{G}+G')| \tag{8.6}$$

This equation is now ensemble averaged yielding

$$\frac{\partial \overline{G}}{\partial t} + \overline{\boldsymbol{v}}\cdot\boldsymbol{\nabla}\overline{G} = \overline{S_D|\boldsymbol{\nabla}G|} - \overline{\boldsymbol{v}'\cdot\boldsymbol{\nabla}G'} \tag{8.7}$$

The right hand terms of this equation can be replaced by introducing a turbulent burning velocity S_T. Following Peters (1992), this is achieved by defining this quantity by :

$$S_T|\boldsymbol{\nabla}\overline{G}| = \overline{S_D|\boldsymbol{\nabla}G|} - \overline{\boldsymbol{v}'\cdot\boldsymbol{\nabla}G'} \tag{8.8}$$

It is however worth noting that this last expression is an approximate equation that attempts to account for turbulent wrinkling effects on the ensemble averaged flame motion. This is still current active research topic Oberlack *et al.* (2001). This process yields a heuristic generalization of the G-equation for the ensemble averaged flame front :

$$\frac{\partial \overline{G}}{\partial t} + \overline{\boldsymbol{v}}\cdot\boldsymbol{\nabla}\overline{G} = S_T|\boldsymbol{\nabla}\overline{G}| \tag{8.9}$$

In the second step, the variables appearing in this equation are written as a sum of a mean field and phase average perturbations around this mean field $< \overline{a}(\boldsymbol{x},t) > = a_0(\boldsymbol{x}) + a_1(\boldsymbol{x},t)$ where $a_0(\boldsymbol{x})$ and $a_1(\boldsymbol{x},t)$ are the mean steady value and its unsteady perturbation. The phase averages of $\overline{G}, \overline{\boldsymbol{v}}, \overline{S}_T$ are written in the following form :

$$< \overline{G}(\boldsymbol{x},t) > = G_0(\boldsymbol{x}) + G_1(\boldsymbol{x},t) \tag{8.10}$$

$$< \overline{\boldsymbol{v}}(\boldsymbol{x},t) > = \boldsymbol{v}_0(\boldsymbol{x}) + \boldsymbol{v}_1(\boldsymbol{x},t) \tag{8.11}$$

$$< \overline{S}_T(\boldsymbol{x},t) > = S_{T_0}(\boldsymbol{x}) + S_{T_1}(\boldsymbol{x},t) \tag{8.12}$$

Applying the average operator to Eq. (8.9) one finds:

$$< \frac{\partial \overline{G}}{\partial t} > + < \overline{\boldsymbol{v}}\cdot\boldsymbol{\nabla}\overline{G} > = < S_T|\boldsymbol{\nabla}\overline{G}| > \tag{8.13}$$

Introducing the decompositions defined previously one obtains :

$$\frac{\partial G_1}{\partial t} + \boldsymbol{v}_0\cdot\boldsymbol{\nabla}G_0 + \boldsymbol{v}_0\cdot\boldsymbol{\nabla}G_1 + \boldsymbol{v}_1\cdot\boldsymbol{\nabla}G_0 + \boldsymbol{v}_1\cdot\boldsymbol{\nabla}G_1 = (S_{T_0}+S_{T_1})|\boldsymbol{\nabla}(G_0+G_1)| \tag{8.14}$$

The previous equation can be simplified by considering that perturbations are small compared to the mean quantities. Neglecting second order terms and introducing the normal vector $\boldsymbol{n}$ to the mean flame front $\boldsymbol{n} = -\boldsymbol{\nabla} G_0/|\boldsymbol{\nabla} G_0|$ one finds after some calculations that

$$|\boldsymbol{\nabla}(G_0 + G_1)| = [(\boldsymbol{\nabla} G_0)^2 + 2\boldsymbol{\nabla} G_0 \cdot \boldsymbol{\nabla} G_1 + (\boldsymbol{\nabla} G_1)^2]^{\frac{1}{2}} \tag{8.15}$$

We neglect the term of second order and we find :

$$|\boldsymbol{\nabla}(G_0 + G_1)| = |\boldsymbol{\nabla} G_0| \left[1 + 2\frac{\boldsymbol{\nabla} G_0}{|\boldsymbol{\nabla} G_0|} \cdot \frac{\boldsymbol{\nabla} G_1}{|\boldsymbol{\nabla} G_0|}\right]^{\frac{1}{2}} \tag{8.16}$$

Then we introduce

$$|\boldsymbol{\nabla}(G_0 + G_1)| \simeq |\boldsymbol{\nabla} G_0| \left[1 - \boldsymbol{n} \cdot \frac{\boldsymbol{\nabla} G_1}{|\boldsymbol{\nabla} G_0|}\right] \tag{8.17}$$

The right hand side in equation (8.14) becomes :

$$(S_{T_0} + S_{T_1})|\boldsymbol{\nabla}(G_0 + G_1)| = S_{T_0}|\boldsymbol{\nabla} G_0| + S_{T_1}|\boldsymbol{\nabla} G_0| - S_{T_0}\boldsymbol{n} \cdot \boldsymbol{\nabla} G_1 \tag{8.18}$$

Introducing this last expression in Eq. (8.14), retaining first order terms and using the fact that the mean flame front is defined by $\boldsymbol{v}_0 \cdot \boldsymbol{\nabla} G_0 = S_{T_0}|\boldsymbol{\nabla} G_0|$ one obtains :

$$\frac{\partial G_1}{\partial t} + \boldsymbol{v}_0 \cdot \boldsymbol{\nabla} G_0 + \boldsymbol{v}_0 \cdot \boldsymbol{\nabla} G_1 + \boldsymbol{v}_1 \cdot \boldsymbol{\nabla} G_0 = S_{T_0}|\boldsymbol{\nabla} G_0| + S_{T_1}|\boldsymbol{\nabla} G_0| - S_{T_0}\boldsymbol{n} \cdot \boldsymbol{\nabla} G_1 \tag{8.19}$$

And then :

$$\frac{\partial G_1}{\partial t} + \boldsymbol{v}_0 \cdot \boldsymbol{\nabla} G_1 + \boldsymbol{v}_1 \cdot \boldsymbol{\nabla} G_0 = S_{T_1}|\boldsymbol{\nabla} G_0| - S_{T_0}\boldsymbol{n}_0 \cdot \boldsymbol{\nabla} G_1 \tag{8.20}$$

It is convenient to rearrange this expression to get a perturbed G-equation for a turbulent flame :

$$\frac{\partial G_1}{\partial t} + (\boldsymbol{v}_0 + S_{T_0}\boldsymbol{n}) \cdot \boldsymbol{\nabla} G_1 = -\boldsymbol{v}_1 \cdot \boldsymbol{\nabla} G_0 + S_{T_1}|\boldsymbol{\nabla} G_0| \tag{8.21}$$

This expression may be rearranged by placing the velocity perturbation on the right hand side, as $\boldsymbol{n} = -\boldsymbol{\nabla} G_0/|\boldsymbol{\nabla} G_0|$ so $-\boldsymbol{v}_1 \cdot \boldsymbol{\nabla} G_0 = \boldsymbol{v}_1 \cdot \boldsymbol{n}|\boldsymbol{\nabla} G_0|$. Noting that the steady front equation $\boldsymbol{v}_0 \cdot \boldsymbol{\nabla} G_0 = S_{T_0}|\boldsymbol{\nabla} G_0|$ can be cast in the form $-\boldsymbol{v}_0 \cdot \boldsymbol{n}|\boldsymbol{\nabla} G_0| = S_{T_0}|\boldsymbol{\nabla} G_0|$ one obtains the final form :

$$\frac{\partial G_1}{\partial t} + (\boldsymbol{v}_0 + S_{T_0}\boldsymbol{n}) \cdot \boldsymbol{\nabla} G_1 = \left[\boldsymbol{v}_1 \cdot \boldsymbol{n} - \frac{S_{T_1}}{S_{T_0}}\boldsymbol{v}_0 \cdot \boldsymbol{n}\right]|\boldsymbol{\nabla} G_0| \tag{8.22}$$

This expression indicates that the perturbed flame motion is controlled by flow velocity perturbations $\boldsymbol{v}_1$ and turbulent flame velocity perturbations S_{T1}.

8.4 Swirling flame transfer function

It is interesting to modify Eq. (8.21) in order to be close to the following equation studied by Schuller *et al.* (2003b) for laminar V flames :

$$\frac{\partial G_1}{\partial t} + (\boldsymbol{v}_0 + S_D\boldsymbol{n})\cdot\boldsymbol{\nabla} G_1 = \boldsymbol{v}_1\cdot\boldsymbol{n}|\boldsymbol{\nabla} G_0| \tag{8.23}$$

Furthermore, we know that the normal to the flame front is defined as $\boldsymbol{n} = -\boldsymbol{\nabla} G_0/|\boldsymbol{\nabla} G_0|$ so $-\boldsymbol{v}_1\cdot\boldsymbol{\nabla} G_0 = \boldsymbol{v}_1\cdot\boldsymbol{n}|\boldsymbol{\nabla} G_1|$. Furthermore, when the flame front is steady without any fluctuations, we have $\boldsymbol{v}_0\cdot\boldsymbol{\nabla} G_0 = S_{T_0}|\boldsymbol{\nabla} G_0|$ and as a consequence $-\boldsymbol{v}_0\cdot\boldsymbol{n}|\boldsymbol{\nabla} G_0| = S_{T_0}|\boldsymbol{\nabla} G_0|$. We finally establish that :

$$\frac{\partial G_1}{\partial t} + (\boldsymbol{v}_0 + S_{T_0}\boldsymbol{n})\cdot\boldsymbol{\nabla} G_1 = \left[\boldsymbol{v}_1\cdot\boldsymbol{n} - \frac{S_{T_1}}{S_{T_0}}\boldsymbol{v}_0\cdot\boldsymbol{n}\right]|\boldsymbol{\nabla} G_0| \tag{8.24}$$

Examining the perturbed G-equation one finds that the two terms appearing in the right hand side $\boldsymbol{v}_1$ and $-(S_{T_1}/S_{T_0})\boldsymbol{v}_0$ act in a similar fashion. In other words perturbations in the turbulent flame velocity and velocity disturbances have similar effects. It is then logical to extract the transfer function for turbulent burning velocity perturbations from the transfer function for flow velocity disturbances. The latter transfer function denoted by $\mathcal{F}^v_{\rm th}$ is known from previous studies, see Schuller *et al.* (2003b). The "V" flame transfer function $\mathcal{F}^v_{\rm th}$ is defined as the ratio of the relative fluctuation of heat release rate $\dot{Q}'_v/\overline{\dot{Q}}_v$ to the relative fluctuations of axial velocity $v'_x/\overline{v}_x$ where $v'_x\boldsymbol{e}_x$ stands for $\boldsymbol{v}_1$.

$$\mathcal{F}^v_{\rm th}(\omega) = \frac{\dot{Q}'_v/\overline{\dot{Q}}_v}{v'_x/\overline{v}_x} \tag{8.25}$$

When v'_x in this expression is replaced by $-S_{T_1}/S_{T_0}\overline{v}_x$, one obtains the flame transfer function due to turbulent burning velocity perturbations :

$$\frac{\dot{Q}'_{S_T}}{\overline{\dot{Q}}_{S_T}} = -\mathcal{F}^v_{\rm th}(\omega)\frac{S_{T_1}}{S_{T_0}} \tag{8.26}$$

The previous results may be combined to obtain the relative heat release fluctuation corresponding to a swirling flame :

$$\frac{\dot{Q}'_s}{\overline{\dot{Q}}_s} = \frac{\dot{Q}'_v}{\overline{\dot{Q}}_v} + \frac{\dot{Q}'_{S_T}}{\overline{\dot{Q}}_{S_T}} \tag{8.27}$$

which leads to :

$$\frac{\dot{Q}'_s}{\overline{\dot{Q}}_s} = \mathcal{F}^v_{\rm th}(\omega)\left[\frac{v'_x}{\overline{v}_x} - \frac{S_{T_1}}{S_{T_0}}\right] \tag{8.28}$$

This yields the global flame transfer function $\mathcal{F}^s_{\text{th}}$ for a swirling flame

$$\mathcal{F}^s_{\text{th}}(\omega) = \frac{\dot{Q}'_s/\overline{\dot{Q}}_s}{v'_x/\overline{v}_x} = \mathcal{F}_v - \mathcal{F}_v \frac{S_{T_1}/S_{T_0}}{v'_x/\overline{v}_x} \tag{8.29}$$

or in a more compact form :

$$\mathcal{F}^s_{\text{th}}(\omega) = \mathcal{F}^v_{\text{th}}(\omega)\left[1 - \frac{S_{T_1}/S_{T_0}}{v'_x/\overline{v}_x}\right] \tag{8.30}$$

To use this expression one has to relate the relative fluctuations in turbulent burning velocity S_{T_1}/S_{T_0} to the incoming velocity modulations. This relation is not known but it is natural to consider that these fluctuations are linked in a linear fashion to the incident perturbations and use the following model :

$$\frac{S_{T_1}}{S_{T_0}} = \chi \frac{v'_\theta}{\overline{v}_\theta} + \zeta \frac{v'_x}{\overline{v}_x} \tag{8.31}$$

where $\overline{v}_\theta$ is the azimuthal component and $\overline{v}_x$ the axial component of the swirling flow. This expression is based on the idea that the incident velocity modulations modify the swirl number and effectively change the turbulent burning velocity. It can be shown that the previous model provides a reasonable description of the signals observed in perturbed swirling flame experiments. The coefficients appearing in Eq. (8.31) are obtained from an adjustment process and from experimental data obtained for flame A (see chapter 6). The same numerical values for these coefficients are kept to explore the response of flame B featuring a higher flow velocity. Coefficients χ and ζ are respectively taken equal to -0.4 and 0.4.

It is next important to specify the field of azimuthal velocity fluctuations in terms of the axial field. Experiments indicate that when the swirler is submitted to axial velocity modulations it generates an azimuthal velocity perturbation. By imposing the unsteady Kutta condition at the trailing edge of the swirler blades one finds that the relative level of fluctuations is the same. However axial velocity disturbances are propagating at the speed of sound while azimuthal velocity perturbations are convected at the speed of the flow. As a consequence, when the flow is injected into the flame tube, all perturbations are convected but a phase shift remains between the two velocity components. This phase has to be taken into account to establish a theoretical flame transfer function. This is accomplished by using expression Eq. (8.31) for perturbations of the turbulent burning velocity and the following relation between axial and azimuthal fluctuations, where ϕ defines the phase shift between these fluctuations :

$$\frac{v'_\theta}{\overline{v}_\theta} = \frac{v'_x}{\overline{v}_x} \exp(i\phi) \tag{8.32}$$

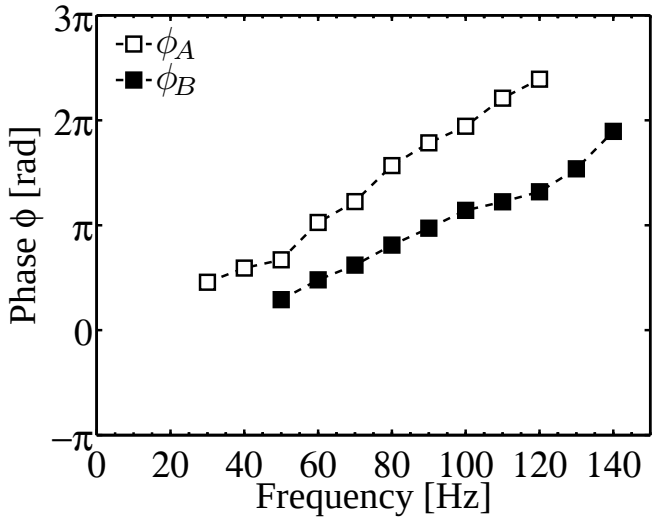

Figure 8.4: Evolution of the phase shift ϕ as a function of the frequency for two operating regimes A and B.

Inserting Eq. (8.31 and Eq. (8.32) in Eq. (8.30) one obtains :

$$\mathcal{F}^s_{\rm th}(\omega) = \mathcal{F}^v_{\rm th}(\omega)\Big[1 - (\zeta + \chi\exp(i\phi))\Big] \tag{8.33}$$

To use this result one has to provide an expression for $\mathcal{F}^v_{\rm th}$. This is obtained from Schuller *et al.* (2003b) and reproduced below for convenience :

$$\mathcal{F}^v_{th}(\omega)(\omega_*,\alpha) = \frac{2}{\omega_*^2}\frac{1}{1-\cos^2\alpha} \times \left[\exp(i\omega_*) - 1 - \frac{\exp(i\omega_*\cos^2\alpha) - 1}{\cos^2\alpha}\right]$$
$$+ \frac{2i}{\omega_*}\frac{1}{1-\cos^2\alpha} \times \Big[\exp(i\omega_*\cos^2\alpha) - \exp(i\omega_*)\Big] \tag{8.34}$$

where $\omega_* = \omega R/S_{T_0}\cos\alpha$, S_{T_0} being the turbulent burning velocity defined by $S_{T_0} = \overline{v}_x\,\sin\alpha$, R the injector tube radius and α the flame angle defined between the flame front and the vertical axis.

The phase shift ϕ has been measured experimentally at the base of the flame and results are plotted in Fig. 8.4. Experiments carried out for two operating regimes corresponding to different bulk velocities in the injector tube : $U_b = 2.67$ m s^{-1} (flame A) and $U_b = 4.13$ m s^{-1} (flame B). Results are : $\phi_A = \omega\tau_A + \phi^0_A$ with $\tau_A = 12$ ms and $\phi^0_A = -1$. For flame B, the phase is given by : $\phi_B = \omega\tau_B + \phi^0_B$ with $\tau_B = 8.5$ ms and $\phi^0_B = -1.5$.

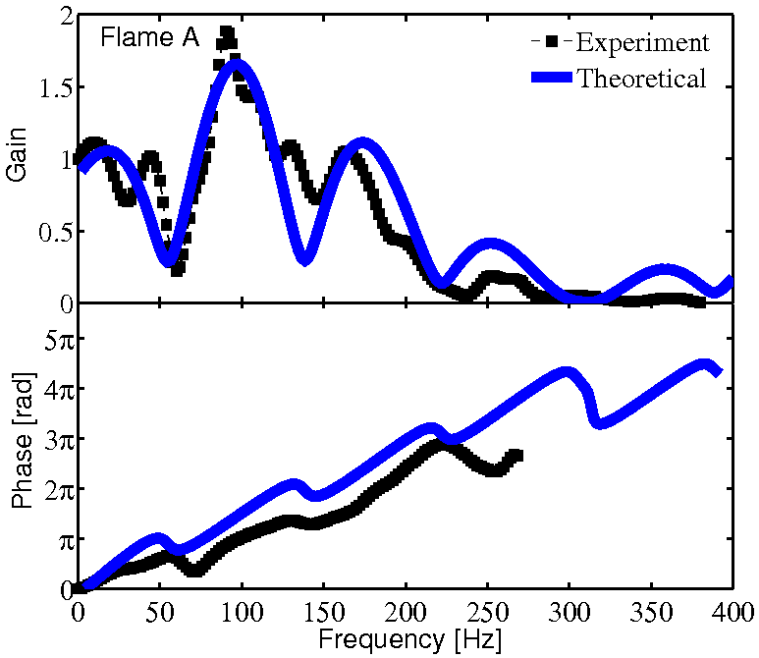

Figure 8.5: Comparisons of experimental $\mathcal{F}^s_{\text{exp}}$ and theoretical $\mathcal{F}^s_{\text{th}}$ swirling flame transfer functions for flame A ($U_b = 2.67$ m s^{-1}).

8.5 Theoretical estimates and experimental data

Experimental data are displayed in Fig. 8.5 and Fig. 8.6 together with theoretical predictions. Flame A is analysed first by examining the evolution of the gain and the phase of the flame transfer function in Fig. 8.5. In the top subfigure, the gain approaches unity in the low frequency limit. It decreases in a first range between 0 and 60 Hz to a value of less than 0.5. From 60 to 100 Hz, the curve features a peak. This peak is the maximum in the frequency range of interest. At 100 Hz, the flame response reaches its highest value. Beyond 100 Hz and until 150 Hz, the gain drops and reaches a value of 0.75. From 150 Hz to 180 Hz, the gain increases and reaches a local maximum of about 1. Beyond 180 Hz the gain decreases and eventually falls below 0.25. The phase, shown in the lower subfigure, increases nearly monotonically with frequency from 0 to 250 Hz. Beyond 250 Hz, the phase is less well defined as the gain is low in that frequency range. Under these conditions phase estimates become less reliable.

Theoretical results closely match experimental data except the phase which is slightly overestimated. It is worth noting that the maximum and minimum gain values are well reproduced and that this is obtained at characteristic frequencies determined experimentally. Mechanisms giving rise to the minimum and

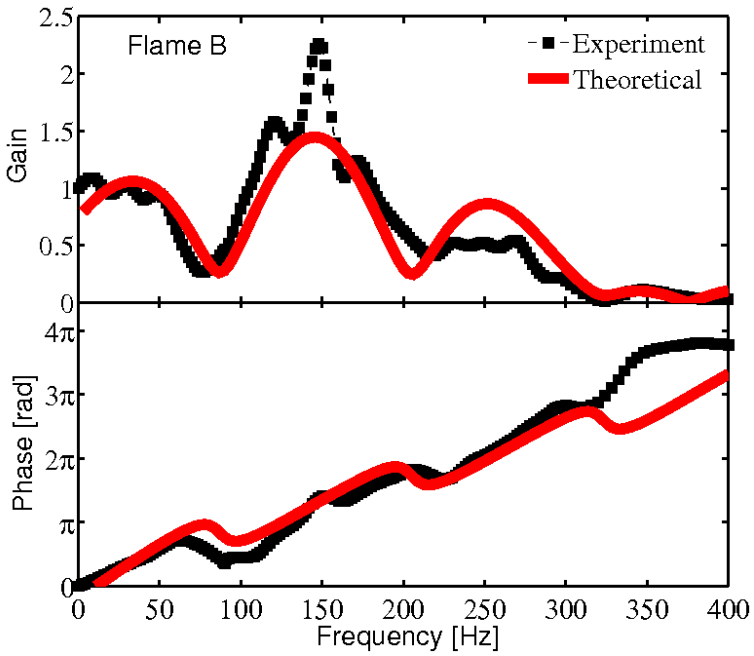

Figure 8.6: Comparisons of experimental $\mathcal{F}^s_{\text{exp}}$ and theoretical $\mathcal{F}^s_{\text{exp}}$ swirling flame transfer functions for flame B ($U_b = 4.13$ m s^{-1}).

maximum gain amplitudes have been investigated previously by examining the swirling flames dynamics. It was concluded that the level of fluctuation in heat release rate is linked to two mechanisms corresponding to a large surface variation at the extremity of the flame and swirl number fluctuations inducing angle variation at the base of the flame. These mechanisms are acting in phase opposition at 60 Hz leading to a low value of the gain and are acting nearly in phase at 90 Hz inducing a strong response.

The second case corresponding to flame B is shown in Fig. 8.6. In the experimental data, the gain is nearly constant and close to a value of one between 0 to 60 Hz. In the range from 60 to 100 Hz, the gain diminishes and reaches a local minimum of 0.3. From 100 to 150 Hz, the gain increases and reaches a local maximum. From 150 to 200 Hz, the gain decreases to a value of 0.6. It remains constant in the frequency range 200-280 Hz. For frequencies exceeding 280 Hz and up to 400 Hz, the gain decreases finally dropping below 0.2. The general trend for the phase is quasi-linear from 0 to 400 Hz but there are undulations. Theoretical prediction agree with these data quite well for this case with only some small differences in the amplitude of the response around 150 Hz and 230 Hz.

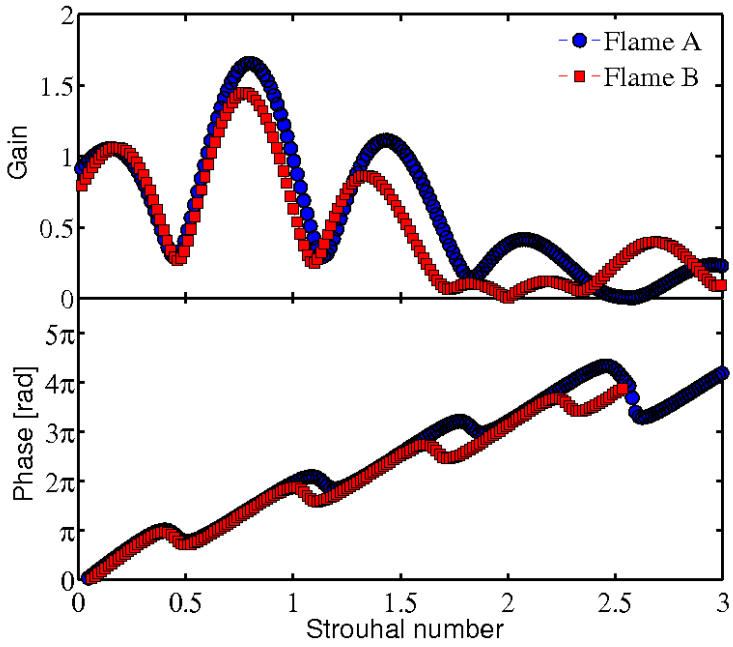

Figure 8.7: Flame transfer functions expressed in term of Strouhal number. Flame A ($U_b = 2.67$ m s^{-1}) and Flame B ($U_b = 4.13$ m s^{-1}).

It is finally worth examining the evolution of the gain and phase of the calculated transfer function as a function of the Strouhal number St $= fd/U_b$ where f is the frequency, d is the injector tube diameter and U_b is the bulk velocity inside the injector tube. Fig. 8.7 displays transfer function gain and phase calculated for flames A and B. The gain curves nearly collapse over the low Strouhal number range up to a value St $= 1.3$ but there are differences indicating that the gain depends on other parameters. Phase curves collapse in the useful range of Strouhal numbers below 1.6. These similarity features suitably reflect those found experimentally.

8.6 Conclusion

The transfer function of premixed swirling flames submitted to velocity disturbances is derived in this article. The analysis is based on an ensemble average perturbed G-equation which describes the dynamics of the mean flame front when it is submitted to external perturbations. It is important to account for the presence of azimuthal velocity perturbations generated by the swirler when this unit is impinged by axial velocity disturbances. These disturbances are propagating at the speed of sound while azimuthal velocity disturbances are convected by

the mean flow. This gives rise to a phase difference between these fluctuations. The combined axial and azimuthal unsteady velocity field modulates the swirl number and this is reflected in perturbations of the turbulent burning velocity. It is shown that the transfer function of swirling flames can be extracted from the transfer function of "V" flames derived in a previous study. This is accomplished by linking the relative variations of the turbulent burning velocity to the relative variations of the axial and azimuthal velocity components and by taking into account the phase difference which exists between these two components at the injector exit section. This phase is here determined experimentally. The model predictions are compared with experimentally determined transfer functions. A good agreement is reached for two operating points. It is also shown that the calculated transfer functions nearly collapse when they are plotted with respect to a Strouhal number based on the bulk velocity inside the injector. Conclusions raised in this paper also apply on radial swirlers where it has been shown that the same mechanism of mode conversion operates for axial or radial swirlers. Specifically, the gain of the flame transfer function for radial swirlers present also the same type of peak and small values at specific frequencies.

Part III

Combustion instabilities of swirling flames

Chapter 9

Combustion instabilities

Abstract : *Thermoacoustic instabilities are analyzed by making use of a nonlinear representation of flame dynamics based on the describing function. In this framework, the flame response is determined as a function of frequency and amplitude of perturbations impinging on the combustion region. The flame describing function has been experimentally determined and is combined with an acoustic transfer matrix representation of the system to provide growth rates and oscillation frequencies as a function of perturbation amplitude. These data can be used to determine regions of instability, frequency shifts with respect to the acoustic eigenfrequencies and they also yield amplitude levels when self-sustained oscillations of the system have reached a limit cycle. This equilibrium is obtained when the amplitude dependent growth rate equals the damping rate in the system. This requires an independent determination of this last quantity which is here based on measurements of the resonance response curve. Results obtained are compared with observations from systematic experiments carried out by varying the test combustor geometrical parameters. The demonstration of the FDF framework in a generic configuration indicates that this can be used in more general situations of technological interest.*

Résumé : *Les instabilités thermo-acoustiques sont analysées au moyen d'une représentation non-linéaire de la dynamique de la flamme basée sur la fonction de transfert généralisée ("Flame Describing Function" ou FDF). Dans ce cadre, la réponse de la flamme est déterminée en fonction de la fréquence et de l'amplitude des perturbations qui interagissent avec la flamme. Cette fonction de transfert généralisée, déterminée expérimentalement, est combinée avec une représentation matricielle de l'acoustique du système et permet un calcul des taux de croissance et des fréquences d'oscillation en fonction de l'amplitude des perturbations. Ces données peuvent être utilisées pour déterminer les régimes d'instabilité, les changements de fréquence et les niveaux d'amplitude au cycle limite. L'oscillation au cycle limite est obtenue lorsque le taux de croissance dépendant de l'amplitude est égal au taux d'amortissement dans le système. Il faut pour cela déterminer la valeur du taux d'amortissement qui est ici déduit de mesures de la courbe de résonance du brûleur. Les résultats obtenus sont comparés à des données d'expériences systématiques effectuées en faisant varier la géométrie du brûleur. Un bon accord est obtenu entre les prévisions et les observations.*

9.1 Introduction

Combustion instabilities research has been quite intense during the recent period in relation with the development of lean premixed combustors but prediction of these phenomena at the design stage still constitutes a challenge. It is known that high performance combustors feature instabilities which are mainly driven by the unsteady heat release rate. In these modes, heat release rate fluctuations are delayed with respect to incident perturbations and give rise to an unstable growth of oscillations Crocco (1968); Putnam (1971); Culick (2001). These perturbations can be generated in many different ways, but in most cases they are associated with convection of hydrodynamic perturbations Candel (2002) or fluctuations of the reactant composition Lieuwen and Zinn (1998).

The standard analysis of combustion instability combines the transfer function of the flame with a description of the system acoustics to determine eigenmodes and growth rates. Previous investigations (for example Schuermans *et al.* (2009); Kim *et al.* (2010a)) indicate that it is possible to find the linear stability map of various types of burners but this is restricted to small perturbations and cannot account for the limit cycle oscillations observed in practice. It is well known that nonlinear mechanisms dominate the dynamics of real systems. This is well illustrated in the case of "V" flame configurations Lawn (2000); Durox *et al.* (2005); Balachandran *et al.* (2005); Külsheimer and Büchner (2002) where one nonlin-

ear interaction takes place between the flame sheet and vortices shed from the injector lip. The "V" flame acts as an amplifier in the low frequency range and the response depends on the amplitude level Durox *et al.* (2009). Nonlinearities determine the limit cycle amplitudes, instability triggering (the mechanism by which an unstable oscillation appears when the system experiences a finite amplitude perturbation), mode switching (the change in frequency observed during operation of practical devices) and hysteresis Wicker and Yang (1996); Dowling (1997); Dowling (1999); Lieuwen and Neumeier (2002a). It has been shown recently that these nonlinearities associated with the combustion dynamics could be represented with a unified framework Noiray *et al.* (2008) in which the flame transfer function (FTF) is replaced by a flame describing function concept (FDF) which depends on the amplitude of perturbations impinging on the flame. A frequency domain stability analysis then yields growth rates and frequencies which depend on amplitude. Application of the FDF to the analysis of the stability of an unconfined multipoint injection laminar burner Noiray *et al.* (2008) indicates that it is possible to predict with reasonable accuracy many of the phenomena listed previously.

The FDF framework is here extended to deal with the dynamics of turbulent flames formed by a swirling injector in a confined geometry. Swirling injection is used in many practical systems like jet engines or gas turbine combustors. The swirling flow establishes a central hot gas recirculation region which stabilizes combustion. Swirling injection is usually adopted to anchor lean premixed combustion but the corresponding flow is highly unsteady and sensitive to acoustic perturbations eventually leading to combustion instabilities. The analysis of these instabilities has been mainly carried out with linear models Lieuwen and Neumeier (2002b); Broda *et al.* (1998); Schuermans *et al.* (1999); Kopitz *et al.* (2005). One of the issues in a nonlinear treatment is to suitably describe the swirling flame dynamics when flow perturbations have a variable level. The difficulty is compounded because the flame structure is complex with a central recirculation zone Syred (2006); Lilley (1977) and flame folding phenomena take place at large amplitude levels Thumuluru *et al.* (2007). In this last reference the swirl number is only estimated ($S = 1$). It is shown in this study that the unsteady shape of the flame is a strong function of the flow rate oscillation level. There are some indications Kang *et al.* (2007) that the dynamics of the flame is only weakly influenced by the swirl number but it is also found Thumuluru *et al.* (2007) that combustion dynamics of swirling flames feature an oscillation in the position and strength of the vortex breakdown region.

It is also indicated in Fritsche *et al.* (2007) that the combustor inlet temperature affects the flame structure leading to different shapes and flame dynamics. Some data indicate that the response saturates when the flow rate fluctuations are augmented. Experimental and numerical transfer function of swirling flames are

reported in Gentemann *et al.* (2004); Hirsch *et al.* (2005) for a frequency range extending from 0 to 400 Hz but effects of velocity perturbation amplitude are not documented and nonlinear effects are not characterized. It is however interesting to note that the transfer function features maximum and minimum gain values in the low frequency range. This has been recently confirmed experimentally by Jones *et al.* (2010) and numerically by Chong *et al.* (2010). A theoretical model based on the vorticity transport equation Hirsch *et al.* (2005) yields transfer functions which apparently match those obtained with two different swirlers of radial and axial types. Another paper Kim *et al.* (2010a) considers combustion instabilities of swirling flames to determine frequencies at the limit cycle but it remains in the linear regime. This also discusses the compact flame assumption with respect to acoustic wavelength. It is shown that in the compact flame regime, accurate predictions of eigenfrequencies and growth rate can be obtained using a global flame transfer function. References Thumuluru *et al.* (2007); Bellows *et al.* (2007) are dealing with the nonlinear effects of flow modulations on the dynamics of confined swirling flames. It is found that as the amplitude of the instability grows, nonlinear saturation limits the level of heat release rate fluctuations and changes the phase of these fluctuations with respect to the incoming perturbations Thumuluru *et al.* (2007). Flame describing function and swirling flame dynamics were investigated in a recent paper Schimek *et al.* (2010) but there are no predictions of frequencies and amplitudes of velocity disturbances at the limit cycle. Another recent paper Kim *et al.* (2010b) examines nonlinear response of swirling flames to equivalence ratio disturbances and shows that the amplitude and frequency dependence of the flame response to equivalence ratio oscillations is almost the same in terms of gain and phase as the flame response to inlet velocity oscillations.

Well controlled experiments are reported in chapter 5 where the dynamics of confined swirling flames is characterized by measurements of the FDF and by an examination of flame patterns during the cycle of oscillation at various levels of external modulation. These data will be used in the next sections to develop a nonlinear analysis of combustion instabilities based on the FDF framework which combines a standard acoustic transfer matrix analysis of the different components forming the system with a nonlinear description of the flame response.

At this point, it is interesting to briefly review the possible approaches of combustion instability analysis and link the present framework to the other current tools. It is possible to distinguish three general classes : (a) Methods based on an acoustic analysis of the system relying on networks of compact acoustic elements and employing a linear transfer function to describe the flame response. These methods are documented in books Poinsot and Veynante (2001); Munjal (1987) and their recent developments in papers by Nicoud *et al.* (2007); Stow and Dowl-

ing (2001); Schuermans *et al.* (2009), (b) Methods based on a projection on the eigenmodes of the system leading to a set of differential equations for the modal amplitudes Culick (1987), (c) Direct methods where Large Eddy Simulations of the complete 3D, compressible Navier-Stokes equations are integrated as illustrated by Selle *et al.* (2004) where the stability of the system is determined by observing the growth or decay of perturbations. The present approach extends the linear techniques of the first group by making use of the describing function concept in a manner introduced by Noiray *et al.* (2008). As in standard linear analysis, the frequency and growth rate are obtained from a dispersion relation and the calculation is carried out in the frequency domain but the dispersion relation here depends on the amplitude of perturbations impinging on the flame. It is thus possible to see how the level affects the growth rate, determine the stability of the system by comparing this rate with the damping rate associated with dissipation processes and find the level of oscillation at the limit cycle when the system is unstable.

This chapter begins with a description of the experimental configuration (section 9.2). Experimental data obtained for the describing function of swirling flames are reviewed in section 9.3. The theoretical model is outlined in section 9.4. Experimental determination of the system acoustic damping is described in section 9.5 together with predictions of self-sustained combustion oscillations of the system. This section also contains a comparison between experiments and calculations.

9.2 Experimental configuration

The combustor comprises an upstream manifold including a settling chamber, a contraction ended by a constant diameter duct equipped with the swirler, a horizontal end piece and a cylindrical flame tube (Fig. 9.1). A driver unit (loudspeaker) may be placed at the back end of this system to measure the flame describing function. An air/methane premixed flow is delivered to the feeding manifold unit through two diametrally opposed apertures. The flow then crosses a grid and a honeycomb to break the largest turbulent scales. The gas then traverses a convergent unit to decrease the boundary layer thickness, reduce the level of turbulence and flatten the velocity profile at the swirler inlet. The flow rotation is generated by the swirler which comprises eight twisted vanes arranged periodically around a central rod (6 mm in diameter). This central rod is terminated with a small cone (10 mm in diameter at the top) which stabilizes the flame during the unsteady motion of the flow. More details on the swirler are given in previous chapters. In this way, flashback is minimized. The outer diameter of the injector is 22 mm. The swirler geometry was designed to obtain a predetermined value of the swirl number corresponding to a flow featuring an inner recirculation

zone. Experimental profiles of axial and azimuthal velocities provide an estimate of the swirl number of about 0.55 (the radius is used in the definition of this number). The tube confining the flame is made of quartz allowing optical access and transmitting the flame radiation in the near ultraviolet. This is used to collect the OH* emission signal from the flame. The tube diameter is 70 mm and the length l_3 can take different values : 100 mm, 150 mm, 200 mm and 400 mm respectively. There are also three lengths l_1 available for the upstream manifold : short (96 mm), medium (160 mm) and long (224 mm). The upstream manifold diameter is 65 mm. The length of the convergent unit is 60 mm. Combination of these elements yields twelve geometrical configurations. The equivalence ratio is set equal to $\phi = 0.7$ in all experiments but the flow velocity in the injection unit can be varied. Two values are investigated in this study corresponding to bulk injection velocities $U_b = 2.67$ m s^{-1} and $U_b = 4.13$ m s^{-1} determined in the injector pipe. The root mean square velocity disturbance u' is measured with a hot wire anemometer. This device is placed in a cylindrical piece (20 mm in height) located on the upstream side of the swirler. The length between the swirler outlet and the backplane of the combustor is 43 mm.

The response of the combustor to external acoustic perturbations is obtained

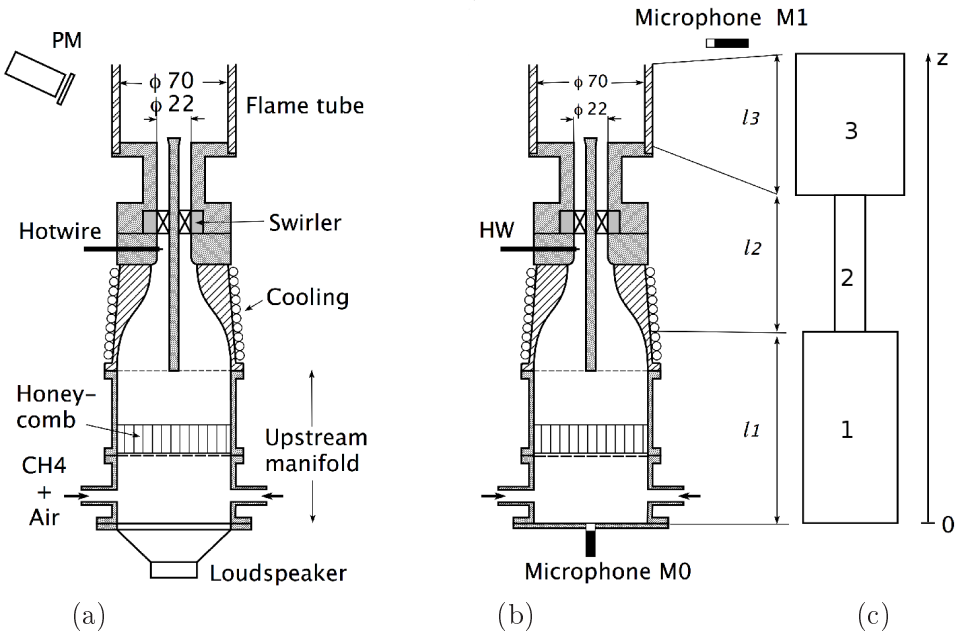

Figure 9.1: (a) : Experimental configuration used to measure flame describing functions. (b) : Without the loudspeaker, this setup is also used to obtain frequencies and amplitude of velocity disturbances u'/U_b under self-sustained limit cycle operation. (c) : Idealized representation of the burner geometry. Three lengths of the upstream manifold l_1 can be used together with three different length of the flame tube l_3.

when it is operating in a steady regime with a loudspeaker placed near the outlet section. This is used to generate harmonic perturbations and oscillations within the system are recorded with a microphone (M_0) located at the base of the burner. A second microphone (M_1) placed in front of the loudspeaker provides a reference signal. The response is then obtained by dividing the cross power spectral density examined at the driving frequency of the signal detected by microphone M_0 by the power spectral density of the signal recorded by microphone M_1. This response is then used to determine the damping rate by examining the quality factor at the resonance peak.

The FDF is obtained by modulating the flame with a driver unit placed at the back end of the system and by simultaneously measuring the velocity oscillation with the hot wire anemometer placed on the upstream side of the swirler and the heat release rate perturbation by detecting the light intensity radiated by OH^* radicals in the flame reaction zone. It has been indicated in chapter 6 that the FDF determined using the axial velocity signal measured with laser Doppler velocimeter downstream the swirler at the flame base yields a similar result. The same conclusion was obtained by Kim *et al.* (2009) showing that the swirler is acoustically transparent. It is known that for premixed flames at a constant equivalence ratio, the heat release rate is nearly proportional to the light intensity I_{OH^*}. Light emission is collected by a photomultiplier located at 25 cm from the burner axis which integrates the global emission signal. This detector is equipped with a narrow bandpass filter centered on the main OH^* peak light radiation in the near UV.

9.3 Swirling flame describing functions

The flame response is here characterized by making use of the describing function Noiray *et al.* (2008). This is accomplished by determining a set of transfer functions constituting the FDF. This quantity, defined by taking the ratio of the relative heat release rate fluctuation to the relative velocity fluctuation, is determined for a range of frequencies and for different levels of incoming velocity perturbations :

$$\mathcal{F}(\omega, u') = \frac{\dot{Q}'(\omega, u')/\overline{\dot{Q}}}{u'(\omega)/\overline{U}} \tag{9.1}$$

The heat release rate is deduced from OH^* emission intensity and the axial velocity disturbance is measured with a hot wire anemometer. The flame describing function can be cast in the form of a complex number in terms of a gain G and a phase difference φ and expressed as :

$$\mathcal{F}(\omega, u') = G(\omega, u')\, e^{i\varphi(\omega, u')} \tag{9.2}$$

The gain reflects the level of response while the phase defines the time lag between velocity and emission signals. The FDFs presented in Fig. 9.2 pertain to flows with a bulk velocity $U_b = 2.67$ m s^{-1} and $U_b = 4.16$ m s^{-1} over a frequency range extending from 0 to 400 Hz and to four velocity modulation levels u'/U_b where u' corresponds to the root mean square (rms) perturbation level determined by the hot wire anemometer. Results are only presented for four discrete levels in Fig. 9.2 but intermediate perturbation amplitudes were also investigated. Systematic experiments indicate that FDF measurements are repeatable and that the uncertainty in the gain does not exceed 5 % at least in the range where this gain takes values greater than 0.2. The same level of uncertainty is found in the relative phase $\Delta\phi/\phi$ measurements.

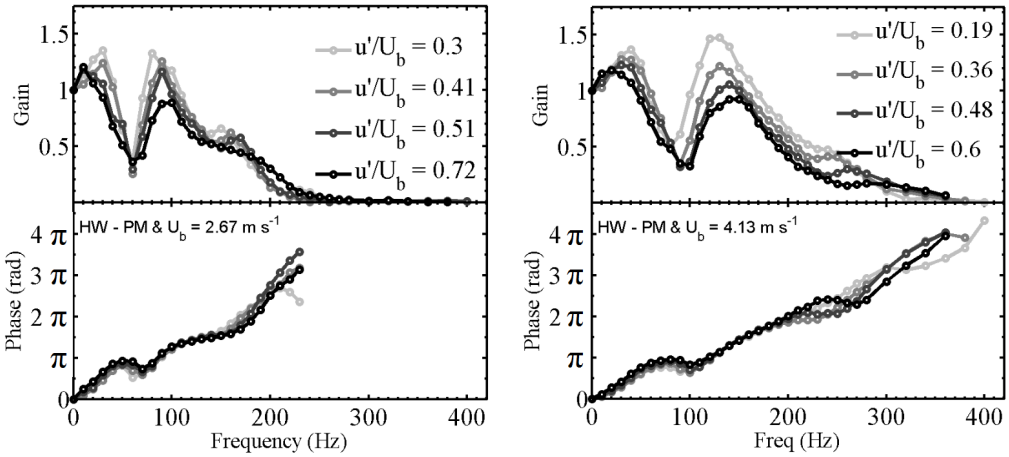

Figure 9.2: Flame Describing Functions for two operating points and for a range of perturbation velocities. Flame A on the left ($U_b = 2.67$ m s^{-1}) and flame B on the right ($U_b = 4.13$ m s^{-1}). Gains and phases are expressed as functions of frequency and ratio of amplitude of the root mean square velocity disturbance to the bulk velocity u'/U_b.

For the first operating point (Fig. 9.2 (a)), the gain approaches one in the low frequency limit. It decreases in a first range between 0 and 60 Hz to a value of less than 0.5. From 60 to 100 Hz, each curve features a peak. For all velocity disturbance levels, this peak is the maximum in the frequency range of interest. At 100 Hz, the flame response is high. Beyond 100 Hz and until 150 Hz, the gain drops again and reaches a value of 0.75 for most of the transfer function curves. From 150 Hz to 180 Hz, the gain increases but reaches a local maximum of about 0.7 for the smallest modulation level and 0.5 for the highest modulation level. Beyond 180 Hz the gain decreases in all cases and its value falls below 0.25. The phase in the bottom plot in Fig. 9.2 (a) increases nearly continuously with frequency from 0 to 250 Hz.There is however a local inflection in the range where the gain features a minimum. This behavior generally corresponds to an

interference process involving two kinds of fluctuations as shown for example in a recent theoretical modeling of the flame transfer function, see previous chapters. Beyond 250 Hz, the phase is less smooth due to the low value of the gain in that frequency range with the consequence that phase estimates become less reliable. The phase signal can be used to determine a global delay of the dynamical interaction between the incoming velocity modulation and the resulting heat release rate perturbation. If the phase varies in an approximately linear fashion with respect to frequency, it is possible to write $\varphi = \omega\tau_{cv}$ where $\omega = 2\pi f$. This can be used to determine a global delay between a velocity perturbation measured at the hotwire location and the flame response which is found hereby independent of the frequency. In a previous work, it was shown that the axial velocity fluctuation measured by the hot wire is equivalent to the axial velocity fluctuation at the base of the flame, see previous chapters. For operating point A, a convective time estimated from : $\tau_{cv} = \varphi/2\pi f$ is approximately equal to 5 ms in the frequency range of interest. This value corresponds to the time required by a disturbance to be convected to the flame and reach the flame edge. The dynamics observed for the second operating point B in Fig. 9.2 (b) is quite similar to that found for point A shown in the left plot but with a shift in frequency. The minimum is around 90 Hz in the second case and the maximum around 130 Hz. It is possible to show that the describing functions for these two velocities are similar when they are plotted with respect to a Strouhal number based on the bulk flow velocity, see previous chapters.

9.4 Theoretical modeling

It is now interesting to show how the previous data can be included in a stability analysis. For this one has to link the flame describing function to the acoustics of the system. The simplified geometry of the burner is sketched in Fig. 9.1(c) which consist in three cylindrical parts. The first one has a length l_1 and corresponds to the upstream manifold part and to the first third of the convergent unit and its diameter is 65 mm. Three cases are examined for l_1 : short, medium and long upstream manifold respectively corresponding to 117.3 mm, 181.3 mm and 245.3 mm. The second element has a length l_2 and is associated to the two others thirds of the convergent unit and to the injector. Its length is 116.7 mm and the diameter is 21.17 mm. This diameter corresponds to the hydraulic diameter of the injector pipe with the rod. Finally, the last element models the flame tube (70 mm in diameter and l_3 in length). The flame is established in a region where the flow area changes abruptly. On its upstream side this area is defined by the injection duct S_2, on its downstream side the area is that of the flame tube S_3. It is thus interesting to consider this geometry and derive the jump condition relating the upstream and downstream perturbed variables. This is ac-

complished by assuming that the flame is compact with respect to the wavelength.

It is convenient to start from a local equation obtained by combining mass and energy balance equations for a reactive medium. Since the flow velocities are small, the Mach number is low and the combustion region is nearly isobaric. One may also neglect the convective terms. Integrating the balance equation over the flame volume V, noting that the product $\rho_0 c_0^2$ (where ρ_0 is the density and c_0 the speed of sound) is constant across the flame and applying Green's theorem one obtains an expression for the integrated volumetric flux in terms of the global heat release fluctuations in the control volume. Using this expression between sections 2 and 3 in the system (plot Fig. 9.1(c)) and assuming that velocity perturbations are uniform in these sections one obtains the following jump condition :

$$S_3 u_3' - S_2 u_2' = \frac{\gamma - 1}{\rho_0 c_0^2} \dot{Q}' \tag{9.3}$$

This expression links velocity perturbations on the upstream and downstream sides of the flame to the unsteady heat release rate $\dot{Q}'$ integrated over the flame volume. The perturbed quantities appearing in this jump condition are not necessarily small. It is now possible to express the integrated heat release rate $\dot{Q}'$ in terms of the flame describing function defined previously Eq. (9.1) and write the jump condition as a function of the gain and phase of the FDF. By combining Eq. (9.1), Eq. (9.2) and Eq. (9.3), one finds :

$$S_3 u_3' - S_2 u_2' = \frac{\gamma - 1}{\rho_0 c_0^2} G e^{i\varphi} \overline{\dot{Q}} \frac{u_2'}{\overline{u}_2} \tag{9.4}$$

It is convenient to express the integrated mean heat release rate in terms of the fresh and burnt gas temperatures which in the present case correspond to T_2 and T_3 : $\overline{\dot{Q}} = \dot{m} c_p (T_3 - T_2)$ where $\dot{m} = \rho_2 \overline{u}_2 S_2$ is the total mass flow rate (we can observe that $\overline{u}_2$ corresponds to U_b). Temperature T_2 and T_3 are respectively equal to 300 K and 1600 K. T_3 is an estimation of the mean temperature in the flame tube taking into account heat losses to the tube with respect to the adiabatic temperature of the flame. The product $\rho_0 c_0^2$ is a constant through the combustion region and can be evaluated in any of the sections belonging to the control volume V. It is convenient to use section 2 and express the sound velocity in that section : $\rho_0 c_0^2 = \rho_2 c_2^2 = \rho_2 \gamma r T_2$. Gathering these various results it is possible to obtain an expression for the ratio of the perturbed volume flow rates on the downstream and upstream sides of the flame $K(\omega, u_2') = (S_3 u_3')/(S_2 u_2')$:

$$K(\omega, u_2') = \left[1 + G e^{i\varphi} \left(\frac{T_3}{T_2} - 1 \right) \right] \tag{9.5}$$

Considering plane wave propagation in the different components of the system with amplitudes A_j and B_j, it is then a simple matter to write that the pressure

and volume flow rate perturbations are continuous at the successive area changes and use equation Eq. (9.5) to link the volumetric flow rate perturbations through the flame. These various equations combine with the boundary conditions at the system backplane (a rigid wall) and exhaust (an open end) to yield a system of linear equations $M \times X = 0$ where M is given by the following matrix :

$$\begin{bmatrix} e^{ik_1l_1} & e^{-ik_1l_1} & -1 & -1 & 0 & 0 \\ 1 & -1 & 0 & 0 & 0 & 0 \\ \frac{S_1}{\rho_1 c_1}e^{ik_1l_1} & \frac{-S_1}{\rho_1 c_1}e^{-ik_1l_1} & \frac{-S_2}{\rho_2 c_2} & \frac{S_2}{\rho_2 c_2} & 0 & 0 \\ 0 & 0 & \frac{KS_2}{\rho_2 c_2}e^{ik_2l_2} & \frac{KS_2}{\rho_2 c_2}e^{-ik_2l_2} & \frac{-S_3}{\rho_3 c_3} & \frac{S_3}{\rho_3 c_3} \\ 0 & 0 & 0 & 0 & e^{ik_3l_3} & e^{-ik_3l_3} \\ 0 & 0 & e^{ik_2l_2} & e^{-ik_2l_2} & -1 & -1 \end{bmatrix}$$

where lengths l_1, l_2, l_3 are defined in Fig. 9.1 (c). k_j is the wavenumber in the j^{th} section and X is a vector of waves amplitudes in the various components of the system :

$$\mathrm{X}^{\boldsymbol{T}} = [A_1 \quad B_1 \quad A_2 \quad B_2 \quad A_3 \quad B_3]$$

This set of equations includes the flame describing function in the factor K defined previously Eq. (9.5). Nontrivial solutions of this system correspond to a vanishing determinant. This defines the dispersion relation which now depends on the level of perturbations impinging on the flame. The determinant of this matrix can be derived analytically and takes the form :

$$\begin{aligned} \mathrm{Det[M]} = \frac{S_1}{\rho_1 c_1}\sin(k_1l_1)\left[\frac{K(\omega,u_2')S_2}{\rho_2 c_2}\cos(k_2l_2)\sin(k_3l_3) + \frac{S_3}{\rho_3 c_3}\sin(k_2l_2)\cos(k_3l_3)\right] \\ -\frac{S_2}{\rho_2 c_2}\cos(k_1l_1)\left[\frac{S_3}{\rho_3 c_3}\cos(k_2l_2)\cos(k_3l_3) - \frac{K(\omega,u_2')S_2}{\rho_2 c_2}\sin(k_2l_2)\sin(k_3l_3)\right] \end{aligned} \tag{9.6}$$

The complex roots $\omega = \omega_r + i\omega_i$ of the dispersion relation $\mathrm{Det[M(\omega,u')]} = 0$ are obtained numerically as a function of the perturbation level. This yields an angular frequency $\omega_r = \omega_r(u_2')$ and a growth rate $\omega_i = \omega_i(u_2')$ which both depend on the amplitude of velocity perturbations impinging on the flame. ω_r corresponds to $2\pi f$ where f is the oscillation frequency. Since flame transfer function were measured at discrete levels, FTF at intermediate oscillation levels were interpolated linearly. One may thus trace the root locus as a function of the amplitude level in a diagram where the frequency is used as ordinate while the growth rate is used as horizontal coordinate. In the absence of damping, the stability of the system is defined by the sign of $\omega_i(u_2')$. If this quantity is positive the oscillation grows and the system is unstable. However, the real system also features a certain amount of damping α. While this quantity is difficult to determine theoretically it can be estimated experimentally by measuring the resonance response of the system when it is submitted to an external forcing as explained in

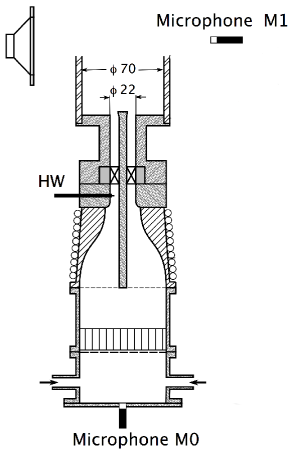

Figure 9.3: Experimental setup used to determine the resonance response of the burner under hot fire conditions. The external excitation is generated with the loudspeaker located at the outlet of the flame tube. Two microphones are used to measure the acoustic response M_0 and M_1 respectively located at the base and at the outlet of the burner.

the experimental configuration section. The damping coefficient is then deduced (see the next section) from the frequency bandwidth of the acoustical response of the system to external modulations. Stability is then governed by the sign of $\omega_i(u_2') - \alpha$. In other words when the growth rate $\omega_i(u_2')$ exceeds the damping rate α, the oscillation amplitude increases. One also deduces that when $\omega_i(u_2') = \alpha$ the system reaches a limit cycle. This is used in what follows to analyze stability and determine the amplitude level at the limit cycle when the system features self-sustained oscillations.

9.5 Experimental results and comparison with predictions

Experimental measurements of the system damping As indicated in the previous section, the growth rate must be compared to the damping coefficient to determine the stability of the system. This coefficient can be estimated from a resonance response by imposing an external modulation under hot fire conditions and measuring the resonance sharpness. The setup used to characterize the response is plotted in Fig. 9.3.

This acoustic response is plotted in Fig. 9.4 and obtained for flame A. From the frequency response one finds the half power points which give the frequency bandwidth Δf of the quality factor. Assuming that the system is analogous to a

harmonic oscillator, one deduces the damping coefficient $\alpha \simeq \pi\Delta f$. The damping has been determined with the burner equipped with the short upstream manifold and the 100 mm flame tube. In this configuration, combustion is stable. In what follows, it will be assumed that the damping does not change with the geometrical characteristics. There are four distinct contribution to the damping depending on the boundary layers, the bulk velocity, the radiated losses and the vortex rollup. The main contribution identified in a separate investigation corresponds to vortex rollup and subsequent dissipation. This contribution to damping will not depend on the size of the upstream manifold and flame tube. The typical value of the damping rate is $\alpha \simeq 55$ s^{-1}. This value is much larger than that found for the same configuration but in the absence of flow and reaction. The measurement itself is imperfect and one should take into account a possible error bar of $\pm$ 10 s^{-1}.

Self-sustained oscillations Self-sustained oscillations are characterized by the level of the root mean square of the pressure fluctuation at the base of the upstream manifold. The signal is obtained with the microphone M_0, see Fig. 9.1 (b). When the rms pressure level is low and broadband, the system is operating in a stable mode. It is oscillating when most of the power is concentrated in a narrow band of frequencies and when the rms pressure exceeds a threshold value which corresponds to the typical noise level in the system and in the present case can be taken equal to 10 Pa. This is illustrated in Fig. 9.5 which displays temporal evolutions of heat release rate fluctuation and pressure inside the upstream manifold for one stable and one unstable case. The geometry is based on the short upstream manifold for the operating point A and the length of the flame

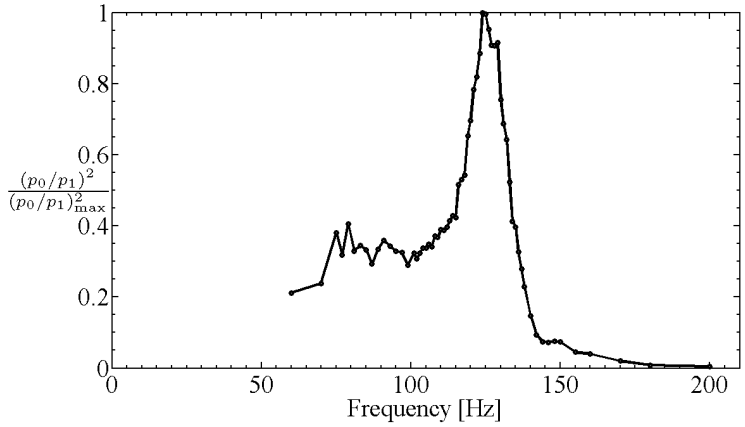

Figure 9.4: Experimental acoustic response of the combustor from $f = 0$ to $f = 200$ Hz obtained under fire condition for flame A with the short upstream manifold and the 100 mm flame tube. This curve is used to determine the damping coefficient α with $\alpha = \pi\Delta f$. Result indicates a damping coefficient equal to $\alpha \simeq 55$ s^{-1}.

tube is varied from $l_3 = 100$ mm to $l_3 = 400$ mm. These signals indicates that the long flame tube leads to an unstable oscillation while the flame is stable when the flame tube is short for the operating point A. One can observed that the pressure signal is quasi sinusoidal meaning that the acoustics remains linear in the system.

Results of systematic experiments are plotted in Fig. 9.6 for flames A and in Fig. 9.7 for flame B. The stars are displayed as a function of geometrical parameters of the configuration : flame tube length and upstream manifold size. Results are given for operating points A and B corresponding to two different bulk velocities in the injection unit. Gray circles indicate stable configurations while black stars indicate self-sustained instabilities. Gray stars corresponds to slightly unstable cases. Both figures indicate when the system is stable or unstable for flames A and B. When the system is equipped with a 400 mm flame tube, it is unstable for all sizes used for the upstream manifold and for both operating points A and B. One observes that for some cases, the amplitudes of velocity u'/U_b is very high. Some fairly high values are reached for u'/U_b and it is possible that a reverse flow occurs during some parts of the modulation cycle.

Limit cycles Results of calculations are plotted in Figs. 9.8, 9.9 and 9.10. Each plot shows the root locus $\omega_i(u'_2), f(u'_2)$ when the relative velocity fluctuation level upstream of the flame is progressively increased. The error bar on the damping rate is also shown in the form of a vertical gray region centered around

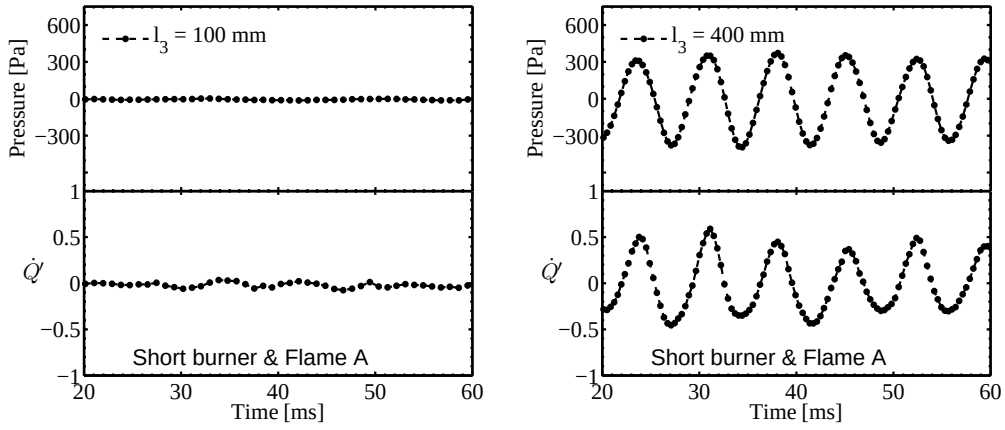

Figure 9.5: Root mean square pressure in Pa measured at the base of the combustor with the microphone M_0 and heat release rate fluctuation $\dot{Q}'$ measured with the photomultiplier. The geometrical configuration is based on the short upstream manifold for flame A and two lengths of the flame tube are matched : (a) : stable case with $l_3 = 100$ mm, (b) : unstable case with $l_3 = 400$ mm.

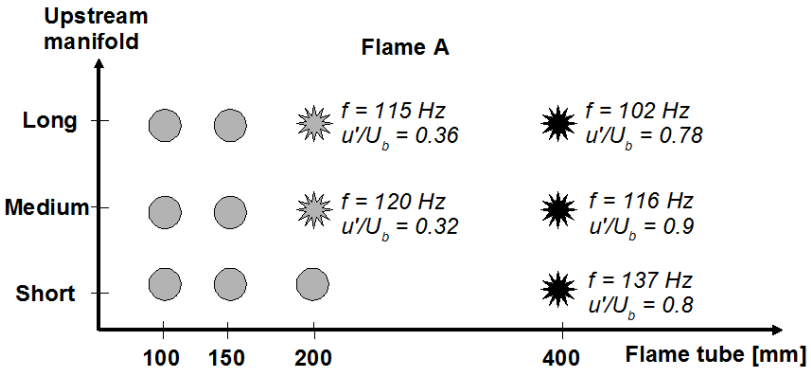

Figure 9.6: Combustor stability map for flame A. The stable configurations are in gray circles while black stars indicate a high level of rms pressure which corresponds to a self-sustained oscillation of the system. Gray stars indicate a slightly unstable configuration.

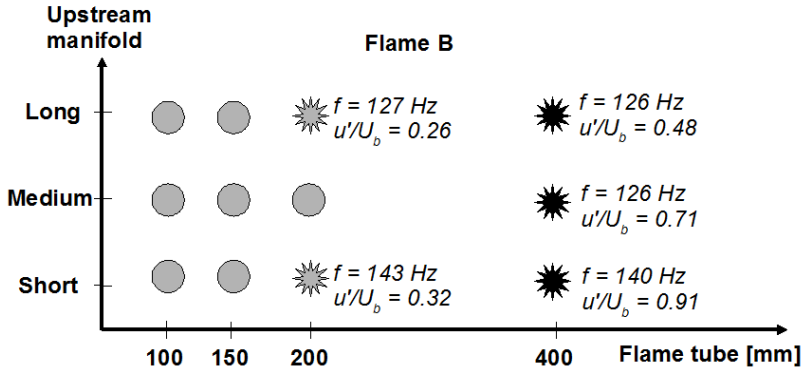

Figure 9.7: Combustor stability map for flame B. The stable configurations are in gray circles while black stars indicate a high level of rms pressure which corresponds to a self-sustained oscillation of the system. Gray stars indicate a slightly unstable configuration.

55 s^{-1}. When the trajectory is on the left of the estimated damping, the system is stable. This corresponds to negative values of $\omega_i(u'_2) - \alpha$ meaning that the pressure fluctuation is damped as a function of time. When the trajectory begins on the right of the region corresponding to the estimated damping the system is unstable and reaches a limit cycle at the cross point between the locus root and the vertical region corresponding to α with the error bar in gray.

The root locus is plotted as a function of frequency f expressed in Hz and growth rate ω_i given in s^{-1} as a function of the velocity disturbance amplitude. Six cases are described, four corresponds to flame A and the others to flame B. The first cases, in Fig. 9.8 (a) and (b), start with a growth rate which is below $\alpha = 55$ s^{-1}

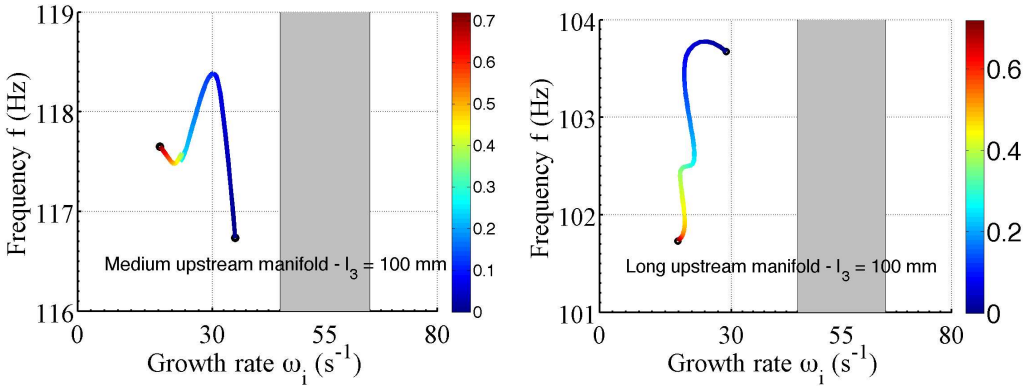

Figure 9.8: Frequency - Growth rate trajectories plotted as a function of the velocity disturbance level u'/U_b. The value of the damping coefficient α is shown in the form of a gray region representing the error bar on this quantity. The stable and unstable regions are located respectively on the left and on the right of the gray region. The root locus is plotted on a color scale as a function of the relative fluctuation u'/U_b. (a) and (b) respectively correspond to a system equipped with the medium and long upstream manifold and for a confinement tube length $l_3 = 100$ mm. Flow conditions are those of flame A.

and at frequencies near 111 Hz and 104 Hz. The trajectory always remains on the left of the damping value indicating that the system is stable. This is indeed what is observed experimentally as shown in Fig. 9.6.

In Fig. 9.9 (a) and (b), both cases are unstable because trajectories start on the right of the gray zone associated to the damping coefficient. But these trajectory are not crossing the damping limit fixed for a value equal to $\alpha = 55$ s^{-1}. Nevertheless, one may get an estimate of the limit cycle. For case (a), this limit cycle is predicted with a frequency f equal to 116.5 Hz and a velocity disturbance amplitude close to 0.8. Experimental values (Fig. 9.6) indicate a frequency equal to 116 Hz and an amplitude level of 0.9 for this operating point. Predictions and experiments are then in good agreement. For case (b), the predicted frequency is $f = 103$ Hz and the velocity amplitude level u'/U_b is 0.8 while experimental results give a frequency of 102 Hz and an amplitude level of 0.78 confirming predictions.

For flame B with the medium upstream manifold and $l_3 = 400$ mm, Fig. 9.10 (a) indicates that the trajectory begins on the right of α and that it crosses the damping boundary for a relatively high value of u'/U_b. The limit cycle is reached for a frequency of 130 Hz for $u'/U_b \simeq 0.55$. This is consistent with experimental observations indicating that the system oscillates at $f = 126$ Hz and that the

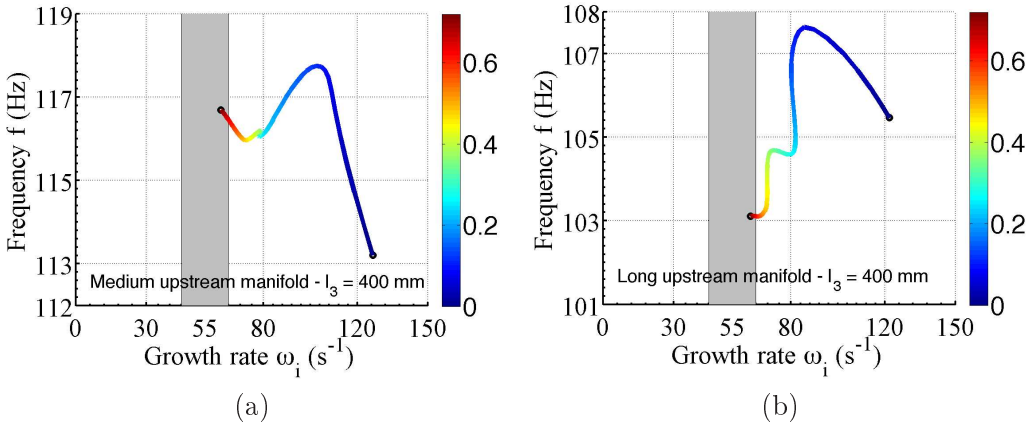

Figure 9.9: Frequency - Growth rate trajectories plotted as a function of the velocity disturbance level u'/U_b. The value of the damping coefficient α is shown in the form of a grey region representing the error bar on this quantity. The stable and unstable regions are located respectively on the left and on the right of the gray region. The root locus is plotted on a color scale as a function of the relative fluctuation u'/U_b. (a) and (b) respectively correspond to a system equipped with the medium and long upstream manifold and for a confinement tube length $l_3 = 400$ mm. Flow conditions are those of flame A.

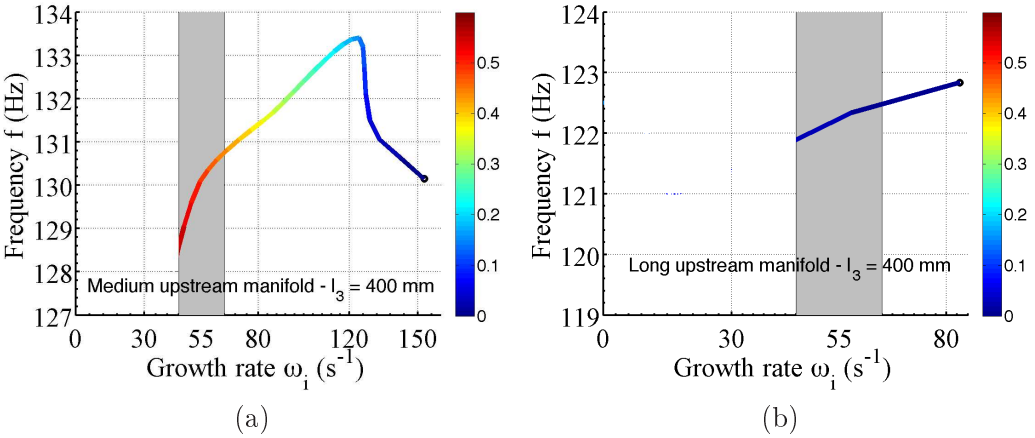

Figure 9.10: Frequency - Growth rate trajectories plotted as a function of the velocity disturbance level u'/U_b. The value of the damping coefficient α is shown in the form of a grey region representing the error bar on this quantity. The stable and unstable regions are located respectively on the left and on the right of the gray region. The root locus is plotted on a color scale as a function of the relative fluctuation u'/U_b. (a) and (b) respectively correspond to a system equipped with the medium and long upstream manifold and for a confinement tube length $l_3 = 400$ mm. Conditions are those of flame B.

amplitude at the limit cycle is $u'/U_b = 0.71$. For flame B with the long upstream manifold and $l_3 = 400$ mm, in Fig. 9.10 (b), the growth rate also exceeds

the damping coefficient α but the trajectory crosses the damping boundary at a much lower value of the relative velocity disturbance $u'/U_b \simeq 0.05$. This is underestimated with what is shown in Fig. 9.6 where the level of oscillation reaches $u'/U_b = 0.4$. One explanation of the difference between predicted estimates and experimental amplitude is that the rms value u' is determined in the prediction with pure harmonic signals while background noise is superimposed in the experiments due to turbulent flow. This may lead in the experiments to slight differences with higher rms values for limit cycles at moderate amplitudes. The predicted frequencies at the limit cycle (130 Hz for case (a) and 122 Hz for case (b)) are also in good agreement with experimental measurements which respectively indicate 126 Hz and 125 Hz.

All results are gathered in Table 9.1. These results support conclusions of a recent work Kim *et al.* (2010a) which discusses the compact flame assumption with respect to acoustic wavelength. In the case of a flame in the compact flame regime, accurate predictions of eigenfrequencies and growth rate can be obtained using a global flame transfer function.

It is interesting to determine the evolution of the growth rate minus the damping coefficient $\omega_i - \alpha$ as a function of the velocity amplitude and the length of the flame tube. When the value of $\omega_i - \alpha$ is equal to zero, the system reaches the limit cycle. In Fig. 9.11, the stability maps for flame A are plotted for two sizes of the upstream manifold. These plots can be used to predict the stable or unstable behavior of a configuration. With the medium size upstream manifold (Fig. 9.11(a)), one finds that for a flame tube of 170 mm in length the combustor is stable. Increasing the flame tube length, the amplitude of the velocity disturbance at limit cycle increases to reach very high levels. It appears that these high amplitude levels have a limit close to 0.8.

Similar results are obtained for flame B in Fig. 9.12, respectively (a) for the medium upstream manifold and (b) for the long one. The case (b) presents a wide stability range for all flame tube sizes. This explains why the limit cycle

Operating point	A	A	B	B
Upstream manifold (burner)	Medium	Long	Medium	Long
Experimental frequency	116 Hz	102 Hz	126 Hz	125 Hz
Predicted frequency	116.5 Hz	103 Hz	130 Hz	122 Hz
Experimental velocity amplitude	0.9	0.78	0.71	0.4
Predicted velocity amplitude	0.8	0.8	0.55	0.05

Table 9.1: Comparison between predictions and experiments at limit cycle for operating points A and B and for a flame tube length $l_3 = 400$ mm.

with the 400 mm flame tube is weakly unstable with flame A (see Fig. 9.10(b)).

9.6 Conclusion

This chapter focuses on the analysis of combustion instabilities of swirling flames in a configuration idealizing typical situations encountered in practice. The ge-

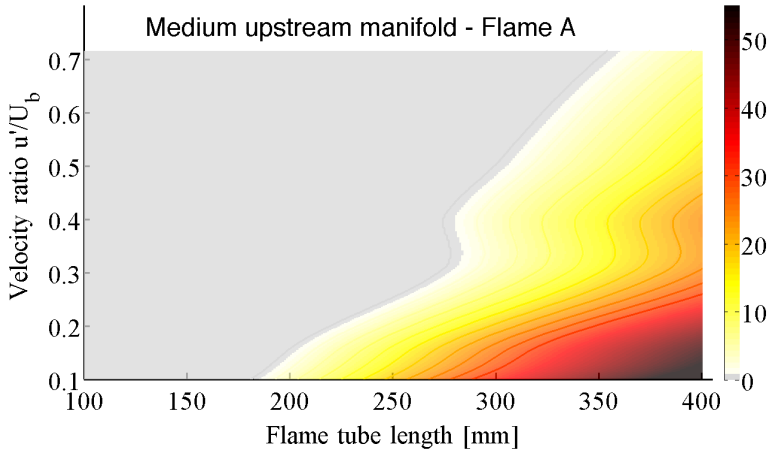

(a)

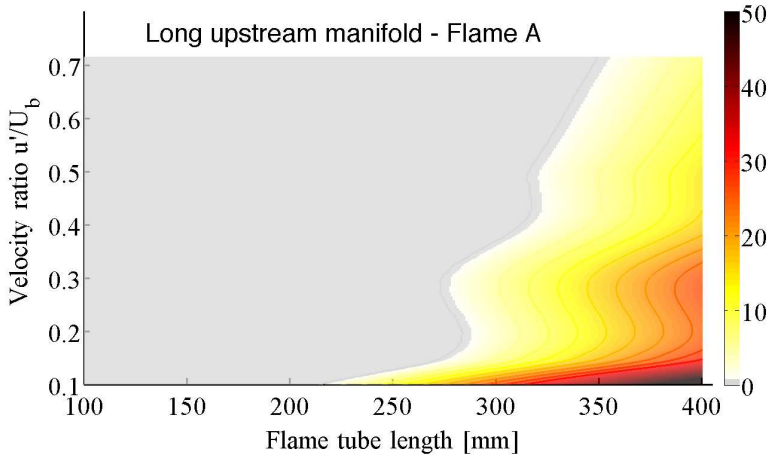

(b)

Figure 9.11: Stability maps of the burner for flame A as a function of the flame tube length varying between 100 and 400 mm. The colorbar indicates values of $\omega_i - \alpha$ in s^{-1} (negative values in the gray region). The line separating gray and white regions corresponds to points where $\omega_i - \alpha = 0$ meaning that the limit cycle is reached. (a) corresponds to the medium upstream manifold while (b) corresponds to the long upstream manifold.

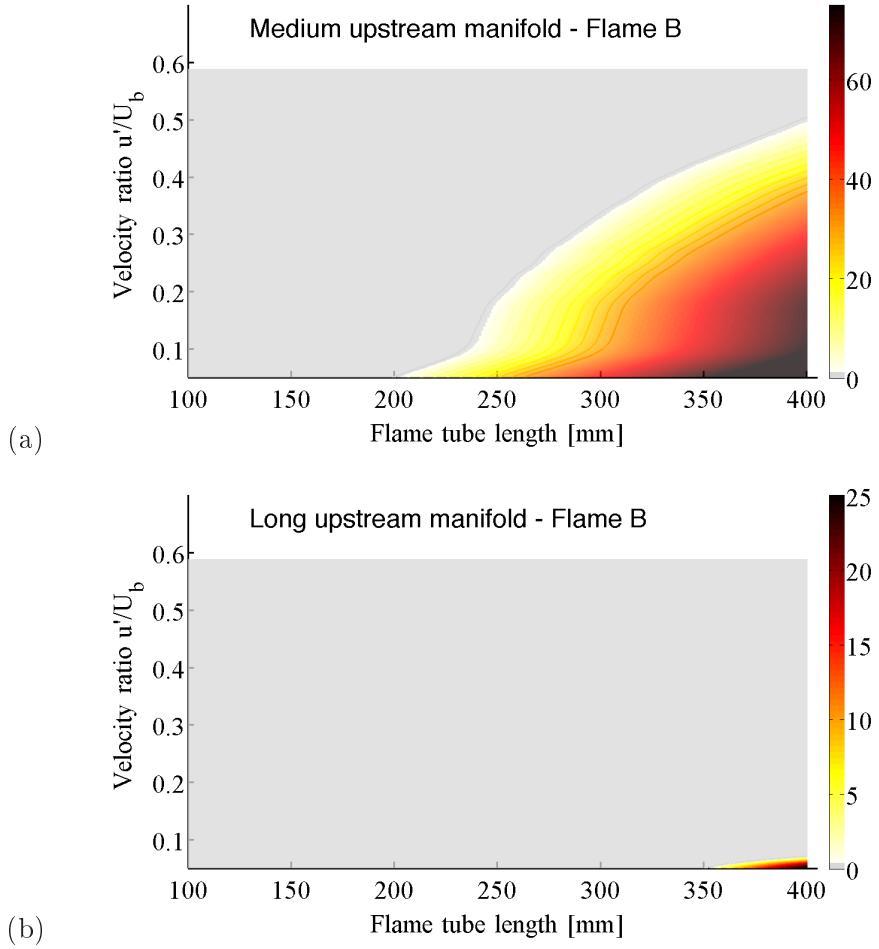

Figure 9.12: Stability maps of the burner for flame B as a function of the flame tube length varying between 100 and 400 mm. The colorbar indicates values of $\omega_i - \alpha$ in s^{-1} (negative values in the gray region). The line separating gray and white regions corresponds to points where $\omega_i - \alpha = 0$ meaning that the limit cycle is reached. (a) corresponds to the medium upstream manifold while (b) corresponds to the long upstream manifold.

ometry can be varied by changing the lengths of the upstream manifold and flame tube. The flame describing function determined experimentally is used to represent the nonlinear response of the combustion process to velocity perturbations of various levels. These data are used in combination with an acoustic transfer matrix analysis to derive a nonlinear dispersion relation (a relation which depends on the amplitude of oscillation). This is then exploited to determine the frequency and growth rate of perturbations in the system as a function of the amplitude of velocity perturbations on the upstream side of the flame. Values of the growth rate are then compared to the damping coefficient of the system ob-

tained from separate experiments to determine stability or instability and obtain the amplitude when the system oscillates at a limit cycle. Theoretical predictions retrieve well experimental observations validating the FDF methodology applied to the case of confined swirling flames.

Conclusion and perspectives

This investigation is concerned with swirling flames dynamics and combustion instabilities induced by the resonant coupling between such flames and system acoustics. This important scientific and technological problem is examined in the case of a turbulent premixed confined swirling combustor. This study may be considered as a continuation of work carried out in four previous doctoral dissertations by (Ducruix (1999), Schuller (2003), Birbaud (2006) and Noiray (2007)) and supervised by Daniel Durox and Sébastien Candel. These previous studies and the present investigation have in common the general method of approach which relies on a combination of experimentation, theoretical modeling and numerical simulation but there are also many novel features leading to a number of new findings :

- The turbulent swirling flame configuration constitutes the main topic of this research (there are some preliminary tests in the work carried out by Birbaud (2006) but the present investigation is more systematic).
- A novel analysis concerning mode conversion taking place in an airfoil cascade or in a swirler is carried out to explore the generation of a vorticity wave when the cascade interacts with acoustic disturbances. The resulting axial and transverse velocity perturbations are characterized and their phase velocities are shown to correspond to the sound velocity and mean flow velocity respectively. The difference in phase velocities of disturbances propagating on the downstream side of the swirler has an important impact on the flow dynamics.
- It is demonstrated that the mode conversion process in the swirler strongly affects the flame response.
- The dynamics of the flame is examined in a unified framework. It is found that the flame response to acoustic disturbances can be suitably represented with a nonlinear method based on the describing function framework. The flame dynamics is investigated experimentally. It is then shown that it reflects the presence of the mode conversion mechanism taking place in the swirler. Scaling rules are derived for the flame response which indicate that the Strouhal number can be used as a fundamental dimensionless group to

collapse data gathered at various points of operation.

- The understanding of the fundamental mechanisms is used to propose a model for the flame transfer function of swirling flames.
- Self-sustained instabilities are analyzed systematically by changing the size of the upstream manifold and the size of the flame tube. The nonlinear stability analysis is shown to provide velocity amplitudes and frequencies at limit cycles which are in fairly good agreement with experimental data.
- It is possible to infer that the understanding of the mechanisms driving the response of the flames can be used to develop passive control strategies and obtain an essentially neutral response to incident perturbations.

The present study is carried out in a confined geometry to reproduce conditions prevailing in applications like jet engines or gas turbines. The experimental layout comprises a swirler designed to anchor a turbulent swirling flame, an upstream manifold and a flame tube featuring adjustable sizes and enabling easy changes in the burner acoustics. Stable or unstable operation is shown to depend on the flame tube length. When the system operates in an unstable regime this corresponds to a coupling by the Helmholtz mode inducing large amplitude oscillations. The self-induced oscillations observed experimentally are retrieved theoretically.

Another novel aspect is a study of the flame dynamics based on Large Eddy Simulations and subsequent comparisons between experimental data and calculations. This study is carried out with the AVBP code. The distributions of heat release rate at various instants during the cycle compare well with experimental measurements. The simulations are used to gain a better understanding of the underlying processes and confirm that the swirler generates a azimuthal velocity disturbances when it interacts with acoustic perturbations.

These studies open new perspectives and can be pursued in various directions.

- Much remains to be done to fully document the dynamics of swirling flames. It has been found that the FDF of swirling flames is sensitive to swirl number level. In this thesis, it has been shown that a slight increase in the swirl number reduces the gain of the FDF and then could be used as a novel passive control strategy. One may try to explore this point by systematically investigating the FDF for a range of swirl numbers.
- The interaction of a vortex with a swirling flow may enhance the understanding of rollup mechanism during self-sustained oscillations. This should be considered theoretically, numerically and experimentally in order to show what one expect physically : increasing the level of swirl might decrease the strength of the vortex.

- The coupling between swirling flames and transverse acoustic modes is important in many applications. This is now being considered in the MICCA project. Further work is being planned to study this coupling in an annular chamber equipped with multiple injectors. Knowledge acquired in the present research can be used to design this chamber and obtain self-sustained azimuthal instabilities.
- A point which needs further examination is the question of damping. It would be useful to pursue the quantification of the damping levels in complex geometries under cold flow and hot fire conditions taking into account dissipation processes associated to rollup, boundary layers, mean flow, presence of hot gases and radiation losses.
- Large Eddy Simulations of perturbed swirling flames need to be developed more systematically to see if the transfer function can be derived from simulations without further need for experiments. This will require a large amount of computer resources which are progressively becoming available.
- The knowledge developed in this research could be used to devise novel control methods for swirling flames. It seems feasible to use the data to adjust the flame dynamics so that the response to disturbances is minimized.

Publications

Journal Publications

- *Dynamics of premixed confined swirling flames.*
  P. Palies, D. Durox, T. Schuller and S. Candel
  Comptes Rendus Mecanique, Combustion for aerospace propulsion, 2009, Vol.337, Issues 6-7, pp 395-405

- *The combined dynamics of swirler and turbulent premixed swirling flames.*
  P. Palies, D. Durox, T. Schuller and S. Candel
  Combustion and Flame, September 2010, Vol.157, Issue 9, pp 1698-1717.

- *Acoustic-convective mode conversion in an airfoils cascade.*
  P. Palies, D. Durox, T. Schuller and S. Candel
  Refereed by reviewers for Journal of Fluid Mechanics.

- *Acoustically perturbed turbulent premixed swirling flame.*
  P. Palies, D. Durox, T. Schuller, L.Y.M. Gicquel and S. Candel
  Refereed by reviewers for Physics of Fluids.

- *A criterion for decoupling chamber from plenum acoustic modes separated by a flame.*
  T. Schuller, D. Durox, P. Palies and S. Candel
  In preparation for Journal of Propulsion and Power.

- *Nonlinear combustion instabilities analysis based on the Flame Describing Function applied to turbulent premixed swirling flames.*

P. Palies, D. Durox, T. Schuller and S. Candel
Refereed by reviewers for Combustion and Flame.

- *Experimental study on effects of swirler geometry and swirl number on flame describing functions.*
  P. Palies, D. Durox, T. Schuller and S. Candel
  Accepted for Combustion Science and Technology.

CONFERENCE PAPERS (PEER-REVIEWED WITH THREE REVIEWERS)

- *Modeling of premixed swirling flames transfer functions.*
  P. Palies, T. Schuller, D. Durox and S. Candel
  Proceedings of the Combustion Institute, Beijing, China, 2010.

- *Swirling flame instability analysis based on the flame describing function methodology.*
  P. Palies, D. Durox, T. Schuller and S. Candel
  ASME Turbo Expo, Glasgow, Scotland, UK, 2010.

CONFERENCE PAPERS (ABSTRACT REVIEWED)

- *Dynamics of premixed confined swirling flames.*
  P. Palies, D. Durox, T. Schuller, P. Morenton and S. Candel
  INCA, INitiative en Combustion Avancées (Advanced Works in Combustion), 2008, Rouen, France.

- *The response of swirling premixed flames to velocity perturbations.*
  P. Palies, D. Durox, T. Schuller and S. Candel
  ECM : European Combustion Meeting, Vienna, Austria, 2009.

- *Flame describing function methodology applied to swirling flame instability analysis.*
  P. Palies, D. Durox, T. Schuller and S. Candel
  EUCASS : European Conference for Aerospace Sciences, Versailles, France, 2009.

- *Swirling flame dynamics and describing function.*
  P. Palies, D. Durox, T. Schuller and S. Candel
  AIAA, Aerospace Sciences Meeting, Orlando, Florida, USA, 2010.

- *Combustion instabilities analysis based on Flame Describing Function applied to swirling flames.*
  P. Palies, D. Durox, T. Schuller and S. Candel
  International Summer School and Workshop on Non-Normal and Nonlinear Effects in Aero and Thermoacoustics, München, Germany, 2010.

OTHERS PUBLICATIONS

- *Dynamique de flammes prémélangées, swirlées et confinées.*
  P. Palies, D. Durox, T. Schuller and S. Candel
  Poster presented at CFTL : Congrès Francophone de Techniques Laser (French Colloquium on Laser Diagnostics), Poitiers, France, 2008.

- *Dynamique de flammes prémélangées, swirlées et confinées.*
  P. Palies, D. Durox, T. Schuller and S. Candel
  Meeting of GFC : Groupement Français de Combustion (French Community in Combustion), Douai, France, 2008.

- *Etude des instabilités d'un brûleur à flammes swirlées. Cycles limites.*
  P. Palies, D. Durox, T. Schuller and S. Candel
  Meeting CRCT : Centre de Recherche sur la Combustion Turbulente (Turbulent Combustion Research Center), Rueil-Malmaison, France, 2010.

Appendix A

Modeling of interaction between swirling jet and vortex

A.1 Introduction

The objective of the present appendix is to derived a simple model to characterize the interaction of a vortex with a swirling jet. Specifically, two sources of vorticity are identified : the first due to the vortex generated by acoustic waves impinging the swirler (ω_θ), the second due to the swirling flow (ω_z). It is shown that both contributions are linked with a simple model. It has been demonstrated in the manuscript that an increase of the swirl number reduces the gain of the flame response. And one reason maybe due to the damping of the rollup mechanism when the level of swirl is increased.

A.2 Equation of motion

The mass balance equation is :

$$\frac{1}{r}\frac{\partial r v_r}{\partial r} + \frac{1}{r}\frac{\partial v_\theta}{\partial \theta} + \frac{\partial v_z}{\partial z} = 0 \tag{A.1}$$

One assumes a constant density flow and inviscid such that the vorticity equation can be written as :

$$\frac{\partial \boldsymbol{w}}{\partial t} + (\boldsymbol{v}\cdot\boldsymbol{\nabla})\boldsymbol{w} = (\boldsymbol{w}\cdot\boldsymbol{\nabla})\boldsymbol{v} \tag{A.2}$$

The radial vorticity component is given by :

$$\frac{\partial w_r}{\partial t} + v_r\frac{\partial w_r}{\partial r} + \frac{v_\theta}{r}\frac{\partial w_r}{\partial \theta} + v_z\frac{\partial w_r}{\partial z} = w_r\frac{\partial v_r}{\partial r} + \frac{w_\theta}{r}\frac{\partial v_r}{\partial \theta} + w_z\frac{\partial v_r}{\partial z} \tag{A.3}$$

The azimuthal vorticity component is given by :

$$\frac{\partial w_\theta}{\partial t} + v_r\frac{\partial w_\theta}{\partial r} + \frac{v_\theta}{r}\frac{\partial w_\theta}{\partial \theta} + v_z\frac{\partial w_\theta}{\partial z} = w_r\frac{\partial v_\theta}{\partial r} + \frac{w_\theta}{r}\frac{\partial v_\theta}{\partial \theta} + w_z\frac{\partial v_\theta}{\partial z} \tag{A.4}$$

The axial vorticity component is given by :

$$\frac{\partial w_z}{\partial t} + v_r\frac{\partial w_z}{\partial r} + \frac{v_\theta}{r}\frac{\partial w_z}{\partial \theta} + v_z\frac{\partial w_z}{\partial z} = w_r\frac{\partial v_z}{\partial r} + \frac{w_\theta}{r}\frac{\partial v_z}{\partial \theta} + w_z\frac{\partial v_z}{\partial z} \tag{A.5}$$

One considers an axysymetric flow and no radial velocity component v_r.

One obtains then for the radial vorticity component :

$$\frac{\partial w_r}{\partial t} + v_z\frac{\partial w_r}{\partial z} = 0 \tag{A.6}$$

For the azimuthal vorticity component :

$$\frac{\partial w_\theta}{\partial t} + v_z\frac{\partial w_\theta}{\partial z} = w_r\frac{\partial v_\theta}{\partial r} + w_z\frac{\partial v_\theta}{\partial z} \tag{A.7}$$

For the axial vorticity component :

$$\frac{\partial w_z}{\partial t} + v_z\frac{\partial w_z}{\partial z} = w_r\frac{\partial v_z}{\partial r} + w_z\frac{\partial v_z}{\partial z} \tag{A.8}$$

This set of three equations are the starting point of the theoretical derivation.

A.3 Model derivation

There is two main sources of vorticity in the present case :

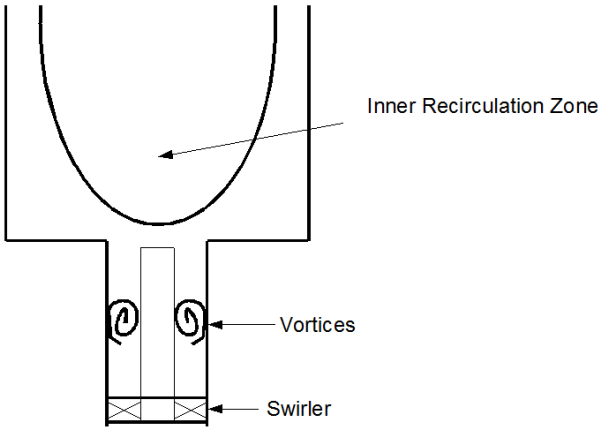

Figure A.1: Example of geometry with swirling jet / vortices interaction. Vortices are shed from the outlet of the swirler and interact with the swirling flow.

- the first contribution is the vorticity associated to the vortex shed at the trailing edge of the swirler generating a azimuthal vorticity component w_θ

- the second is the vorticity associated to the swirling flow with an axial component w_z

One assumes that w_r is zero.

Furthermore, according to Eq. (A.1) and previous hypothesis, one has :

$$\frac{\partial v_z}{\partial z} \simeq 0 \tag{A.9}$$

Finally, it remains for the azimuthal vorticity component Eq. (A.7) :

$$\frac{\partial w_\theta}{\partial t} + v_z \frac{\partial w_\theta}{\partial z} = w_z \frac{\partial v_\theta}{\partial z} \tag{A.10}$$

And for the axial vorticity equation Eq. (A.8) :

$$\frac{\partial w_z}{\partial t} + v_z \frac{\partial w_z}{\partial z} = 0 \tag{A.11}$$

One can sum these two equations, respectively Eqs. (A.10) and (A.11) to obtain :

$$\frac{\partial}{\partial t}(w_\theta + w_z) + v_z \frac{\partial}{\partial z}(w_\theta + w_z) = w_z \frac{\partial v_\theta}{\partial z} \tag{A.12}$$

One can also assume that $v_\theta = v_\theta(r)$ and so :

$$\frac{\mathrm{d}}{\mathrm{d}t}(w_\theta + w_z) = 0 \tag{A.13}$$

This last equation balances effects of vorticity due to the vortex (ω_θ) and the swirling jet (ω_z).

One can determine both contributions w_θ and w_z.

It is known that w_θ is defined as :

$$w_\theta = \left[\frac{\partial v_r}{\partial z} - \frac{\partial v_z}{\partial r}\right]\mathbf{e}_\theta \tag{A.14}$$

While w_z is defined as :

$$w_z = \frac{1}{r}\left[\frac{\partial}{\partial r}(r v_\theta) - \frac{\partial v_r}{\partial \theta}\right]\mathbf{e}_z \tag{A.15}$$

Taking into account previous hypothesis, respectively no radial flow and axisymmetric configuration, one obtains :

$$w_\theta = -\frac{\partial v_z}{\partial r}\mathbf{e}_\theta \tag{A.16}$$

which reflects the vorticity term ω_θ induced by the vortex. While w_z is induced by the swirling jet :

$$w_z = \frac{1}{r}\left[\frac{\partial}{\partial r}(rv_\theta)\right]\mathbf{e}_z \tag{A.17}$$

One can use a vortex model, the isentropic vortex to continue the analysis. The expression of the velocity v_z for an isentropic vortex is given by :

$$v_z(r) = \frac{\Gamma^v}{R_c}\exp\left(-\frac{r^2}{2R_c^2}\right) \tag{A.18}$$

where R_c is the radius of the vortex, r the current radius and Γ^v the circulation of the vortex. Then, one has :

$$w_\theta = \frac{r\Gamma^v}{2R_c^3}\exp\left(-\frac{r^2}{2R_c^2}\right) \tag{A.19}$$

The expression of the velocity v_θ for a swirling flow can be modeled as a solid body rotation with : $v_\theta(r) = \Omega^s\, r$. Then : $w_z = 2\Omega^s$. According to Eq. (A.13), one has :

$$w_\theta + w_z = K \tag{A.20}$$

where K is a constant. By substituting expressions for both vorticity terms ω_θ and ω_z in Eq. (A.20), one has :

$$\frac{r\Gamma^v}{2R_c^3}\exp\left(-\frac{r^2}{2R_c^2}\right) + 2\Omega^s = K \tag{A.21}$$

One obtains finally :

$$\Gamma^v = 2\frac{R_c^3}{r}[K - 2\Omega^s]\exp\left(\frac{r^2}{2R_c^2}\right) \tag{A.22}$$

This last expression shows that increasing the rotation rate Ω^s of the flow results in a decrease of the incident vortex strength Γ^v.

Appendix B

Reconstruction de signaux

Problématique Cette annexe a pour objectifs de présenter deux méthodes de reconstruction de signaux utiles pour accéder à la valeur de la fluctuation de pression acoustique en un point où cette quantité ne peut être mesurée expérimentalement. La première méthode utilise une représentation fréquentielle et s'appuie sur la transformée de Hilbert. On passe ainsi par le signal analytique. La seconde méthode réalise une extrapolation directe dans le domaine temporel. Dans les deux cas, la reconstruction est valide pour une distance Δx, entre le point 1 de mesure et le point 2 de reconstruction, suffisamment faible et telle que : $k\Delta x << 1$ où k représente un nombre d'onde typique $k = 2\pi/\lambda$. Ce critère indique que la distance Δx ne doit pas être trop grande par rapport à la longueur d'onde. Lorsqu'il est respecté, l'extrapolation des champs d'onde est facilement réalisée au moyen d'un développement en série de Taylor. Nous étudions par simulation numérique les deux méthodes pour deux cas connus : une onde plane progressive et une onde stationnaire. Ces deux situations génériques vont permettre de valider la méthode.

On suppose que la pression et la vitesse acoustique sont connues au point 1. Il est alors naturel de faire appel à l'équation de bilan de quantité de mouvement linéarisée dans un milieu au repos. Celle-ci est donnée sous la forme :

$$\rho_0 \frac{\partial \mathbf{v}}{\partial t} = -\nabla p \tag{B.1}$$

On peut alors travailler sur cette équation en supposant des solutions harmoniques pour les champs de pression et de vitesse. Celles-ci prenant alors la forme canonique $a(x,t) = a(x)e^{-i\omega t}$. L'expression suivante relie le gradient de pression à la fluctuation de vitesse au point de mesure.

$$\rho_0 \, i \, \omega \, v_1 = \frac{\partial p}{\partial x} \tag{B.2}$$

En utilisant un développement de Taylor à l'ordre 3 pour le calcul de la fluctuation de pression, on obtient :

$$p_2 = p_1 + \Delta x \frac{\partial p}{\partial x} + \frac{\Delta x^2}{2}\frac{\partial^2 p}{\partial x^2} + \frac{1}{6}(\Delta x)^3 \frac{\partial^3 p}{\partial x^3} + o[(\Delta x)^4] \tag{B.3}$$

Méthode fréquentielle Pour obtenir la dérivée seconde de la pression, on peut partir de l'équation d'onde :

$$\frac{1}{c_0^2}\frac{\partial^2 p}{\partial t^2} - \frac{\partial^2 p}{\partial x^2} = 0 \tag{B.4}$$

qui devient dans le cas harmonique :

$$\frac{\partial^2 p}{\partial x^2} = -k^2 p \tag{B.5}$$

La dérivée troisième s'obtient facilement en dérivant cette expression puis en utilisant le bilan de quantité de mouvement linéarisé.

$$\frac{\partial^3 p}{\partial x^3} = -k^2 \frac{\partial p}{\partial x} = -\rho_0 i\omega k^2 v \tag{B.6}$$

Dès lors, la combinaison des équations Eqs. (B.3), (B.5) et (B.6) donne :

$$p_2 = p_1 + \frac{\partial p}{\partial x}\Delta x - \frac{1}{2}(k\Delta x)^2 p_1 - \frac{1}{6}k^2(\Delta x)^3 \frac{\partial p}{\partial x} \tag{B.7}$$

En injectant alors l'expression du gradient de pression de l'équation Eq. (B.2) dans l'équation Eq. (B.7), on obtient :

$$p_2 = \rho_0\, i\, \omega\, v_1 \Delta x \left[1 - \frac{1}{6}(k\Delta x)^2\right] + p_1 \left[1 - \frac{(k\Delta x)^2}{2}\right] \tag{B.8}$$

Cette dernière expression donne bien la pression à reconstruire en 2 en fonction de la fluctuation de vitesse et de la pression au point 1. Pour utiliser cette expression en partant de signaux réels, il faut d'abord recalculer des signaux analytiques en applicant la transformée de Hilbert. L'équation Eq. (B.8) est alors directement applicable aux signaux analytiques $\hat{p}_1$, $\hat{p}_2$ et $\hat{v}_1$. On obtient alors en prenant la partie réelle de l'équation Eq. (B.8) le signal temporel de pression p_2. On applique dans les deux paragraphes suivants la méthode à un signal connu : une onde plane progressive.

On considère donc maintenant une onde plane progressive. Le champ de pression a dans ce cas pour expression :

$$p(x,t) = p_0 \cos(kx - \omega t) \tag{B.9}$$

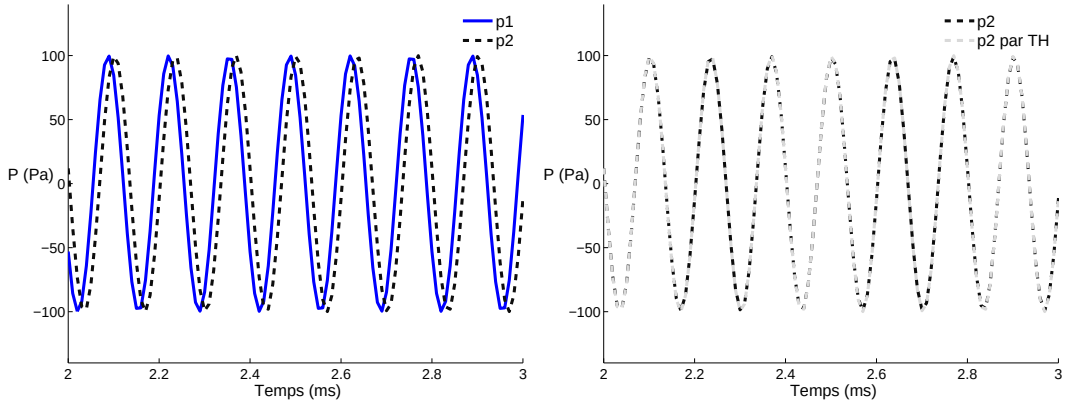

Figure B.1: A gauche, amplitudes des signaux de pression, à des abscisses séparés d'une distance $\Delta x = 5$ cm. A droite, reconstruction du signal de pression au point 2 suivant l'équation Eq. (B.8). On utilise les signaux de pression et de vitesse détectés au point 1. f = 750Hz

où p_0 est une amplitude. La figure B.1 montre l'évolution de cette onde aux abscisses x_1 et x_2. En d'autres termes, on observe le déphasage des signaux associés à $p(x,t)$. La figure donne le signal détecté en x_2 et le résultat obtenu en reconstruisant ce signal à partir de la pression et de la vitesse au point 1. On présente sur le second graphique la reconstruction du signal en comparaison avec le signal réel.

On observe ainsi que la reconstruction du signal est d'une très bonne qualité. Il est difficile de faire apparaître une différence entre les signaux réel et reconstruit.

Méthode temporelle

- Généralités
  Une autre approche consiste à déterminer l'expression de p_2 en utilisant une formulation temporelle. Cette méthode est plus générale que la méthode fréquentielle car elle s'applique à des signaux dont les variations temporelles sont arbitraires. On part la encore des équations de l'acoustique et on utilise des approximations centrées des dérivées. Pour cela, on représente la pression au point 2 sous la forme d'un développement de Taylor (B.3) comme précédemment et on calcule chaque terme du développement en s'appuyant sur l'équation d'onde et le bilan de quantité de mouvement linéarisé :

$$\frac{\partial p}{\partial x} = -\rho_0 \frac{\partial v}{\partial t} \tag{B.10}$$

$$\frac{\partial^2 p}{\partial x^2} = \frac{1}{c_0^2} \frac{\partial^2 p}{\partial t^2} \tag{B.11}$$

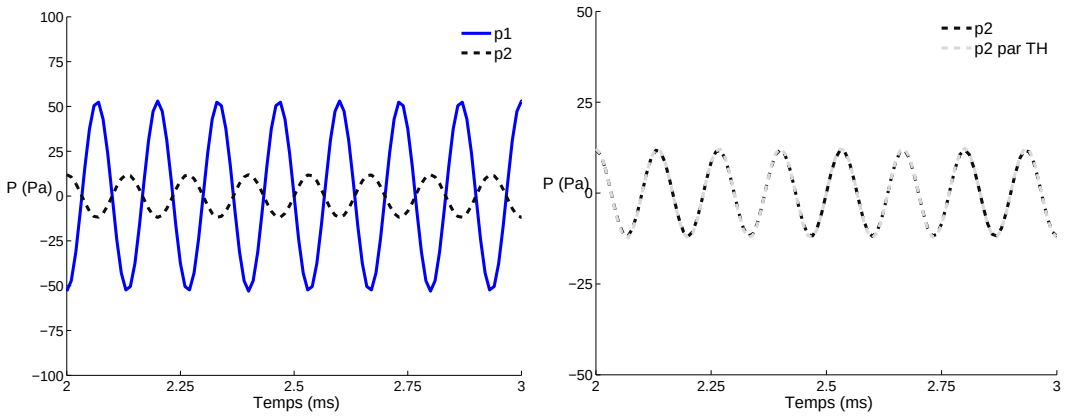

Figure B.2: A gauche, amplitudes des signaux de pression, calculés à des abscisses séparés d'une distance de $\Delta x = 5$ cm. A droite, reconstruction du signal de pression à partir des signaux de pression et de vitesse détectés au point 1.

On a alors :

$$p_2 = p_1 - \rho_0 \frac{\partial v}{\partial t}\Delta x + \frac{1}{2}\frac{\partial^2 p}{\partial x^2}\Delta x^2 \tag{B.12}$$

Il est ensuite nécessaire de calculer les dérivées temporelles des termes de gauche. Il vient :

$$\frac{\partial v}{\partial t} = \frac{v(t+\Delta t) - v(t-\Delta t)}{2\Delta t} \tag{B.13}$$

$$\frac{\partial^2 p}{\partial t^2} = \frac{p(t+\Delta t) - 2p(t) + p(t-\Delta t)}{(\Delta t)^2} \tag{B.14}$$

En substituant ces expressions dans le développement en série de Taylor (B.3), on obtient :

$$p_2 = p_1 - \rho_0 \frac{v(t+\Delta t) - v(t-\Delta t)}{2\Delta t}\Delta x + \frac{1}{2}\frac{1}{c_0^2}\frac{\partial^2 p}{\partial t^2}\Delta x^2 \tag{B.15}$$

- Onde plane progressive et onde stationnaire
  On peut à nouveau comparer les résultats d'extrapolation au champ exacte. La figure [B.3] donne une représentation du champ de pression p_2 et du champ de pression estimé dans le cas d'une onde plane progressive. La figure donne les signaux extrapolé et théorique pour le cas d'une onde stationnaire. Ces deux figures montrent que la méthode d'extrapolation est bien adaptée.

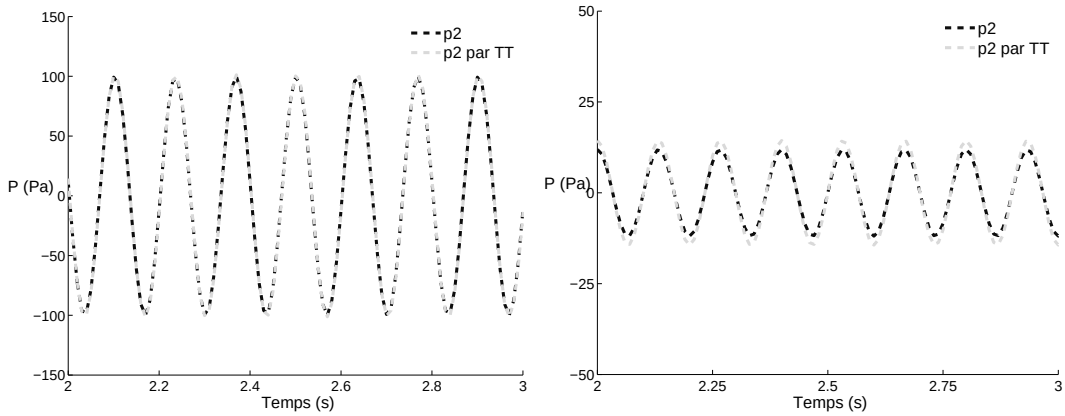

Figure B.3: A gauche, reconstruction du signal de l'onde plane progressive au point 2 avec la méthode temporelle pour une distance de 5 cm entre les deux abscisses x_1 et x_2. A droite, reconstruction du signal de pression au point 2 avec la méthode temporelle pour une distance de 3 cm.

Appendix C

Convergent effect on the swirl number

We now investigated the effect of a change in the section area downstream the swirler. We assume that the fluid particule as the following velocity vectors components $\mathbf{v}(\mathbf{r},t) = v_\theta\,\mathbf{e}_\theta + v_z\,\mathbf{e}_z$. The swirl number is still :

$$S = \frac{\int_0^R \rho v_\theta v_z 2\pi r^2 dr}{R\int_0^R (\rho v_z^2 + p)2\pi r\,\mathrm{dr}} \tag{C.1}$$

The mass balance for a fixed control volume V encompassing the cross section change is :

$$\frac{d}{dt}\int_V \rho\,dV + \int_A \rho\mathbf{v}.\mathbf{n}\,dA = 0 \tag{C.2}$$

The surface A can be divided in three boundary surfaces of the control volume V where A_1 is the inlet surface, A_2 the outlet surface and Σ the lateral surface. The only non zero contributions come from the inlet and the outlet surfaces. We finally obtain for an incompressible flow :

$$v_{z2} = v_{z1}\,\frac{A_1}{A_2} \tag{C.3}$$

To understand the effect of a geometrical change on the swirl number, we also need to analyze the evolution of the azimuthal component v_θ through the change in cross section. So we used the azimuthal momentum equation under its conservative form :

$$\frac{\partial \rho v_r v_\theta}{\partial r} + \frac{\partial \rho v_\theta v_z}{\partial z} + 2\rho\frac{v_\theta v_r}{r} = 0 \tag{C.4}$$

One can assume that the radial velocity component is small compared to the other components and neglect terms containing v_r :

$$\frac{\partial \rho v_\theta v_z}{\partial z} = 0 \tag{C.5}$$

This expression can be integrated in the z direction :

$$\int_{z_1}^{z_2} \frac{\partial \rho v_\theta v_z}{\partial z} dz = 0 \tag{C.6}$$

This yields :

$$v_{\theta 2} v_{z2} = v_{\theta 1} v_{z1} \tag{C.7}$$

Which is also :

$$\frac{v_{z1}}{v_{z2}} = \frac{v_{\theta 2}}{v_{\theta 1}} \tag{C.8}$$

One can consider a convergent unit where the section A_2 is smaller than A_1. As v_{z2} is stronger than v_{z1}, one deduces that $v_{\theta 2}$ is lower than $v_{\theta 1}$. One can then examine the different terms of the swirl number. In the numerator :

$$\int_0^{R_2} \rho v_{\theta 2} v_{z2}\, 2\pi r^2\, dr < \int_0^{R_1} \rho v_{\theta 1} v_{z1}\, 2\pi r^2\, dr \tag{C.9}$$

As R_2 is smaller than R_1, the product of the axial velocity by azimuthal velocity is conserved. In the denominator, one finds :

$$R \int_0^R (\rho v_z^2 + p)\, 2\pi r\, dr \tag{C.10}$$

We used the axial momentum equation under it conservative form :

$$\frac{\partial \rho v_r v_z}{\partial r} + \frac{\partial \rho v_z^2}{\partial z} + \rho \frac{v_z v_r}{r} = -\frac{\partial p}{\partial z} \tag{C.11}$$

Eliminating terms containing v_r :

$$\frac{\partial \rho v_z^2}{\partial z} = -\frac{\partial p}{\partial z} \tag{C.12}$$

and integrating this equation along the z axis.

$$\int_{z_1}^{z_2} \frac{\partial (\rho v_z^2 + p)}{\partial z} dz = 0 \tag{C.13}$$

One obtains :

$$\rho v_{z_2}^2 + p_2 = \rho v_{z_1}^2 + p_1 \tag{C.14}$$

The denominator only depends on the square of the section area. Furthermore, as the outlet radius R_2 is smaller than the radius R_1, one has :

$$R_2 \int_0^{R_2} (\rho v_{z2}^2 + p_2)\, 2\pi r\, dr < R_1 \int_0^{R_1} (\rho v_{z1}^2 + p_1)\, 2\pi r\, dr \tag{C.15}$$

We observed finally that both numerator and denominator have the same behavior decreasing proportionally with the radius. As their ratio is linearly proportional to the radius R, the swirl number decreases in a constriction.

It is also possible to show this result by making use of swirl number correlations like those given by Gupta *et al.* (1984) and defining $\tan\phi = v_\theta / v_z$.

$$S = \tan\phi \, \frac{\int_0^R r^2 \,\mathrm{dr}}{R \int_0^R r \,\mathrm{dr}} \tag{C.16}$$

Such that :

$$S = \tan\phi \, \frac{R^3/3}{R\, R^2/2} \tag{C.17}$$

One finds that $S = (2/3)\tan\Phi$ and finally : $S = (2/3)(v_{\theta 1}/v_{z1})$.

The ratio of the swirl numbers between the inlet and the outlet is then :

$$\frac{S_1}{S_2} = \frac{v_{\theta 1}/v_{z1}}{v_{\theta 2}/v_{z2}} \tag{C.18}$$

This can be expressed in terms of cross section area by making use of Eq. (C.3) and Eq. (C.8) :

$$\frac{S_1}{S_2} = \frac{v_{\theta 1}}{v_{\theta 2}} \frac{v_{z2}}{v_{z1}} = \left(\frac{v_{z2}}{v_{z1}}\right)^2 = \left(\frac{A_1}{A_2}\right)^2 \tag{C.19}$$

This last expression shows that a change in the section area induces a change in swirl number.

Appendix D

Formulaire

Cette annexe récapitule quelques formules utilisées pour determiner la richesse d'un mélange et les fractions massiques des espèces.

La réaction de combustion du méthane et de l'air s'écrit dans des proportions stoechiométriques comme :

$$\mathrm{CH_4} + 2\,(\mathrm{O_2} + 3.76\mathrm{N_2}) \quad \rightarrow \quad \mathrm{CO_2} + 2\,(\mathrm{H_2O} + 3.76\mathrm{N_2}) \tag{D.1}$$

Pour une richesse inférieure à la stoechiométrie, cette équation devient :

$$\phi\mathrm{CH_4} + 2\,(\mathrm{O_2} + 3.76\mathrm{N_2}) \quad \rightarrow \quad \phi(\mathrm{CO_2} + 2\,\mathrm{H_2O}) + 2\,[(1-\phi)\mathrm{O_2} + 3.76\mathrm{N_2}] \tag{D.2}$$

où ϕ est la richesse du mélange. Celle-ci est définie comme le ratio des rapports de mélange local α et stoechiométrique α_s. Le rapport de mélange étant défini par : $\alpha = \dot{m}_{CH_4}/\dot{m}_{air}$ où $\dot{m}_{CH_4}$ et $\dot{m}_{air}$ sont les débits masses de combustible et d'air. Le calcul du rapport de mélange α_s est donné par :

$$\alpha_s = \frac{M_C + 4M_H}{2(M_{O_2} + 3.717N_2)} \tag{D.3}$$

Les masses molaires de l'hydrogène, du carbone, de l'azote et de l'oxygène sont respectivement : 1, 12, 14 et 16 g.mol^{-1}. Le rapport de mélange α_s a donc pour valeur 0.059. Par définition de la richesse, on peut écrire :

$$\dot{m}_{CH_4} = \phi\alpha_s\dot{m}_{air} \tag{D.4}$$

De plus, le débit massique total $\dot{m}$ s'exprime comme la somme du débit de combustible et d'air :

$$\dot{m} = (1 + \phi\alpha_s)\dot{m}_{air} \tag{D.5}$$

En ce qui concerne les fractions massiques des espèces, celles-ci s'écrivent :

$$Y_{CH_4} = \frac{\dot{m}_{CH_4}}{\dot{m}} = \frac{\phi\alpha_s \dot{m_{air}}}{(1+\phi\alpha_S)\dot{m}_{air}} \tag{D.6}$$

et

$$Y_{O_2} = \frac{\dot{m}_{O_2}}{\dot{m}} = \frac{\dot{m}_{O_2}}{\dot{m}_{air}}\frac{\dot{m}_{air}}{\dot{m}} \tag{D.7}$$

Or le rapport $\dot{m}_{O_2}/\dot{m}_{air}$ est la fraction massique de d'oxygène dans l'air :

$$Y_{O_2} = \frac{2M_{O_2}}{2M_{O_2} + 3.717M_{N_2}} \tag{D.8}$$

Cette fraction massique d'oxygène dans l'air a pour valeur 0.235. Ainsi, les équations (D.6) et (D.7) conduisent à :

$$Y_{CH_4} = \frac{\phi\alpha_s}{1+\phi\alpha_s} \tag{D.9}$$

et

$$Y_{O_2} = \frac{0.235}{1+\phi\alpha_s} \tag{D.10}$$

Il est intéressant de récapituler, dans le tableau D.1 les valeurs numériques précédentes pour ensuite les utiliser dans un code de calcul.

Richesse	0.7	0.8	0.9	1
Y_{CH_4}	0.0397	0.0451	0.0504	0.0558
Y_{O_2}	0.2257	0.2244	0.2231	0.2219

Table D.1: Évolution des fractions massiques en fonction de la richesse

References

Alekseenko, S., V. Dulin, Y. Kozorezov, and D. Markovich (2008). Effect of axisymmetric forcing on the structure of a swirling turbulent jet. *International Journal of Heat and Fluid Flow 29*, 1699–1715. *(p. 142)*

Armitage, C. A., R. Balachandran, E. Mastorakos, and R. S. Cant (2006). Investigation of the nonlinear response of turbulent premixed flames to imposed inlet velocity oscillations. *Combustion and Flame 146*, 419–436. *(p. 7, 111, 191)*

Baillot, F., D. Durox, and R. Prudhomme (1992). Experimental and theoretical study of a premixed vibrating flame. *Combustion and Flame 88*(2), 149–168. *(p. 77, 190)*

Bake, F., C. Richter, B. Muhlbauer, N. Kings, I. Rohle, F. Thiele, and B. Noll (2009). The Entropy Wave Generator (EWG) : A reference case on entropy noise. *Journal of Sound and Vibration 326*, 574–598. *(p. 76)*

Balachandran, R., B. O. Ayoola, C. F. Kaminski, A. P. Dowling, and E. Mastorakos (2005). Experimental investigation of the nonlinear response of turbulent premixed flames to imposed inlet velocity oscillations. *Combustion and Flame 143*, 37–55. *(p. 111, 112, 191, 208)*

Bellows, B. D., M. K. Bobba, A. Forte, J. M. Seitzman, and T. Lieuwen (2007). Flame transfer function saturation mechanisms in a swirl-stabilized combustor. *Proceedings of the Combustion Institute 31*, 3181–3188. *(p. 7, 45, 111, 112, 121, 142, 191)*

Bellows, B. D., M. K. Bobba, J. M. Seitzman, and T. Lieuwen (2007). Nonlinear flame transfer function characteristics in a swirl-stabilized combustor. *Journal of Engineering for Gas Turbines and Power 129*(4), 954–961. *(p. 5, 7, 45, 111, 112, 121, 210)*

Bellows, B. D., Q. Zhang, Y. Neumeier, T. Lieuwen, and B. Zinn (2003). Forced response studies of a premixed flame to flow disturbances in a gas turbine combustor. In *AIAA-2003-824, Aerospace Sciences Meeting and Exhibit*, Reno, NV. *(p. 112)*

Billant, P., J. Chomaz, and P. Huerre (1998). Experimental study of vortex breakdown in swirling jets. *Journal of Fluid Mechanics 376*, 183–219. *(p. 34)*

Birbaud, A., D. Durox, and S. Candel (2006). Upstream flow dynamics of a

laminar premixed conical flame submitted to acoustic modulations. *Combustion and Flame 146*(3), 541–552. *(p. 6, 77)*

Birbaud, A., D. Durox, S. Ducruix, and S. Candel (2007). Dynamics of free jets submitted to upstream acoustic modulations. *Physics of fluids 19*(1). 013602. *(p. 77)*

Birbaud, A. L. (2006). *Dynamique d'intéractions sources des instabilités de combustion*. Châtenay-Malabry, France: Ph. D. thesis, Lab. EM2C, Ecole Centrale Paris. *(p. 229)*

Bloxsidge, G., A. Dowling, and P. Langhorne (1988). Reheat buzz: an acoustically coupled combustion instability. Part 2. Theory. *Journal of Fluid Mechanics 193*, 445–473. *(p. 54)*

Borghesi, G., F. Biagioli, and B. Schuermans (2009). Dynamic response of turbulent swirling flames to acoustic perturbations. *Combustion Theory and Modelling 13*(3), 487–512. *(p. 7, 13, 112, 191, 192)*

Bourhela, A. and F. Baillot (1998). Appearance and stability of a laminar conical premixed flame subjected to an acoustic perturbation. *Combustion and Flame 114*(3), 303–318. *(p. 77)*

Boyer, L. and J. Quinard (1990a). On the dynamics of anchored flames. *Combustion and Flame 82*(1), 51–65. *(p. 77)*

Boyer, L. and J. Quinard (1990b, October). On the dynamics of anchored flames. *Combust. Flame 82*(1), 51–65. *(p. 141)*

Broda, J. C., S. Seo, R. J. Santoro, G. Shirhattikar, and V. Yang (1998). An experimental study of combustion dynamics of a premixed swirl injector. *Proceedings of the Combustion Institute 27*, 1849–1856. *(p. 110, 209)*

Candel, S. (1972). *Analytical studies of some acoustical problems of jet engines*. Ph. D. thesis, California Institute of Technology, Pasadena, California, USA. *(p. 76)*

Candel, S. (2002). Combustion Dynamics and Control : Progress and Challenges. *Proceedings of the Combustion Institute 29*, 1–28. *(p. 5, 53, 110, 157, 158, 208)*

Candel, S., D. Durox, S. Ducruix, A.-L. Birbaud, N. Noiray, and T. Schuller (2009). Flame dynamics and combustion noise: progress and challenges. *International Journal of Aeroacoustics 8*(1), 1–56. *(p. 9)*

Chang, L., T. Komarek, R. Kaess, S. Foller, and W. Polifke (2009). Flame transfer function measurements and instability frequency using a thermoacoustic model. In *Proceedings of ASME Turbo Expo 2010*, Volume GT2010-22769, Glasgow, UK. *(p. 191)*

Chigier, N. and A. Chervinsky (1967). Experimental investigation of swirling vortex motion in jets. *Journal of Applied Mechanics 34*, 443–451. *(p. 33, 34)*

Chong, L., T. Komarek, R. Kaess, S. Foller, and W. Polifke (2010). Identification of flame transfer functions from LES of a premixed swirl burner. In *ASME Paper GT2010-22769, ASME Turbo Expo 2010*, Glasgow, Scotland.

(p. 210)

Coli, O. and M. Rudgyard (2000). Development of high-order Taylor-Galerkin schemes for LES. *Journal of Computational Physics 162*(2), 338–371. *(p. 164)*

Colin, O., F. Ducros, D. Veynante, and T. Poinsot (2000). A thickened flame model for large eddy simulations of turbulent premixed combustion. *Physics of Fluids 12*(7), 1843. *(p. 163)*

Crocco, L. (1968). Research on combustion instability in liquid propellant rockets. *Proceedings of the Combustion Institute 12*, 85–99. *(p. 5, 208)*

Crow, S. and F. Champagne (1971). Orderly structure in jet turbulence. *Journal of Fluid Mechanics 48*(3), 547–591. *(p. 77)*

Culick, F. (1987). A note on Rayleigh's criterion. *Combustion Sciences and Technology 56*, 159–166. *(p. 211)*

Culick, F. (2001). Dynamics of combustion systems : fundamentals, acoustics and control. In *RTO AVT Course on "Active control of engine dynamics"*, Brussels, Belgium. *(p. 5, 110, 208)*

Culick, F. and V. Yang (1995). *Progress in astronautics and aeronautics: liquid rocket engine combustion instability*, Volume 169, Chapter 1: Overview of combustion instabilities in liquid-propellant rocket engines, pp. 3–37. AIAA. *(p. 54)*

Culick, F. E. C. (2006). *Unsteady motions in combustion chambers for propulsion systems*. AGARDograph, NATO/RTO-AG-AVT-039. *(p. 53)*

Cumpsty, N. (1979). Jet engines combustion noise : pressure, entropy and vorticity perturbations produced by unsteady combustion or heat addition. *Journal of Sound and Vibration 66*(4), 527–544. *(p. 8, 79)*

Cumpsty, N. and F. Marble (1977a). Core noise gas turbine exhausts. *Journal of Sound and Vibration 54*(2), 297–309. *(p. 77)*

Cumpsty, N. and F. Marble (1977b). The interaction of entropy fluctuations with turbine blade rows; a mechanism of turbojet engine noise. *Proceedings of the Royal Society London Series A357*, 323–344. *(p. 8, 54, 62, 63, 76, 79, 80, 81, 85, 129, 174)*

De Luca, L., E. Price, and M. Summerfield (1992). Nonsteady burning and combustion stability of solid propellants. *Progress in astronautics and aeronautics 143*. *(p. 5)*

De Soete, G. (1964, Juin). Etude des flammes vibrantes - Application a la combustion turbulente. *Revue de l'institut francais du pétrole et annales du combustible liquide XIX*(6). *(p. 77)*

Dotson, K., S. Koshigoe, and K. Pace (1997). Vortex shedding in a large solid rocket motor without inhibitors at the segmented interfaces. *Journal of Propulsion and Power 13*, 197–206. *(p. 77)*

Dowling, A. P. (1997). Nonlinear self-excited oscillations of ducted flame. *Journal of Fluid Mechanics 346*, 271–290. *(p. 9, 209)*

Dowling, A. P. (1999). A kinematic model of ducted flame. *Journal of Fluid*

Mechanics 394, 51–72. *(p. 9, 141, 191, 209)*

Dowling, A. P. and S. R. Stow (2003). Acoustic Analysis of Gas Turbine Combustors. *Journal of Propulsion and Power 19*(5), 751–764. *(p. 54)*

Ducros, F., F. Nicoud, and T. Poinsot (1998). Large Eddy Simulations of compressible flows on hybrid mesches. *Turbulent Shear Flows 11*, 28.1–28.6. *(p. 163)*

Ducruix, S. (1999). *Dynamique des intéractions Acoustique-Combustion*. Châtenay-Malabry, France: Ph. D. thesis, Lab. EM2C, Ecole Centrale Paris. *(p. 229)*

Ducruix, S., D. Durox, and S. Candel (2000). Theoretical and experimental determination of the transfer function of a laminar premixed flame. *Proceedings of the Combustion Institute 28*, 765–773. *(p. 6, 141)*

Ducruix, S., T. Schuller, D. Durox, and S. Candel (2003). Combustion dynamics and instabilities: Elementary coupling and driving mechanisms. *Journal of Propulsion and Power 19*(5), 722–734. *(p. 5, 158)*

Durox, D., A. L. Birbaud, and S. Candel (2004, Sept.). Dynamique de l'écoulement dans les flammes oscillantes prémélangées. In *9eme Congrès Francophone de Vélocimétrie Laser*, Institut Von Karman & Université de Bruxelles, Belgium. AFVL. *(p. 43)*

Durox, D., S. Ducruix, and F. Lacas (1999). Flow seeding with an air nebulizer. *Experiments in Fluids 27*, 408–413. *(p. 43)*

Durox, D., T. Schuller, and S. Candel (2002). Self-Sustained Oscillations of a Premixed Impinging Jet Flame on a Plate. *Proceedings of the Combustion Institute 29*, 69–75. *(p. 65)*

Durox, D., T. Schuller, and S. Candel (2005). Combustion dynamics of inverted conical flames. *Proceedings of the Combustion Institute 30*, 1717–1724. *(p. 6, 111, 141, 190, 208)*

Durox, D., T. Schuller, N. Noiray, and S. Candel (2009). Experimental analysis of nonlinear flame transfer functions for different flame geometries. *Proceedings of the Combustion Institute 32*, 1391–1398. *(p. 112, 140, 209)*

Eckstein, J., E. Freitag, C. Hirsch, and T. Sattelmayer (2006). Experimental study on the role of entropy waves in low-frequency oscillations in a RQL combustor. *Journal of Engineering for Gas Turbines and Power, ASME Trans. 128*, 264–270. *(p. 54)*

Ffwocs-Williams, J. and M. S. Howe (1975). The generation of sound by density inhomogeneities in low Mach number nozzle flows. *Journal of Fluid Mechanics 70*, 605–622. *(p. 76)*

Fleifil, M., A. Annaswamy, Z. Ghoneim, and A. Ghoniem (1996). Response of a laminar premixed flame to flow oscillations : a kinematic model and thermoacoustic instability results. *Combustion and Flame 106*(4), 487–510. *(p. 191)*

Freitag, M. and J. Janicka (2007). Investigation of a strongly swirled unconfined premixed flame using LES. *Proceedings of the Combustion Institute 31*,

1477–1485. *(p. 111)*

Fritsche, D., M. Füri, and K. Boulouchos (2007). An experimental investigation of thermoacoustic instabilities in a premixed swirl-stabilized flame. *Combustion and Flame 151*, 29–36. *(p. 6, 110, 209)*

Galley, D. (2006). *Etude de la stabilisation de flammes turbulentes prévaporisées prémélangées pauvres*. Ph. D. thesis, Laboratoire EM2C, Ecole Centrale Paris. *(p. 18, 21)*

Gentemann, A., C. Hirsch, K. Kunze, F. Kiesewetter, T. Sattelmayer, and W. Polifke (2004). Validation of flame transfer function reconstruction for perfectly premixed swirl flames. In *ASME Paper GT2004-53776, ASME Turbo Expo 2004*, Vienna, Austria. *(p. 112, 130, 142, 191, 210)*

Glegg, S. (1999). The response of a swept blade row to a three-dimensional gust. *Journal of Sound and Vibration 227*(1), 29–64. *(p. 8, 79)*

Greitzer, E., C. Tan, and M. Graf (2004). *Internal Flow - Concepts and Applications*. Cambridge University Press. *(p. 8, 79)*

Grinstein, F. and C. Fureby (2005). LES studies of the flow in a swirl gas combustor. *Proceedings of the Combustion Institute 30*, 1791–1798. *(p. 111)*

Gupta, A., D. Lilley, and N. Syred (1984). *Swirl flows*. Abaqus Press. *(p. 12, 26, 28, 33, 34, 43, 110, 146, 249)*

Harrje, D. and F. Reardon (1972). Liquid rocket combustion instabilities. *SP-194*. *(p. 5)*

Hirsch, C., D. Fanaca, P. Reddy, W. Polifke, and T. Sattelmayer (2005). Influence of the swirler design on the flame transfer function of premixed flames. In *ASME Paper GT2005-68195, ASME Turbo Expo 2005*, Nevada, USA. *(p. 8, 21, 80, 112, 141, 152, 158, 210)*

Horlock, J. (1978). *Actuator disk theory - Discontinuities in thermo-fluid dynamics*. McGraw-Hill International Book Co. *(p. 8, 79)*

Howe, M. S. (1975). Contributions to the theory of aerodynamic sound, with application to excess jet noise and the theory of the flute. *Journal of Fluid Mechanics 71*(4), 625–673. *(p. 76)*

Huang, Y. and V. Yang (2005). Effect of swirl on combustion dynamics in a lean-premixed swirl-stabilized combustor. *Proceedings of the Combustion Institute 30*, 1775–1782. *(p. 13, 111, 142, 143, 159)*

Huang, Y. and V. Yang (2009). Dynamics and stability of lean-premixed swirl-stabilized combustion. *Progress in Energy and Combustion Sciences 35*, 293–384. *(p. 5, 6, 13, 79, 110, 111, 113, 130, 142, 143, 159, 192)*

Hunt, J., A. Wray, and P. Moin (1988). Eddies, stream, and convergence zones in turbulent flows. *Technical Report CTR-S88, Center for Turbulence Research*. *(p. 184)*

Iacona, E., J. Taine, and B. Tamain (2009). *Les enjeux de l'énergie*. Dunod. *(p. 4)*

Ishizuka, S., T. Murakami, T. Hamasaki, K. Koumura, and R. Hasegawa

(1998). Flame speeds in combustible vortex rings. *Combustion and Flame 113*, 542–553. *(p. 132)*

Ivanic, T., E. Foucault, and J. Pecheux (2003). Dynamcis of swirling jet flows. *Experiments in Fluids 35*, 317–324. *(p. 26, 33, 34)*

Janardan, B. A., B. R. Daniel, and B. T. Zinn (1976). Measurements of Acoustic responses of Gaseous Propellant Injectors. *Journal of Sound and Vibration 47*(4), 559–569. *(p. 54)*

Jones, B., J. Lee, B. Quay, D. Santavicca, K. Kim, and S. Srinivasan (2010). Flame response mechnanisms due to velocity perturbations in a lean premixed gas turbine combustor. In *ASME Paper GT2010-22380, ASME Turbo Expo 2010*, Glasgow, Scotland. *(p. 210)*

Kaji, S. and T. Okazaki (1970). Propagation of sound waves through a blade row. 1. Analysis based on semi-actuator disk theory. *Journal of Sound and Vibration 11*(3), 339. *(p. 8, 79)*

Kang, D. M., F. E. C. Culick, and A. Ratner (2007). Combustion dynamics of a low-swirl combustor. *Combustion and Flame 151*, 412–425. *(p. 110, 111, 145, 209)*

Kauffmann, A., F. Nicoud, and T. Poinsot (2002). Flow forcing techniques for numerical simulations of combustion instabilities. *Combustion and Flame 131*(4), 371–385. *(p. 165)*

Kaufmann, A., F. Nicoud, and T. Poinsot (2002). Flow forcing techniques for numerical simulation of combustion instabilities. *Combustion and Flame 131*, 371–385. *(p. 191)*

Külsheimer, C. and H. Büchner (2002). Combustion dynamics of turbulent swirling flames. *Combustion and Flame 131*, 70–84. *(p. 5, 7, 45, 111, 112, 121, 142, 143, 208)*

Keller, J. (1995). Thermoacoustic oscillations in combustion chambers of gas turbines. *AIAA Journal 33*(12), 2280–2287. *(p. 7, 111)*

Kendrick, D., T. Zsak, and E. Zukoski (1996). *Unsteady Combustion*, Chapter 3. An experimental and numerical investigation of premixed combustion in a vortex in a laboratory dump combustor, pp. 33–69. Kluwer Academic Publishers. *(p. 54)*

Kim, D., J. G. Lee, B. D. Quay, D. Santavicca, K. Kim, and S. Srinivasan (2010). Effect of flame structure on the flame transfer function in a premixed gas turbine combustor. *Journal of Engineering for Gas Turbines and Power 132*(2), 757–765. *(p. 5, 7, 111, 112, 117, 159)*

Kim, K., H. Lee, J. Lee, B. Quay, and D. Santavicca (2009). Flame transfer function measurements and instability frequency prediction using a thermoacoustic model. In *ASME Paper GT2009-60026, Proceedings of ASME Turbo Expo 2009*, Orlando, USA. *(p. 112, 159, 160, 213)*

Kim, K., J. Lee, H. Lee, B. Quay, and D. Santavicca (2010). Characterization of forced flame response of swirl-stabilized turbulent lean-premixed flames in a gas turbine combustor. *Journal of Engineering Gas Turbines*

and Power 132, 4. *(p. 113, 119, 160, 191)*

Kim, K., J. Lee, B. Quay, and D. Santavicca (2010a). Spatially distributed flame transfer functions for predicting combustion dynamics in lean premixed gas turbine combustors. *Combustion and Flame (In Press) 10.1016/j.combustflame.2010.04.016*. *(p. 208, 210, 224)*

Kim, K., J. Lee, D. Quay, and D. Santavicca (2010b). Experimental investigation of the nonlinear response of swirl stabilized flames to equivalence ratio oscillations. In *ASME Paper GT2010-23023, ASME Turbo Expo 2010*, Glasgow, Scotland. *(p. 210)*

Koch, W. (1971). Transmission of sound waves through a blade row. *Journal of Sound and Vibration 18*(1), 111. *(p. 8, 79)*

Komarek, T. and W. Polifke (2010). Impact of swirl fluctuations on the flame response of a perfectly premixed swirl burner. *Journal of Engineering for Gas Turbine and Power 132*(061053). *(p. 8, 13, 21, 80, 113, 130, 143, 159, 192)*

Kopitz, J., A. Huber, and T. Sattelmayer (2005). Thermoacoustic Stability Analysis of an Annular Combustion Chamber With Acoustic Low Order Modeling and Validation Against Experiment. In *ASME Paper GT2005-68797*, Reno, Nevada, USA, pp. 583–593. *(p. 209)*

Kopitz, J. and W. Polifke (2008). CFD-based application of the Nyquist criterion to thermo-acoustic instabilities. *Journal of Computational Physics 227*(14), 6754–6778. *(p. 191)*

Kornilov, V., R. Rook, J. ten Thije Boonkkamp, and de Goey L.P.H. (2009). Experimental and numerical investigation of the acoustic response of multi-slit Bunsen burners. *Combustion and Flame 156*(10), 1957–1970. *(p. 190)*

Kornilov, V. N., K. R. A. M. Schreel, and L. P. H. de Goey (2007). Experimental assessment of the acoustic response of laminar premixed Bunsen flames. *Proceedings of the Combustion Institute 31*, 1239–1246. *(p. 77, 141)*

Kulkarni, R. and F. Nicoud (17-20 May 2010). Predicting the amplitude of limit cycles by using a Helmholtz solver. In *International Summer School and Workshop on Non-Normal and Nonlinear Effects in Aero and Thermoacoustics*, Munchen, Germany. Technische Universitat Munchen. *(p. 140)*

Lawn, C. J. (2000). Thermo-acoustic frequency selection by swirled premixed flames. *Proceedings of the Combustion Institute 28*, 823–830. *(p. 110, 208)*

Lee, S., S. Seo, J. Broda, S. Pal, and R. Santoro (2000). An experimental estimation of mean rate and flame structure during combustion instability in a lean premixed gas turbine combustor. *Proceedings of the Combustion Institute 28*, 775–782. *(p. 45, 110, 121)*

Lefebvre, A. (1998). *Gas turbine combustion*. Taylor and Francis. *(p. 53, 54, 62)*

Leyko, M., F. Nicoud, and T. Poinsot (2009). Comparison of direct and indirect combustion noise mechanisms in a model combustor. *AIAA Journal 47*(11),

2709–2716. *(p. 76)*

Liang, H. and Maxworthy (2005). An experiment investigation of swirling jets. *Journal of Fluid Mechanics 525*, 115–159. *(p. 34)*

Lieuwen, T. (2005). Nonlinear kinematic response of premixed flames to harmonic velocity disturbances. *Proceedings of the Combustion Institute 30*, 1725–1732. *(p. 53, 191)*

Lieuwen, T. and Y. Neumeier (2002a). Nonlinear pressure-heat release transfer function measurements in a premixed combustor. *Proceedings of the Combustion Institute 29*, 99–105. *(p. 9, 209)*

Lieuwen, T. and Y. Neumeier (2002b). Thermoacoustics stability chart for high-intensity gas turbine combustion systems. *Combustion Sciences and Technology 174*, 99–128. *(p. 209)*

Lieuwen, T. and B. Zinn (1998). The role of equivalence ratio fluctuations in driving combustion instabilities in low NOx gas turbines. *Proceedings of the Combustion Institute 27*, 1809–1816. *(p. 5, 7, 111, 208)*

Lieuwen, T. C. and V. Yang (Eds.) (2005). *Combustion instabilities in gas turbines, Operational experience, Fundamental mechanisms, and Modeling*, Volume 210 of *Progress in Astronautics and Aeronautics*. American Institute of Aeronautics and Astronautics, Inc. *(p. 5, 110, 157, 158)*

Lilley, D. (1977). Swirl flows in combustion : a review. *AIAA Journal 15*(8), 1065–1078. *(p. 110, 209)*

Lipatnikov, A. and P. Sathiah (2005). Effects of turbulent flame development on thermoacoustic oscillations. *Combustion and Flame 142*, 130–139. *(p. 191, 192)*

Lohrmann, M., H. Buchner, N. Zazalis, and W. Krebs (2003). Flame transfer function charcteristics of swirl flames for gas turbine applications. In *Proceedings of the ASME Turbo Expo*, Volume GT2003-38113, Atlanta, USA. *(p. 191)*

Lucca-Negro, O. and T. O'Doherty (2001). Vortex breakdown : a review. *Progress in Energy and Combustion Science 27*(4), 431–481. *(p. 18)*

Marble, F. and S. Candel (1977). Acoustic disturbance from gas nonuniformities convected through a nozzle. *Journal of Sound and Vibration 55*, 225–243. *(p. 76)*

Martin, C., L. Benoit, Y. Sommerer, F. Nicoud, and T. Poinsot (2006). LES and acosutic analysis of combustion instability in a staged turbulent swirled combustor. *AIAA Journal 44*(4), 741–750. *(p. 164)*

Mattingly, J. and G. Oates (1986). An experimental investigation of the mixing of coannular swirling flows. *AIAA Journal 24*, 785–792. *(p. 33, 34)*

Meier, W., P. Weigand, X. R. Duan, and R. Giezendanner-Thoben (2007). Detailed characterization of the dynamics of thermoacoustic pulsations in a lean premixed swirl flame. *Combustion and Flame 150*, 2–26. *(p. 6, 110)*

Mongia, H. (2004). Perspective of combustion modeling for gas turbine combustors. *AIAA Paper 2004-0156 156*, 1–33. *(p. 111)*

Morfey, C. (1973a). Amplification of aerodynamic noise by convected flow inhomogeneities. *Journald of Sound and Vibration 31*(4), 391–397. *(p. 76)*

Morfey, C. (1973b). Rotating blades and aerodynamic sound. *Journal of Sound and Vibration 28*(3), 587–617. *(p. 8, 79)*

Munjal, M. L. (1987). *Acoustics of Ducts and Mufflers*. John Wiley & Sons, Inc., New York. *(p. 56, 210)*

Nicoud, F., L. Benoit, C. Sensiau, and T. Poinsot (2007). Acoustic Modes in Combustors with Complex Impedances and Multidimensionnal Active Flames. *AIAA Journal 45*(2). *(p. 54, 211)*

Noiray, N. (2007). *Linear and nonlinear stability analysis of acoustic-combustion instabilities, application to multipoint injection systems and passive control strategies*. Ph. D. thesis, Ecole Centrale Paris. *(p. 229)*

Noiray, N., D. Durox, T. Schuller, and S. Candel (2006). Self-Induced Instabilities of Premixed Flames in a Multiple Injection Configuration. *Combustion and Flame 145*(3), 435–446. *(p. 6, 54)*

Noiray, N., D. Durox, T. Schuller, and S. Candel (2008). A unified framework for nonlinear combustion instability analysis based on the flame describing function. *Journal of Fluid Mechanics 615*, 139–167. *(p. 9, 12, 53, 114, 140, 209, 211, 213)*

Noiray, N., D. Durox, T. Schuller, and S. Candel (2009). Mode conversion in acoustically modulated confined jets. *AIAA Journal 47*(9), 2053–2062. *(p. 77)*

Oberlack, M., H. Wenzel, and N. Peters (2001). On symmetries and averaging of the G-equation for premixed combustion. *Combustion Theory and Modeling 5*(3), 363–383. *(p. 196)*

Oschwald, M., Z. Farago, G. Searby, and F. Cheuret (2008). Resonance frequencies and damping of a combustor acoustically coupled to an absorber. *Journal of Propulsion and Power 24*(3), 524–533. *(p. 54)*

Palies, P. (2010). *Dynamique et Instabilités de Combustion des Flammes Swirlées*. Ph. D. thesis, Ecole Centrale Paris. *(p. 34)*

Palies, P., D. Durox, T. Schuller, and S. Candel (2010). The combined dynamics of swirler and turbulent premixed swirling flames. *Combustion and Flame 157*(9), 1698–1717. *(p. 5, 21)*

Palies, P., D. Durox, T. Schuller, P. Morenton, and S. Candel (2009). Dynamics of premixed confined swirling flames. *Comptes Rendus Mecanique 337*(6-7), 395–405. *(p. 41)*

Paschereit, C., E. Gutmark, and W. Weisenstein (2000). Excitation of thermoacoustic instabilities by interaction of acoustics and unstable swirling flow. *AIAA Journal 38*(6), 1025–1034. *(p. 7, 111)*

Paynter, G. (1997). Response of two dimensional cascade to an upstream disturbance. *AIAA Journal 35*(3), 434–440. *(p. 79)*

Peake, N. and E. Kerschen (1997). Influence of mean loading on noise generated by the interaction of gusts with a flat-plate cascade : usptream radiation.

Journal of Fluid Mechanics 347, 315–346. *(p. 8, 79)*

Penner, J., D. Lister, D. Griggs, D. Dokken, and M. McFarland (1999). Aviation and the global atmosphere. *Technical report, Intergovernmental Panel on Climate Change (WMO and UNEP). (p. 4)*

Perterson, R. and H. Emmons (1961). Stability of laminar flames. *Phys. Fluids*, 456–464. *(p. 141)*

Peters, N. (1992). A spectral closure for premixed turbulent combustion in the flamelet regime. *Journal of Fluid Mechanics 242*, 611–629. *(p. 196)*

Plee, S. and A. Mellor (1978). Review of flashback reported in prevaporizing/premixing combustors. *Combustion and Flame 32*, 193–203. *(p. 5, 110, 157)*

Poinsot, T. and S. Lele (1992). Boundary conditions for direct simulations of compressible viscous flows. *Journal of Computational Physics 101*(1), 104–129. *(p. 165)*

Poinsot, T., A. Trouve, D. Veynante, S. Candel, and E. Esposito (1987). Vortex-driven acoustically coupled combustion instabilities. *Journal of Fluid Mechanics 177*, 265–292. *(p. 7, 45, 54, 111)*

Poinsot, T. and D. Veynante (2001). *Theoretical and Numerical Combustion*. Philadelphia: Edwards. *(p. 54, 57, 210)*

Preetham, T. Kumar, and T. Lieuwen (2007). Response of premixed flames to flow oscillations : unsteady curvature effects. In *AIAA Paper 2007-0176*. *(p. 191)*

Preetham, S., H. Santosh, and T. Lieuwen (2008). Dynamics of laminar premixed flames forced by harmonic velocity disturbances. *Journal of Propulsion and Power 24*(6), 1390–1402. *(p. 113, 141, 159, 191)*

Putnam, A. (1971). *Combustion driven oscillations in industry*. New-York: Elsevier. *(p. 5, 208)*

Ribeiro, M. and J. Whitelaw (1980). Coaxial jets with and without swirl. *Journal of Fluid Mechanics 96*, 769–795. *(p. 33, 34)*

Rienstra, S. and A. Hirschberg (2005). *An Introduction to Acoustics*. Eindhoven University of Technology: Report IWDE 92-06. *(p. 65)*

Rockwell, D. and E. Naudascher (1979). Self-sustained oscillation of impinging free shear layers. *Annual Review of Fluid Mechanics 11*, 67–94. *(p. 77)*

Rossiter, J. E. (1964). Wind tunnel experiments on the flow over rectangular cavities at subsonic and transonic speeds. Technical report, Aeronautical Research Council, Ministry of Aviation, London. *(p. 77)*

Roux, S., G. Lartigue, T. Poinsot, U. Meier, and C. Berat (2005). Studies of mean and unsteady flow in a swirled combustor using experiments, acoustic analysis, and large eddy simulations. *Combustion and Flame 141*, 40–54. *(p. 20, 111)*

Sajben, M. and H. Said (2001). Acoustic-wave/blade-row interactions establish boundary conditions for unsteady inlet flows. *Journal of Propulsion and Power 17*(5), 1090–1099. *(p. 80, 84)*

Sarkpaya, T. (1971). On stationnary and travelling vortex breakdowns. *Journal of Fluid Mechanics 45*, 545–559. *(p. 18)*

Sathiah, P. and A. Lipatnikov (2007). Effects of turbulent flame speed development and axial convective waves on oscillations of a long ducted flame. *Combustion Science and Technology 179*(7), 1433–1449. *(p. 191)*

Sattelmayer, T. (2003). Influence of the combustor aerodynamics on combustion instabilities from equivalence ratio fluctuations. *Journal of Engineering for Gas Turbines and Power, ASME Trans. 125*, 11–19. *(p. 54)*

Sattelmayer, T. and W. Polifke (2003). Assessment of methods for the computation of linear stability of combustors. *Combustion Science and Technology 175*(3), 453–476. *(p. 54)*

Schadow, K. C., E. Gutmark, K. J. Wilson, and R. A. Smith (1990). Multi-step design to reduce combustion instabilities. *Journal of Propulsion and Power 6*, 407–411. *(p. 54)*

Schimek, S., J. Moeck, and C. Paschereit (2010). An experimental investigation of the nonlinear response of an atmospheric swirl-stabilized premixed flame. In *ASME Paper GT2010-22827, ASME Turbo Expo 2010*, Glasgow, Scotland. *(p. 210)*

Schönfeld, T. and M. Rudgyard (1999). Steady and unsteady flows simulations using the hybrid flow solver AVBP. *AIAA Journal 37*(11), 1378–1385. *(p. 13, 85, 162)*

Schuermans, B., F. Guethe, D. Pennel, D. Guyot, and C. Paschereit (2009). Thermoacoustic modeling of a gas turbine using transfer functions measured at full engine pressure. In *ASME paper GT2009-59605, ASME Turbo Expo 2009*, Florida, USA. *(p. 110, 208, 211)*

Schuermans, B., W. Polifke, and C. Paschereit (1999). Modeling transfer matrices of premixed flames and comparison with experimental results. In *International Gas Turbine and Aeroengine Congress and Exhibition*, Indianapolis, USA. *(p. 209)*

Schuller, T. (2003). *Mécanismes de couplage dans les Intéractions Acoustique-Combustion*. Châtenay-Malabry, France: Ph. D. thesis, Lab. EM2C, Ecole Centrale Paris. *(p. 57, 229)*

Schuller, T., D. Durox, and S. Candel (2003a). Self-Induced Combustion Oscillations of Laminar Premixed Flames Stabilized on Annular Burners. *Combustion and Flame 135*, 525–537. *(p. 6, 45, 54, 65, 77)*

Schuller, T., D. Durox, and S. Candel (2003b). A unified model for the prediction of laminar flame transfer functions : comparisons between conical and V-flame dynamics. *Combustion and Flame 134*, 21–34. *(p. 113, 141, 191, 192, 198, 200)*

Searby, G., A. Nicole, M. Habiballah, and E. Laroche (2008). Prediction of the efficiency of acoustic damping cavities. *Journal of Propulsion and Power 24*(3), 516–523. *(p. 54)*

Selle, L., L. Benoit, T. Poinsot, F. Nicoud, and W. Krebs (2006). Joint use of

compressible large-eddy simulation and Helmholtz solvers for the analysis of rotating modes in an industrial swirled burner. *Combustion and Flame 145*, 194–205. *(p. 54, 85)*

Selle, L., G. Lartigue, T. Poinsot, R. Koch, K. Schildmacher, W. Krebs, a. P. Prade, B., and D. Veynante (2004). Compressible large eddy simulation of turbulent combustion in complex geometry on unstructured meshes. *Combustion and Flame 137*, 489–505. *(p. 20, 211)*

Sengissen, A., J. Van Kampen, R. Huls, G. Stoffels, J. Kok, and T. Poinsot (2007). LES and experimental studies of cold and reacting flow in a swirled partially premixed burner with and without fuel modulation. *Combustion and Flame 150*, 40–53. *(p. 7, 111)*

Shanbhogue, S., D. Shin, H. Santosh, D. Plaks, and T. Lieuwen (2009). Flame sheet dynamics of bluff body stabilized flames during longitudinal acoustic forcing. *Proceedings of the Combustion Institute 32*(2), 1786–1893. *(p. 77, 113, 141, 159)*

Shin, D., S. Shanbhogue, and T. Lieuwen (2008). Premixed flame kinematics in an axially decaying harmonically oscillating vorticity field. *AIAA Paper*. 2008-5042. *(p. 159)*

Staffelbach, G., L. Gicquel, G. Boudier, and T. Poinsot (2009). Large Eddy Simulation of self excited azimuthal modes in annular combustors. *Proceedings of the Combustion Institute 32*, 2909–2916. *(p. 13, 85, 162)*

Stöhr, M., R. Sadanandan, and W. Meier (2009). Experimental study of unsteady flame structures of an oscillating swirl flame in a gas turbine model combustor. *Proceedings of the Combustion Institute 32*, 2925–2932. *(p. 9)*

Stone, C. and S. Menon (2002). Swirl control of combustion instabilities in a gas turbine combustor. *Proceedings of the Combustion Institute 29*, 155–160. *(p. 113)*

Stow, S. and A. Dowling (2001). Thermoacoustic oscillations in an annular combustor. *ASME paper GT0037*. *(p. 211)*

Straub, D. and G. Richards (1999). Effect of axial swirl vane location on combustion dynamics. In *ASME Turbo Expo*, Volume 99-GT-109, Indianapolis, USA. *(p. 141, 143)*

Syred, N. (2006). A review of oscillation mechanisms and the role of the precessing vortex core (PVC) in swirl combustion systems. *Progress in Energy and Combustion Science 32*, 93–161. *(p. 19, 110, 209)*

Syred, N. and J. Beer (1972). The damping of precessing vortex cores by combustion in swirl generators. *Astraunica Acta 17*, 783–801. *(p. 19)*

Thumuluru, S. and T. Lieuwen (2009). Characterization of acoustically forced swirl flame dynamics. *Proceedings of the Combustion Institute 32*, 2893–2900. *(p. 141)*

Thumuluru, S., H. Ma, and T. Lieuwen (2007). Measurements of the flame response to harmonic excitation in a swirl combustor. *AIAA Journal*. *(p. 7, 45, 110, 111, 112, 121, 158, 191, 209, 210)*

Tran, N., S. Ducruix, and T. Schuller (2009). Passive control of the inlet acoustic boundary condition of a swirled turbulent burner. *Journal of Engineering for Gas Turbines and Power, Accepted.* *(p. 54)*

Vanierschot, M. and E. Van den Bulck (2008). Influence of swirl on the initial merging zone of a turbulent annular jet. *Physics of fluids 20.* 105104. *(p. 142, 183)*

Wang, S., S. Hsieh, and V. Yang (2005). Unsteady flow evolution in swirl injector with radial entry. I. Stationnary conditions. *Physics of Fluids 17*(045106). *(p. 142, 159)*

Wang, S. and V. Yang (2005). Unsteady flow evolution in swirl injector with radial entry. II. External excitations. *Physics of Fluids 17*(045107). *(p. 8, 13, 21, 79, 113, 130, 143, 159, 192)*

Weigand, P., W. Meier, X. Duan, W. Stricker, and M. Aigner (2006). Investigations of swirl flames in a gas turbine model combustor I. Flow field, structures, temperature, and species distributions. *Combustion and Flame 144*, 205–224. *(p. 5, 7, 111)*

Wicker, J.M., G. W. K. S. and V. Yang (1996). Triggering of longitudinal combustion instabilities in rocket motors: nonlinear combustion response. *Journal of Propulsion and Power 12*, 1148–1158. *(p. 9, 209)*

You, D., Y. Huang, and V. Yang (2005). A generalized model of acoustic response of turbulent premixed flame and its application to gas-turbine combustion instability analysis. *Combustion Science and Technology 177*, 1109–1150. *(p. 192)*

Yu, K., A. Trouvé, and J. Daily (1991). Low-frequency pressure oscillations in a model ramjet combustor. *Journal of Fluid Mechanics 232*, 47–72. *(p. 7, 53, 54, 111)*